# Flexible Optoelectronic Biointerfaces Using Quantum Dots and Pseudocapacitive Materials For Photoelectric Stimulation of Neurons

by

**Onuralp Karatüm**

A Dissertation Submitted to the
Graduate School of Sciences and Engineering
in Partial Fulfillment of the Requirements for
the Degree of

Doctor of Philosophy

in

Electrical and Electronics Engineering

KOÇ ÜNİVERSİTESİ

March 2023

# Flexible Optoelectronic Biointerfaces Using Quantum Dots and Pseudocapacitive Materials For Photoelectric Stimulation of Neurons

Koç University

Graduate School of Sciences and Engineering

This is to certify that I have examined this copy of a doctoral dissertation by

**Onuralp Karatüm**

and have found that it is complete and satisfactory in all respects,
and that any and all revisions required by the final
examining committee have been made.

Committee Members:

_____
Assoc. Prof. Dr. Sedat Nizamoğlu (Advisor)

_____
Prof. Dr. Alphan Sennaroğlu

_____
Asst. Prof. Dr. Levent Beker

_____
Assoc. Prof. Dr. Onur Ferhanoğlu

_____
Prof. Dr. Burçin Ünlü

Date: _____

*To Hatice Polat...*

# ABSTRACT

## Flexible Optoelectronic Biointerfaces Using Quantum Dots and Pseudocapacitive Materials for Photoelectric Stimulation of Neurons

**PhD Thesis**

**Onuralp Karatüm**
**Doctor of Philosophy in Electrical and Electronics Engineering**
**March 2023**

Bioelectronic medicine offers significant benefits against a wide variety of neurological disorders such as Parkinson's disease, depression, retinal degeneration, and hearing loss. Today neurostimulation constitutes a market size on the order of several billion dollars and it is one of the gold-standards practiced in neuroscience field for unraveling the working principles of brain. Fundamentally, it utilizes electrical stimulation to control and modulate the neural signals at single cell and network level. The conventional electrical stimulation devices use wires to induce potential differences for producing ionic currents at the abiotic-biotic interface. However, wired electrodes increase the surgical invasiveness and complexity, and adds to the surgery time of implants. Moreover, wires can be dislocated and fractured due to unintentional tissue movements, which can lead to unwanted side effects. Alternatively, optoelectronic biointerfaces convert light to photovoltages and provide localized and nongenetic neural stimulation without requiring wired systems. However, little attention has been paid to the applicability of non-silicon optoelectronics in neural stimulation.

Colloidal quantum dots (QDs) exhibit promising optoelectronic properties for neural stimulation such as high absorption coefficient, which allows fabrication of flexible and light-weight devices; tunable absorption profile, which facilitates extension of frequency spectrum from visible to near-infrared (NIR) region; and excellent optical stability, which minimizes the photobleaching and photodegradation effects during long-term use. Despite the ubiquitous use of QDs in different optoelectronic applications (e.g., light-emitting devices, solar cells, and photodetectors), their use in neural stimulation has been limited. This thesis investigates the use of QDs for developing novel photovoltaic neurostimulators that can be built on flexible substrates with ultra-thin layers; have high photoresponsivity with improved charge injection; and offer a wide operation window that covers visible and near-infrared (NIR) spectrum.

So far, most neural stimulation studies by optoelectronic biointerfaces focused on

activation of neurons by inducing action potentials. However, neural silencing is also beneficial for examination of neural mechanisms. For that, we demonstrate that indium phosphide (InP)-based QDs can be integrated into two different photovoltaic device architectures to build neural stimulating and silencing photoelectrodes. We nanoengineer InP/ZnS core/shell nanostructure and device structure to maximize the Faradaic photocurrent to control neural activity. Instead of Faradaic charge injection, which raises concerns due to the possibility of irreversible chemical reactions at the electrode-electrolyte interface, capacitive charge injection is a safer mechanism because of the charging/discharging of the double layer capacitance, which does not involve direct charge transfer between the electrode and electrolyte. For that, we introduced a QD-polymer donor-acceptor nanoheterojunction to generate capacitive photocurrent and control the faradaic and capacitive components of the photoresponse that leads to capacitive-dominant charge injection by optimizing the nanoheterojunction parameters.

One of the main drawbacks of capacitive photostimulation electrodes has been the limited photogenerated charge densities due to the fast photocurrent spikes by the double-layer. We show that this problem can be overcome by integrating supercapacitor ruthenium oxide ($RuO_2$) into a photocapacitive device architecture. $RuO_2$ integration leads to over-an-order-of-magnitude improved charge injection density owing to the high interfacial capacitance of $RuO_2$ resulting from reversible redox reactions. This enables safe photostimulation of hippocampal neurons with light intensities below 1 mW $mm^{-2}$ via visible light. Furthermore, shifting the photoresponse spectrum to NIR wavelengths is advantageous to enhance the light penetration depth into the tissues. For that we demonstrate NIR-sensitive QD-based neurostimulators in a flexible and ultrathin device structure that operates within the ocular safety limits.

The findings reported in this thesis are important in terms of improving efficiency, safety, and applicability of QD-based optoelectronic neural interfaces in different neurostimulation scenarios. Demonstrated high photoresponsivity levels, safe charge injection mechanisms, and NIR-operation are especially valuable for building safe and efficient optoelectronic neuroprostheses. Thus, this thesis paves the way toward a QD-based photovoltaic retinal implant against blindness due to degeneration of photoreceptors.

# ÖZETÇE

## Nöronların Fotoelektrik Uyarımı için Kuantum Nokta ve Pseudokapasitör Malzeme Tabanlı Esnek Optoelektronik Biyoarayüzler

**Doktora Tezi**

**Onuralp Karatüm**
**Elektrik Elektrik Mühendisliği Doktora**
**Mart 2023**

Biyoelektronik tıp Parkinson hastalığı, depresyon, retinal dejenerasyon ve işitme kaybı gibi birçok farklı nörolojik hastalıkların tedavisi için önemli faydalar sunmaktadır. Günümüzde nörouyarım birkaç milyar dolar ölçeğinde bir market büyüklüğüne sahiptir ve aynı zamanda nörobilim alanında beynin çalışma mekanizmalarının açığa çıkarılmasında kullanılan temel yöntemlerden bir tanesidir. Nörouyarım temel olarak elektrik uyarımını kullanarak tek hücre ve ağ düzeyinde nöral sinyallerin modüle edilmesini hedefler. Geleneksel elektrik uyarım aygıtları abiyotik-biyotik arayüzlerde bir potansiyel farkı oluşturarak iyonik akım üretmek için kablolu sistemler kullanır. Fakat, kablolu elektrot kullanımı implantasyon sırasında cerrahi invazifliği ve karmaşıklıkları arttırmakta ve cerrahi operasyon süresini uzatmaktadır. Ayrıca, implant edilmiş kablolar istemsiz doku hareketleri sebebiyle yer değişikliği ve kırılmaya uğrayabilir, bu da istenmeyen yan etkilere sebep olabilir. Alternatif olarak, optoelektronik biyoarayüzler ışığı fotovoltaja çevirerek kablolara ihtiyaç duymadan lokalize ve genetik olmayan bir nöral uyarım sağlar. Ancak şimdiye kadar silikon temelli olmayan optoelektronik teknolojilerin nöral uyarım alanındaki uygulamaları yeterince ilgi görmemiştir.

Kolloidal kuantum noktalar (KN) nöral uyarım uygulamaları için avantajlı optoelektronik özelliklere sahiptir. Örneğin, yüksek soğurma katsayıları sayesinde esnek ve hafif aygıtların üretimine izin verir; ayarlanabilir soğurma profilleri sayesinde frekans spektrumunun görünür dalga boylarından kızılötesine kadar genişletilmesini sağlar; ve üst düzey optik stabiliteleri sayesinde uzun süreli kullanımlarda fotodegradasyon etkilerinin minimize edilmesinin önünü açarlar. KN'ın ışık yayan diyotlar, güneş pilleri ve fotodetektörler gibi farklı optoelektronik teknolojilerdeki yaygın kullanımına karşın nöral uyarım alanındaki kullanımı sınırlı kalmıştır. Bu tez, KN'ın esnek substratlar üzerine inşa edilebilen, yüksek foto-duyarlılık ve arttırılmış yük enjeksiyon kapasitesine sahip olan ve görünür ve kızılötesini kapsayan geniş bir çalışma aralığında opere eden özgün fotovoltaik nörouyarıcıların geliştirilmesinde kullanımını incelemektedir.

Şimdiye kadar, optoelektronik biyoarayüzler ile yapılan çoğu nöral uyarım çalışması nöronların aksiyon potansiyeli indüklenmesi ile aktive edilmesine odaklanmıştır. Fakat nöral mekanizmaların incelenmesinde nöral susturma da nöral uyarım gibi kullanışlı bir uygulamadır. Bunun için tezimizde öncelikle indiyum fosfat (InP) tabanlı KN'ın iki farklı fotovoltaik aygıt mimarisine entegrasyonu ile nöral uyarım ile birlikte nöral susturma fonksiyonuna da sahip fotoelektrotlar üretilebileceğini gösterdik. İndiyum fosfat/çinko sülfit çekirdek/kabuk yapısının ve aygıt mimarisinin nanomühendislik aracılığıyla optimizasyonu ile nöral aktivitenin kontrolü için faradayik fotoakımı maksimize ettik. Elektrot-elektrolit arayüzünde geri dönüştürülemez kimyasal reaksiyonlara sebebiyet verebilecek faradayik yük enjeksiyonuna kıyasla elektrotla elektrolit arasında yük transferi olmadan çift katmanlı kapasitörün yüklenme/boşalmasıyla çalışan kapasitif yük enjeksiyonu daha güvenli bir metottur. Bu sebeple, kapasitif akım üretebilmek ve fotoakımın kapasitif ve faradayik bileşenlerini kontrol edebilmek amacıyla KN-polimer donör-alıcı nanoheteroeklem yapısını ileri sürdük ve bu yapının kapasitif ağırlıklı yük enjeksiyon mekanizmasına sahip olması için nanoheteroeklem parametrelerini optimize ettik.

Kapasitif fotouyarım elektrotlarının temel dezavantajlarından birisi çift-katmanın yüklenme/boşalması esnasındaki hızlı fotoakım yükseliş/inişleri sonucu sınırlı miktarda fotoyük yoğunluğu üretebilmesidir. Tezimizde bu problemin süperkapasitör rutenyum oksit ($RuO_2$) malzemesinin fotokapasitif aygıt mimarisine entegrasyonu ile çözülebileceğini gösterdik. $RuO_2$ entegrasyonu, $RuO_2$'nin geri dönüşebilir redoks reaksiyonlar sonucu oluşan yüksek arayüz kapasitansı sayesinde yük enjeksiyon yoğunluğunda on katın üzerinde bir artışa yol açmıştır. Bu da birincil hipokampal nöronların 1 mW $mm^{-2}$ ışık şiddetinin altındaki görünür ışık ile güvenli bir şekilde fotouyarımını sağlamıştır. Buna ek olarak, ışık duyarlılık spektrumunu kızılötesi dalga boylarına kaydırmak dokulara ışık penetrasyonunu arttıracağı için avantaj oluşturur. Bu amaçla son olarak kızılötesine duyarlı, KN tabanlı, esnek ve ultra-ince yapıda ve oküler güvenlik limitleri içerisinde uyarım yapabilen nörouyarım aygıtları gösterdik.

Bu tezde sunulan bulgular KN tabanlı optoelektronik nöral arayüzlerin verimliliklerini, ve güvenli çalışmalarını iyileştirmek ve farklı nörouyarım senaryolarında kullanımlarını göstermek açısından önem arz etmektedir. Elde edilen yüksek fotoduyarlılık seviyeleri, güvenli yük enjeksiyon mekanizmaları ve kızılötesinde operasyon gibi bulgular özellikle güvenli ve verimli optoelektronik nöral protezlerin geliştirilmesi için değerlidir. Böylelikle bu tez fotoreseptörlerin dejenerasyonu sonucu oluşan körlüğe karşı KN tabanlı fotovoltaik retinal implantların geliştirilmesinin yolunu açmaktadır.

# ACKNOWLEDGMENTS

First and foremost, I would like to thank my advisor Prof. Sedat Nizamoğlu, who provided me with incalculable amount of technical, scientific, and motivational support during my PhD. His motivation for achieving the most difficult tasks and his endless curiosity for revealing the unknown have always inspired me and will continue to do so throughout my future career. Moreover, his warm and friendly personality created a fun atmosphere during our conversations and discussions on basically any issue. I feel privileged working with him and owe him many thanks.

I would like to thank my thesis committee members, Prof. Alphan Sennaroğlu and Prof. Levent Beker, for their support and guidance throughout my thesis progress. I also thank Prof. Onur Ferhanoğlu and Prof. Burçin Ünlü for attending my thesis defense as jury members and providing valuable feedbacks for improving my thesis.

Many thanks to the former and current members of IDEALAB for contributing to this thesis by questioning, commenting, discussing, and creating the best work environment that I could have imagined.

I thank my father, my mother, and my brother from the bottom of my heart for their endless love and support.

Finally, I thank my friends, and coci & the red ball.

I acknowledge the financial support of the Scientific and Technological Research Council of Turkey (TÜBİTAK) (2211/A National PhD Scholarship Program, Project No. 119N544), and European Research Council (ERC) under the European Union's Horizon 2020 Research and Innovation Programme (639846, 101045289).

# TABLE OF CONTENTS

# LIST OF TABLES

# LIST OF FIGURES

# Chapter 1

# INTRODUCTION

Neural stimulation is an important field of bioelectronics that aims to provide non-invasive and precise stimulation of neurons. Modulation of neural activity has unrevealed the mechanisms of numerous neural processes and it has also been used for therapeutic purposes for Although the conventional way to control the neural activity is direct electrical stimulation, there is an active search for wireless and less invasive alternatives. Optical neuromodulation is a rapidly growing field due to the inherently noninvasive nature of light and the exceptional spatiotemporal resolution provided by optical systems. Benefiting from these advantages, optical neuromodulation platforms have had a far-reaching impact specifically in neuroscience research and certain systems have already been translated into clinical studies.

Among optical techniques, optogenetics has been the dominating technique since its discovery in the early 2000s because of its unmatched spatiotemporal resolution. However, the genetic manipulation involved in optogenetics raises important concerns when it comes to human studies and clinical applications. This limitation triggered the emergence of nongenetic optical techniques for modulating neural activity such as photoelectrochemical, photothermal, and photoacoustic neurostimulation. Among such nongenetic platforms, optoelectronic neural interfaces draw attention because of their high temporal resolution, wireless and minimally invasive operation, and their well-understood electrical stimulation route. Optoelectronic neural interfaces already showed promising performance in cultured neuron studies and high-resolution in vivo neurostimulation studies. Specifically, due to their operational similarities with the retinal photoreceptors, optoelectronic neural interfaces have been widely studied for retinal prosthetic devices for the treatment of retinal degeneration diseases.

To date, various semiconductor materials have been used to build effective optoelectronic neural interfaces. Silicon has been the primary choice due to the maturity and efficiency of silicon photodiodes and photovoltaics. Moreover, its absorption in near-infrared spectrum makes it advantageous for operation in the tissue transparency window. Later, different studies investigated the potential of inorganic nanocrystals and organic semiconductors and paved the

way for further investigation of these material platforms for optoelectronic neural stimulation. One of the major advantages of organic semiconductors and inorganic nanomaterials compared to silicon is their higher absorption coefficients in visible and NIR spectrum, which enables fabrication of thinner, thus, flexible devices that can offer enhanced mechanical conformability while interfacing these devices with neural tissues. However, efficiency of these devices in terms of light-to-charge conversion is still lower than silicon-based ones. Hence, innovative device designs and alternative interdisciplinary approaches are required to build more efficient devices with safe charge injection mechanisms to perform photostimulation with low light intensities.

Colloidal quantum dots (QDs) are one of the primary materials in the optoelectronic technologies because of their outstanding optoelectronic and structural properties such as tunable absorption/emission profile, high absorption coefficient, high photoluminescence quantum yield, and structural versatility owing to enabling core/shell structures and doping with another material. Such features of QDs led to the development of efficient light-emitting devices (LEDs) and photovoltaic devices in the optoelectronics field. Moreover, they have shown successful performance in bioimaging studies due to their photostability. However, their application in neural stimulation field lagged behind silicon and organic semiconductors. An important part of this thesis (Chapter 3 and 6) demonstrates this unrevealed potential of QDs for optoelectronic neural stimulation applications and shows effective QD-based devices that can stimulate neurons in a temporally precise manner in visible and NIR spectrum. The remaining parts of the thesis address two critical aspects of optoelectronic neural interfaces, i.e., the charge injection mechanism (Chapter 4) and photogenerated charge density (Chapter 5), and provide strategies for building safer and more efficient optoelectronic neural stimulation devices. The organization of this thesis is as follows:

The first chapter provides a general introduction about optical stimulation, optoelectronic neural interfaces and different material systems used in optoelectronic neural interfaces.

The second chapter gives basic background information regarding the electrical properties of cells, action potential generation in excitable cells, different neural stimulation techniques (i.e., electrical, thermal, mechanical, optical) and their advantages/disadvantages. We elaborate on the operation principles of photovoltaic neural interfaces, quantum dots and their use in optoelectronic neural interfaces, and strategies to improve photocapacitive device efficiencies as these are the main subjects of this thesis.

The third chapter demonstrates how quantum dots can be used to design and fabricate

optoelectronic devices that can modulate neural activity in both directions, i.e., by inducing depolarization or hyperpolarization. This chapter is important as it shows how heavy-metal-free quantum dots can be integrated into different photovoltaic device architectures for performing neural stimulation and silencing.

The fourth chapter shows the formation of a nanoheterojunction between a quantum dot and an organic polymer and its integration into a thin-film photovoltaic device for developing heavy-metal-free quantum dot-based neural interfaces that have capacitive-dominant charge injection mechanism to obtain safer optoelectronic neural interfaces.

The fifth chapter presents a detailed investigation on the amalgamation of supercapacitor technology and optoelectronics in one device design to improve the photogenerated charge density of capacitive optoelectronic neural interfaces. We integrated ruthenium oxide ($RuO_2$) supercapacitor material into an organic photovoltaic device architecture to build flexible and light-efficient neural interfaces that operate via capacitive and reversible faradaic charge injection mechanisms.

The sixth chapter covers the development of a quantum dot-based optoelectronic neural interface that can stimulate primary neurons in NIR spectrum. This study is critical for combining the knowledges of the previous studies to develop a supercapacitor-integrated quantum dot-based neural interface, and on top of that, shifting the device operation spectrum to NIR for modulating neural activity in tissue transparency window.

The seventh chapter concludes the thesis by providing an overlook of the outcomes of the covered studies, their contribution to the field, and future aspects of the findings.

# Chapter 2

# BACKGROUND

The history of neurostimulation dates to Ancient Greece. Descriptions of numbness producing electric fishes (electric ray, torpedo ray) can be found in the scripts of Plato, Aristotle, Pliny, and Plutarch.[1] Roman physician Scribonius Largus attempted to use the electricity of torpedo ray to alleviate headache by placing a live torpedo fish over the scalp.[2] A Persian eleventh century physician, Ibn-Sidah, suggested that electrostimulation with a live electric fish can be used in the treatment of epilepsy.[3] Throughout the earlier stages of neurostimulation, further studies attemted to use the bioelectricity generated by electric fish for the treatments of gout, depression, and seizures.[4]

The discovery of animal electricity by Luigi Galvani and the pioneering neurostimulation experiments on the human brain in the eighteenth century[4, 5] along with the developments in the instrumental recording of electrophysiological events[6] led to better understanding and use of neurostimulation not only for therapeutic purposes, but also for unravelling the working principles of brain. Today, stimulation of central and peripheral nervous systems is a well-established paradigm both for fundamental research and therapeutic applications. Neurostimulation allowed Krause to generate the first detailed map of the human motor cortex in early twentieth century.[7] This was further improved by Penfield et. al., leading to the expanded map of the human motor cortex that shows the localization of various brain functions. [8] Neurostimulation has also paved the way for proposing effective treatments for various disorders such as stroke, epilepsy, depression, visual and hearing dysfunctions, tremor, Parkinson's disease, and Alzhemier.[9] Certain neurostimulation techniques received the approval of the Food and Drug Administration (FDA) for treating different neurological disorders: deep brain stimulation (DBS) for the treatments of Parkinson's disease, dystonia, and essential tremor and transcranial magnetic stimulation (TMS) for major depressive disorder.[10]

Non-contact stimulation methods remove the need for surgery as they enable reaching neurons in the central or peripheral nervous systems by the penetration of waves into the brain or

peripheral nerves. Optical and magnetic stimulation tools use electromagnetic waves, while ultrasound stimulation employs acoustic waves to reach and influence the desired neural tissues via non-invasive routes. Intact animal and human nerves deep inside the brain or other body parts can be stimulated this way without making any contact to the body. Indeed, different regions of the electromagnetic and acoustic spectrum have been studied for altering the electrical activity of neural tissues. Figure 1 shows a schematic of the electromagnetic and acoustic spectrum, indicating the intervals of frequencies used for neural stimulation applications.

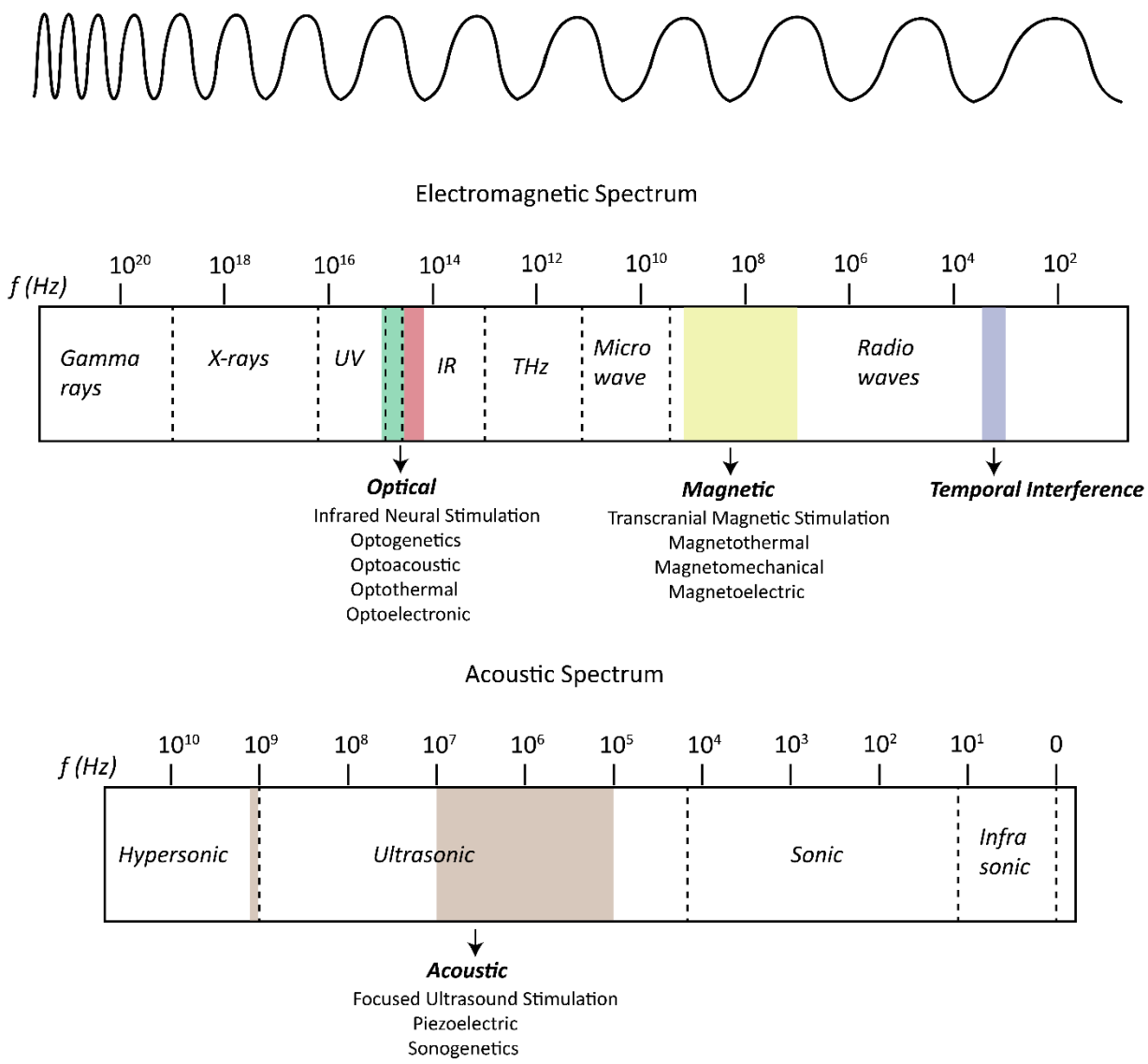


**Figure 1:** Electromagnetic and acoustic spectrum with the shaded areas that show the frequency intervals that are used for neural stimulation applications.

## *2.1 Modulation Mechanism of Neural Activity*

### *2.1.1. Membrane Potential*

Modulation of neural activity occurs through modulation of membrane potential. Cell membrane (or plasma membrane) consists of a phospholipid bilayer that separates the intracellular and extracellular environment. Plasma membrane maintains an electrical potential difference between the intracellular and extracellular environment, which is called membrane potential of a cell. This potential difference arises from the intracellular and extracellular ion concentration differences. The ionic concentration differences cause diffusion of ions through the membrane. Since the ion channels on the membrane are selectively permeable to certain ions, ionic diffusion in a particular direction (i.e., intracellular to extracellular or vice versa) causes electrical charging of the membrane that operates against the diffusion gradient. This system reaches to an equilibrium at a certain electric potential, i.e., membrane potential, for which there is no net ionic movement through the membrane. In fact, each ion (e.g., Sodium ($Na^+$), Potassium ($K^+$), Chloride ($Cl^-$), and Calcium ($Ca^{2+}$) has its own equilibrium potential which is described by Nernst equation:

$$\boldsymbol{V_{eq} = \frac{RT}{zF}\ ln([ion]_{out} / [ion]_{in}))} \quad (1)$$

where $V_{eq}$ is the equilibrium potential of the ion, $R$ is the universal gas constant, $T$ is the absolute temperature, $z$ is the valence of the ion, $F$ is Faraday's constant, and $[ion]_{out}$ and $[ion]_{in}$ are the extracellular and intracellular ion concentrations, respectively. Each ion has its own Nernst potential that forms an equilibrium between the ionic movements due to diffusion and electric potential. However, as the plasma membrane is permeable to multiple ions (e.g., $Na^+$, $K^+$, $Cl^-$), the membrane potential is obtained by considering the contribution of each ion and calculated by the Goldman-Hodgkin-Katz equation:

$$\boldsymbol{V_m = \frac{RT}{F}\ \frac{p_{Na}[Na^+]_o + p_K[K^+]_o + p_k[Cl^-]_i}{p_{Na}[Na^+]_i + p_K[K^+]_i + p_k[Cl^-]_o}} \quad (2)$$

where $V_m$ is the membrane potential and $p_{Na}$, $p_K$, $p_{Cl}$ are the relative permeability of membrane for $Na^+$, $K^+$, $Cl^-$ ions. The equation contains $Na^+$, $K^+$, and $Cl^-$ ions because the plasma membrane of excitable cells are permeable to these ions.

### *2.1.2. Action Potential*

The Goldman-Hodgkin-Katz equation gives the resting membrane potential of an excitable

cell when there is no external or internal stimuli. The typical resting membrane potential of neurons is around -70 mV, although this number can differ from neuron to neuron depending on various intrinsic and extrinsic factors such as ionic permeabilities, ionic concentrations and temperature. Change in membrane potential towards positive values is called depolarization and towards more negative values is called hyperpolarization of the membrane. When neurons are depolarized a certain amount such that the membrane potential exceeds the 'threshold potential', neurons generate an electrical signal called 'action potential', which is characterized by a rapid depolarization/repolarization incidence in the membrane potential (Figure 2).

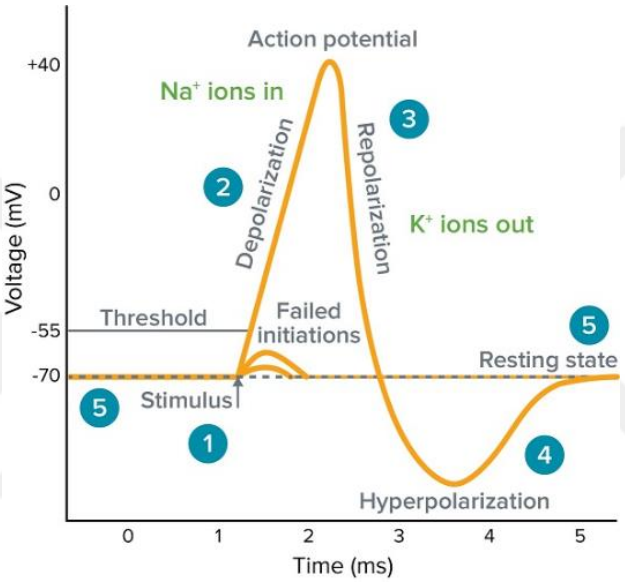


**Figure 2:** Simplified demonstration of different phases of action potential generation.

Action potential is an all-or-nothing event, and it is believed to be the fundamental communication signal between the excitable cells. Thus, the primary aim of neural stimulation devices and systems is to induce action potentials in excitable cells. Evoking action potentials in a temporally precise manner with high temporal resolution is critical for controlled modulation of neural activity.

In their renowned paper,[11] Alan Hodgkin and Andrew Huxley described the electrical behavior of plasma membrane when there is a flow of electric current through the membrane. They model the plasma membrane as an electric circuit consisting of a capacitor ($C_M$) that is formed due to the insulating bilayer structure of the membrane, voltage sources due to the equilibrium potentials of each ion, voltage-dependent conductance of $Na^+$ and $K^+$ ions, and finally a leakage conductance for small amount of $Cl^-$ and other ion movements (Figure 3). Based on this parallel-conductance circuit representation, they can mathematically describe the

initiation and propagation of action potentials in excitable cells by solving a set of nonlinear differential equations.[11]

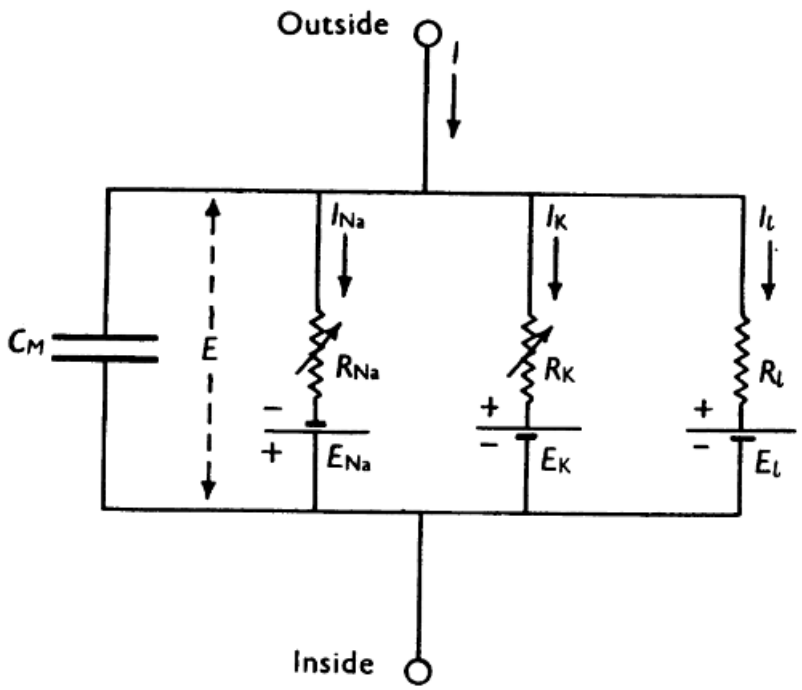


**Figure 3:** Electrical representation of cell membrane. $I_{Na}$, $I_K$, and $I_L$ correspond to $Na^+$ current, $K^+$ current, and leakage current; E is membrane potential; $E_{Na}$, $E_K$, and $E_L$ are equilibrium potentials for $Na^+$, $K^+$, and leakage ions other than $Na^+$ and $K^+$; $C_M$ is membrane capacitance; $R_{Na}$, $R_K$, and $R_L$ represent conductance of $Na^+$, $K^+$, and leakage ions, respectively.[11]

Hodgkin-Huxley model revolutionized the biophysical understanding of the electrical properties and behavior of neurons in the presence of external stimulation. Today, we know that action potentials can be evoked not only by electrical stimuli, but also mechanical, thermal, and optical stimuli as well. This led to the emergence of various neuromodulation techniques that exploit the advantageous properties of magnetic waves, acoustic waves, and light.

### *2.2 Electrical Stimulation*

The conventional way to modulate neural activity is extracellular electrical stimulation. In this technique, a stimulation electrode that is positioned near an excitable tissue injects electrical charges into the extracellular medium, which causes perturbation of the potential outside the cellular membrane. This leads to depolarization or hyperpolarization of membrane potential. Depolarization can evoke action potentials, while hyperpolarization can prevent action potential firing, i.e., induce neural silencing.

### *2.3 Magnetic Stimulation*

Capability of low radio frequency magnetic fields (up to 100 MHz) to penetrate into the body with marginal attenuation renders them eligible for reaching and stimulating the deep structures of the body. Due to its effective non-contact penetration into the body, magnetic waves offer non-invasive routes for neural stimulation and modulation purposes. Magnetic fields can either stimulate tissues by mutual induction phenomenon as with transcranial magnetic stimulation (TMS), or by triggering magnetic micro/nanoparticles, which in turn convert the magnetic energy into thermal, mechanical, or electrical energy that would activate or suppress the neurons.

Faraday showed that an electrical current is produced in a coil when another current-carrying coil is placed nearby. This is because an electrical current passed through a coil produces a magnetic flux. If the magnetic flux is time-varying, it induces an electric field in a medium it traverses, regardless of the conductivity of the medium. That medium is basically the stimulated tissues in TMS. Since the biological tissues are conductive due to their ionic composition, the produced electric field induces an electrical current in the tissue, leading to stimulation or suppression of the tissue's electrical activity as in direct electrical stimulation. This electromagnetic induction mechanism enables a non-contact route for generating electrical currents in the intact brain or peripheral nerves when a current-carrying coil is placed above the related area, e.g., scalp.

Apart from TMS, magnetic field can be used to modulate the activity of excitable cells via electro/mechano/thermotransducer micro/nanomaterials. These forms of neuromodulation can enhance spatial selectivity to single neuron level because the size of the transducer materials can be on the order of the size of the neurons. Such indirect use of magnetic waves for activating micro/nanomaterials in the vicinity of neural tissues shows promise for stimulation of deep brain structures in intact animals with high spatial resolution.

### *2.4 Mechanical Stimulation*

Ultrasound is the main realm in the domain of mechanical control of neural activity. The first observations of the bioeffects of ultrasound date back to 1920s.[12] Then, the pioneering studies on the generation of focused ultrasound and its interaction with biological tissues were conducted in 1940s and 1950s.[13] Focusing ultrasound waves was a groundbreaking step due to three main reasons: i) it allows the achievement of much higher local intensities at the desired spot, which maximizes the effect, ii) it greatly enhances specificity, iii) it minimizes the possible damage to the nontargeted tissues traversed by the applied wave.

Apart from its use for direct neuromodulation, ultrasound can function as an indirect transducer for modulating neural activity. One such strategy is to employ focused ultrasound for activating piezoelectric nanoparticles that are internalized into the cell or coupled to the plasma membrane and neurites. Sonication of such piezoelectric nanostructures renders the conversion of mechanical energy to electric current, which stimulates or suppresses the neural activity.[14] Sonogenetics is another strategy that exploits ultrasound to remotely activate the cells that are genetically made sensitive to ultrasound to modulate the neural activity.[15] These strategies might allow reaching resolutions well below the size of the ultrasound focus. Besides, they do not require surgical operations for delivering ultrasound as in optogenetics. Focused ultrasound is favorable for such indirect modulation strategies owing to its effective penetration into the biological tissues, which can reach to tens of centimeters depending on several factors such as carrier frequency and acoustic impedance of the tissue.

## *2.5 Light-based Neuromodulation*

### *2.5.1 Optogenetics*

Optogenetics uses genetic engineering to express light-sensitive ion channels on the cellular membrane and this way controls the electrical activity of neurons by using light without any intermediate device.[16] The discovery of this technique had a revolutionizing impact on neuroscience research as it can provide millisecond timescale control of neural activity with cell-type specificity.[17] After its first demonstration on mammalian neurons in 2005,[18] this technique has been used to effectively investigate the neural mechanisms of numerous overt and covert behaviors such as locomotion,[19] feeding,[20] learning,[21] decision making,[22] fear memory,[23] mating,[24] and addiction.[25] Today, it is a mature technique that is straightforwardly used in many different research settings. Depending on the expressed protein on the membrane, light can depolarize or hyperpolarize the membrane potential, thus, optogenetics can perform neural silencing besides neural stimulation.[26] Moreover, different wavelengths can be used for stimulation and silencing, providing experimental flexibility.[27]

Although the exceptional spatiotemporal resolution of optogenetics render this technique a powerful neuroscience tool, its use in clinical trials has been limited to one study,[28] potentially because of the concerns over genetic modification in humans and also the possible immune system complications that can arise due to the expression of viral vectors in human body.[29] Furthermore, optogenetics can be invasive especially for deep tissue applications since the opsins are sensitive to visible light and visible light has poor tissue penetration. Thus, light-delivery tools such as optical fibers or micro-LEDs should be inserted in the body to illuminate

the stimulation spot, and this increases the invasiveness of this technique.[30] As there is still no NIR-sensitive opsin, recent efforts focused on using upconversion nanoparticles to perform deep-tissue optogenetics.[31] However, the nanoparticles have their own complications such as toxicity, removal after injection, and possibility of cellular intake.[30] Hence, emergence of nongenetic and less invasive techniques might be a good alternative for optogenetics.

### *2.5.2 Photothermal*

Light can be converted to heat via photothermal nanoparticles, and this phenomenon can be used to modulate neural activity in two different ways. First, the rapid temperature change near the cellular membrane can generate capacitive membrane currents, which leads to action potential firing.[32] This technique is also called as "optocapacitive" stimulation. Gold nanoparticles and silicon nanowires are the typical materials used in optocapacitive stimulation.[33] In this technique, the important parameter is the rate of change in temperature rather than the change magnitude. The timescale of optocapacitive stimulation is on the order of milliseconds. On the other hand, slower temperature changes (e.g., second-scale) can also modulate neural activity by affecting the conductance of temperature-sensitive ion channels.[34] This is achieved by light-to-heat conversion by photothermal nanoparticles and genetic expression of temperature-sensitive on the cellular membrane unless there are intrinsically expressed temperature-sensitive ion channels. NIR-sensitive nanotransducers can be used to enhance the tissue penetration and devise remotely modulated photothermal stimulation systems that have minimal invasiveness.[35]

### *2.5.3 Photoacoustic*

Another promising method that emerged more recently is photoacoustic stimulation. By using the acoustic waves resulting from photoacoustic conversion, neurons can be stimulated via mechanical forces.[36] Similar to thermally induced capacitive currents, mechanical deformation of the membrane bilayer can also generate membrane capacitive currents that induce action potentials.[37] Apart from that, mechanical stimulation of neurons can also result from activation of mechanosensitive ion channels.[38] Although there are only several studies demonstrating photoacoustic stimulation of neurons in the literature, the technique already showed successful results for in vitro and in vivo conditions.[39]

### *2.5.4 Photovoltaic*

American Chemical Society.)

As this thesis focuses on design, fabrication and application of photovoltaic devices in neurostimulation applications, we will provide a detailed coverage of photovoltaic design principles and the charge injection processes at the device-electrolyte interface leading to modulation of membrane potential. Although photovoltaic devices have been conventionally used in solar energy harvesting applications, the principle of light-to-electric conversion has also found applications in neurostimulation field. As light is converted into electric current for stimulation of neurons, the fundamental mechanism is essentially electrical stimulation. That is why the charge injection processes at the device-electrolyte interface are analogous to electrical stimulation electrodes.

Photovoltaic devices convert light into electrical energy via the absorption of light by the photoactive semiconductor layer and the dissociation of photogenerated charges within the device (Figure 4a). Because of the electronic band alignment in device architecture, the photogenerated charges are dissociated (Figure 4b), and one type of charge is accumulated on the biointerface-electrolyte interface where neurons are positioned. The charge accumulation on the interface generates photocurrent in the electrolyte via capacitive and/or faradaic processes, which then depolarizes or hyperpolarizes the neural membrane potential depending on the direction of the photocurrent.

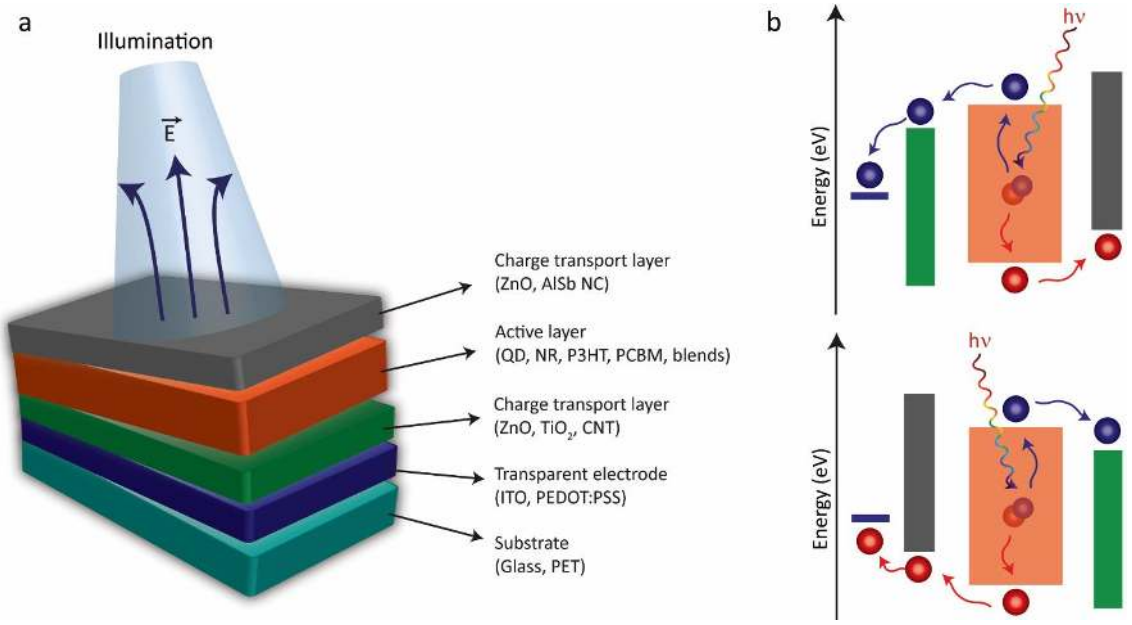


**Figure 4: a)** Schematic diagram of a generic photovoltaic architecture. **b)** Energy band diagram of regular (top) and inverted optoelectronic system (bottom). The layers represent the corresponding layers in (a). Exciton generation occurs in the active layer upon illumination. Dissociation of the

electron and the hole toward the charge transport layers, and the interfacial polarity depends on the band energy levels between the layers (i.e. positive for the regular and negative for the inverted architectures).

### *2.5.4.1 Primary Charge Injection Mechanisms at the Device-Electrolyte Interface*

In a photovoltaic neural interface, the photogenerated electrons or holes that accumulate close to the electrode/electrolyte interface induce electrochemical processes in the aqueous cellular environment. Those processes perturb the distribution of ions such as sodium, potassium, and chloride near the neural membrane, which leads to activation or suppression of neural activity. Depending on the interfacial impedance, one of the two primary charge injection mechanisms, faradaic or capacitive, take place at the electrode-electrolyte interface. These two mechanisms were illustrated in Figure 5a. In most cases, however, interfacial impedance involves both a double layer capacitance, a charge transfer resistance, and a Warburg impedance for representing the diffusion processes in the presence of reversible reactions (Figure 5b).

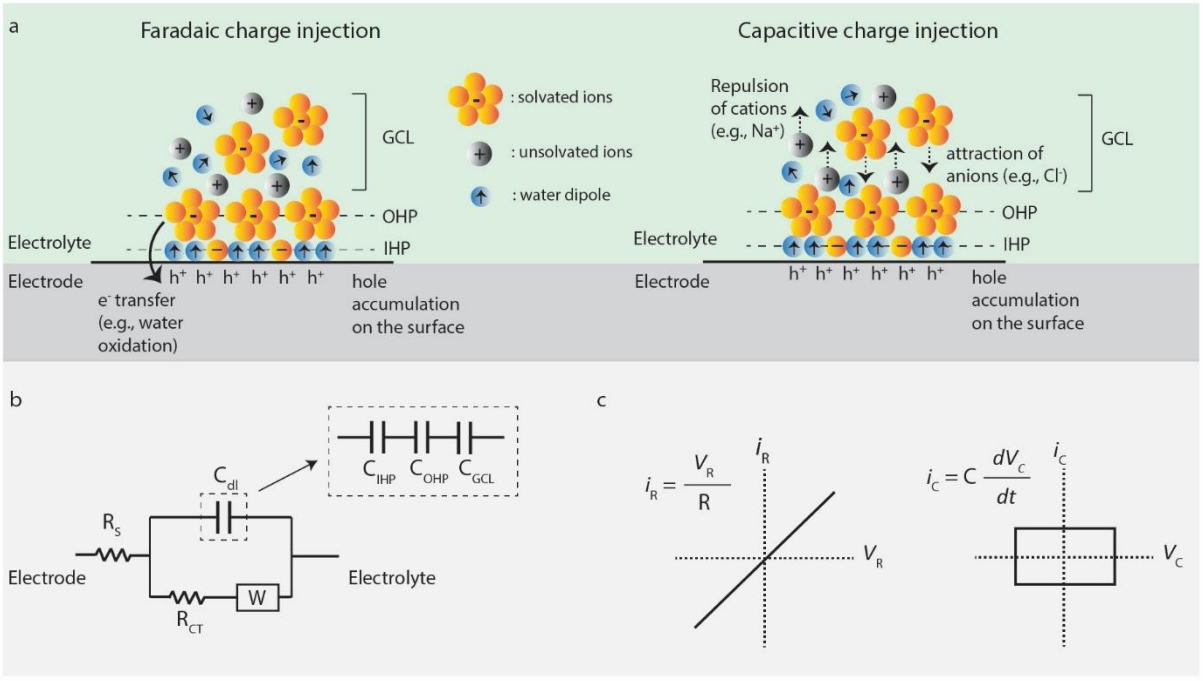


**Figure 5: Primary charge injection mechanisms in QD-based biointerfaces. a)** Illustration of faradaic and capacitive charge injection mechanisms. Electrons or holes accumulate on the biointerface surface, inducing faradaic or capacitive charge injection in the electrolyte (hole accumulation was shown as a representative case). IHP: Inner Helmholtz Layer, OHP: Outer Helmholtz Layer, GCL: Gouy-Chapman diffuse-charge layer. **b)** Electrical equivalent circuit model of the electrode-electrolyte interface. $C_{dl}$ represents double layer capacitance and is equivalent to series sum of IHP, OHP, and GCL capacitances. $R_{CT}$ and $R_s$ denotes charge transfer resistance and solution resistance. W represents Warburg impedance. **c)** Typical current-voltage profiles of resistive and capacitive elements.

### *i) Faradaic Charge Injection*

Faradaic charge injection mechanism involves electron exchange between neural interface and electrolyte (Figure 5a). Charge transfer can take place in both ways, i.e., by injecting electrons into or extracting electrons from the electrolyte. These different electron transfer routes lead to different faradaic reactions at the electrode-electrolyte interface. Electron injection into the electrolyte would cause reduction reactions (e.g., reactive oxygen species (ROS) generation), while electron removal from the electrolyte would lead to oxidation reactions. Thus, the direction of photocurrent gives information on the possible faradaic reactions occurring at the device-electrolyte interface. The occurrence of electron transfer between a neural interface and electrolyte depends mainly on two conditions. First, there should be a favorable energy state for electrons to move in the electrolyte. Second, the electric potential at the device/electrolyte interface should be in the range that is required for the occurrence of electron transfer reaction (see the review by Kumsa et. al. for the detailed description of electron transfer processes between a stimulation electrode and electrolyte)[81]. When both conditions are satisfied and reactants are present at the electrode/electrolyte interface, reversible or irreversible faradaic reactions can arise.

In irreversible faradaic processes, the reaction product moves away from the reaction site faster than the electron transfer rate, meaning there is no charge storage at the interface and the reaction products cannot be reversed back to their reactant form.[82] The unrecovered products diffusing into the electrolyte alter the physiochemical properties of the environment, posing potentially harmful effects to both neurons and biointerface. In this case, the dominant charge injection process is resistive, and the interfacial current-voltage (IV) profile in an ideal case, where double layer capacitor is negligible, can be represented with a resistor IV shown in Figure 5c.

Reversible faradaic reactions have much faster electron transfer rates compared to irreversible processes. Since the reaction products move away from the reaction site at a slower rate compared to the electron transfer rate, there is a charge storage in the interface in reversible faradaic reactions. Due to closeness of reaction products to the interface, the products can be recovered back to their initial reactant form if the polarity of the electric potential is reversed.[82] In an ideal case where the charge transfer resistance is infinite, this results in an IV profile of a capacitor at the electrode-electrolyte interface (Figure 5c).

Although the reduction oxidation processes occurring at electrode-electrolyte interface have been studied for conventional electrodes like Au and Pt,[40, 41] redox processes at the interface

of QD biointerface and physiological medium (e.g., artificial cerebrospinal fluid (aCSF) or phosphate buffered saline (PBS)) has not been elucidated yet. Dye-sensitized solar cells (DSSCs) are more mature technology with a similar operation principle to QD-based biointerfaces in the sense that they both operate in an electrochemical medium. However, the electrolytes used in DSSCs are different than aCSF or PBS. Thus, more studies are needed for understanding the faradaic reactions occurring at QD biointerface-aCSF (or PBS) interface.

One recent study investigated the possible faradaic reactions occurring at InP QD-based biointerface-aCSF interface.[42] The followed strategy was to investigate the photocurrent response of the biointerfaces in modified aCSF solutions, each is deficient of one constituent, to understand the faradaic processes according to the changes in the photocurrent in response to the removal of a constituent. This showed that the oxidation reactions at QD-aCSF interface involve reactions with HEPES and water, while the reduction reactions are mostly occurring with water.[42] Another possible strategy for identifying the faradaic processes could be the cyclic voltammetry (CV) analysis of QD biointerfaces in solutions of the constituent materials of aCSF or PBS.[40] The resistive-like behaviors in CV measurements indicate the presence of faradaic reactions and the corresponding potential values would enable the identification of oxidized or reduced constituent.

***ii) Capacitive Charge Injection***

When there is no net charge transfer between a neural interface and electrolyte, photocurrent can be generated by redistribution of ions in the extracellular medium. Upon illumination of a QD-based biointerface, one type of charge carrier accumulates on the surface of the device, causing a change in the net charge of the surface. This induces the movement of oppositely charged ions close to the surface and similarly charged ions away from the surface, leading to formation of a double layer capacitor in the device/electrolyte interface. The double layer consists of three different layers, namely Inner Helmholtz Plane (IHP), Outer Helmholtz Plane (OHP), and diffuse charge layer (Figure 5a). IHP is formed by adsorbed ions onto the surface and preferentially oriented water molecules forming hydration sheath. OHP mostly contains solvated ions that are not able to penetrate the hydration sheath. Finally, diffuse layer contains both solvated and unsolvated ions whose density decreases with the distance from the electrode-electrolyte interface. Hence, the total double layer capacitance ($C_{dl}$ in Figure 5b) is composed of serially connected IHP, OHP and diffuse layer capacitances.[83] Ideally, pure capacitive electrodes have infinite charge transfer resistance ($R_{CT}$ in Figure 5b), meaning that the charge transfer rate is zero at the electrode-electrolyte interface and all current flows

through the double layer capacitor as displacement current, which leads to a capacitor IV profile at the interface (Figure 5c).

Since capacitive stimulation involves a reversible charging/discharging process and does not cause electron exchange between the device and electrolyte, the physiochemical properties of the electrolyte such as electro-neutrality and pH are preserved. This renders capacitive charge injection mechanism as a safer alternative to irreversible faradaic processes, which motivates researchers to introduce viable methods for tuning the capacitive and faradaic components of the injected charge to minimize the faradaic and maximize the capacitive charge injection.

### *2.5.5 Quantum Dots for Optoelectronic Neuromodulation*

The interest in quantum dots began with the discovery of quantum size effects in semiconductor nanocrystals. The synthesis of the first quantum dots in a dielectric glass matrix was followed by their colloidal synthesis in a liquid medium. Moreover, the theoretical studies aimed to model and understand the charge carrier behavior in quantum-confined crystal structures.[45–50] Now, it is well known that the squeezing of excitons in quantum dots leads to size-dependent electronic and optical properties (Figure 6a), which makes them attractive materials for various applications such as light-emitting diodes, lasers, solar cells, luminescent solar concentrators, biomarkers, and biolabels.[17,51–53]

Optoelectronic properties of quantum dots were progressively improved via advancements in the field of nanochemistry. Novel synthesis methods resulted in "high-quality" nanocrystals that have near-unity photoluminescence quantum yield (PLQY), narrow emission linewidths, sharp absorption profiles, and atomic-level size tunability.[54–56] For that, production of core/shell nanostructures (Figure 6b), where a small bandgap core nanocrystal is covered with a larger bandgap shell material,[57] is an effective approach to engineer electronic and optical properties of QDs. Shell growth renders superior surface properties to QDs owing to the passivation of surface trap states and tunable energy levels, leading to enhanced optoelectronic characteristics and optical and chemical stability.[57,58] It should be noted that the desired optoelectronic properties typically differ depending on the application. For example, while QDs with near-unity PLQY are advantageous for light-emitting devices, there is no clear evidence that they are favorable or unfavorable for neural interfaces.

Depending on the electronic energy level alignment between the core and shell materials in a core/shell QD nanostructure, QDs are categorized into different types (Figure 6c). In type-I QDs (e.g., CdSe/CdS, CdSe/ZnS QDs), shell material has a higher conduction band and lower

valence band energies compared to the core material, which results in the confinement of electrons and holes in the core with high exciton binding energies. On the contrary, in type-II QDs (e.g., CdS/ZnSe, CdTe/CdSe, InP/ZnO QDs), one type of charge carrier localizes in the core, while the other charge carrier moves to shell due to the favorable conduction or valence band energy level of the shell. Moreover, quasi-type-II QD band structure exhibits only partial delocalization of one charge carrier to shell (Figure 6c). Compared to type-I QDs, the exciton binding energies of type-II QDs are lower due to the increased physical distance that causes reduced Coulombic force between the bound electrons and holes.[59] Besides, the increased distance between electron and hole leads to reduced radiative recombination rates and increased recombination lifetimes in type-II or quasi-type-II QDs.[60] The increased fluorescence lifetime enables the detection of time-gated signals to monitor cellular behavior.[20] Likewise, the increase in recombination lifetime is beneficial for charge carrier interactions and transfer with the neighboring materials.

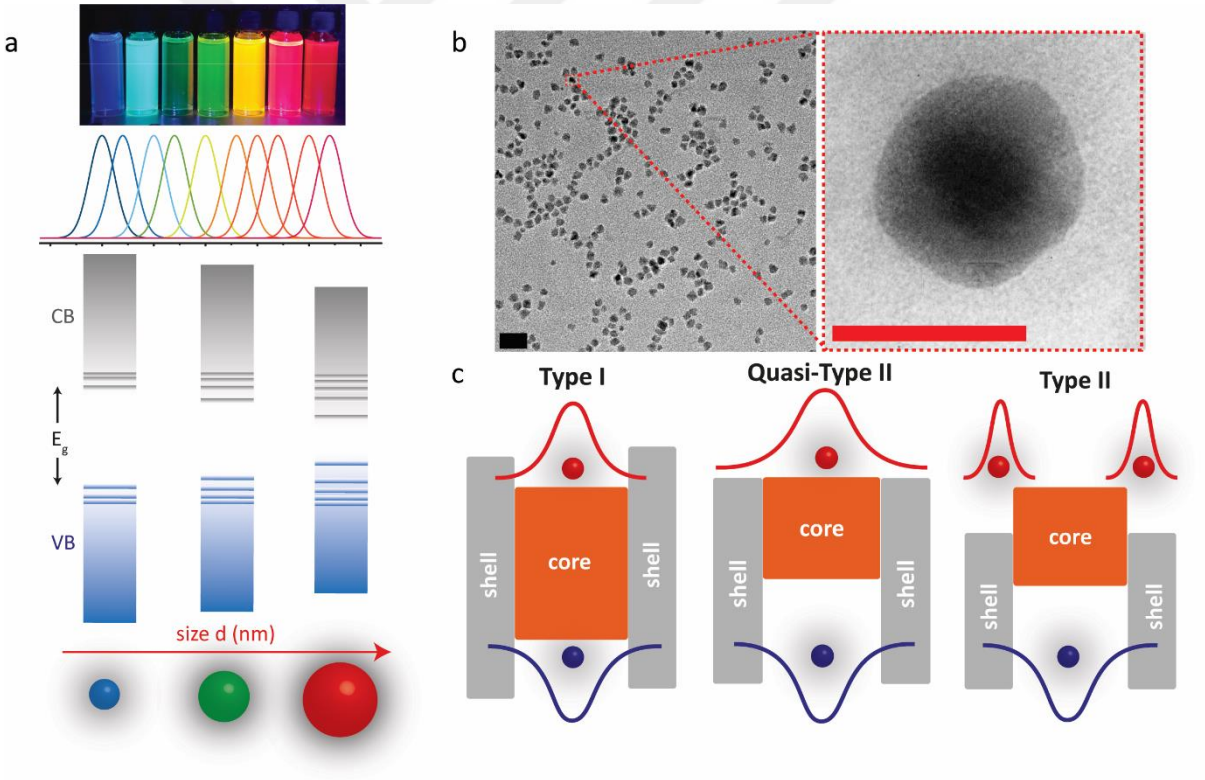


**Figure 6: a)** Quantum dots with stepping emission from blue to red (top). Representative photoluminescence spectrum for different size quantum dots (middle). Representative conduction and valance band diagram for different sizes of semiconductor quantum dots (bottom). **b)** Representative TEM images for core/shell quantum dots (scale bars: 20 and 5 nm, respectively). **c)** Core/shell semiconductor nanoparticle systems with type I, quasi-type II and type II band alignment.

One notable recently emerged application of QDs is neural interfaces. Being efficient absorbers in the visible to near-IR spectrum, QDs are promising materials for photoactive neural interfaces [61]. QDs can be functionalized to couple them directly with the cell membrane within only nanometer-scale distances using certain antibodies or peptides.[20,62] For example, avidin-conjugated QDs have been utilized for cell labeling and imaging by attaching through the biotin, the affinity pair of avidin.[63,64] Moreover, the excitation of QDs can potentially alter the membrane potential due to the electric field generated by the electron-hole separation in the excited QDs. For QDs, there are three possible configurations for cellular stimulation (Figure 7): (i) free-standing interaction in the extracellular medium with cells, (ii) direct interaction with cellular attachment using surface functionalization, and (iii) integration of QDs into photovoltaic devices either as the photoactive material or electron/hole transport layer. The free-standing configuration is not feasible due to the strong decay of the electric field generated by the QDs. Furthermore, the screening effect should be considered since the extracellular medium hosts polarized ions, mobile charge carriers, that can dampen the generated electric field. Moreover, as the voltage-gated ion channels require 5-10 mV potential difference for switching,[39] the effective stimulation distance is even shorter than the effective electric field volume if the screening effect is also considered. Therefore, the first configuration requires QDs to be in the vicinity of the targeted cells. However, the loading concentration should be increased to have more QDs interacting closely with the cells, which is not desired due to increased cytotoxicity with higher concentrations. To overcome this problem, the second configuration is convenient to bind QDs to targeted cells without increasing the loading concentration. The advances in bioconjugation schemes and QD surface functionalization have been already proven for bioimaging and targeted treatments using peptide-coated, avidin-coated, and many other techniques.[20] The same Debye length limitation also applies for the second configuration, but advantageously, the screening effect is almost diminished.[22,65]

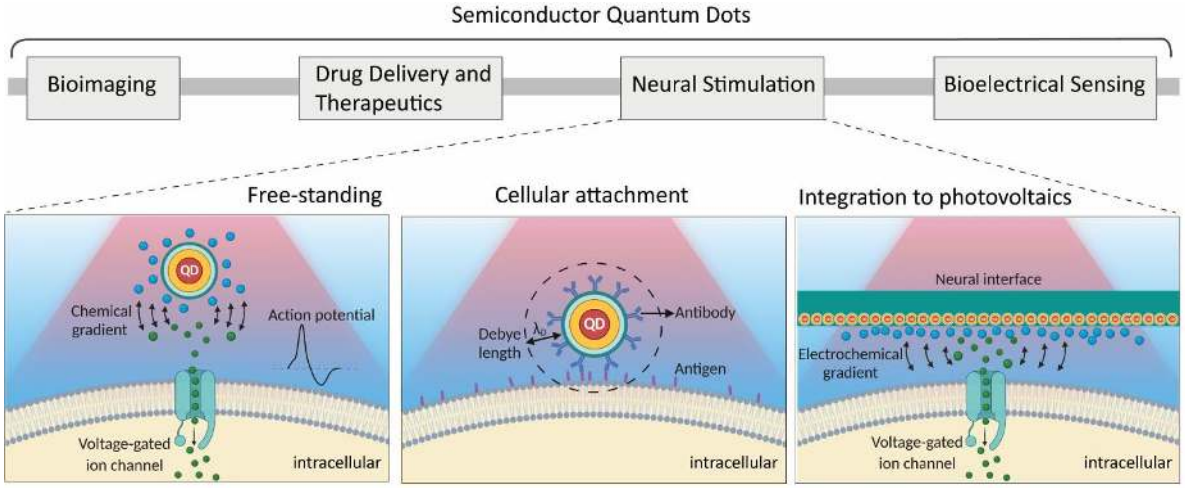


**Figure 7:** Biomedical applications of semiconductor quantum dots (top). Schematics for the three main configurations leading to neural stimulation using quantum dots (bottom).

On the other hand, layered photovoltaic architectures with QDs, such as in Figure 4a, have exhibited more convenient fabrication procedures and promising results in comparison with the other configurations. Solid films of QDs can effectively convert light energy into ion-based electrical current (photocurrent) in electrolytes, which can extracellularly stimulate nearby neurons. Indeed, this photoelectrical stimulation route using QD films was proven to be effective with few early pioneering studies.[66,67] Later, inspired from QD-based solar cell devices combined with a bioelectrical perspective, the ability to integrate QD films into various device architectures (e.g., combining QDs with electron and/or hole transport materials, heterojunctions of QDs with semiconducting organic polymers) while considering the device-electrolyte interactions led to the advanced quantum dot opto-bioelectronic devices for optical control of neurons.[68–70]

Electron and hole localization within QD heterostructure influences the performance and/or charge injection mechanism of the QD-based biointerfaces. Remarkably, the carrier localization in QDs can be tuned by proper choice of core and shell materials. The conduction and valence band energy alignment of core and shell materials lead to formation of type-I, quasi-type-II, or type-II QDs that can directly control the electron and hole wavefunctions, i.e. the spatial separation of electron-hole pairs.[78] Moreover, while keeping the heterojunction same, the thickness of the shell also influences the carrier localization that shifts the oscillator strength of electronic transitions and thus the absorption profile.[79] For neural interfaces this nanoengineering ability at single nanomaterial level is unique in comparison with their polymeric and metallic counterparts. For example, the photocurrent generation by a QD-based neural interface was shown to be enhanced when a type-I QD (InP core) was replaced with its

type-II counterpart (InP/ZnO) in the same device architecture.[68] One of main factors leading this improvement was reduced electron-hole wavefunction overlap, which facilitates more effective charge transfer to the nearby electron acceptor layer due to increased spatial separation of charges in type-II QD and reduced surface defects. This ability provides a promising route for tuning the contribution of capacitive and faradaic charge injection processes at the device-electrolyte interface as well.[80]

# Chapter 3

# Nanoengineering InP Quantum Dot-Based Photoactive Biointerfaces for Optical Control of Neurons



## *3.1 Introduction*

Studies showed that both inhibition and stimulation of neural activity can provide a useful toolbox against neurological diseases. On one side, hyperpolarization of neural membrane can lead to inhibition of the activity of neurons and thus suppression of neurological disorders such as epileptic seizures. On the other side, increasing neural activity through low frequency or high frequency stimulation of neurons as in the case of deep brain stimulation is an effective and clinically approved tool for the treatment of certain neurological disorders such as Parkinson's disease and depression [43]. Hence, biointerfaces that can perform hyperpolarization and depolarization in a controlled fashion can be effective for therapeutic purposes. To that end, we fabricated biointerfaces based on a biocompatible photoactive layer of InP/ZnS core/shell QDs and an intermediate layer of metal oxide nanoparticles. We designed two different device architectures, namely type I and type II, to achieve bidirectional stimulation and compared their performances by analyzing their photoelectrical responses to determine the most effective configurations. After having bidirectional photoresponse, we optimized the nanostructure of the photoactive layer by comparing the performances of only InP core QDs and InP/ZnS core/shell QDs. Moreover, we explored the correlation between photocurrent and photoactive layer thickness in the biological medium by conducting electrochemical experiments in artificial cerebrospinal fluid (aCSF), which revealed the optimum photoactive layer thickness maximizing the photoelectrical response. The electrophysiology recordings confirmed the successful photoelectrical coupling of the biointerfaces to neural membrane that allows optical control of the electrical activity of primary hippocampal neurons. Thanks to the nanoengineering of the photoactive biointerfaces, while type II biointerfaces induce

depolarization of neural membrane and evoke recurring action potentials, type I biointerfaces hyperpolarize the neural membrane.

### *3.2 Quantum dot properties and biointerface design*

The search for toxic-heavy-metal-free QDs has led to the synthesis of QDs made of III-V semiconductors (such as InP and AlSb [44]). Compared to II-VI QDs, which have large Phillips ionicity, III-V QDs are more robust in terms of optical stability due to the high covalency (lower Phillips ionicity) of their structure [45, 46]. InP is one of the most widely studied III-V QD, and it has no intrinsic toxicity [47, 48, 49]. Based on these reasons, we decided to use InP core and InP/ZnS core/shell QDs as the photoactive layer of our biointerfaces.

We synthesized InP core QDs via hot injection method and grew ZnS shell for the formation of InP/ZnS core/shell nanostructure.[50] The transmission electron microscopy (TEM) analysis of InP core and InP/ZnS core/shell QDs (Figure 8a, Appendix A Figure 28, 29) show an increase in the mean particle size from 3.2 nm to 4.5 nm diameter, indicating the formation of ZnS shell with a thickness of 0.65 nm and leading to a red shift in the photoluminescence (PL) spectrum. Moreover, the powder X-ray diffraction (XRD) analysis shows the crystal structure of the QDs by indicating zinc-blende crystal structures for InP and ZnS, respectively (Figure 8B).

We next investigated the optical properties of QDs. Figure 8C and 8D show the absorption and photoluminescence (PL) spectrum of the synthesized InP QDs and InP/ZnS QDs at the same concentration level (60 mg/mL), respectively. Both QDs absorb visible spectrum up to the red spectral region, and InP/ZnS QDs have higher absorbance than InP. In an integrated sphere system, the PL quantum yields (PL QY) of InP and InP/ZnS QDs were measured as 3% and 18%, respectively. 6-fold increase in quantum yield indicates the successful passivation of nonradiative recombination sites such as surface trap states [51].

Using the synthesized QDs, we fabricated biointerfaces by solution-processing the constituent layers. The biointerfaces were fabricated in two different configurations, called type I and type II (Figure 8E). The device structures of type I and type II biointerfaces, and their corresponding energy band diagrams are presented in Figure 8E and 8F, respectively. ZnO and $TiO_2$ nanoparticles in the device structures serve the purpose of blocking holes and controlling the electron movement, i.e. the photocurrent direction within the devices. Since the high annealing temperature of $TiO_2$ might damage QD layer, ZnO was used as the top layer in type I device structure.

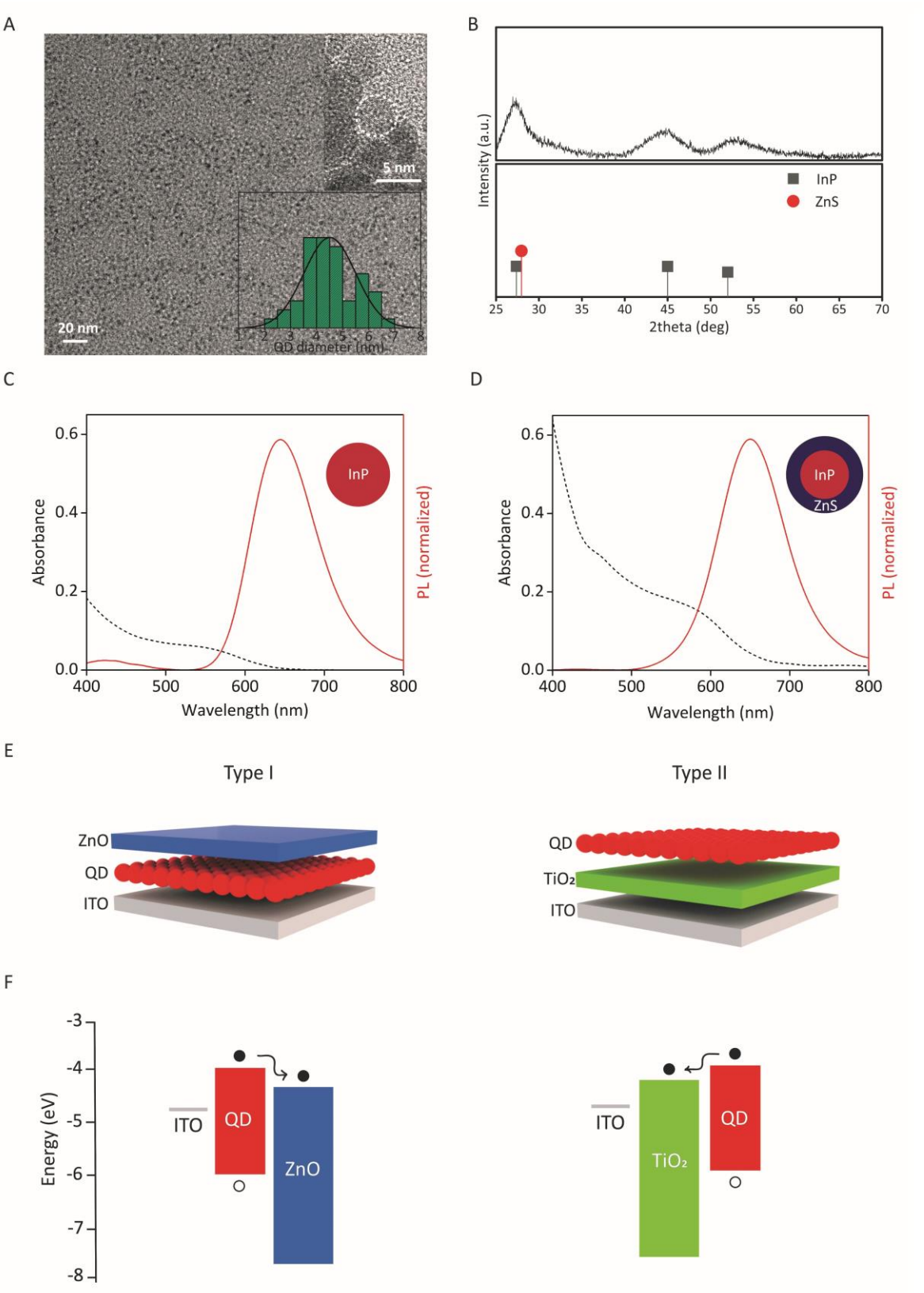


**Figure 8:** Structural and optical properties of QDs, device structures, and energy diagrams. **a)** TEM image of InP/ZnS core/shell QDs. Inset shows the corresponding size distribution and HRTEM image. **b)** XRD pattern of

InP/ZnS core/shell QDs. The XRD peak positions of zinc blende bulk InP (JCPDS No. 32-0452) and bulk ZnS (JCPDS No. 80-0020) were shown. **c), d)** Absorption and emission spectrum of InP core and InP/ZnS core/shell quantum dots (QDs), respectively. **e)** (Left) type I and (right) type II biointerface configurations. Either InP core or InP/ZnS core/shell QDs were used as QD layer. **f)** Energy band diagrams of (left) type I and (right) type II biointerfaces. The energy levels were taken from our previous study and literature.[52, 53] The displacement of electrons (filled circles) and holes (empty circles) was shown.

### *3.3 Photoelectrical performance of biointerfaces*

Charging/discharging dynamics and the maximum photovoltage produced by the biointerfaces are important parameters to understand their light-triggered neuromodulation potential. Figure 9A shows the electrochemical setup for the characterization of the InP QD-based biointerfaces. We place the electrodes in artificial cerebrospinal fluid (aCSF), which is commonly used as an extracellular solution for neural tissues and electrophysiology (see Appendix A for the preparation of aCSF) [54]. We measure their photocurrent and photovoltage via a three-electrode setup under light illumination with LED light source (445 nm nominal wavelength, optical power density ranging between 0.1 mW $mm^{-2}$ and 0.57 mW $mm^{-2}$). (Figure 9a). As it is evident from the electron migration directions shown in Figure 8f, we observe oppositely directed photocurrents in type I and type II devices. This is because the ZnO layer blocks the photogenerated holes at the QD layer from moving to the surface, which results in electron accumulation on the ZnO-electrolyte interface. In contrast, photogenerated holes are blocked by the $TiO_2$ layer in type II devices, which causes hole accumulation on the QD-electrolyte interface. Thus, by properly engineering the band alignment of the constituent materials, we can control the direction of electron flow and the type of charge that will be accumulate on the device-electrolyte interface. In that sense, type I and type II biointerfaces will generate opposite polarity photocurrents and reverse membrane potential variation; in other words, type I biointerface will bring membrane potential to more negative values (hyperpolarization) and type II biointerface will increase membrane potential (depolarization).

Figure 9b and 9c demonstrate the photocurrent density of the two types of devices incorporated with either InP core QDs or InP/ZnS core/shell QDs as the photoactive layer. In type I and II devices, we observe 10-fold and 13-fold higher photocurrent levels for the core/shell QDs compared to biointerfaces with core QDs, respectively. We ascribe this to the following two reasons: i) InP/ZnS core/shell QDs have higher absorbance compared to InP QDs (Figure 9c and Figure 9d), which leads to higher number of photogenerated excitons in the InP/ZnS layer compared to InP layer; ii) decreasing the number of trap states by successful shell passivation of the InP core, which is supported by quantum yield enhancement, leads to higher currents.

Due to stronger photocurrent generation, we decided to use InP/ZnS core/shell QDs inside type I and type II devices.

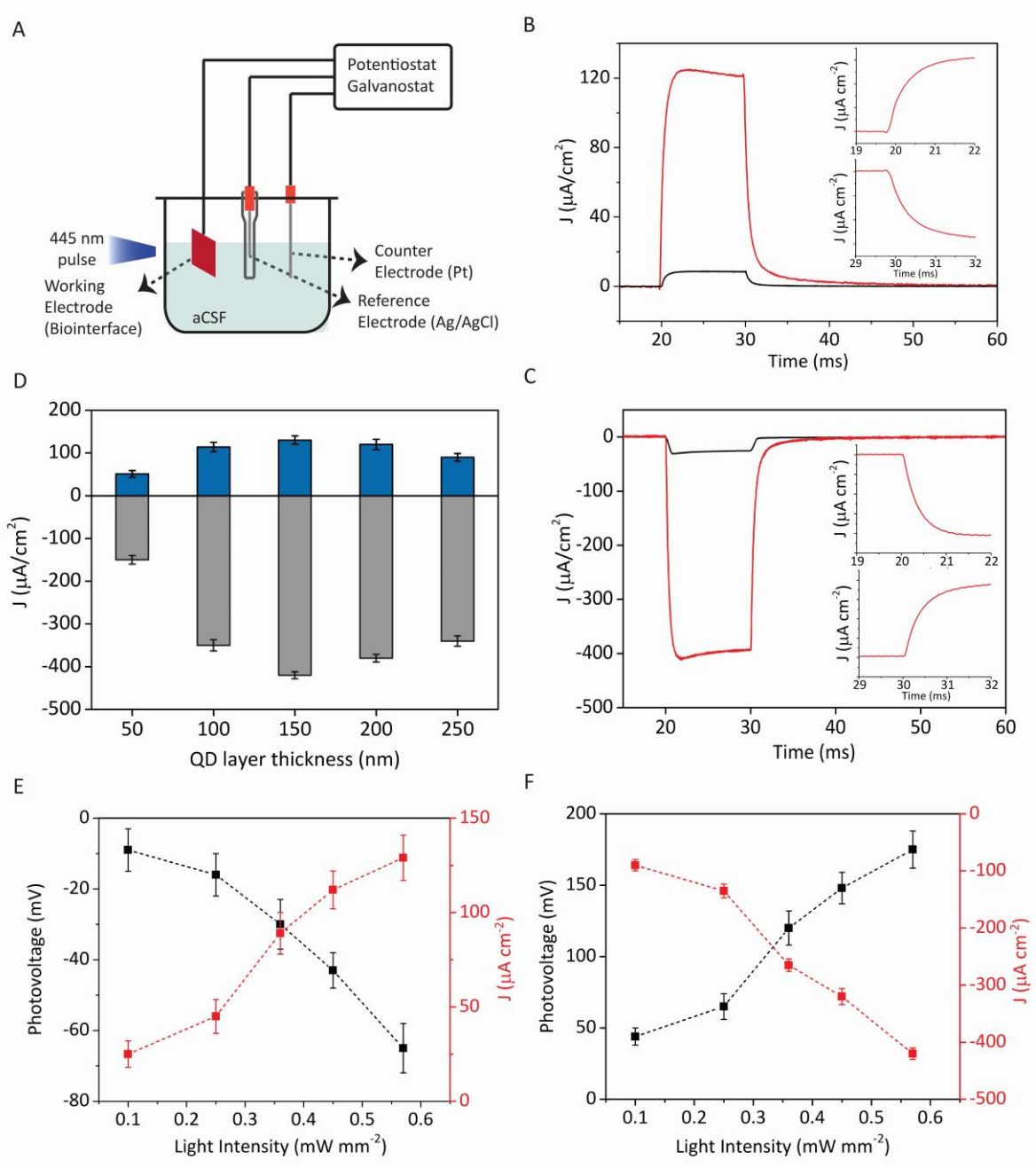


**Figure 9: Characterization of the photoelectrical performance of biointerfaces. a)** Three-electrode electrochemical photocurrent measurement setup. **b), c)** Photocurrent density of type I (b) and type II (c) devices in biological medium (illumination: blue LED at the wavelength of 445 nm, 10 ms pulse width, 0.57 mW $mm^{-2}$ optical power density). Black lines represent when InP core QDs are used as a photoactive layer, while red lines show when InP/ZnS core/shell QDs are used as a photoactive layer. Inset (b), (c) top: Zoomed rising parts of photocurrents. Inset (b), (c) bottom: Zoomed falling parts of photocurrent. **d)** Photocurrent densities of type I (blue bars) and type II (gray bars) biointerfaces as a function of photoactive layer thickness. **e), f)** Photovoltage

and photocurrent density responses of type I (e) and type II (f) devices under different light intensities (illumination: blue LED at 445 nm, 10 ms pulse width).

Different than capacitive double layer charging mechanism, the charging/discharging dynamics of photoelectrochemical current generation mechanism is dependent on the rates of electron transfer at electrode-electrolyte interface and the arrival rate of reaction ions to the interface [55]. Capacitive biointerfaces have fast charging dynamics with rise times on the order of tens or hundreds of microseconds [56, 57], whereas the decay times might be in milliseconds range [58]. On the other hand, faradaic devices have typically longer rise/fall times due to the slower charging-discharging kinetics governed by electron transfer rate and availability of ions at the reaction site [55, 59, 60]. In this context, the photocurrents in Figure 9b and 9c rise to their maximum levels and falls back to their steady-state levels in less than 3 ms (insets of Figure 9b and 9c), which presents suitable charging/discharging dynamics for typical neuromodulation frequencies varying from few Hz to tens of Hz [61] (the photoresponses of the biointerfaces for 5 ms and 1 ms pulses can be seen in Appendix A Figure 30).

We next investigated the current densities of our biointerfaces under illumination with different optical power densities and the resulting photovoltages (Figure 9e and 9f). The type I and type II biointerfaces can produce more than 25 mV photovoltage under a low optical power density of 0.1 mW $mm^{-2}$. For the highest intensity of 0.57 mW $mm^{-2}$, type I and type II biointerfaces produce -65 ± 7 mV and 175 ± 13 mV photovoltages under 10 ms pulse, respectively. These numbers are promising for potential photostimulation applications considering the reported photovoltage values in a previous QD-based study that can evoke neural activity [62], and also previous organic semiconductor-based biointerface studies that reported similar or lower photovoltage values and still effectively stimulate neurons [57, 63, 64].

Moreover, the integrated area under the photocurrent transients is an important metric in terms of showing the charge injection quantities of the biointerfaces. We calculated the peak charge injection levels of type I biointerfaces as 1.29 $\mu$C $cm^{-2}$, and type II biointerfaces as 4.12 $\mu$C $cm^{-2}$, which are at similar levels with the threshold charge density values of neural prostheses [61].

### *3.4 Photocurrent maximization via device engineering*

The effect of photoactive layer thickness on optoelectronic device performance has been investigated in the literature, especially for solar cells [65, 66]. Regarding that, however, it is possible that the optoelectronic devices working in the biological medium have different

dynamics. Indeed, our biointerfaces operate in aCSF, which consists of certain physiological ions and agents such as $K^+$, $Na^+$, $Cl^-$, HEPES and glucose dissolved in deionized water. Operation in such medium will result in different values of charge carrier parameters (e.g. mobility, diffusion length, etc.) compared to the investigated cases in the literature. Thus, the examination of the dependence of the biointerface performance to photoactive layer thickness in the biological medium provides valuable insight for photoactive stimulation devices.

Figure 9d shows the current density responses of type I and type II devices in aCSF medium for different photoactive layer thicknesses. We observe the same behavior in both types of devices, in which the photocurrent first increases up to certain photoactive layer thickness. Further increasing the thickness causes photocurrent to decrease. In other words, there is an optimum thickness, which results in the maximum photocurrent generation from the devices. The optimum thickness strongly depends on the depletion width and the minority carrier diffusion length. Depletion width is the region where the photogenerated charges are efficiently extracted. The generated charge carriers within a diffusion length of the space charge layer are also harvested with a high probability. If the photoactive layer is thicker than the optimum thickness, extracted charges recombine in the neutral region, which decreases the extraction efficiency. On the other hand, thinner photoactive layer is disadvantageous due to insufficient absorption.

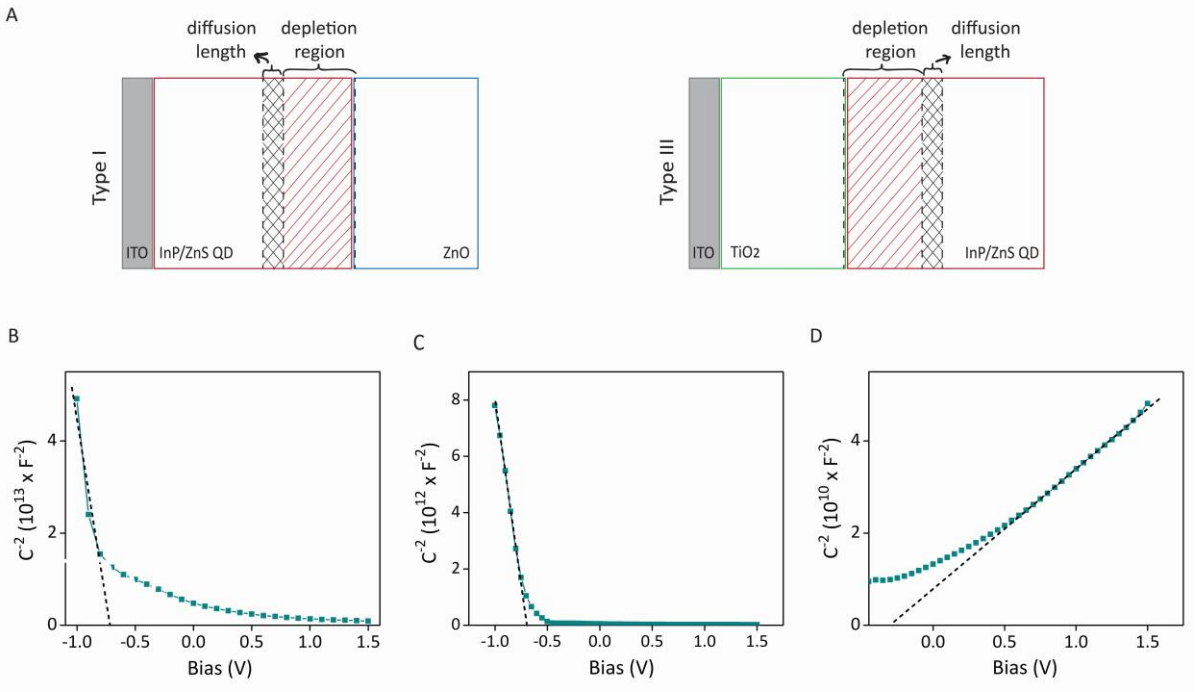


**Figure 10: Depletion layer and diffusion width analysis of biointerface for photocurrent maximization. a)** The schematic showing the formation of depletion width and diffusion length on the photoactive layer, which

both contribute to the photocurrent production. **b), c), d)** Mott-Schottky capacitance-voltage analysis of ITO/QD, ITO/$TiO_2$, ITO/ZnO devices in aCSF medium with three-electrode configuration. Dashed lines show the linear fit.

To investigate the internal operation of our devices, we conducted Mott-Schottky analysis and electrical impedance spectroscopy (EIS), which together allow us to investigate the charge-carrier dynamics and calculate the depletion width and minority carrier diffusion length [67]. Mott-Schottky analysis can be applied to the devices that contain a semiconductor-semiconductor junction in which one semiconductor is much more doped than the other one [68]. In such a device, the depletion layer capacitance can be measured as a function of bias. The measured capacitance ($\boldsymbol{C}$) and applied bias ($\boldsymbol{V}$) are correlated to each other with the following expression [69]:

$$C^{-2} = \frac{2(V_{bi}-V)}{A^2 q\varepsilon\varepsilon_0 N} \tag{3}$$

where $V_{bi}$ is the built-in voltage, $A$ is the device area, $q$ is the elementary charge, $\varepsilon$ is the dielectric constant of the material, $\varepsilon_0$ is the permittivity of free space, and $N$ ($N_a$ for acceptor type, $N_d$ for donor type) is the doping concentration of the material.

The equation (3) and the individual capacitance-voltage measurements of ITO/QD, ITO/$TiO_2$, and ITO/ZnO devices in aCSF solution (Figure 10b, 10c, 10d) yielded the carrier concentrations of QD, $TiO_2$, and ZnO as $N_a = 7.4 \times 10^{16}\ cm^{-3}$, $N_a = 1.3 \times 10^{18}\ cm^{-3}$, and $N_d = 6.5 \times 10^{20}\ cm^{-3}$, respectively. The fact that the doping concentrations of ZnO and $TiO_2$ are much higher than the doping concentration of InP/ZnS QD indicates the formation of a space charge layer in the QD-ZnO and $TiO_2$-QD junction. The presence of a depletion layer can also be inferred from the Mott-Schottky analysis of type I and type II devices, which both show bias dependent capacitance behavior (Appendix A Figure 31). It also implies that the depletion width will be predominantly in the QD layer in both types of devices. Thus, we can show the formation of depletion width and minority carrier diffusion length on the device schematic as in Figure 10a. Since ZnO and $TiO_2$ have very low absorption in the blue spectral region due to their large band gaps, their contribution to the photocurrent production is negligible. Therefore, we can disregard the diffusion length in those layers. As the individual Mott-Schottky analysis of the QD layer revealed, the minority carrier in the InP/ZnS QD layer is electrons. As a result, we need to obtain the depletion width extending into the photoactive layer, and electron diffusion length for type I and type II devices. The depletion width ($w$) extending into the QD layer can be determined from the following relation [66]:

$$w_1 = \left(\frac{2N_2\varepsilon_1\varepsilon_2(V_{bi}-V)}{qN_1(\varepsilon_1N_1+\varepsilon_2N_2)}\right)^{\frac{1}{2}} \quad (4)$$

where $\varepsilon_1$ and $\varepsilon_2$ are the permittivity of side 1 and side 2 (side 1 is taken as InP/ZnS, side 2 is ZnO in type I, TiO2 in type II devices), $N_1$ and $N_2$ are the doping concentrations of side 1 and side 2. Extracting the built-in voltage of type I and type II devices from the capacitance-voltage plots in Appendix A Figure 31, equation (4) yields the depletion width of type I structure as 122 nm and type II structure as 94 nm.

To find the electron diffusion length, we conducted EIS analysis to type I and type II electrodes (Appendix A Figure 32). By fitting the EIS plots with an equivalent circuit (Appendix A Figure 32e) and extracting the electrical parameters obtained from the fitted circuit. The electron diffusion length in type I and type II devices were determined as 43 nm and 91 nm, respectively (Appendix A Table 2). Consequently, the sum of depletion width and diffusion length is ∼165 nm for type I and ∼185 nm for type II devices, which both match on the order of magnitude with the photoactive layer thickness that maximizes the photocurrent (∼150 nm) in Figure 9d.

### *3.5 Stability and biocompatibility of biointerfaces*

To test the reproducibility of the signals, we performed accelerated ageing test as reported in previous studies [70]. We placed the biointerfaces in physiological solution aCSF and kept them at 87°C for 12 days. We measured the photovoltages of the biointerfaces each 48h via three-electrode electrochemical setup in galvanostatic mode. Assuming body temperature of 37°C, acceleration factor *f* at 87°C corresponds to 32 ($f = 2^{\Delta t/10}$, $\Delta t = 87 - 37 = 50$), hence yielding the simulated period of 384 days (∼12 months). Both type I and type II biointerfaces preserved their performance for the period of 12 months with less than 15% decrease in photovoltage (Figure 11a).

Although the biocompatibility of InP-based QDs were studied in detail [48, 71, 72], the effect of the biointerfaces used in this study on the viability and metabolic activities of primary neurons should be quantified for their potential use as neurostimulators. We studied the biocompatibility of our biointerfaces by performing cell viability analysis via MTT toxicity assay and immunofluorescence imaging. The effect of the biointerfaces on metabolic activities of primary hippocampal neurons were assessed and compared with ITO control samples after 48-hour incubation in the neuron growth medium (Figure 11b). The MTT results indicate that the biointerfaces did not have an adverse effect on cell viability of primary hippocampal

neurons. Neurons grown on type I and type II biointerfaces demonstrate comparable levels of cell viabilities with respect to the reference ITO substrate, which is known as a biocompatible material for neural cells. No significant decrease on cell viability primary neurons observed in type I and type II biointerfaces compared to ITO. Besides, immunofluorescence images of primary hippocampal neuron culture on type I, type II and ITO control samples taken at day 0 and day 14 indicates the maintained cell viability and morphology (Figure 11c), which agrees with MTT assay results.

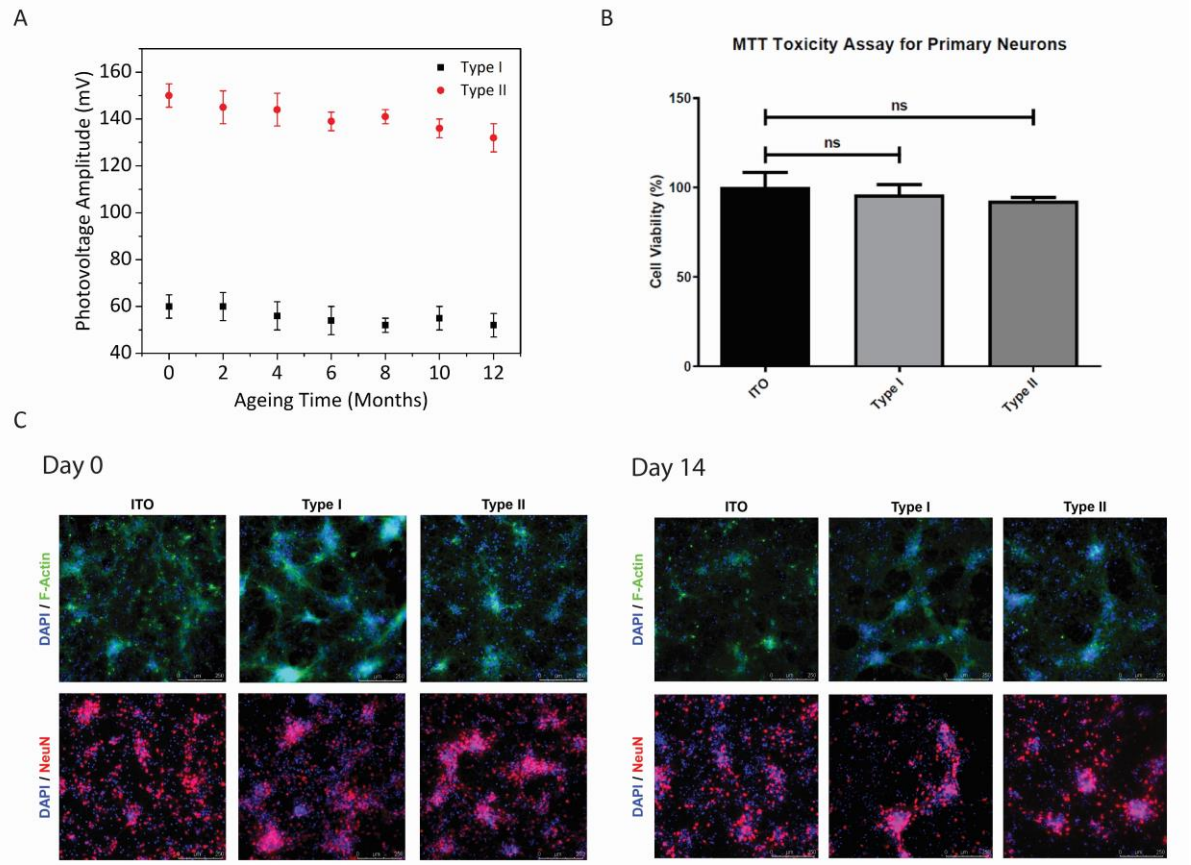


**Figure 11: Stability and biocompatibility of biointerfaces. a)** Photovoltage measurements of type I and type II biointerfaces in an accelerated ageing test for ageing period of 12 months (mean ± s.d. for N = 4). **b)** Cell viabilities of primary hippocampal neurons cultured on type I and type II biointerfaces obtained from MTT biocompatibility assay analysis. Data was presented in a column graph plotting the mean with the standard deviation (mean ± s.d.) (Four technical replicates were used in each of the three different experiments). Unpaired, two-tailed t-test was performed to determine the level of significance and *$p < 0.05$ was considered as statistically significant. **c)** Immunofluorescence images of primary hippocampal neurons and glia on type I, type II biointerfaces and ITO controls at Day-0 and Day-14 after primary neuron isolation protocol. Primary hippocampal neurons co-stained with DAPI (blue), a DNA marker, Anti-NeuN antibody (red), a neural nucleus marker, and Anti-F-actin antibody (green), a cytoskeleton marker (scale bar: 250 µm).

### *3.6 Neural photostimulation with optimized biointerfaces*

We next conducted *in vitro* single-cell electrophysiology experiments with the type I and type II biointerfaces to show the light-induced effects on neural cell membranes under pulsed LED illumination (445 nm nominal wavelength, 2 mW $mm^{-2}$ optical power density). The primary hippocampal neurons were cultured on top of our biointerfaces and the transmembrane voltage changes on their cell membrane were measured via patch clamp setup in whole-cell configuration. Figure 12a shows the schematic of electrophysiology recording experiment with primary neurons. The QD/ZnO and $TiO_2$/QD heterostructures for type I and type II biointerfaces serve as the active area that photogenerates charge carriers, while conductive ITO back contact serves as the return electrode in the stimulation experiments. Following the charge separation at the QD-ZnO or QD-$TiO_2$ heterojunction, one type of charge carrier is moved to the electrode-electrolyte interface, giving rise to photoelectrochemical reactions with the electrolyte that leads to the photocurrent generation. The reactions occurring at the active area-electrolyte interface are balanced with the counter reactions taking place at ITO-electrolyte interface, completing the current loop (see Appendix A Figure 33 for the characterization of photoelectrochemical processes taking place with the electrolyte).

In the single cell electrophysiology experiments, transmembrane voltage is defined as the electrical potential difference between the intracellularly recorded voltage at the patched membrane region and distant reference electrode placed in the extracellular medium. As expected from the reverse photocurrent directions of type I and type II biointerfaces, photoexcitation of the biointerfaces leads to countereffects on transmembrane voltages of primary neurons. Figure 12b shows the effect of type I and type II biointerfaces on neural transmembrane voltage together with ITO control sample when we illuminate them with 10 ms pulses. Type I biointerface hyperpolarizes the neural membrane, while type II biointerface depolarizes the membrane and evokes action potential. The neurons on ITO control sample did not show light-induced transmembrane potential change. We also checked repetitive photostimulation of neurons by applying consecutive pulses. Type I biointerfaces induce hyperpolarization of transmembrane voltage reproducibly via 1 Hz excitation (Figure 12c). In the same figure, we also observe the increase in the hyperpolarization amplitude as the pulse width is increased from 10 ms (12c top) to 50 ms (12c middle) and 200 ms (12c bottom). The hyperpolarization amplitude increased from 24 ± 3 mV for 10 ms to 34 ± 4 mV for 50 ms and 45 ± 6 mV for 200 ms (mean ± s.d. N = 6). This behavior is indicative of resistive coupling of the photocurrent to the neural membrane rather than capacitive coupling. One main advantage

of resistive processes is their high charge capabilities [55, 61], which makes them favorable for both direct electrical stimulation (e.g., iridium oxide electrodes) and optical stimulation interfaces (e.g., HgTe QD-based [73] and silicon nanowire stimulators [74]). This is reflected in the performance of type II biointerfaces, which can successfully elicit reproducible action potentials by depolarizing the neural membrane through continuous charge injection during the 'light on' periods. Photoexcitation of type II biointerfaces with 10 ms pulses (445 nm, 2 mW mm$^{-2}$ optical power density) at 1 Hz, 2 Hz and 5 Hz frequencies led to reproducible firing of primary neurons with success rates over 85%, while the spike rate is still over 50% for 10 Hz (Figure 12d) (see Appendix A Figure 34 for 10 Hz stimulus response).

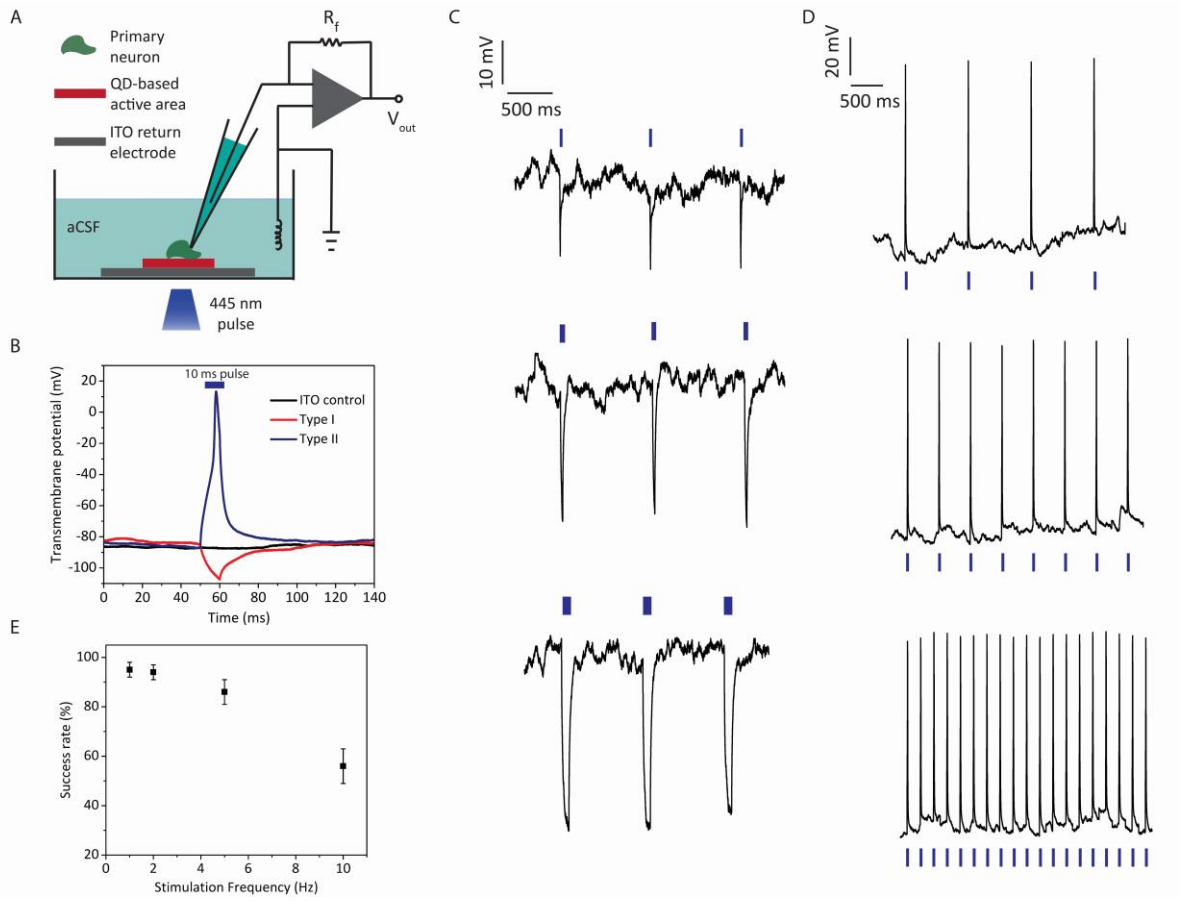


**Figure 12: Light-induced electrophysiology recordings of primary hippocampal neurons cultured on biointerfaces. a)** Schematic of the single cell electrophysiology setup. **b)** Transmembrane potential recordings of neurons on type I, type II and ITO control samples (illumination: blue LED at 445 nm, 10 ms pulse width, 2 mW mm$^{-2}$ optical power density; blue bar indicates the 10 ms 'light on' interval). **c)** Neural membrane recordings of hippocampal neurons on type I biointerfaces for 1 Hz stimulus with different pulse widths (top: 10 ms, middle: 50 ms, bottom: 200 ms) (illumination: blue LED at 455 nm, 2 mW mm$^{-2}$ optical power density; blue bars indicate the 'light on' intervals). **d)** Neural membrane recordings of hippocampal neurons on type II biointerfaces for 1 Hz, 2 Hz and 5 Hz stimulus (The membrane response to 10 Hz stimulus is shown in Appendix A Figure 34) (illumination: blue LED at 445 nm, 10 ms pulse width, 2 mW mm$^{-2}$ optical power density; blue bars indicate the

'light on' intervals). **e)** Success rate of action potential firing for type II biointerfaces for 1 Hz, 2 Hz, 5 Hz, 10 Hz stimulus frequencies (mean ± s.d. for N = 6).

### *3.7 Conclusion*

Quantum dots have been one of the central nanomaterials for neural interfaces together with π-conjugated organic and silicon-based inorganic systems [75, 76]. One of the major challenges of quantum dot-based neural interfaces is the use of toxic heavy metal content (cadmium or mercury-based) quantum dots. InP-based quantum dots show a promising non-toxic alternative to be used for neural interfaces owing to the composition of III-V elements with covalent bonds in their structure and not containing highly toxic elemental compound [46]. In addition to the previous reports showing the biocompatibility of InP-based QDs for both *in vitro* and *in vivo* [48, 59, 72], our study showed the biocompatibility of InP QD-based type I and type II biointerfaces on primary hippocampal neurons *in vitro*, which are commonly used neural cell type to observe neurotoxicity. Moreover, the Bohr exciton radius of InP (~ 9 nm) is larger than CdSe (~ 5 nm), which gives a high-level controlling ability of electron and hole energy levels. Type I and type II heterostructures also offer another degree of freedom for wavefunction engineering for potential neuromodulation applications [77].

The comparison of the photoelectrical performance of InP core and InP/ZnS core/shell photoactive layers has crucial importance as the shell deposition is an important practice for decreasing the cytotoxic effects of QDs, but little was known about the impact of shell coverage to the performance of QD based biointerfaces [75]. We demonstrated that shell growth facilitates substantial enhancement of photoelectrochemical current levels. In addition to the quantum dot level control, their optoelectronic engineering offers the ability to demonstrate unconventional biointerfaces using non-radiative energy transfer, like in photosynthesis processes of plants [59].

The photocurrent maximization procedure and agreement with the electrochemical measurements of the biointerfaces presented in this study show promise for future QD-based non-genetic neuromodulation studies. The electrophysiology experiments indicate the potential of the biointerfaces, demonstrating reproducible hyperpolarization and depolarization of primary neural membrane, which triggers neurons to fire light-induced action potentials. Besides, the light intensity levels used in the photostimulation experiments in this study for are below the levels for the photothermal stimulation of neurons [78].

In conclusion, our findings show that QD core/shell heterostructure, device configuration, choice of photoactive layer and the thickness of the photoactive layer are all effective on the

performance of photoelectric biointerfaces. The ability to control the direction and strength of the stimulation is possible through proper band alignment engineering, nanostructure engineering and optimization of the photoactive layer thickness. Therefore, the systematic engineering of the device parameters and the quantum dot nanostructure in this study leads to the fabrication of effective InP quantum dot-based photoactive biointerfaces that can optically control the electrical activity of neurons.

# Chapter 4

# Quantum Dot and Electron Acceptor Nano-Heterojunction for Photo-induced Capacitive Charge-Transfer

(Reprinted (adapted) with permission from Karatum O*, et al.* (2021) Quantum Dot and Electron Acceptor Nano-Heterojunction for Photo-induced Capacitive Charge-Transfer. *Scientific Reports* 11, 2460. Copyright 2021 Springer Nature.)

## *4.1 Introduction*

The charge injection mechanism at the device/tissue interface is an important parameter that affects the efficiency and safety of neuromodulating devices. The safe modulation of neural activity requires the avoidance of irreversible faradaic reactions, which might be harmful to the biological tissues.[55, 61] In that regard, capacitive stimulation is accepted as a safe method that modulates the cell membrane by inducing transient displacement currents without any direct charge transfer from the electrode to the biological medium.[55, 61] Hence, both electrical and optical neurostimulators are material- and device-wise engineered to induce capacitive currents. For example, titanium nitride (TiN)-based capacitive electrodes for electrical stimulation inject charges through the electrode-electrolyte double layer.[79] The capacity of such electrodes charging and discharging the double layer can be improved by additional dielectric coatings of tantalum/tantalum oxide ($Ta/Ta_2O_5$). Moreover, silicon, organic semiconductors and carbon nanotubes have been used for capacitive photostimulation of neurons.[80, 81]

Colloidal quantum dots (QDs) are promising nanomaterials for neural interfaces due to their advantageous structural and optoelectronic properties such as tunable bandgap, high absorption in the visible spectrum, solution processability and stability.[82] Photostimulation devices based on HgTe, CdSe and InP QDs were previously reported in the literature that can efficiently stimulate neurons and evoke action potentials.[59, 60, 73, 83] These devices, however, either contain toxic-heavy-metals or operate photoelectrochemically, both of which might harm the tissues in the long-term use. Heavy-metal-free QD-based neural interfaces that have

dominant capacitive charge injection have not been reported in the literature yet.

In this study, we demonstrate QD-fullerene donor-acceptor nano-heterojunction photoelectrodes that produce capacitive-dominant photoresponse. For that we nanoengineer toxic-heavy-metal-free InP-based QDs and QD-fullerene nano-heterojunctions. While InP/ZnS QD leads to faradaic charge transfer, lower exciton binding energy and better passivation of surface traps of InP/ZnO/ZnS nanostructure facilitated capacitive charge transfer, which is maximized by tuning the donor-acceptor ratio. Therefore, we found out that the carrier localization and surface states of quantum dots at the nano-heterojunction has a vital role for the control of the bioelectrical currents.

### *4.2 Device design and fabrication*

Fig. 13 demonstrates the device architecture and corresponding energy band diagram of the photoelectrodes. The intermediate layer of ZnO nanoparticles serves for electron transport and hole blocking purposes due to its high electron mobility and large energy barrier at the valence band, respectively. Owing to the electron accepting property of fullerenes and the energy alignment of the QD and [6,6]-phenyl C61 butyric acid methylester (PCBM), the photoactive layer consisting of InP-based QD and a fullerene derivative of PCBM forms a donor-acceptor nano-heterojunction. PCBM captures the photogenerated electrons from the quantum dots and the holes remain in the QDs.[84]

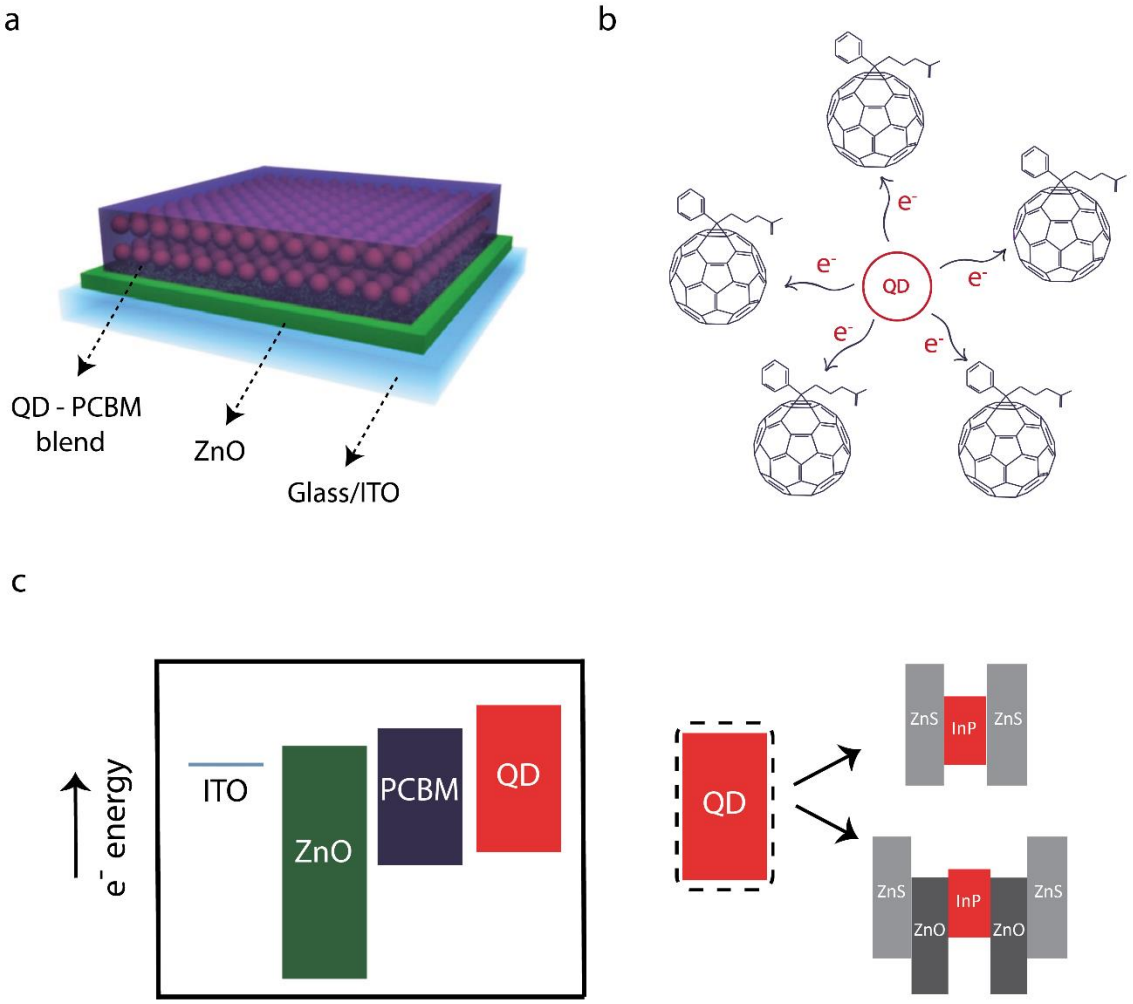


**Figure 13: a)** The schematic of the quantum dot and PCBM nano-heterojunction device structure, and **b)** the electron transfer from the InP-based quantum dots to PCBM. **c)** The energy band alignment based on our previous reports.[53, 85] InP/ZnS core/shell and InP/ZnO/ZnS core/shell/shell QDs were incorporated into the photoelectrode architecture.

### *4.3 Properties of QDs*

InP-based QDs were used for bio-applications because of their intrinsically non-toxic and heavy metal free composition.[49] We synthesized InP core QDs via hot injection method and grew ZnS and ZnO shells for the formation of InP/ZnS core/shell and InP/ZnO/ZnS core/shell/shell nanostructures (see methods for the details of the synthesis).[50, 60] The transmission electron microscopy (TEM) analyses of InP core, InP/ZnS, InP/ZnO and InP/ZnO/ZnS QDs reveal their mean particle sizes as 3.3 nm, 4.7 nm, 4.3 nm and 5.3 nm, respectively, revealing the successful shell growth. (Appendix B Figure 36, 37, 38, and Figure 14a). X-ray diffraction (XRD) analysis of InP/ZnO/ZnS QDs shows the corresponding crystallographic diffraction peaks of InP, ZnS and ZnO indicating formation of InP/ZnO/ZnS

core/shell/shell nanostructures (Fig. 14b) X-ray photoelectron electroscopy (XPS) analysis of InP core, InP/ZnO, InP/ZnO/ZnS and energy dispersive X-ray spectroscopy (EDS) of InP/ZnO/ZnS were provided in Appendix B to further confirm the growth of ZnO and ZnS shells in InP/ZnO/ZnS core/shell/shell nanostructure.

We next investigated the optical properties of the QDs. Fig. 14c shows the absorption and photoluminescence (PL) spectrum of InP core, InP/ZnS and InP/ZnO/ZnS QDs. The conduction band energy levels of InP and ZnO were expected to lead to a type-II behavior in InP/ZnO/ZnS QD, where electron tends to delocalize to the ZnO shell, while the hole is confined in the core. This causes a significant red-shift in the absorption and emission spectrum of InP/ZnO/ZnS compared to InP core and type-I InP/ZnS QDs (Fig. 14c) (normalized absorption profiles can be seen in Appendix B Figure 39). Moreover, growing ZnS and ZnO shells on InP core leads to enhanced photoluminescence quantum yield (PLQY) values, which are 7%, 28%, and 70% for InP core, InP/ZnS, and InP/ZnO/ZnS, respectively (Fig. 14d). The significant enhancement in the PLQY of InP/ZnS and InP/ZnO/ZnS nanocrystals indicates the successful passivation of nonradiative surface states.[86]

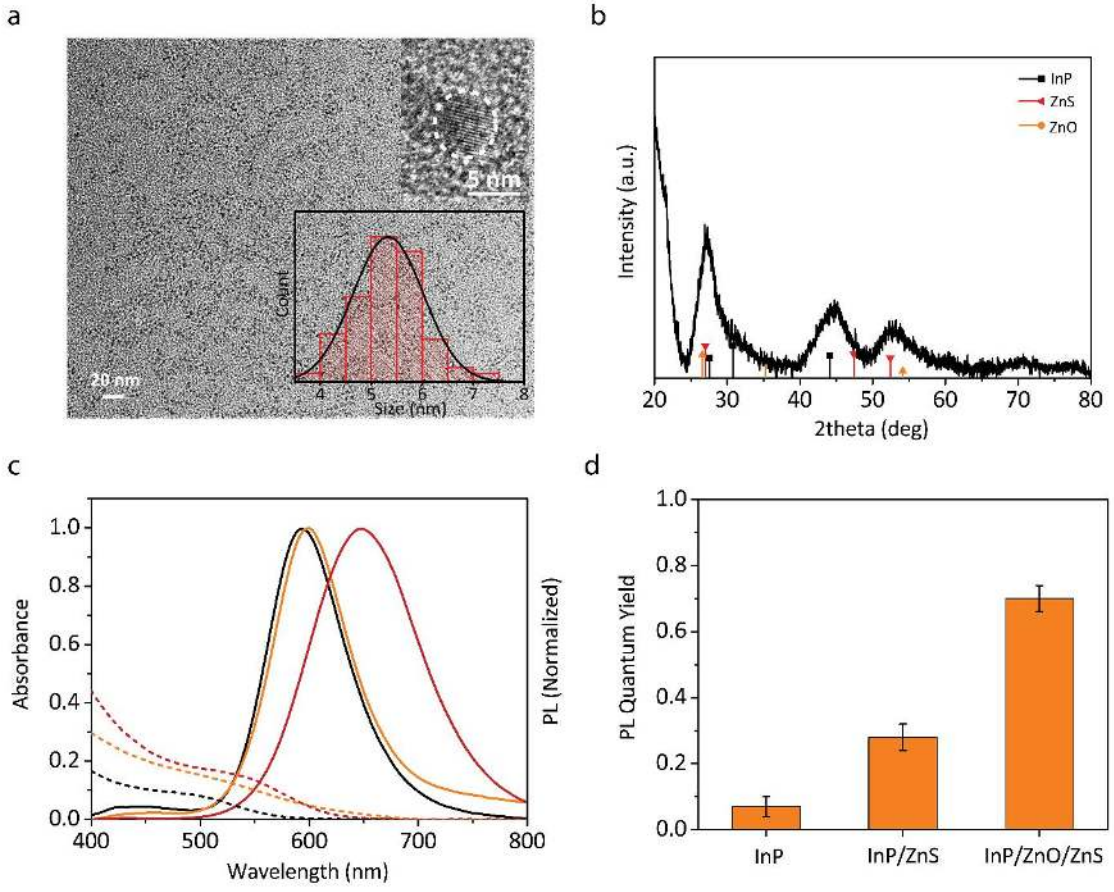


**Figure 14:** Structural and optical properties of QDs. **a)** TEM image of InP/ZnO/ZnS QD. Scale bar is 20 nm. Insets: HR-TEM image of InP/ZnO/ZnS QD with 5 nm scale bar (top), the size distribution (N = 200) (bottom).

**b)** XRD pattern of InP/ZnO/ZnS QD. **c)** Absorption and emission spectrum of InP core (black), InP/ZnS (orange) and InP/ZnO/ZnS (red) QDs dispersed in toluene each at the concentration of ~0.5 micromolar. **d)** PL quantum yields of InP, InP/ZnS and InP/ZnO/ZnS QDs (Measured in an integrating sphere with excitation wavelength of 375 nm).

### *4.4 Quantum mechanical simulations*

**Table 1**. Materials parameters used in the calculations.

| Materials | $m_e/m_0$ | $m_h/m_0$ | $\varepsilon_s/\varepsilon_0$ | $E_c$ (eV) | $E_v$ (eV) | $E_g$ (eV) | $E_p$ (eV) |
|---|---|---|---|---|---|---|---|
| InP | 0.08[87] | 0.69[87] | 12.9[87] | -4.8[88] | -6.14[88] | 1.34[88] | 17[87] |
| ZnS | 0.25[87] | 0.59[87] | 8.9[87] | -3.9[88] | -7.62[88] | 3.72[88] | |
| ZnO | 0.24[89] | 0.78[89] | 8.8[90] | -5.18[88] | -8.58[88] | 3.40[88] | |

To investigate the electronic properties of the QDs in detail, we conducted quantum mechanical calculations by solving self-consistently the Poisson-Schrödinger equations in the effective mass approximation and using BenDaniel-Duke boundary conditions.[91] The material parameters used in the calculations are listed in Table 1. All Coulombic interactions have been taken into account on both energy eigenvalues and wavefunctions.[91] At the end of the calculations, single particle energies of electron and hole and corresponding radial wavefunctions have been determined. Using these values, exciton binding energies, overlap integrals, oscillator strengths, absorption wavelengths, and transition energies have also been calculated. Figure 15 shows the confinement potential profiles, and electron and hole density functions for InP core (top panel), InP/ZnS core/shell (middle panel) and InP/ZnO/ZnS core/shell/shell (bottom panel) QDs. It should be noted that the maximum values of the density functions are normalized to unity for the consistency of scaling. When we look at the top panel of the Figure 15, we see that both electron and hole wavefunctions are confined completely in the core region meaning that the exciton binding energy will be large due to strong attractive Coulomb interaction between the electron and hole. In InP/ZnS core/shell QD, although the electron and the hole are still confined to the InP core, a small portion of the electron wavefunction penetrates to the ZnS shell and hence, it is expected that the exciton binding energy will be smaller when it is compared to the single InP core QD. The exciton binding

energies in these structures is calculated as 116 meV and 100 meV for InP and InP/ZnS QD, respectively. Moreover, although InP/ZnO/ZnS QD has a type-II energy band alignment as seen from potential profile in the bottom panel of Figure 15, the electron density does not localize completely in ZnO shell and expands through the whole structure due to its light effective mass, smaller spatial volume and also smaller potential depth, while the hole is completely confined in the InP core. This spatial expansion of electron density decreases the attractive Coulomb energy, i.e. the binding energy, between electron and hole. As a result, InP/ZnO/ZnS QD has a lower binding energy, i.e. 88 meV, compared to the binding energies of type-I InP core and InP/ZnS core/shell QDs. Electron delocalization to the shell indicates a possible transition from type-I to type-II heterostructure[60], which are known to be more favorable for photovoltaic applications and exciton dissociation.[92, 93] This transition can also be deduced from the electron-hole wavefunction overlap ratio. The overlap value is 0.89 for InP core QD and 0.76 for InP/ZnS core/shell QD, while it is considerably lower (0.52) for InP/ZnO/ZnS QD.

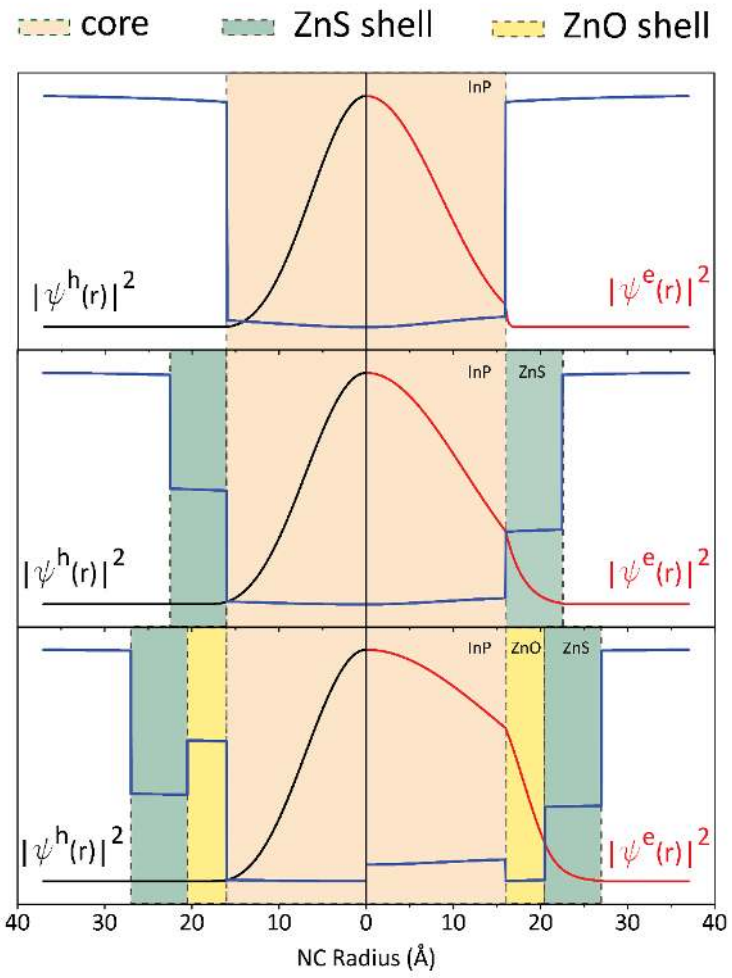


**Figure 15:** Radial distributions of electrons and holes throughout the InP core (top panel), InP/ZnS core/shell (middle panel) and InP/ZnO/ZnS core/shell/shell (bottom panel) quantum dots. The colored areas show the core

region, ZnS shell region, and ZnO shell region. Blue lines show the respective conduction and valence band potential profile of each QD. The bending of the potential profiles is due to attractive Coulomb potential between the electron and hole.

### *4.5 Photoresponse characterization and optimization*

We investigate the photoresponse of InP/ZnO/ZnS QD-PCBM nano-heterojunction photoelectrodes (see Appendix B for the preparation of QD:PCBM blend and the corresponding absorption profiles in Appendix B Figure 40). Figure 16a shows the photocurrent/photovoltage measurement configuration. We use a three-electrode electrochemical setup while illuminating the samples with a pulsed LED (see Methods for the details of the measurement setup). The photoresponse analysis was performed in the artificial cerebrospinal fluid (aCSF) to mimic the working conditions in a biological medium. InP/ZnO/ZnS QD-based devices display rapid charging/discharging spikes with rise/fall times of 200 µs (Figure 16b). The amplitude of the transient capacitive peaks for the QD:PCBM 1:1 and QD:PCBM 1:3 devices (57 µA $cm^{-2}$ and 45 µA $cm^{-2}$) are close to each other, while it is substantially lower for the QD:PCBM 1:7 devices (15 µA $cm^{-2}$) (Figure 16b) (1:1, 1:3, 1:7 are the QD:PCBM volume ratios in the blend). Here, QD-PCBM blend consists of electron-donating QD and electron-accepting PCBM, and the number of acceptors per each donor, i.e. the QD:PCBM ratio, affect the photoresponse of the device.[93] Sufficiently high number of acceptors per each donor lead to an efficient charge separation. However, at QD:PCBM 1:7 ratio, the imbalance of acceptors per each donor prevents the effective transfer of separated charges to the other layers due to unbalanced charge transportation between QD and PCBM materials.[94] Moreover, the ratio of capacitive current to electrochemical current is maximum in the QD:PCBM 1:3 device (2.5), while it is similar for QD:PCBM 1:1 and QD:PCBM 1:7 devices (1.43 and 1.47) (Figure 16c). This indicates that the most effective photoactive layer for the highest ratio of capacitive photocurrent is InP/ZnO/ZnS-PCBM 1:3 blend, which provides both high transient peak and 2.5 times greater capacitive photocurrent compared to the photoelectrochemical/resistive current (Figure 16c). The corresponding photovoltage values for the devices with different ratios of QD:PCBM are shown in Figure 16d. These photovoltages show the highest values that can be produced by the devices. Our best performing QD:PCBM 1:3 device can generate 46 ± 4 mV photovoltage, which would be sufficient to induce action potentials on excitable cells.[62]

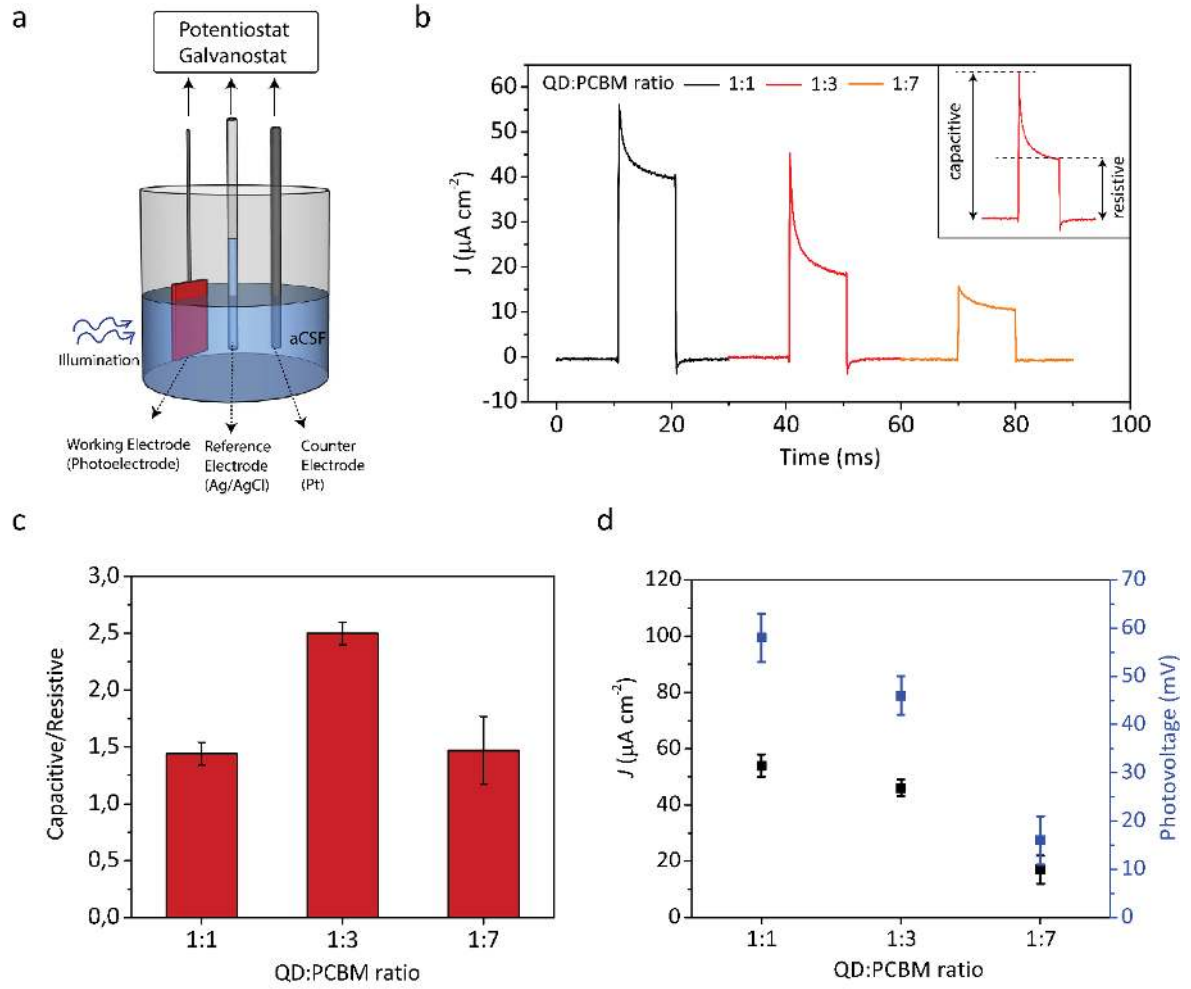


**Figure 16:** Photocurrent measurement configuration and response of InP-based devices. **a)** Three-electrode photocurrent/photovoltage measurement setup used for the photoresponse analysis of the photoelectrodes. **b)** Photocurrent density traces of the devices with InP/ZnO/ZnS:PCBM volume ratios of 1:1 (black), 1:3 (red), 1:7 (orange). Inset shows the components of the photocurrent. Capacitive and resistive components of the photocurrents were defined based on another study.[80] Capacitive current is the peak photocurrent reached after the light onset, while resistive current is the photocurrent remained after 90% of the illumination duration passed. **c)** The ratios of the capacitive to resistive components for devices with different QD:PCBM mixing ratios. **d)** Peak photocurrent density and photovoltage values for different mixing ratios. Illumination: 10 ms pulsed LED with 445 nm nominal wavelength and optical power density of 57 mW $cm^{-2}$ (N = 4).

Figure 17a shows the photoelectrical response of the nano-heterojunction devices with InP/ZnS quantum dot at the QD:PCBM 1:3 ratio. We observe that the steady-state photocurrent under continuous light intensity indicates that the photocurrent is dominated by electrochemical processes. The trace in Figure 17a also shows that the InP/ZnS-based device shows significantly slower charging/discharging dynamics with rise/fall times of 2 ms compared to 200 µs of InP/ZnO/ZnS based devices. The reasons behind the different behaviors of InP/ZnS-based and InP/ZnO/ZnS-based devices can be attributed to the processes at the

QD-PCBM nano-heterojunction and electrolyte interface (Figure 17b). The incident light pulse will be absorbed by quantum dots, leading to the generation of electron-hole pairs. These electron-hole pairs are bound together with an exciton binding energy, $E_b$, which were calculated for each QD via the quantum mechanical simulations. For efficient charge separation, the energy offset between the lowest unoccupied molecular orbit (LUMO) levels of the donor and acceptor materials should be sufficiently large to overcome $E_b$.[95] Our quantum mechanical simulations showed that type-II InP/ZnO/ZnS QD has a significantly lower $E_b$ compared to InP/ZnS. Hence, InP/ZnO/ZnS-based devices have a more efficient charge separation compared to InP/ZnS-based ones.

At the QD-PCBM interface, the electron is transferred to PCBM, while the hole stays trapped in the QD. Due to the much higher molar ratio of PCBM in the QD:PCBM blend, each QD is surrounded by multiple PCBM (check the schematic in Figure 13b for a qualitative demonstration). Thus, most of the device-electrolyte interface will be covered by PCBM. The potential barrier due to the band bending at the PCBM-electrolyte interface blocks the electrons from migrating to the solution and ZnO layer captures the electrons. As a result, holes trapped in the QDs, which are away from the surface, induce the formation of an oppositely charged double layer at the electrolyte interface, generating a capacitive photocurrent. The direction of the photocurrent from the electrode to electrolyte also confirms the hole-based displacement current. However, the existence of the surface states still mediate charge exchange at the interface, leading to photoelectrochemical processes.[96] Owing to its higher PL QY and core/shell/shell nanostructure of InP/ZnO/ZnS, which implies an improved passivation of surface states compared to InP/ZnS, the InP/ZnO/ZnS-based interfaces advantageously have low photoelectrochemical charge transfer with the electrolyte. Consequently, while type-I InP/ZnS-based devices produce predominantly photoelectrochemical current, type-II InP/ZnO/ZnS-based devices can generate capacitive currents, which was facilitated by the effective charge separation and less amount of nonradiative recombination sites of InP/ZnO/ZnS QDs.

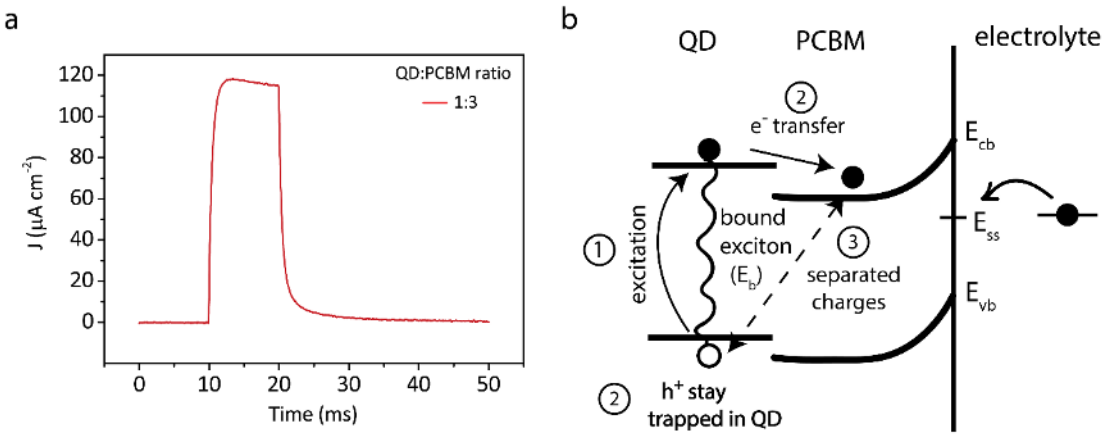


**Figure 17: a)** Photocurrent density of the InP/ZnS-based photoelectrode with InP/ZnS:PCBM ratio of 1:3. **b)** Schematic showing qualitatively the proposed ongoing processes at the QD:PCBM-electrolyte interface upon illumination. The processes are numbered according to their occurrence sequence. $E_{cb}$, $E_{vb}$, $E_{ss}$ stands for conduction band, valence band and surface state energy levels, respectively.

### *4.6 Conclusion*

In this study, we report the first-time demonstration of heavy-metal-free and capacitive QD:fullerene nano-heterojunction devices for prospective non-invasive QD-based neurostimulation applications. For that, we synthesized type-I InP/ZnS core/shell and type-II InP/ZnO/ZnS core/shell/shell nanostructures. We tested their photoresponses in a nano-heterojunction of QD:PCBM donor-acceptor system for effective exciton dissociation and charge transfer. InP/ZnO/ZnS-based nano-heterojunction achieved photocurrent with capacitive dominance, which has 2.5 times higher capacitive photocurrent than the resistive photocurrent, while InP/ZnS-based devices are predominantly governed by photoelectrochemical processes. We ascribe that difference to the following two main reasons: i) The type-II band structure of InP/ZnO/ZnS QD results in a lower exciton binding energy compared to type-I InP/ZnS, leading to more effective charge separation. ii) The core/shell/shell composition of InP/ZnO/ZnS yields fewer surface states, which diminishes the possible charge transfer between electrolyte and surface states. The conceptual understanding and the unconventional device structures in this study pave the way toward safe and effective quantum dot-based biointerfaces.

# Chapter 5

# $RuO_2$ Supercapacitor Enabled Flexible, Safe and Efficient Optoelectronic Neural Interface

(Reprinted (adapted) with permission from Karatum O*, et al.* (2022) $RuO_2$ Supercapacitor Enabled Flexible, Safe and Efficient Optoelectronic Neural Interface. *Advanced Functional Materials* 2109365. Copyright 2022 John Wiley and Sons.)

## *5.1 Introduction*

For organic optoelectronic neural interfaces, stimulation mechanism and efficiency of conversion of light to ionic currents is important to ensure safe operation without damaging tissues and to enhance the dynamic range of the devices, respectively. Since irreversible faradaic reactions can change the pH and deteriorate homeostasis of the cellular environment, operation using double layer capacitance or reversible faradaic reactions is critical for safe stimulation.[97] In fact, supercapacitors, which show high promise for energy storage applications, are based on fast and reversible reduction-oxidation (redox) reactions at the electrode-electrolyte interface, which yield notably large interfacial capacitance values.[98] This phenomenon can be fundamentally used for photostimulation of neurons by organic neural interfaces.[99] Among pseudocapacitive materials (e.g., PEDOT:PSS[56, 100]), $RuO_2$ is one of the most studied supercapacitor materials as it has the highest specific capacitance (~1000 F $g^{-1}$).[101, 102] Although different ruthenium complexes (e.g., $Ru^{2+}/Ru^{3+}$) have been previously used as anticancer agents[103], supercapacitor $RuO_2$ has attracted little attention for biomedicine[104] and bioelectronics[105, 106], and has not been explored for organic optoelectronic neural interfaces yet.

Here, we demonstrate that $RuO_2$ supercapacitor significantly boosts photogenerated charge injection densities over 20-fold in biological fluid of artificial cerebrospinal fluid (aCSF) in comparison with the control devices without $RuO_2$. It enables safe, repetitive, and low-light intensity photostimulation of hippocampal neurons below 1 $mW.mm^{-2}$. More interestingly, we developed an all-solution-processed fabrication (on a flexible substrate) of organic optoelectronic neural interfaces by sensitive incorporation of $RuO_2$ via electrochemical

deposition that allowed high-level control and optimization of charge injection density. The results point out that $RuO_2$ is a powerful material option for flexible optoelectronic neural interfaces and its electrochemical integration enables biocompatible, robust, and highly light-sensitive devices for future retinal implants.

### *5.2 Electrochemical analysis of $RuO_2$ and device development*

The solution-processed fabrication of the optoelectronic neural interface started with the sequential spin-coating of ZnO nanoparticles (NPs) and P3HT:PCBM bulk heterojunction (BHJ) thin films on fluorine doped tin oxide (FTO)/indium tin oxide (ITO) substrates (Figure 18a). During these steps, a part of the substrate was covered with a mask to prevent the deposition of ZnO NPs and P3HT:PCBM BHJ to the area where $RuO_2$ return electrode will be formed. Then, after removal of the mask, $RuO_2$ layer was coated on FTO/ITO via cyclic voltametric deposition.[107]

We investigated the structural properties of $RuO_2$ films having different number of electrodeposition cycles (5, 15, 25, 40, 60). The atomic force microscopy (AFM) (Appendix C Figure 47) revealed surface morphology of $RuO_2$ coatings, which have root-mean-square (RMS) surface roughness of 15.8, 15.6, 18.4, 22.9 and 23.1 nm for 5-, 15-, 25-, 40- and 60-cycle $RuO_2$ coatings, respectively. Considering the maximum diffusion length of protons in $RuO_2$ ($\sim 20$ nm), those roughness values are at desirable levels for facilitating ion transportation during fast redox reactions.[108] X-ray photoelectron spectroscopy (XPS) analysis of Ru $3d_{5/2}$ spectrum (Appendix C Figure 48) indicates that high amount of Ru(IV) species due to the peak at 281.4 eV corresponds to $RuO_2.xH_2O$[109, 110], which are involved in the reversible redox reactions of $Ru^{4+}/Ru^{3+}$ couple.[111] Scanning electron microscopy (SEM) images of $RuO_2$ coatings show a porous film morphology with progressively narrowing pore sizes as deposition cycle increases (Figure 18b; see Appendix C Figure 49 for SEM images of all five coatings). Advantageously porous coatings of capacitive materials offer potentially high electrochemical surface area/geometrical surface area (ESA/GSA) ratio for high charge capacities, which can be optimized by controlling the thickness through deposition cycles (Figure 18c).[112]

To assess the effectiveness of $RuO_2$ coatings under physiological conditions, we performed cyclic voltammetry (CV) and electrochemical impedance spectroscopy (EIS) in artificial cerebrospinal fluid (aCSF). Figure 18d displays the cyclic voltammograms of $RuO_2$ coatings

after different amounts of deposition cycles. The symmetric and quasi-rectangular shapes of cyclic voltammograms of $RuO_2$ coatings reveal the capacitive behavior of films through reversible redox reactions. Based on cyclic voltammograms, we calculated the capacitance and cathodic charge storage capacity ($CSC_c$), which is commonly used as a characterization parameter for stimulation electrodes. Capacitance and $CSC_c$ follows a similar sigmoidal-like trend (Figure 18e). For the 5-cycle $RuO_2$ deposition, whose thickness is ~ 10 nm (Figure 18c), the $CSC_c$ is 2.5 ± 0.51 mC $cm^{-2}$ (mean ± s.d.), which is similar to the reported value for ~ 10 nm SIROF coating.[112] For 60-cycle $RuO_2$ (~ 110 nm), $CSC_c$ reaches to 19.8 ± 1.7 mC $cm^{-2}$ (mean ± s.d.), which is on the same order with sputtering.[105] In the range where our biointerfaces operate (0 – 0.5 V) the capacitive charge-transfer mechanism is evident (Figure 18f).

The long-term stability of 60-cycle $RuO_2$ deposition, which has the highest capacitance and $CSC_c$, was evaluated by subjecting the $RuO_2$ coating to 10000 continuous CV cycles (Figure 18g). The current density due to the interfacial capacitance of $RuO_2$ is well-preserved after 10000 cycle, which denotes its excellent long-term stability. Finally, Figure 1h shows the Nyquist plots of $RuO_2$ coatings obtained by EIS analysis. We fitted the high frequency region with a resistance (R) and the low frequency region with a resistance-constant phase element (R-Q) (Appendix C Figure 50). In the high frequency region, 5-, 15-, and 25-cycle $RuO_2$ coatings exhibited similar resistances, while 40- and 60-cycle $RuO_2$ coatings display increased resistances possibly due to their higher film thickness and narrower pore sizes (Appendix C Table 3). In the low frequency region, imaginary impedance was gradually decreasing as the cycle number increased (Appendix C Table 3), indicating higher capacitance values for thicker films as we observed in CV measurements. Even though the capacitance value from the CV followed the trend of the number of deposition cycles, the capacitance measured using EIS showed 25 cycles as an outlier, which is probably because of the increased resistance and thus lower porosity.

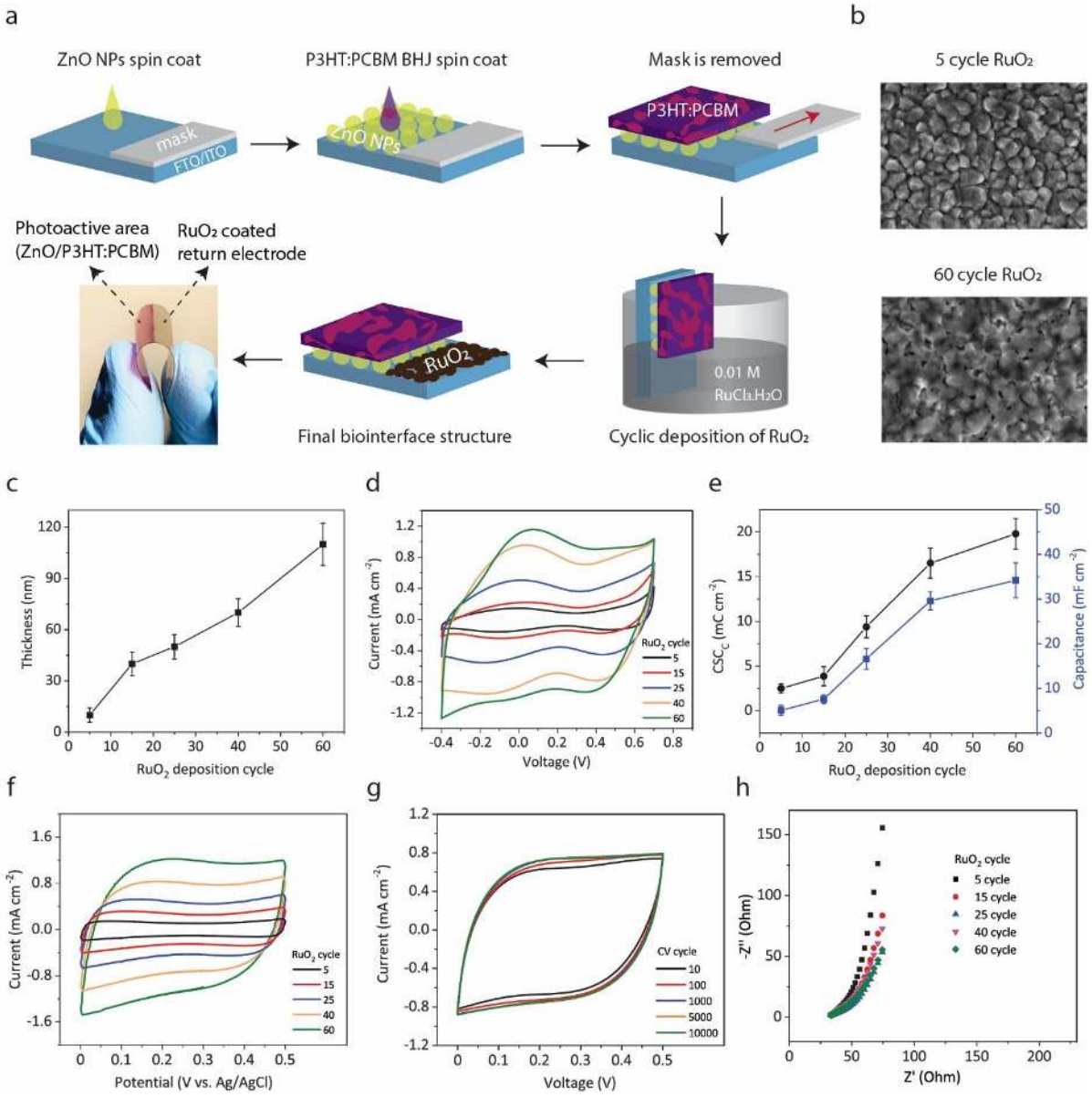


**Figure 18: Fabrication of $RuO_2$-based optoelectronic biointerfaces, and structural and electrochemical characterization of $RuO_2$ coatings. a)** Sequential fabrication of $RuO_2$ based biointerfaces with an image of the produced flexible device. **b)** Surface SEM images of 5-cycle and 60-cycle $RuO_2$ coatings. **c)** Thickness of $RuO_2$ coatings as a function of deposition cycle. **d)** Cyclic voltammograms of $RuO_2$ coatings from -0.4 to 0.7 V range, which is within the water electrolysis window.[105] Scan rate is 50 mV $s^{-1}$. **e)** Cathodic charge storage capacity ($CSC_c$) and capacitance of $RuO_2$ coatings extracted from CV measurements shown in (d). **f)** Cyclic voltammograms of $RuO_2$ coatings in the operation range of the biointerfaces (0 – 0.5 V). Scan rate is 50 mV $s^{-1}$. **g)** Long-term cyclic stability of 60-cycle $RuO_2$ coating measured over 10000 cycles in 0 – 0.5 V. Scan rate is 100 mV $s^{-1}$. **h)** Electrochemical impedance measurement of $RuO_2$ coatings within the frequency range of 1 – 10000 Hz.

### *5.3 Open-circuit photoelectrical response*

High CSC and capacitance of $RuO_2$ indicates its potential for achieving improved charge injection levels for the optoelectronic neural interface. To experimentally test that, we studied

the effect of $RuO_2$ on the photoresponse of a control device. In our device architecture, ZnO/P3HT:PCBM photovoltaic heterostructure serves as the photocurrent-generating electrode. P3HT:PCBM BHJ absorbs the impinging light and afterwards electron-hole pairs are dissociated at the donor-acceptor interface. Free electrons are transferred toward FTO/ITO through ZnO NPs. ZnO layer serves as the hole blocker due to its valence band energy level and electron transporter owing to its high electron mobility.[77] The device design consists of ZnO/P3HT:PCBM layer over 1 $cm^2$ area of FTO/ITO coated substrate and electrodeposited $RuO_2$ film over the remaining 0.5 $cm^2$ area of the same substrate (Figure 19a). The control devices are bare FTO/ITO as the return electrode without $RuO_2$ coating.

We analyzed the photoelectrical performance of the control and $RuO_2$ biointerfaces by comparing their charge-injection performances in a wireless, free-standing measurement setup (Figure 19b). Devices were placed in aCSF and injected charge was measured in voltage clamp mode with a patch pipette that is positioned close to the biointerface surface (< 5 µm). This measurement configuration demonstrates the ability of biointerfaces to perturb the local electric equilibrium at the device-electrolyte interface, revealing the potential of the biointerface to stimulate neurons. The photoresponse of the control devices were characterized by an initial capacitive peak triggered by light onset and a second peak with a smaller magnitude taking place with the end of illumination (Figure 19c). The capacitive onset peak decays rapidly to its ground level, meaning no significant capacitive current is flowing under steady illumination condition because of the double layer capacitance with minimal Faradaic reactions under steady photovoltage.[113] This considerably limits the amount of injected charge required for effective stimulation of neurons.

After $RuO_2$ deposition, the reversible surface redox processes induced by the coating leads to remarkable amount of additional charge injection into the electrolyte due to the enhancement of the return electrode capacitance (Figure 19c).[114] The steady photovoltage during illumination evokes reversible Faradaic reactions on the $RuO_2$ surface, predominantly redox reactions of $Ru^{4+}/Ru^{3+}$ couple[105, 111], leading to formation of a redox capacitance, which is embedded in the redox impedance of return electrode, in addition to the double-layer capacitance (Appendix C Figure 51). Considering that the double layer capacitance of typical organic electrode-electrolyte interfaces is on the order of 1 to few 10s of µF $cm^{-2}$,[115, 116, 117] the double layer capacitance of $RuO_2$-electrolyte interface is expected to be on the similar order. However, the redox impedance, which includes the pseudocapacitance of $RuO_2$ and is in

parallel to the double layer capacitance, significantly boosts the interfacial capacitance of the return electrode, which is counter-balanced by faradaic reactions at P3HT:PCBM-electrolyte interface (Appendix C Figure 52). As a result, the onset photocurrent peak increased more than 2-fold (Appendix C Figure 53). Noticeably, the amount of the total charge injection substantially increased, which can be controlled with the deposition cycles. While the charge injection capacity of control devices was 2.54 ± 1.26 pC (mean ± s.d.), for 5-cycle-$RuO_2$ biointerfaces it jumped to 29.8 ± 8.12 pC (mean ± s.d.), indicating more than an order of magnitude increase. For 60 cycles the injected charge reached 57.1 ± 13.67 pC (mean ± s.d.), corresponding to over 20-fold enhancement compared to control devices (Figure 19d). If the counter-balancing faradaic reactions at P3HT:PCBM-electrolyte interface are suppressed, the charge injection performance of $RuO_2$-based biointerfaces notably decreases (Appendix C Figure 52), which confirms that the observed improvement in photoresponse is due to the redox impedance of $RuO_2$. As a further control experiment, we checked whether $RuO_2$ generates photocurrent by itself, and verified that $RuO_2$ layer alone produces only a marginal photocurrent, which is at least two orders of magnitude lower than the photovoltaic part (Appendix C Figure 54). Since the best performing device is 60 cycle $RuO_2$, the rest of the experiments were conducted with 60 cycle $RuO_2$ biointerfaces (referred as '$RuO_2$ BI' in the rest of the text).

Temporal characteristics of the generated photocurrent provides information about the maximum achievable stimulus frequencies. Figure 19e shows photocurrents of $RuO_2$ BI under pulsed illumination for pulse-widths of 10 ms, 5 ms, 1 ms, 500 µs and 200 µs. The capacitive onset peak was preserved even for 200 µs pulse, implying that high frequency stimulus, e.g., 100 Hz, can be applied via $RuO_2$ BI. For example, when we applied 1 ms 100 Hz pulsed excitation, the photocurrent peak and shape was well-preserved throughout the repeated photoexcitation cycles (Appendix C Figure 55). Lastly, we evaluated the spatial distribution of the photoresponse by measuring the amount of charge injection while moving the patch pipette in horizontal and vertical directions, starting from the center of the illumination spot (radius R = 160 µm) (Figure 19f inset). Charge injection decays in an exponential fashion in both directions as the pipette was gradually moved away from the spot center (Figure 19f), suggesting a localized charge injection primarily governed by illumination spot area. In horizontal direction, the measured charge was still over 90% at the spot edge (1R away from the center) and it drops to 62% 2R away from the center. This represents a relatively slower decay compared to a previous study[118], most likely due to the device geometry with large return electrode.

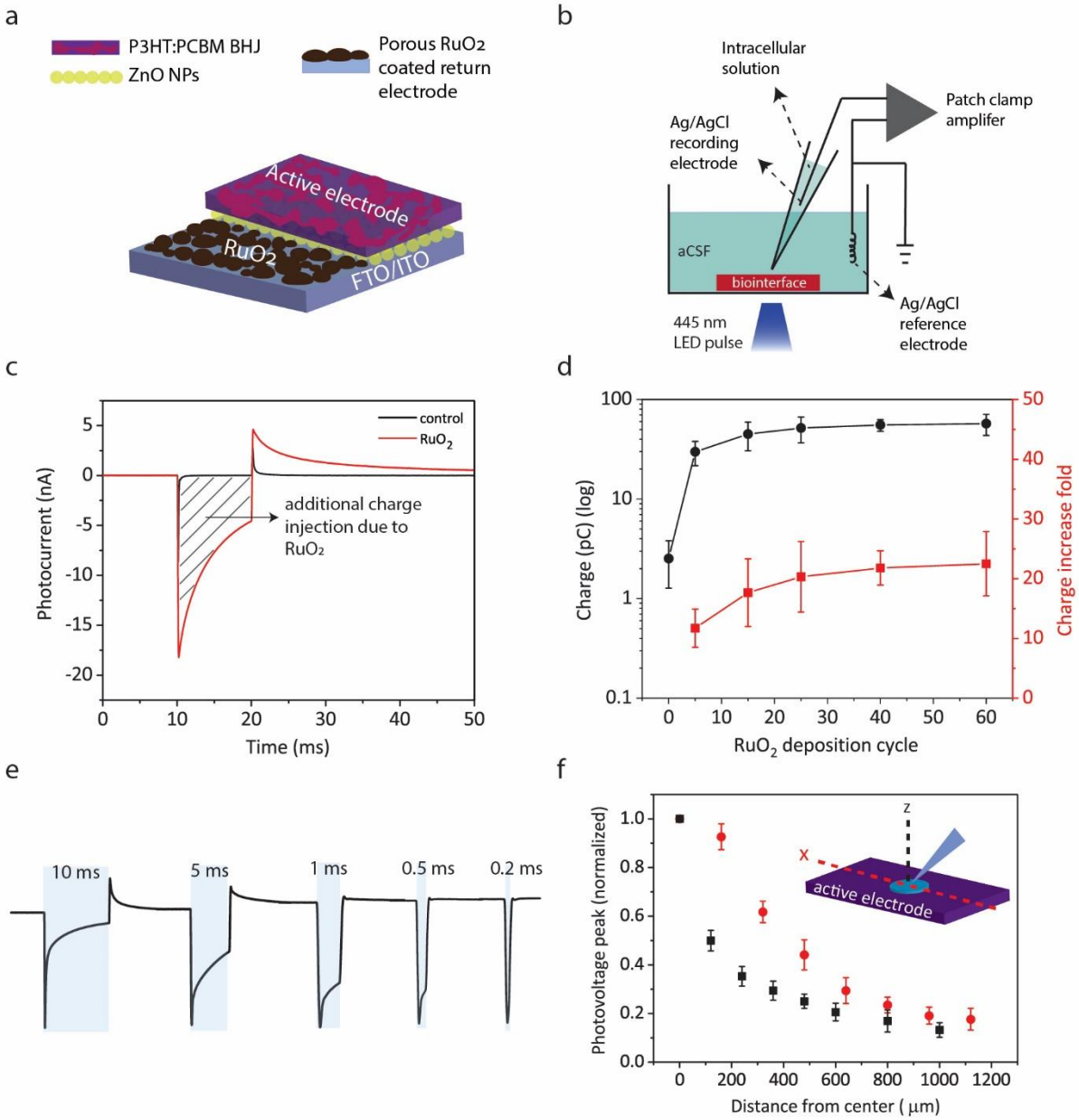


**Figure 19: Effect of $RuO_2$ on the biointerface photoresponse. a)** Schematic of the $RuO_2$ integrated biointerface architecture. Control device is the same structure without $RuO_2$ coating. **b)** Schematic of the photoresponse characterization setup. Stimulation light source is an LED (445 nm nominal wavelength, 1.9 mW $mm^{-2}$ optical power density) and the recording tool is a patch clamp amplifier with a micropipette that is positioned less than 5 µm from the biointerface surface. **c)** Photocurrent generated by control and $RuO_2$ biointerfaces at the device-electrolyte interface. 10 ms light pulse with 2 mW $mm^{-2}$ optical power density was applied when t = 10 ms. The simplified equivalent circuit of the interface is shown in Appendix C Figure 51. **d)** Injected charge levels extracted from the photocurrent measurements of control and $RuO_2$ biointerfaces (mean ± s.d. for N = 8). Zero deposition cycle represents the control device. Right axis shows the amount of enhancement in the injected charge for each $RuO_2$ coating. **e)** Photocurrent responses of 60-cycle $RuO_2$ biointerface for different pulse-width illuminations. Shaded areas represent 'light-on' periods. **f)** Spatial distribution of injected charge at increasing distances from the illumination spot center horizontally (x) and vertically (z). Inset illustrates the measurement configuration, where the blue circle designates the illumination spot (320 µm diameter, 10 ms pulse).

### *5.4 Short-circuit photoelectrical response*

To quantify the photoelectrical response of $RuO_2$ BI, we measured its photoresponse via a three-electrode potentiostat/galvanostat system (Figure 20a). Working electrode was connected to the FTO/ITO back electrode, while the counter and reference electrodes were floating in the ionic aCSF medium.[42] The intensity dependent photocurrent and photovoltage measurements in Figure 20b and 20c showed the maximum achievable current density of 6 mA $cm^{-2}$ and 290 mV photovoltage for $RuO_2$ BI under 445 nm 85 mW $cm^{-2}$ LED illumination, respectively. Integrating the area under the photocurrent-time traces corresponds to the injected charges for each illumination intensity (Figure 20d) and $RuO_2$ BI has charge injection density of more than 10 μC $cm^{-2}$ for intensities greater than 30 mW $cm^{-2}$. This charge injection level is sufficiently high according to the reported threshold charge density values for stimulation of human epiretinal, cortical, auditory brainstem and subthalamic nucleus neurons.[112] In addition, $RuO_2$ BI has more than an order of magnitude higher charge injection capacity compared to control devices (Figure 20d).

Previously we showed that high frequency stimulus (e.g., 100 Hz) via short pulses (e.g., 1 ms) can be applied with $RuO_2$ BI. Now, we demonstrate that even for such short pulse durations, the charge density of $RuO_2$ BI is in the μC $cm^{-2}$ range. For 1 ms pulse, injected charge density is 2.4 ± 0.56 μC $cm^{-2}$ (mean ± s.d.), while it is 1.6 ± 0.66 μC $cm^{-2}$ (mean ± s.d.) for 500 μs pulse (Figure 20e inset), which are still near the thresholds for stimulation of certain neural tissues (e.g., subthalamic nucleus, auditory brainstem).[112] Moreover, for lower stimulus frequencies 20 ms pulse would result in a high charge density of 20.2 ± 2.44 μC $cm^{-2}$ (mean ± s.d.) (Figure 20e).

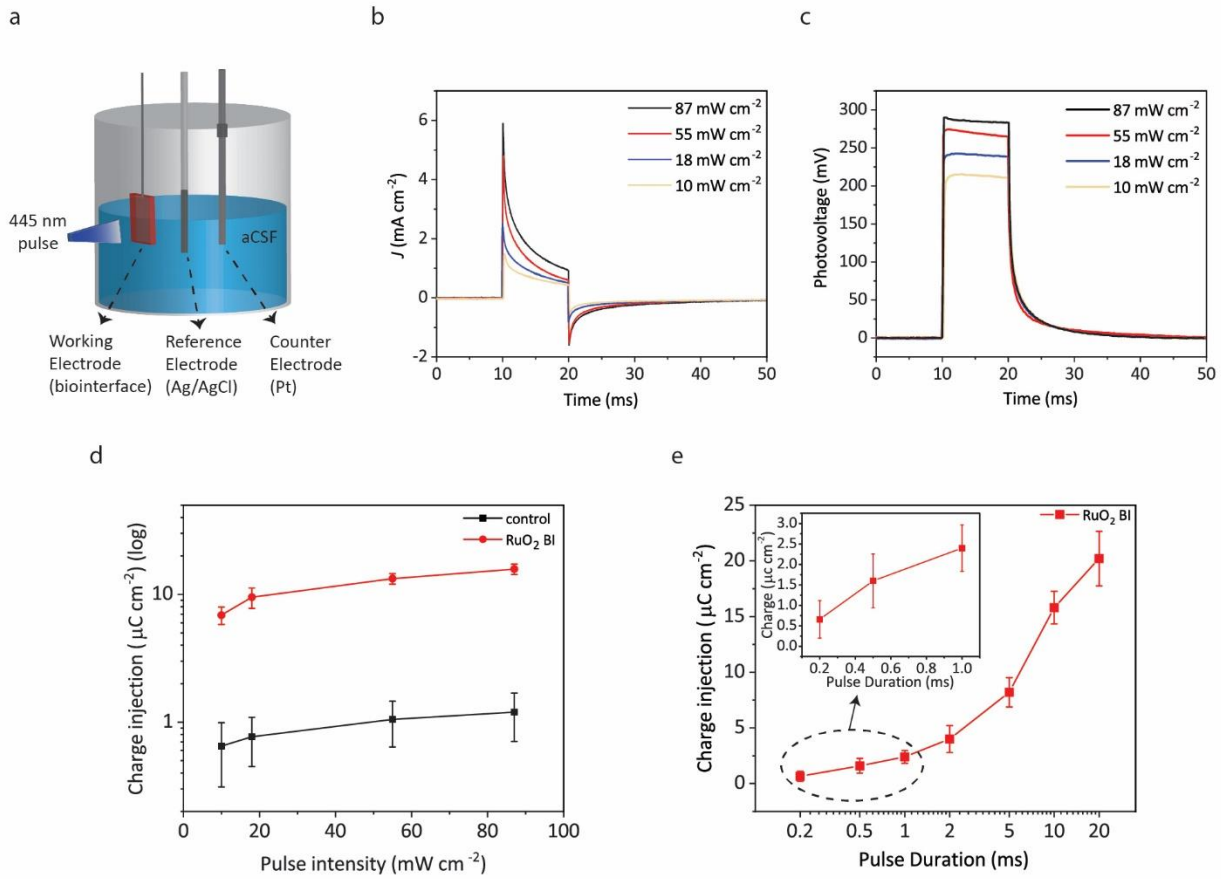


**Figure 20: Photoelectrochemical performance of the optimized $RuO_2$ biointerface ($RuO_2$ BI). a)** Illustration of the photocurrent/photovoltage measurement setup. Stimulation source is an LED (445 nm nominal wavelength, 10 ms pulses with optical power density ranging from 10 to 87 mW $cm^{-2}$) and the recording tool is a three-electrode electrochemical setup connected to a potentiostat/galvanostat. 0.5 $cm^2$ of biointerface area is immersed in the aCSF electrolyte. **b)** Photocurrent density, and **c)** photovoltage of $RuO_2$ BI as a function of illumination intensity. Light pulse is applied when t = 10 ms. **d)** Injected charge into the aCSF electrolyte as a function of pulse intensity for control device and $RuO_2$ BI for 10 ms pulsed excitation (mean ± s.d. for N = 8). **e)** Injected charge levels of $RuO_2$ BI for different pulse-width excitations (mean ± s.d. for N = 8). Inset zooms into the first three data points encircled by the dashed ellipse.

### *5.5 Stability, toxicity and intracellular stress analysis*

We tested the stability and biocompatibility of $RuO_2$ BI and checked whether repeated photoexcitation of $RuO_2$ BI causes ROS intake by neurons or not. Stability was studied by investigating the charge injection performance of $RuO_2$ BI after detailed tests including low temperature sterilization, accelerated passive and reactive ageing, and repeated photoexcitation experiments. Low temperature hydrogen peroxide ($H_2O_2$) plasma sterilization is an FDA approved technique for testing medical devices.[119] After application of low temperature $H_2O_2$ plasma sterilization, the charge injection levels of $RuO_2$ BI reduced to 78 ± 9% (mean ± s.d.) of its pre-sterilization value (Figure 21a). The sterilized $RuO_2$ BI samples

were further subjected to accelerated reactive ageing test, where we kept the samples in $H_2O_2$-added aCSF at 87°C oven and quantified their charge injection performance after each 48 h, which corresponds to a simulated ageing period of 2 months. After ageing period of 12 months, $RuO_2$ BI preserved 76 ± 8% of its post-sterilization and 60 ± 6% of its pre-sterilization charge injection values indicating robust operation of $RuO_2$ BI under harsh ageing conditions (Figure 21b). At this point, we wondered whether the reduction in charge injection values of $RuO_2$ BI is due to the degradation of ZnO/P3HT:PCBM active electrode or $RuO_2$ coating. The EIS measurements of active electrode and $RuO_2$ coating before and after plasma sterilization and reactive ageing tests showed that impedance-frequency behavior of $RuO_2$ is preserved after the tests, while the response of active electrode deviated from its pre-sterilization behavior (Appendix C Figure 56). This implies that performance drop is primarily due to the degradation of the photoactive electrode, which can be prevented via gold layer deposition on top of the electrode[117], and $RuO_2$ remains intact under harsh ageing conditions. Furthermore, $RuO_2$ BI exhibits excellent stability under passive accelerated ageing test, showing no significant decrease in the charge injection performance after 24 months (Figure 21b). Moreover, the charge retention performance of $RuO_2$ BI was tested under repeated 10000 cycle pulsed photoexcitation. After 10000 illumination cycle, 84 ± 4.8 % of injected charge was conserved while the shape of photocurrent is preserved during turn-on and -off of the illumination (Figure 21c inset), implicating the conserved capacitive functionality of the biointerfaces (Figure 21c).

To evaluate the cytotoxicity of $RuO_2$ BI, we conducted in vitro biocompatibility test with primary hippocampal neurons via MTT toxicity assay and immunofluorescence imaging before and after 14 days of neuron culture. MTT analysis showed that neurons on $RuO_2$ BI demonstrates statistically nonsignificant difference of cell viability compared to biocompatible ITO samples after 48-hour incubation period (Figure 21d). This result is supported by immunofluorescence images of ITO and $RuO_2$ samples. Day 0 and day 14 images of ITO and $RuO_2$ BI demonstrated preserved cell viability and morphology for both sample types, suggesting low cytotoxicity of $RuO_2$ BI for primary hippocampal neurons (Figure 21e).

Despite the reversibility of $RuO_2$-induced redox reactions, we wanted to reassure that $RuO_2$ BI does not create ROS in the electrolyte upon photoexcitation. To validate that, we quantified the amount of ROS intake of hippocampal neurons cultured on $RuO_2$ BI by measuring the fluorescence intensity of $H_2$-DFCDA agent after subjecting the biointerfaces to 10000-cycle photoexcitation (Figure 21f, 21g). We used neurons on bare FTO as negative control, on bare

FTO treated with 100 μM $H_2O_2$ as positive control and on $RuO_2$ BI before photostimulation as control groups. Expectedly, neurons on positive control samples show high fluorescence intensity due to the intake of $H_2O_2$ in the extracellular medium. On the other hand, there is no statistical difference between the fluorescence intensities of neurons grown on bare FTO, $RuO_2$ BI before photostimulation, and $RuO_2$ BI after photostimulation (Figure 21f). Hence, repeated photoexcitation of $RuO_2$ BI does not cause intracellular oxidative stress for neurons, which indicates the absence of ROS formation in the aCSF. This suggests a safe photostimulation mechanism for $RuO_2$ BI. This is further supported by the pH measurement of extracellular medium during 40000-cycle photoexcitation of $RuO_2$ BI (Appendix C Figure 57). pH values measured after each 10000-cycle photoexcitation do not show significant differences, implying that the chemical composition of aCSF is not altered by irreversible faradaic processes during repeated photoexcitation.

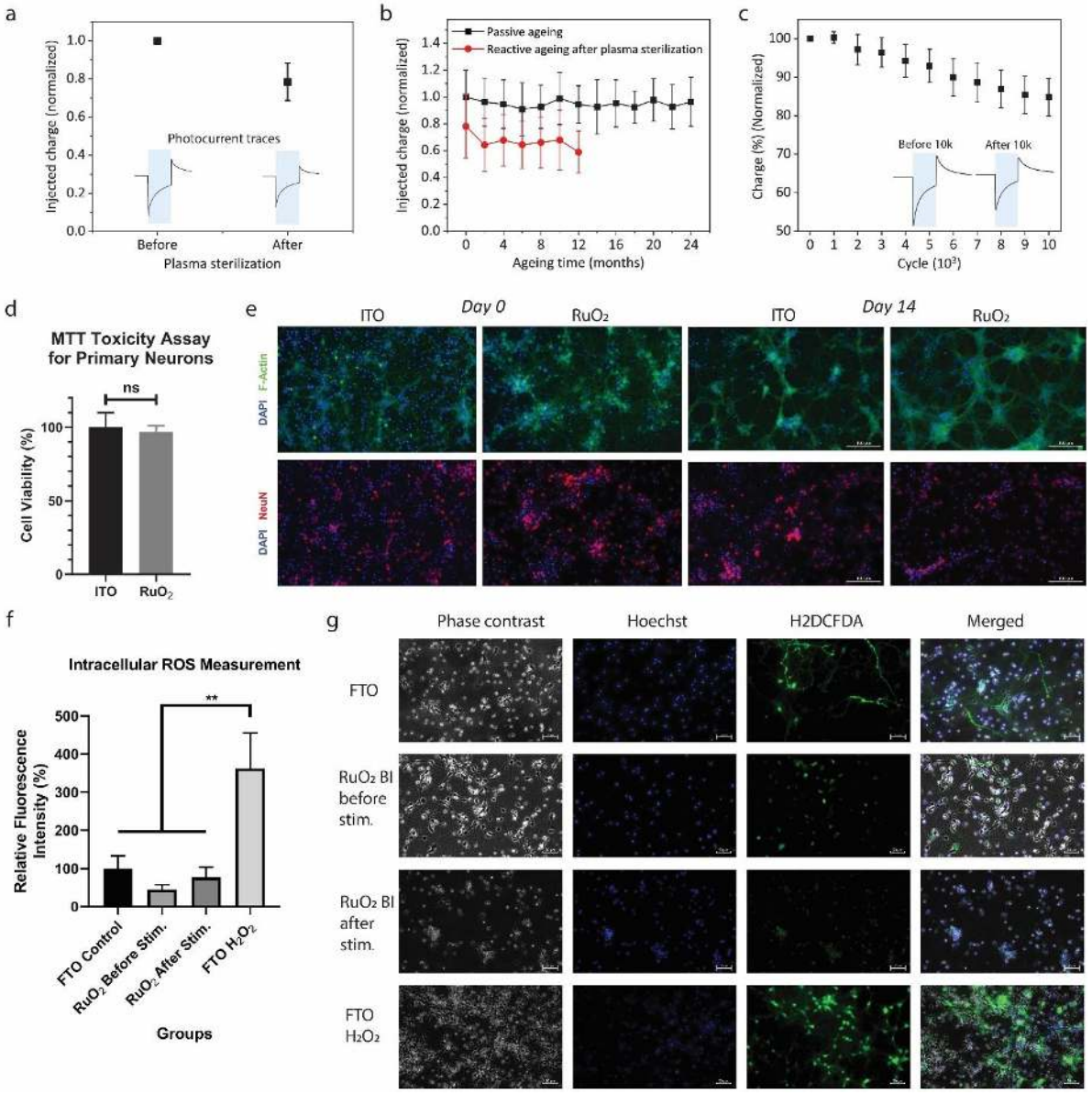


**Figure 21: Stability, biocompatibility, and intracellular oxidative stress analysis. a)** Charge injection performance of $RuO_2$ BI before and after low temperature $H_2O_2$ plasma sterilization (mean ± s.d. for N = 3). The sum of three $RuO_2$ BI before the sterilization is normalized to 1. Inset shows photocurrent traces before and after the sterilization. **b)** Variation of $RuO_2$ BI charge injection levels during the passive and reactive accelerated ageing tests (mean ± s.d. for N = 3). Reactive ageing test was applied to the biointerfaces that underwent through plasma sterilization. **c)** Photocyclic stability of $RuO_2$ BI showing the variation of injected charge during the application of 10000 photoexcitation pulse (mean ± s.d. for N = 4). Illumination: 5 Hz stimulus frequency, 10 ms pulse-width, 2 mW $mm^{-2}$ optical power density. Inset shows photocurrent traces before and after 10000 photocycles. **d)** MTT assay analysis for quantifying cell viabilities of primary hippocampal neurons cultured on $RuO_2$ BI (mean ± s.d. for N = 4). Bare ITO sample, which is known to be biocompatible, was used as control. The level of significance was calculated using an unpaired, two-tailed t-test; *p < 0.05 was evaluated as statistically significant. **e)** Immunofluorescence images of ITO and $RuO_2$ BI samples obtained at day 0 and day 14 to observe the cell viability and morphology of hippocampal neurons after 14 days of culture. **f)** Quantification of ROS intake, i.e. intracellular oxidative stress, of neurons cultured on $RuO_2$ BI after subjecting the biointerfaces to 10000 photoexcitation cycle (mean ± s.d. for N = 3). Illumination: 5 Hz stimulus frequency, 10 ms pulse-

width, 2 mW $mm^{-2}$ optical power density. $RuO_2$ before stimulation samples are control, bare FTO is negative control, bare FTO with $H_2O_2$ is positive control. The fluorescence intensity of negative control is normalized to 100%. **g)** Fluorescence microscope images of FTO, $RuO_2$ before stimulation, $RuO_2$ after stimulation and FTO with $H_2O_2$ samples stained with Hoechst and H2DCFDA, which were used to calculate the relative intracellular fluorescence intensities.

### *5.6 Light-induced neural activity recordings*

We finally explored the light-induced effect of $RuO_2$ BI on primary hippocampal neurons by measuring single-cell intracellular membrane potential and current with respect to a distant Ag/AgCl electrode via a patch-clamp setup. Figure 22a illustrates the measurement configuration, where $RuO_2$ BI is operating wirelessly (i.e., electrically floating in aCSF) to photostimulate the cultured neurons. First, we checked if photoexcitation of $RuO_2$ BI can open voltage-gated sodium channels and induce inward sodium current, which is an essential component for eliciting action potential. As an initial control experiment, we measured the current-voltage characteristics of hippocampal neurons under dark conditions by applying different membrane holding voltages via the amplifier (Appendix C Figure 58). Rapid negative inward currents, which originate from voltage-gated sodium channels, start to appear at holding voltage of -50 mV. These sodium inward currents for -50, -30, -10 mV holding potentials are followed by slower outward potassium currents (Appendix C Figure 58a). When we add voltage-gated sodium channel blocker QX-314 chloride[120] into the intracellular solution, negative inward currents are no longer observed, confirming that they are due to voltage-gated sodium channels (Appendix C Figure 58b). Under light conditions without any external stimulus from amplifier, photoexcitation of $RuO_2$ BI with 5 ms pulses of 2.4 mW $mm^{-2}$ illumination intensity induced fast sodium inward currents followed by a slower outward potassium current, a typical current profile observed during an action potential (Figure 22b).[121] Lower light intensity, 0.6 mW $mm^{-2}$, did not result in the same response, which possibly led to a subthreshold stimulation. As a control experiment, we added QX-314 chloride to the intracellular solution. As in previous experiment, since photoexcitation of $RuO_2$ BI leads to rapid sodium inward current and slower outward potassium current for neurons under standard conditions, the inward sodium current is nearly vanished in the existence of QX-314 chloride (Figure 22c). These experiments denote that $RuO_2$ BI activates voltage-gated sodium channels of hippocampal neurons upon photoexcitation, which is expected to elicit action potentials.

To verify the firing of neurons, we conducted current clamp recordings to examine their intracellular membrane potential with respect to a distant Ag/AgCl electrode. The recordings demonstrate that light-induced photoresponse of $RuO_2$ BI reproducibly stimulates neurons

under 5 ms pulsed excitation with stimulus frequencies of 5, 10, and 20 Hz (Figure 22d). Evoked action potentials are temporally precise and some peaks are followed by after depolarizations, which frequently occurs during firing of hippocampal neurons.[122] The spikes with 5 ms pulses are induced by minimum 2.4 mW $mm^{-2}$ light intensity. Figure 5e displays that longer pulses with lower illumination intensities, 10 ms at 1.25 mW $mm^{-2}$ and 20 ms at 0.65 mW $mm^{-2}$, can also elicit action potentials. As pulse-width increases, the minimum required power for photoactivation decreases. However, the minimum total energy for evoking action potentials stays nearly constant as expected for extracellular stimulation electrodes.[123] The resultant action potential success rates show similar fashions for 5, 10, and 20 ms pulses, showing slight decrease as the stimulus frequency is increased. The success rates stay above 80% for all pulse-widths and stimulus frequencies, except for 5 ms 20 Hz pulse, which is 69% ± 3.2 (mean ± s.d.) (Figure 22f). Higher success rates for longer pulse-widths are ascribed to continuous charge injection during light-on periods due to $RuO_2$ return electrode. On the other hand, action potential latencies are directly proportional with the pulse-widths (Figure 22g). Overall, the electrophysiology recordings signify the effective photostimulation performance of $RuO_2$ BI indicated by temporal precision, rapid reversibility, and short latencies.

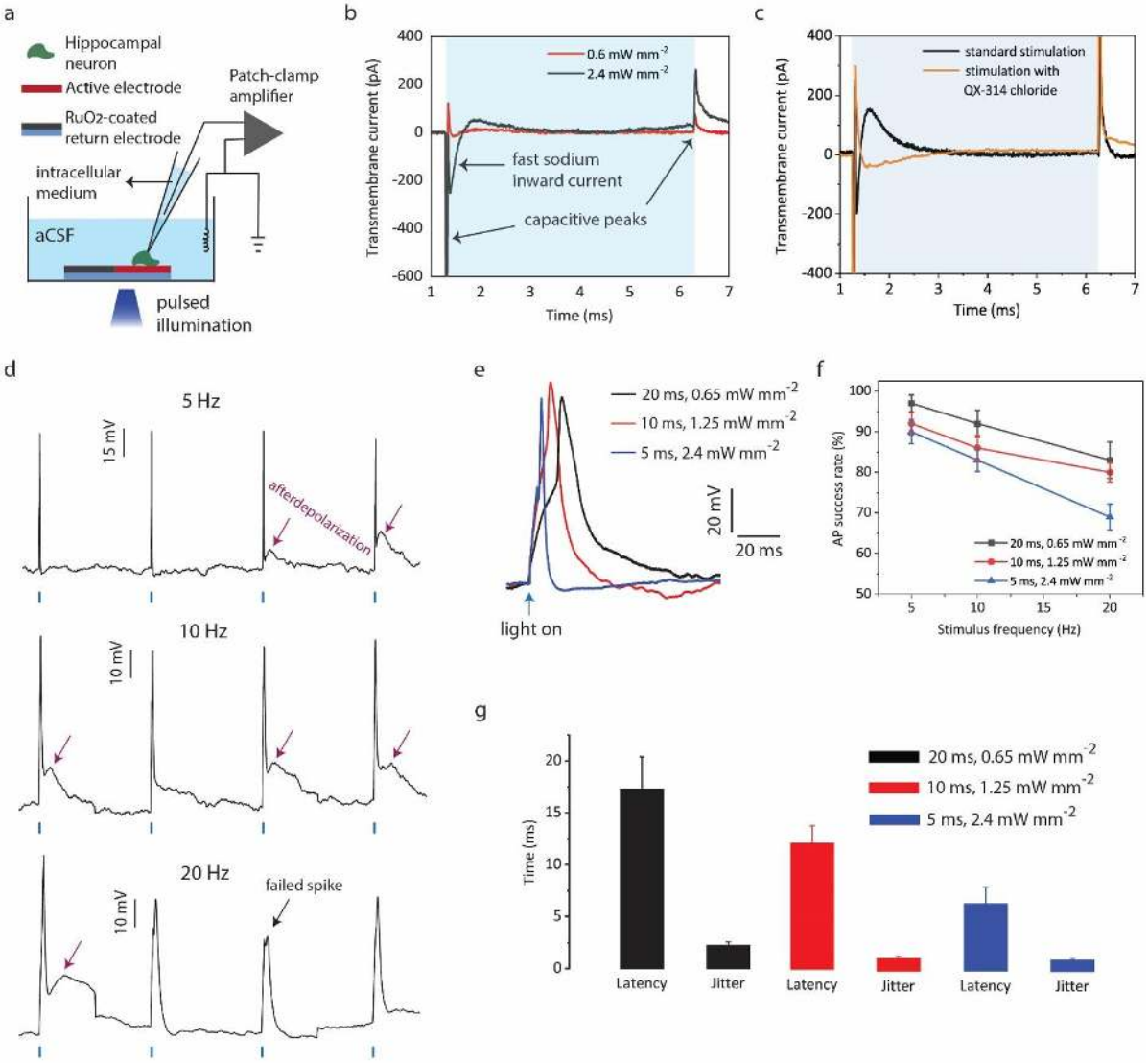


**Figure 22: Photostimulation of primary hippocampal neurons via $RuO_2$ BI. a)** Schematic of single-cell patch-clamp electrophysiology setup under illumination for light-triggered intracellular membrane voltage and current characterization with respect to a distant Ag/AgCl electrode. **b)** Membrane current in whole-cell voltage-clamp mode under different light-intensity illuminations (λ = 445 nm). Shaded area indicates the applied light duration period of 5 ms. **c)** Membrane current of neurons under standard conditions and after blocking the voltage-gated sodium channels via QX-314 chloride. Illumination parameters: 445 nm, 5 ms pulse-width, 2.4 mW $mm^{-2}$ light intensity. Shaded area indicates the 5 ms light-pulse period. **d)** Reproducible firing of hippocampal neurons for 5, 10, and 20 Hz stimulus frequencies. Illumination parameters: λ = 445 nm, 5 ms pulse-width, 2.4 mW $mm^{-2}$ light intensity. Blue bars indicate the start of pulses. Purple arrows show afterdepolarization occurrences. For action potential traces, the capacitive artefacts at the onset and offset of light were eliminated because of downsampling the current clamp data (Appendix C Figure 59). Action potentials for 10 ms and 20 ms pulses were shown in Appendix C Figure 60. **e)** Action potential traces for 5, 10, 20 ms pulse-widths with minimum power densities required to elicit firing. Each trace is the average of ten different spikes. **f)** Action potential success rates of 5, 10, 20 ms pulses for 5, 10, 20 Hz stimulus frequencies (mean ± s.d. for N = 10). **g)** Mean latency and jitter for 5, 10, 20 ms pulsed stimulations. Latency is the time between light-onset and action potential peak, while jitter is the standard deviation of latencies (mean ± s.d. for N = 10).

### *5.7 Conclusion*

This study demonstrated the potential of pseudocapacitive material of $RuO_2$ to realize highly light-sensitive organic optoelectronic biointerfaces. One major obstacle for organic optoelectronic biointerfaces, especially capacitive ones, has been the difficulty of achieving high photogenerated charge densities[116], and the proposed strategy in this report can be an important step towards realizing much elevated charge injection densities. Although other alternatives such as dielectric $SiO_2$ coating and pseudocapacitive PEDOT:PSS coating were used to enhance the interfacial capacitance,[56, 100, 124] our findings show that $RuO_2$ distinctively outperforms those materials in terms of their contribution to charge injection densities. Moreover, the increased charge injection efficiency allows for neurostimulation with shorter pulses and latencies that can enable improved temporal control.

Advantageously, $RuO_2$ can be directly integrated into a wide variety of device architectures[116, 125] to improve the device performance levels via the low-cost electrodeposition technique and even on non-planar substrates. Comparatively, iridium oxide in the form of SIROF was shown to perform well in a silicon-based planar photodiode architecture in terms of its contribution to charge injection performance[126], however, sputtering is a relatively complex and expensive method compared to solution-processing techniques. Recently it was demonstrated that sputtered $RuO_2$ exhibits similar charge storage/charge injection performances with SIROF, indicating its high potential for electrical stimulation/recording electrodes.[105, 106] Here, electrodeposition of $RuO_2$ also performs at similar levels of SIROF and sputtered $RuO_2$, together with the advantage of simple device fabrication. Stability, biocompatibility, and safe stimulation pathway through highly reversible charge transfer reactions demonstrated by intracellular oxidative stress measurements of $RuO_2$-based biointerface show high potential for *in vivo* applications. Moreover, the effective performance of $RuO_2$ can motivate the investigation of alternative pseudocapacitive coating materials for neural interfaces. Carbon materials (e.g., carbide-derived carbon), metal oxides (e.g., manganese oxide) and conducting polymers (e.g., polypyrrole) can be promising due to their high capacitance, low toxicity, and reversible charge injection mechanisms.[101]

In conclusion, our findings pave the way toward building safe and highly efficient optoelectronic biointerfaces by using pseudocapacitive $RuO_2$. The biointerfaces showed improved photoelectrical performance parameters compared to control samples, i.e., increased

capacitive photocurrent peak and higher charge storage/injection efficiencies. Detailed electrochemical analysis of $RuO_2$ coating revealed the reversible nature of redox reactions, indicating a safe charge injection mechanism for $RuO_2$-based optoelectronic biointerfaces, which was further supported by intracellular ROS measurements. Excitation of $RuO_2$-based biointerfaces via short light pulses can activate voltage-gated sodium channels, which leads to reproducible action potential firing on primary hippocampal neurons. Consequently, the safe and efficient stimulation mechanism obtained by simple solution-processed $RuO_2$ integration shows great promise for building flexible, low-cost, biocompatible, stable, and highly light-sensitive optoelectronic biointerfaces for future retinal prosthesis.

# Chapter 6

# Electrical Stimulation of Neurons with Quantum Dots via Near-infrared Light

(Reprinted (adapted) with permission from Karatum O*, et al.* (2022) Electrical Stimulation of Neurons with Quantum Dots via Near-infrared Light. *ACS Nano* 16, 5, 8233–8243. 

## *6.1 Introduction*

In the optical spectrum, near-infrared (NIR) light advantageously allows higher penetration depth into body because of the marginal tissue absorption and scattering[127]; removes the implantation requirement of electrical or optical signal delivery components into tissue, and enables application of higher photon flux within safe light exposure limits because of lower photon energies compared to visible light. For example, upconversion nanoparticles (NPs) recently rendered NIR-sensitivity to optogenetic systems operating in the visible spectrum, and overcame the light penetration limitation of visible light and implantation requirement of light-delivery fibers into the tissue.[31] Because of these benefits, there is an increasing trend for developing NIR-sensitive nanoparticles, devices, and systems operating at NIR spectrum to control neural activity.[30, 64, 128, 129]

Bioelectronic medicine enables the treatment of diseases via stimulation of cells without any drug delivery or genetic variation of native tissue. Among different device configurations, photovoltaic biointerfaces advantageously offer a wireless and battery-free neurostimulation tool that removes the need of wires leading surgical complication and replacement of the battery. For example, silicon photovoltaic biointerfaces enable shorter and simpler surgical procedure for retinal implants, and they convert NIR-light to ionic currents for stimulation of the tissue, which enabled successful clinical outcomes to recover of the vision against blindness due to age-macular degeneration.[130] However, the low absorption coefficient of silicon at NIR (383 $cm^{-1}$ at 880 nm) necessitates 30-µm thick and rigid photoactive layer.[131] Thin and flexible optoelectronic devices can be a better alternative to fit into the curvature of

tissue. For example, recently organic pigments and polymers as photoactive layers enabled flexible photocapacitors as cuff-electrodes on peripheral nerves and implants fitting to the curvature of the retina, respectively.[132]

Alternatively, colloidal quantum dots (QDs) have unique size tunable bandgap via quantum confinement effect, solution-processable fabrication and high absorption coefficient for thin photoactive layers.[133] In addition, they have high optical stability with minimal photobleaching or chemical degradation.[82] So far, core or core/shell structures of different QDs like mercury telluride (HgTe), cadmium selenide (CdSe), indium phosphide (InP), and aluminum antimonide (AlSb) were successfully used in photovoltaic biointerface architectures for photostimulation of neurons, but their operation was limited within the visible range.[42, 60, 134] Alternatively, lead sulfide (PbS), which has a Bohr exciton radius of 18 nm and bulk bandgap of 0.41 eV, enables sensitive tuning of absorption edge within NIR spectral range.[135]

Here, we developed flexible NIR-sensitive biointerfaces by using quantum dots. Integration of ultrathin PbS QD layer of ~25 nm into a multilayered photovoltaic architecture generates a capacitive photoresponse, which is a safe charge injection mechanism for extracellular neurostimulation. The charge injection density of the biointerfaces was significantly enhanced by modifying the return electrode with supercapacitor ruthenium dioxide ($RuO_2$) coating. Efficient photoconversion in physiological medium leads to generation of temporally precise action potentials in hippocampal neurons under 780 nm photoexcitation with more than 80% success rates up to 20 Hz stimulation frequency within the ocular safety limits. The biointerfaces are resistant to various stress tests and chronic photoexcitation and show low cytotoxicity for in vitro hippocampal neuron cultures. Altogether, NIR-sensitive QD-based biointerface architecture presented herein has great potential for building minimally invasive neurostimulators for performing brain, cardiac, and retinal stimulation.

### *6.2 Biointerface design and operation*

QD-based biointerface architecture consists of ruthenium oxide ($RuO_2$) coated ITO return electrode, ZnO electron transport/hole-blocking layer, NIR-absorbing PbS QD layer, and P3HT hole transport layer (Figure 23a). Thus, the device architecture consists of an active electrode (ZnO/PbS/P3HT/ITO) for photocurrent generation and a return electrode ($RuO_2$/ITO), which completes the electrical path of photocurrent. All the layers are solution-processed on ITO/PET substrate, resulting in a flexible QD-based biointerface (QD-BI) (Figure 23b left). The cross-sectional scanning electron microscopy (SEM) image of QD-BI

shows individual layer thicknesses as 50 nm, 25 nm, and 50 nm for ZnO, QD, and P3HT layers, respectively (Figure 23b top right). Together with ITO back electrode (~130 nm), the electronic layers of biointerfaces are ~250 nm thick, which is advantageous for fabricating lightweight and flexible stimulation electrodes. Moreover, the surface SEM image of $RuO_2$ coating demonstrates a porous film morphology (Figure 23b bottom right), leading to a high electrochemical surface area/geometrical surface area (ESA/GSA) ratio that is favorable for obtaining a large interfacial capacitance.[112] Transmission electron microscopy (TEM) analysis of QDs revealed the mean particle size as 3.6 ± 0.5 nm (Appendix D Figure 61), and high-resolution TEM (HR-TEM) image clearly displays the fine crystallinity of QD nanostructure (Figure 23c). Energy band alignment of the device architecture is favorable for separating the electron-hole pairs that are photogenerated at the QD layer (Figure 23d), while 1.1 eV bandgap of the QDs provides NIR-sensitivity to our biointerfaces resulting in an absorption spectrum covering NIR-I region (760 - 900 nm) and extending into NIR-II region (1000 – 1700 nm) (Figure 23e).[36] This provides our biointerfaces with a wide operation spectrum. However, as the absorption of light by water increases significantly beyond 900 nm, we use photoexcitation wavelength of $\lambda$ = 780 nm in our experiments.

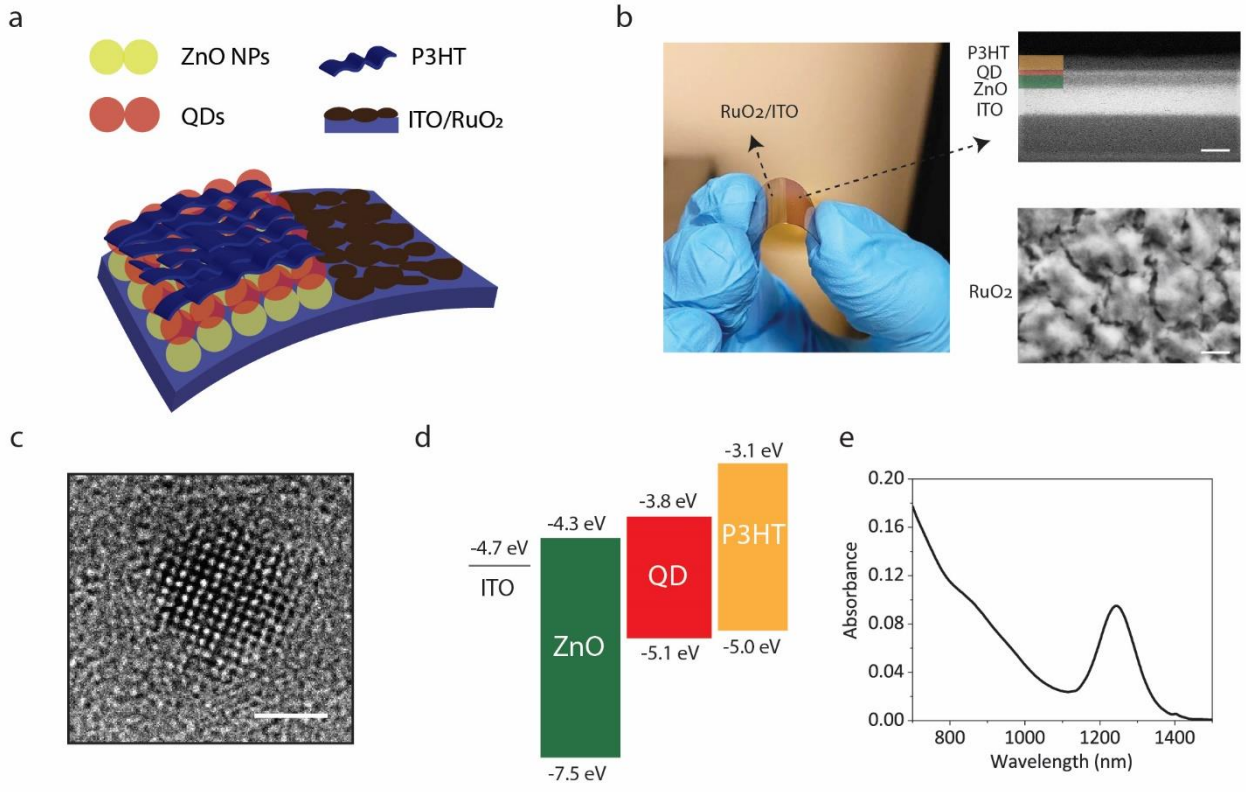


**Figure 23: Biointerface design and properties. a)** Schematic of the multilayered biointerface architecture and **b)** Left: Photograph of a typical device fabricated on a flexible PET substrate. Right: SEM image of QD-BI (top,

scale bar is 100 nm) and $RuO_2$ coating (bottom, scale bar is 200 nm). **c)** High-resolution transmission electron microscopy TEM (HR-TEM) image of the PbS QDs integrated into photovoltaic device. Scale bar is 2 nm. **d)** Electronic energy levels of each layer and their alignment with respect to vacuum level. The levels were obtained from our previous studies.[113, 136] **e)** Absorption spectrum of QDs between 700 – 1500 nm wavelengths. The device absorbance is shown in Appendix D Figure 62.

Each layer in the device architecture contributes to the photoelectrical performance of the biointerface, which are schematically summarized in Figure 24a. We quantified the effect of each step in the device development by measuring the interfacial photocurrent and photocharges generated at the device-electrolyte interface using a patch clamp setup (Figure 24b). Photoactive QD layer absorbs the incoming NIR photons and generates electron-hole pairs. To effectively separate these charge pairs, we integrated ZnO NP layer between ITO and QD layer to form a charge separation heterojunction. Previous reports noted that air-exposed fabrication of PbS QD layer leads to p-type doping,[137, 138] while ZnO is inherently an n-type material.[139] This leads to an effective charge separation at QD-ZnO interface by formation of excitonic or depleted heterojunction[139], leading to the generation of capacitive response in ITO/ZnO/PbS structure, while ITO/PbS structure by itself has nearly zero photocurrent under NIR illumination (Figure 24c). Addition of P3HT layer on top of ITO/ZnO/PbS structure provides further improved charge separation due to its favorable highest occupied molecular orbital (HOMO) level for hole transfer. This leads to 2.1 ± 0.3 (mean ± s.d. for N = 6) times increase in the capacitive onset peak (Figure 24d). In addition to improved capacitive response, we integrated high-capacitance $RuO_2$ layer to the return electrode to boost the charge injection density of the biointerfaces. Charge injection density increases by more than an order-of-magnitude with $RuO_2$-integration (Figure 24e) because of the large interfacial capacitance of $RuO_2$ resulting from fast and reversible redox reactions. Thus, $RuO_2$-integrated-ITO/ZnO/PbS/P3HT architecture yielded the champion photoelectrical performance in terms of capacitive response and charge injection density.

We also explored the suitability of QD-BI to high-frequency neurostimulation (on the order of tens of Hz). Since $RuO_2$ coating on return electrode increases the time constant, the decay of photocurrent to its baseline value is slower after the light offset. This can cause charge accumulation at the electrode-electrolyte interface when high frequency pulses are applied and the charging at the interface would affect the resting potential of neurons that are cultured on QD-BI. We tested the deviation of photovoltage from its baseline under different pulse

frequencies. Under 100 Hz stimulus with 1 ms pulse-width, the electrode-electrolyte interface rapidly charges at the beginning of the pulse-train and charging is saturated after few hundred milliseconds (Figure 24f). Consequently, base photovoltage shifts by 2.7 ± 0.15 mV (mean ± s.d. for N = 6). We similarly quantified the amount of baseline shift for different frequencies (Figure 24g), which reveals that the effect of charging at the electrolyte interface is marginal, i.e., less than few millivolts. Hence, we expect no significant charging at the device-neuron interface during photostimulation experiments.

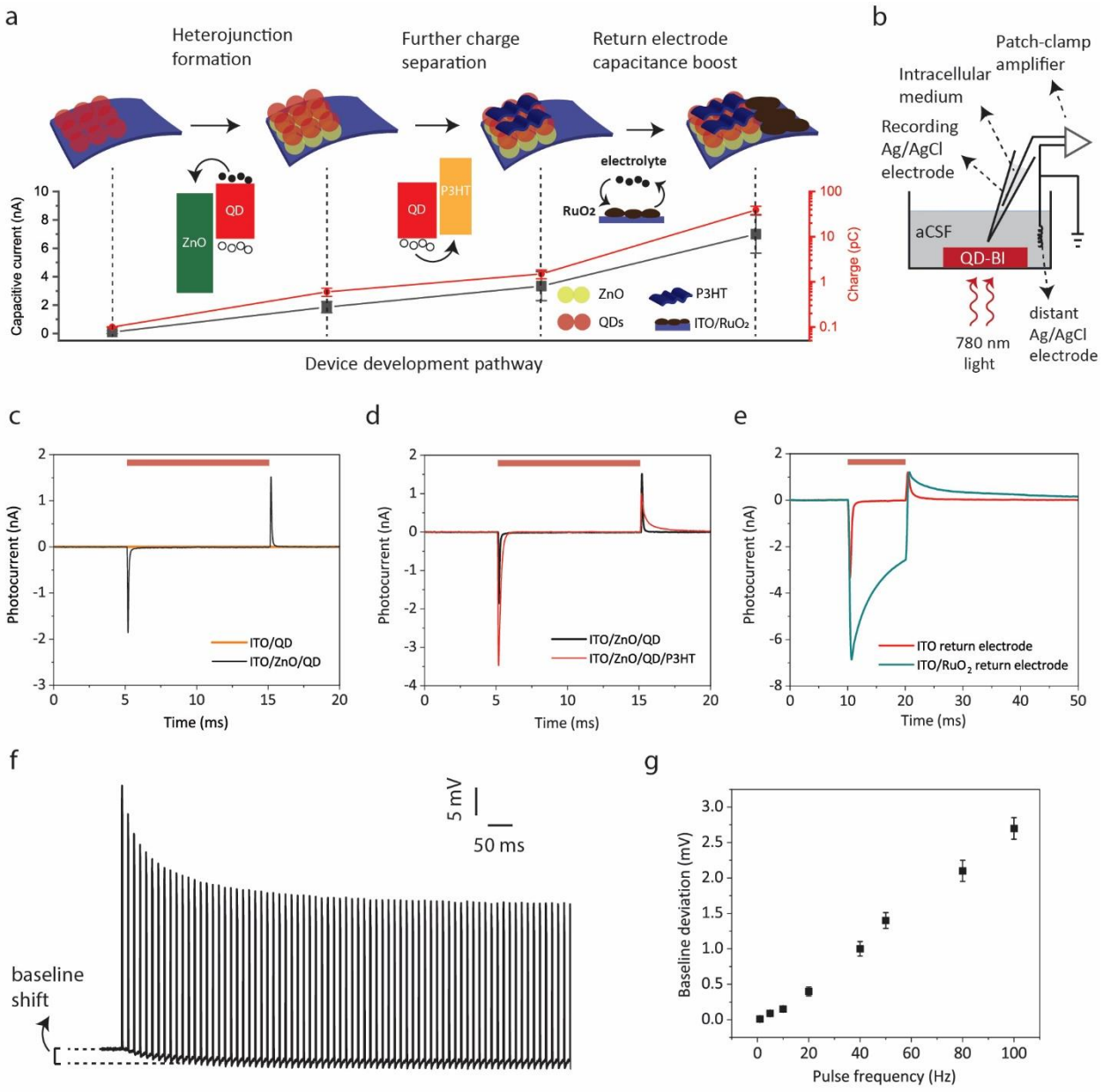


**Figure 24: Photoelectrical characterization and device development. a)** A schematic presenting the origins of the device development pathway. Filled circles and empty circles represent electrons and holes, respectively. The plot below displays the evolution of capacitive onset current and photogenerated charge amplitude (mean ± s.d. for N = 6), which were measured with the setup described in (b) under 10 ms light pulses. Capacitive current stands for the peak photocurrent at the light onset.[117] **b)** Illustration of the open-circuit photocurrent/photovoltage measurement setup. A patch-clamp amplifier in voltage-clamp mode was used to record the photocurrents

between the recording Ag/AgCl electrode and a distant Ag/AgCl reference electrode by positioning the patch-pipette close (< 5 µm) to the device-electrolyte interface. Electrolyte is artificial cerebrospinal fluid (aCSF), which mimics the in vivo extracellular medium of neurons (The absorption spectrum of aCSF is provided in Appendix D Figure 63). Effect of **c)** ZnO, **d)** P3HT, and **e)** $RuO_2$ layers on the photocurrent response of the biointerfaces. Red bars indicate light-on periods. **f)** Photovoltage of QD-BI under 1 ms pulses applied at 100 Hz pulse frequency. **g)** Deviation of the baseline photovoltage under 1 ms pulses for different pulse frequencies (mean ± s.d. for N = 6). For all measurements in this figure, optical power density was 5 mW $mm^{-2}$ and patch-pipette resistance was 5 MΩ.

Short-circuit photoelectrical response of the biointerfaces is useful for evaluating the photoconversion efficiency of the electrodes. We measured the short-circuit photocurrent of QD-BI via a conventional three-electrode setup. Working electrode (WE) is connected to the return electrode of QD-BI, while reference electrode (RE) and counter electrode (CE) are floating in the ionic medium of artificial cerebrospinal fluid (aCSF) (Figure 25a). Application of 10 ms pulses of 780 nm with 1 mW $mm^{-2}$ optical power density resulted in 550 µA $cm^{-2}$ peak current density for QD-BI (Figure 25b). This corresponds to 5.5 mA/W responsivity. For a comparison, we checked the current density of QD-BI under 940 nm light as well and observed that the current density is higher for 780 nm (Appendix D Figure 64), which we ascribe to the elevated absorbance of aCSF for wavelengths above 900 nm (Appendix D Figure 63). Figure 25c shows the photocurrent and photovoltage as a function of light intensity, which has almost linear dependence between photoresponse and incident power indicating single-photon-absorption induced photocurrent. Photocurrent in Figure 25b decays slowly because of the increased time constant by the integration of $RuO_2$ to the return electrode and this significantly improves the charge injection density of QD-BI required for efficacious stimulation of neurons. We quantified the charge injection performance of QD-BI by calculating the areas under the photocurrent-time traces for different pulse-widths (Figure 25d) and for different light intensities (Figure 25e). Accordingly, QD-BI delivers more than 5 µC $cm^{-2}$ charge for 20 ms pulses with 1 mW $mm^{-2}$ light intensity, which is in the range of threshold charge levels for stimulation of different structures like optic nerve, auditory nerve and subthalamic nucleus.[112] Due to the experimental configuration in this measurement, the maximum light intensity is 1 mW $mm^{-2}$, while in the photostimulation experiment setup, light intensity can reach up to 7 mW $mm^{-2}$, which means that the charge density will be further increased. Favorably, these intensities are below the ocular safety limits for pulse durations between 0.1 – 20 ms for stimulus frequencies of 1, 5, 10, 20 Hz (Appendix D Figure 65).

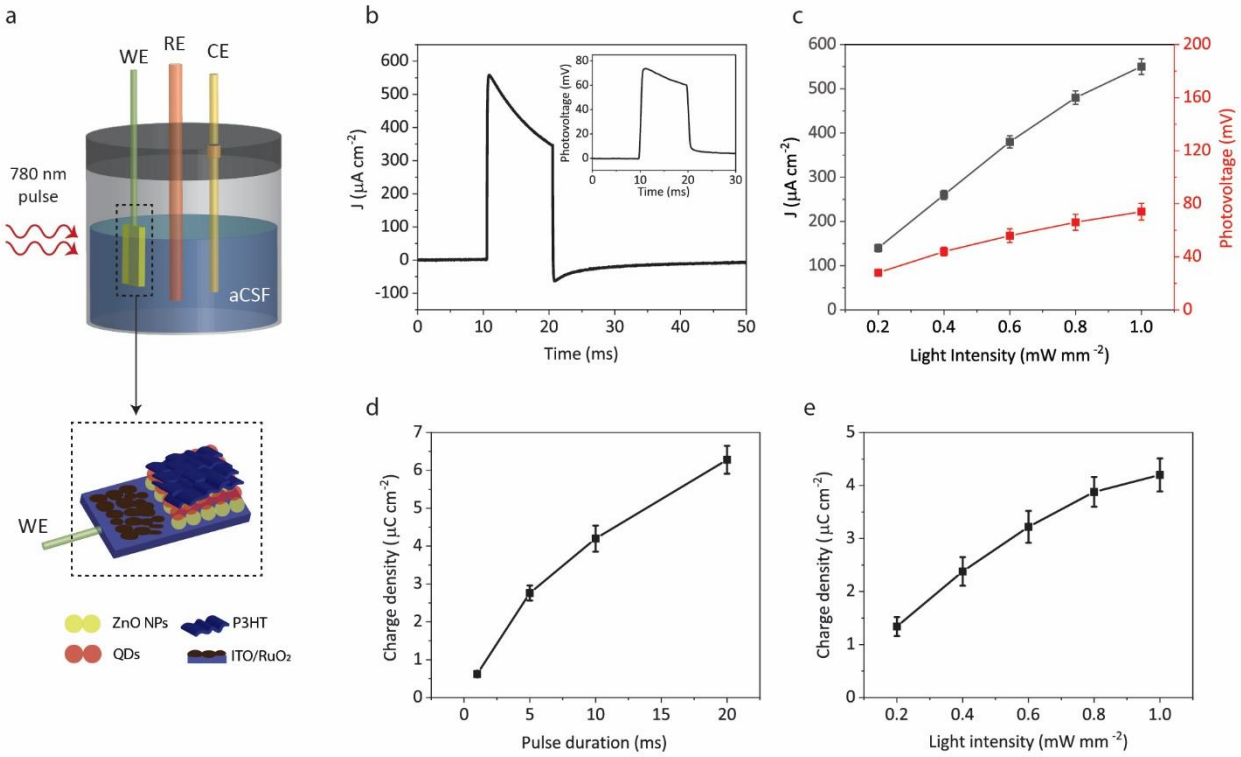


**Figure 25: Current and charge density of the biointerfaces. a)** Three-electrode setup for characterization of short-circuit photoelectrical response of QD-BI with ITO return electrode as working electrode (WE), platinum counter electrode (CE) and Ag/AgCl reference electrode (RE). Dashed area was zoomed below for denoting the connection and device architecture. **b)** Photocurrent response of QD-BI measured under 780 nm light pulse with 10 ms pulse-width, 1 mW mm$^{-2}$ light intensity, 1 Hz pulse frequency. Inset shows the photovoltage under same conditions. **c)** Photocurrent density and photovoltage of QD-BI as a function of light intensity (mean ± s.d. for N = 6). Photogenerated charge density of QD-BI as a function of **d)** pulse duration and **e)** light intensity (mean ± s.d. for N = 4). The light intensity was 1 mW mm$^{-2}$ in (d) and pulse duration was 10 ms in (e) (mean ± s.d. for N = 6).

### *6.3 Stability and biocompatibility of QD-BI*

To evaluate the photoelectrical performance of QD-BI, we measured the photovoltage and charge density of our devices after subjecting them to several sterilization procedures. This accelerated stress test gives information about the stability of devices under standard sterilization steps. Sequential application of $O_2$ plasma sterilization, ethanol rinsing, overnight incubation in cell culture medium, UV sterilization, and second ethanol rinsing steps did not lead to a significant change in the photovoltage peak and charge density of QD-BI (Figure 26a). We also checked the impedance of pristine and sterilized electrodes via electrochemical impedance spectroscopy (EIS), which revealed that device impedance was not notably affected by the sequential sterilization procedure (Figure 26b), indicating that no considerable

damage has occurred during the accelerated stress test. The photostability of electrodes under repeated photoexcitation is also critical for anticipating the long-term operation of biointerfaces in a possible implant condition. The measurements of photovoltage peak of QD-BI under 100 Hz photoexcitation after 20 minutes, which corresponds to 120000 photoexcitation cycle, showed that 82 ± 3 % of photovoltage peak was preserved after the photostability test (Figure 26c). For the origin of degradation, we consider that QDs are oxidizing due to repeated photoexcitation and being in oxygen environment. According to the previous literature, rather than the intrinsic characteristics, the choice of ligand directly affects degradation processes in PbS QDs.[140] Even though small oleic acid-capped PbS QDs are optically stable, the QDs used in this study with a first excitonic peak around 1.2 µm may not be perfectly stable in that sense, which can be either solved by decreasing the size of QDs or synthesizing QDs with enhanced Cl ions on the surface.[137, 141] Also, we do not observe a significant variation in the pH of the aCSF during repeated photoexcitation (Appendix D Figure 66). Altogether, these experiments demonstrate that QD-BI retain their functionality in aCSF medium under different stress-inducing factors like sterilization tests and repeated photoexcitation.

We tested the viability of primary hippocampal neurons cultured on QD-BI via MTT cytotoxicity analysis to assess the biocompatibility of the biointerfaces. Cell viability of neurons cultured on QD-BI and ITO control substrates was compared after 48h incubation in the cell culture medium. Neurons cultured on QD-BI showed high cell viability and did not show any significant viability difference compared to the ones that are cultured on ITO control samples, indicating the low cytotoxicity of QD-BI for in vitro hippocampal neurons (Figure 26d). Moreover, immunofluorescence images of neurons on QD-BI and ITO control substrates taken at the first (day 0) and fourteenth day (day 14) of incubation demonstrated that neurons still survive and preserve their morphology on both QD-BI and ITO samples after two weeks of incubation (Figure 26e). Here, we consider that even though the heavy metal content of QDs is a possible source of toxicity, the biocompatible P3HT overcoating encapsulates the QDs and decreases the toxicity for the time period that we investigate the in vitro condition. Similarly, it was previously shown that encapsulation of QDs via heavy-metal-free inorganic shell or organic coatings significantly suppresses the potential toxicity.[142]

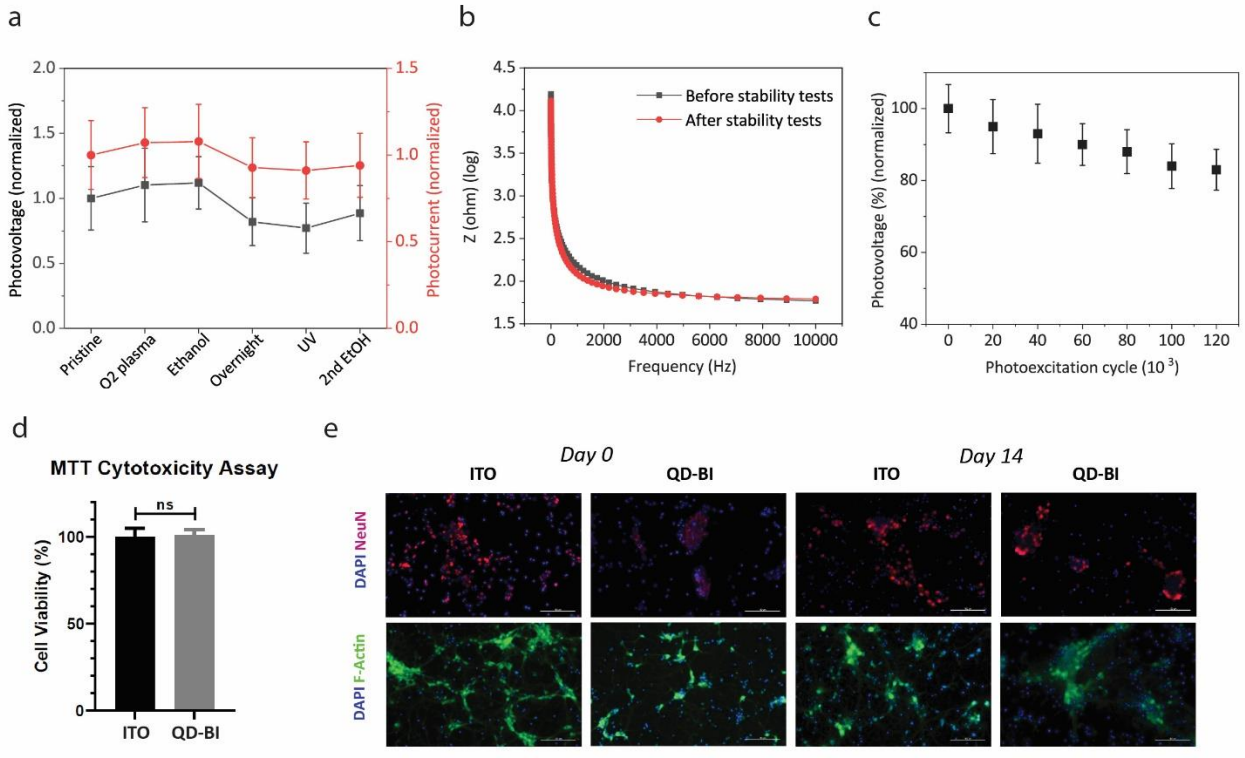


**Figure 26: Stability and biocompatibility tests. a)** Photovoltage and photocurrent peak and of QD-BI under accelerated stress test (mean ± s.d. for N = 4). Measurements of the two parameters were taken after each step, i.e., $O_2$ plasma sterilization, EtOH (ethanol rinsing), Overnight (overnight incubation in cell culture medium), UV sterilization, and second ethanol rinsing. **b)** Impedance measurement of QD-BI before and after the accelerated stress test between 1 – 10000 Hz frequencies (Traces represent the average of four different samples). **c)** Photovoltage peak of QD-BI under 100 Hz photoexcitation for 20 minutes (corresponding to 120000 cycle) photostability test (mean ± s.d. for N = 4). Illumination: 100 Hz stimulus frequency, 5 ms pulse-width, 7 mW $mm^{-2}$ optical power density. **d)** MTT cytotoxicity analysis of primary hippocampal neurons cultured on QD-BI and ITO control samples (mean ± sem for N = 4). The level of significance was calculated using an unpaired, two-tailed t-test; *$p < 0.05$ was evaluated as statistically significant. **e)** Immunofluorescence images of primary hippocampal neurons cultured on QD-BI and ITO control samples at day 0 and day 14 of incubation (each image is the average of four different images taken from four different areas). Primary hippocampal neurons were co-stained with DAPI (blue), Anti-NeuN (red), and Anti-F-actin (green). Scale bar: 100 µm.

### *6.4 Photostimulation of primary neurons*

Stable operation and biocompatibility of QD-BI together with their effective photoelectrical performance point out its potential for light-induced electrical neurostimulation. To validate this, we performed single-cell intracellular recording experiments with patch-clamp whole-cell configuration. Primary hippocampal neurons were cultured on QD-BI and their light-induced transmembrane potential (defined as the intracellular membrane potential with respect to a distant Ag/AgCl electrode) behaviors were recorded in current-clamp mode under 780 nm pulsed excitation (Figure 27a).

Light intensity impinging on the biointerface directly affects the response of neurons to photoexcitation. For lower light intensities, neurons exhibit subthreshold membrane responses. After a certain intensity level, neurons start to fire action potentials because of the suprathreshold depolarizing effect of QD-BI (Figure 27b). To understand the required amount of membrane depolarization for observing suprathreshold membrane response, we examined the transmembrane current of neurons in whole-cell mode while gradually increasing the membrane holding potential in voltage-clamp mode. At -70 mV holding voltage, the transmembrane current is almost zero. When we increase the holding potential by -10 mV steps, we start to observe a fast negative inward current at -30 mV. This negative current is representative of fast sodium inward current observed during an action potential, which is followed by slower outward potassium current (Figure 27c). This means that the depolarization of transmembrane potential on the order of 40 mV is expected to elicit action potential firing. When we increase the holding potential to -10 mV, we again notice the rapid sodium inward current with a lower latency compared to -30 mV holding potential as expected.

Next, we characterized the amount of transmembrane depolarization under different intensities and how these reflect into the ratio of successful/unsuccessful spikes of action potential for each intensity. To quantify the magnitude of depolarization without inducing action potentials, we blocked the voltage-gated sodium channels by adding 5 mM QX-314 chloride into the intracellular solution. We observe an almost linear dependence of depolarization magnitude to the light intensity (Figure 27d). 4.2 mW $mm^{-2}$ light intensity generates 35 ± 8.5 mV depolarization and low (5 ± 4.5 %) successful spike rate at 1 Hz with 20 ms pulse duration because only a minor part of the pulses produces suprathreshold (greater than ~40 mV) transmembrane depolarization. For 5.6 mW $mm^{-2}$ intensity, depolarization and spike rate increases to 40 ± 8.1 mV and 45 ± 9 %, respectively. Spike rate jumps to 88 ± 6 % for 7 mW $mm^{-2}$ light intensity, meaning that the generated transmembrane depolarization (52 ± 9.2 mV) is sufficient for most of the pulses to elicit firing. QD-BI can also evoke reproducible action potentials for higher frequency stimuli such as 10 Hz and 20 Hz as well (Figure 27e). The spike success rates for 1, 10, and 20 Hz frequencies are all above 80%, indicating an efficient coupling of the photoresponse of biointerfaces to the neural membrane (Figure 27f). Moreover, after the application of photostimulus of 1, 10, and 20 Hz frequencies for a duration of 1 minute, there is only a marginal change (maximum of 3.2 ± 1.3 mV at 20 Hz) in the resting membrane potential of neurons (Figure 27f). Finally, we calculated the mean latency and jitter parameters for the successful spikes induced by QD-BI as 15.4 ± 2.4 ms and 2.2 ±

0.4 ms for 20 ms pulse-width photostimulus, respectively (Figure 27g).

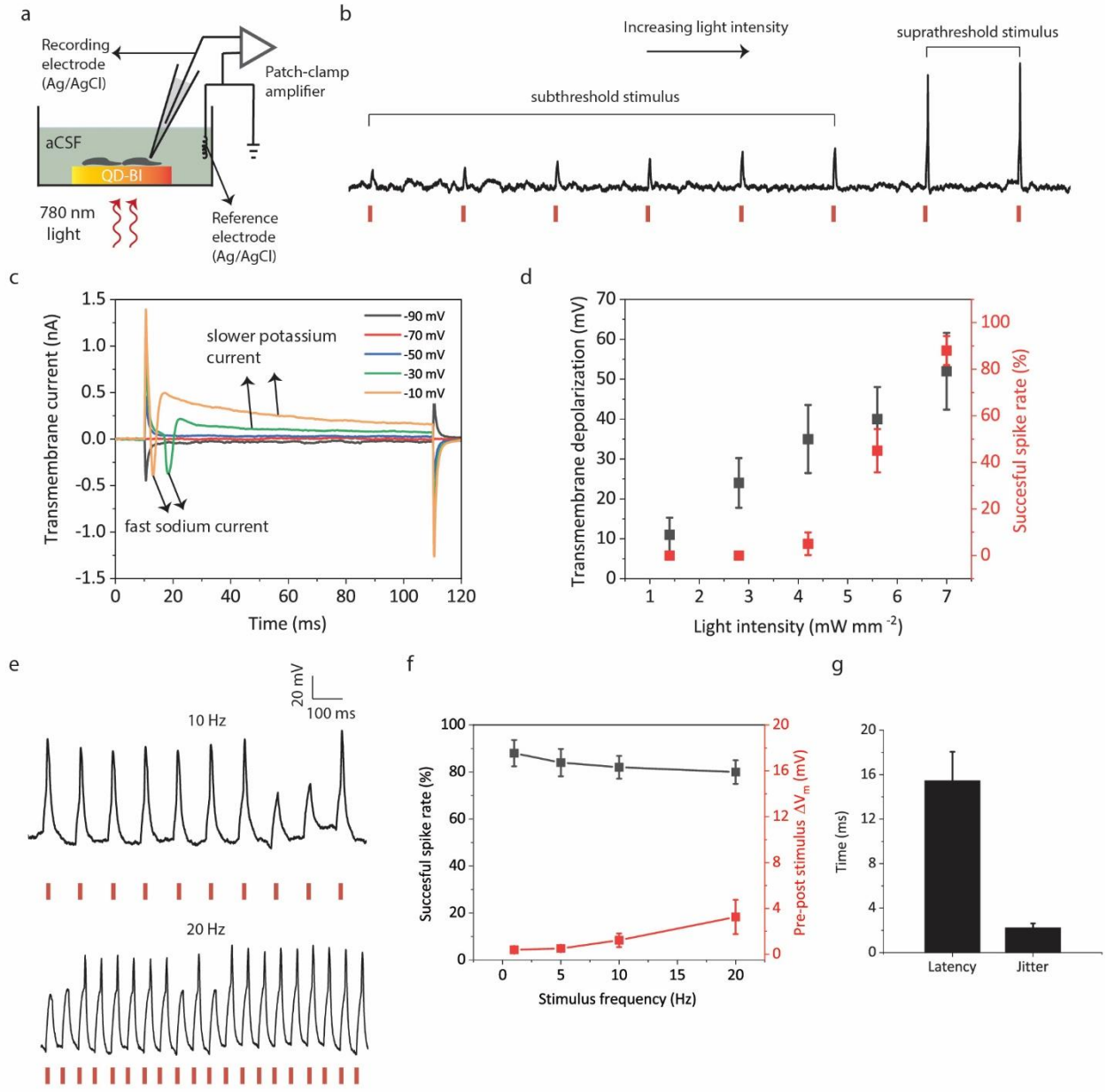


**Figure 27: Light-induced neural stimulation. a)** Simplified schematic of intracellular recording setup using patch-clamp amplifier. Biointerfaces are electrically floating in extracellular solution of aCSF. **b)** Current-clamp recordings of hippocampal neurons under gradually increased light intensity. The intensity in the beginning (4.2 mW $mm^{-2}$) was increased by 0.4 mW $mm^{-2}$ at each pulse. **c)** Transmembrane current recording of neurons in whole-cell, voltage-clamp mode for different membrane holding potentials. **d)** Dependence of transmembrane depolarization and spike success rate to the light intensity impinging on QD-BI (mean ± s.d. for N = 4). **e)** Current-clamp recordings of neurons under repeated photostimulus for 10 Hz and 20 Hz frequencies under 7 mW $mm^{-2}$, 20 ms pulses. The stimulation artefacts at the onset and offset of light is eliminated because of downsampling of current clamp data (Appendix D Figure 67). **f)** Dependence of spike success rate and $\Delta V_m$ (difference in the membrane potential before and after 1 min of stimulus) to photostimulus frequency under 7 mW $mm^{-2}$, 20 ms pulses (mean ± s.d. for N = 4). **g)** Mean latency of action potentials and jitter (standard deviation

of latencies for all firing neurons) for 7 mW $mm^{-2}$, 20 ms pulses (mean ± s.d. for N = 4 neurons).

### *6.5 Conclusion*

This study demonstrated a QD-based NIR-responsive photovoltaic biointerface. For operation in tissue transparency window, we chose an NIR-absorbing QD and combined it with ZnO NP layer to achieve effective charge separation and capacitive photoresponse. Addition of P3HT hole transport layer further improved the photoresponse by capturing holes, while $RuO_2$ coating on the return electrode led to a large return electrode capacitance and high charge injection density. All these layers were coated via solution-processed techniques, indicating the simple and low-cost manufacturability of QD-based biointerfaces.

Analysis of the photocharge generation of QD-BI in the ionic medium showed that the dominant charge injection mechanism is capacitive at the electrode-electrolyte interface,[143] which is a safe alternative to irreversible faradaic charge injection.[77] Moreover, addition of $RuO_2$ to the return electrode introduces fast and reversible faradaic processes at the $RuO_2$-electrolyte interface, which are counter-balanced by the faradaic reactions occurring at the active electrode (ZnO/PbS/P3HT)-electrolyte interface. We did not observe any sign of presence of irreversible faradaic reactions during the photostimulation experiments in terms of pH variation, cell viability, and degradation of biointerface.

Even though silicon photodiodes have been applied to NIR photovoltaic stimulation and showed high efficiency,[126, 144] its transition to flexible device architectures has not occurred yet. Nanomaterial forms of silicon has been integrated into flexible device structure, but their spectrum have remained in the visible region.[145] On the other hand, although the potential of organic biointerfaces was revealed with a computational study for retinal implants,[129] only one recent report experimentally demonstrated neuromodulation at NIR.[64]

High absorption coefficient of the QDs[135] and the effective device design of our biointerfaces resulted in photostimulation of neurons with light intensities below the ocular safety limits (Appendix D Figure 65), which is critical for retinal prosthetic devices. The maximum permissible exposure values are higher for NIR light compared to visible light, which renders NIR-responsive biointerfaces more suitable for ophthalmic applications.[146] Furthermore, the retinal receptors are responsive to visible spectrum, but not to NIR wavelengths, thus flexible NIR-responsive biointerfaces combined with smart googles with NIR-projectors have high

potential to be used to recover vision against retinal degeneration diseases. In addition, NIR light can penetrate a few cm deep into the brain and such NIR-responsive biointerfaces can be also used for brain stimulation as well by engineering them according to the required tissue-mechanics.

In conclusion, we presented a QD-based biointerface that can trigger NIR-light-induced action potentials on hippocampal neurons in tissue transparency window. Favorably, biointerfaces can be fabricated on a flexible substrate using simple solution-processed methods, and an ultrathin QD layer in a well-designed photovoltaic architecture results in efficient capacitive photocurrent generation that leads to temporally precise and reproducible photostimulation of neurons. QDs with their exceptional optoelectronic and bioconjugation properties hold high promise for next-generation neural interfaces.

# Chapter 7

# CONCLUSION

The ubiquitous use of neurostimulation in the academic, clinic, and industrial settings triggers emergence of alternative techniques to control neural activity with less invasiveness, higher spatiotemporal resolution, and through more energy-efficient routes. In that sense, optoelectronic control of neural activity brings advantages of tether-free communication with neurons and high-level spatial and temporal control compared to non-optical techniques, without requiring genetic manipulations. In recent years, alternative to conventional silicon optoelectronics, organic semiconductors and inorganic semiconductor nanocrystals (especially QDs) have found significant applications in different optoelectronic devices such as LEDs, photodetectors, and solar cells. However, non-silicon optoelectronic neurostimulators have not attracted such attention. This thesis demonstrates innovative device design and development strategies to utilize the advantageous optical and electrical properties of QDs for building more energy-efficient and less invasive optoelectronic neurostimulators that can find applications in different animal studies and pave the way for developing effective neural prosthetic devices in the future.

The key achievements of this thesis can be summarized as following:

- Our study in Chapter 3 described how one can control the photoelectrochemical current generated at the photovoltaic device-electrolyte interface to perform depolarization and hyperpolarization using toxic-metal-free QDs.
    - Controlling the charge migration in the multilayered QD-based photovoltaic devices led to the generation of cathodic and anodic photoelectrochemical currents.
    - We maximized the generated photoelectrochemical current by engineering the QD nanostructure and photoactive layer thickness optimizations.
    - Optimized type-I devices can hyperpolarize neurons via 445 nm pulsed-light, which can be used for neural silencing applications.

  - Optimized type-II devices can evoke light-induced action potentials in primary hippocampal neurons at 1, 2, 5, and 10 Hz via 445 nm pulsed-light, which can be used for neural activation applications.
- Our study in Chapter 4 showed how to control the charge injection mechanism at the photovoltaic device-electrolyte interface using a QD-PCBM donor-acceptor nanoheterojunction.
  - Through forming a charge separation junction at QD-PCBM donor-acceptor heterojunction, the neural interface can generate a capacitive photocurrent.
  - Generation of capacitive photocurrent is important for avoiding possible irreversible faradaic reactions at device-electrolyte interface.
  - Capacitive photocurrent generation can be maximized by controlling the QD core/shell nanostructure and the QD:PCBM ratio in the nanoheterojunction.

- Our study in Chapter 5 demonstrated exploiting pseudocapacitance phenomenon by using $RuO_2$ return electrode for improving charge injection efficiency of photovoltaic neurostimulators for enabling low-light-intensity stimulation of neurons.
  - $RuO_2$ coating enhances the charge injection densities over 20-fold.
  - Electrochemical deposition of $RuO_2$ is a cost-effective and simple fabrication technique that allows thickness-controlled return electrode capacitance.
  - Integration of $RuO_2$ return electrode into an conventional organic P3HT:PCBM photovoltaic device led to stimulation of neurons with light intensities below 1 mW $mm^{-2}$.

- Our study in Chapter 6 showed the development of a NIR-sensitive QD-based neural interface that can stimulate neurons via 780 nm pulsed-light.
  - NIR wavelengths have greater tissue penetration compared to visible light. Thus, these devices can be used for wireless and remote activation of deep neural structures in brain, retina, and heart without requiring the implantation of light sources.
  - Ultrathin QD layer (25 nm) can generate sufficient photocurrent for stimulation. This way, we can build thin and flexible devices which are favorable for preventing mechanical mismatches with tissues.
  - Used light intensities (7 mW $mm^{-2}$) is below the maximum permissible limits according to Ocular Safety Standards. Hence, these devices show promise for minimally invasive retinal stimulation.

Overall, these studies significantly contributed to the optoelectronic neurostimulation field by providing effective strategies for understanding and controlling the charge injection mechanisms, improving the light-sensitivity by combining energy storage technologies with photovoltaic device architectures and extending the photoresponse spectrum of QD-based neurostimulators into NIR wavelengths. Future studies focusing on in vivo applications of these devices can be valuable for evaluating the potential of these approaches for building effective neural prostheses to be used in brain, heart, and retina.

# Appendix A

## InP core and InP/ZnS core/shell QD synthesis

InP/ZnS QDs with 1 monolayer shell were synthesized by hot injection method.[147] For the core synthesis, firstly, 56 mg (0.01 mmol) stearic acid (SA), 86 mg zinc undecylenate (0.01 mmol) and 96 mg (0.2 mmol) hexadecylamine (HDA) were mixed in a three-neck flask with 6 ml 1-Octadecene (ODE). Afterwards 44 mg (0.1 mmol) indium chloride ($InCl_3$) into the solution in nitrogen atmosphere. The solution was heated to 120°C and evacuated 20 min in order to provide oxygen and water-free reaction medium. Then, the solution was refilled with a nitrogen atmosphere and heated to 230°C. At this temperature, 1 ml of Tris(trimethylsilyl) phosphine $P(TMS)_3$ stock solution (0.2 mmol) was injected to the solution and it was kept at 230°C 20 min. Before the shelling process, the solution was cooled down to room temperature and half of the solution was taken and labeled as core solution. For preparing InP/1ZnS at room temperature, 54 mg zinc diethyldithiocarbamate (0.15 mmol) and 2 ml ODE were added into the solution, respectively. After that, the solution was heated up to 180°C and stirred 30 min. The solution was cooled down to room temperature and purified by washing toluene and ethanol. At the final stage, QDs were re-dispersed in toluene.

## ZnO nanoparticles synthesis

ZnO nanoparticles were synthesized using a previously reported method [53]. Tetramethylammonium hydroxide (TMAH) dissolved in ethanol (0.55 M) was slowly added to the solution of zinc acetate dihydrate dissolved in dimethyl sulfoxide (DMSO) (0.5 M). After 1h stirring at room temperature, the solution was washed twice and dispersed in ethanol at a concentration of 50 mg $ml^{-1}$.

## Biointerface fabrication

The ITO coated glass substrates were first cleaned by sonicating in detergent solution, deionized water, acetone, and isopropanol consecutively for 15 min each. The cleaned substrates were applied 15 min of UV ozone treatment before moving to layer depositions. $TiO_2$ layer on ITO was formed using a commercially available $TiO_2$ paste (Sigma Aldrich) by doctor blading followed by annealing at 400°C for 1 h. ZnO layer was deposited by spin-

coating the 50 mg $ml^{-1}$ ZnO nanoparticles solution at 2000 rpm, and baked at 100°C for 30 min. The InP/ZnS core/shell QD film was formed by spin coating its 60 mg $ml^{-1}$ solution in toluene at 2000 rpm. For multilayer coating, each layer was treated with 3-mercaptopropionic acid in methanol and then rinsed with methanol, both spin-cast at 2000 rpm, before moving to the coating of next QD layer. After the multilayer coating, the QD film was baked at 100°C for 30 min. The layer thicknesses were characterized by atomic force microscopy (AFM, Bruker, Dimension Icon) in tapping mode with three different scan sizes (40×40 $\mu m^2$, 20×20 $\mu m^2$, 10×10 $\mu m^2$).

**Optical Characterization**

UV/visible absorption and photoluminescence spectra of InP core and InP/ZnS core/shell QDs were obtained using Edinburgh Instruments Spectrofluorometer FS5. Quantum yield measurements were conducted in the integrating sphere module of FS5.

**Photoresponse analysis**

The photocurrent/photovoltage response of our biointerfaces was measured with Autolab Potentiostat Galvanostat PGSTAT302N (Metrohm, Netherlands) using a three-electrode setup consisting of Ag/AgCl as the reference electrode, platinum rod as the counter electrode and the thin film samples as the working electrode in artificial cerebrospinal fluid (aCSF) solution. To be able to extract the charge densities ($\mu$C $cm^{-2}$) of the biointerfaces, 1 $cm^2$ area of thin film samples was immersed in aCSF to obtain the current density ($\mu$A $cm^{-2}$) for all the photocurrent measurements. aCSF solution was prepared by mixing the following materials in distilled water: 10 mM of 4-(2-hydroxyethyl)-1-piperazineethanesulfonic acid (HEPES), 10 mM of glucose, 2 mM $CaCl_2$, 140 mM of NaCl, 1 mM of $MgCl_2$, 3 mM of KCl. After mixing, the pH of aCSF solution was adjusted to 7.4 by adding a stoichiometric amount of NaOH. Light pulses were applied via Thorlabs M450LP1 LED with 445 nm nominal wavelength and the LED spectrum is provided in our previous study [67]. The blue LED was driven with Thorlabs DC2200 - High-Power 1-Channel LED Driver. Newport 843-R power meter was used to measure the optical power of incident light on the devices. The illumination intensities were selected at the levels that can induce sufficient charge generation for stimulation of neurons (orders of $\mu$C $cm^{-2}$) [61].

**Electrochemical analysis**

Autolab Potentiostat Galvanostat PGSTAT302N (Metrohm, Netherlands) was used for

electrochemical characterizations. For capacitance-voltage measurements, a three-electrode set up consisting of Ag/AgCl as the reference electrode, platinum rod as the counter electrode and the thin film samples as the working electrode were used. The CV scans were monitored between certain voltage intervals for different device structures. During the measurement, the AC amplitude was kept 10 mV (RMS) to maintain the linearity of the response and measuring frequency was fixed at 1 kHz. The electrochemical impedance spectroscopy (EIS) was performed in frequency response analysis (FRA) potential scan mode. The blue illumination was applied to the devices while varying the frequency between 1 Hz - 10 kHz at 10 mV (RMS) AC voltage perturbation. The fitting of the responses was performed in NOVA software to extract the electrical parameters.

**Primary Neuron Isolation**

All experimental procedures have been approved by the Institutional Animal Care and Use Committees of Koç University (Approval No: 2019.HADYEK.023) according to Directive 2010/63/EU of the European Parliament and of the Council on the Protection of Animals Used for Scientific Purposes. Hippocampal regions were extracted from decapitated E15-E17 Wistar Albino rats and were placed immediately in ice-cold Hank's Balanced Salt Solution (HBSS, Thermo Fisher Scientific, MA, USA). The hippocampi were incubated in %0.25 Trypsin-EDTA solution (Thermo Fisher Scientific, MA, USA) with %2 DNase-I supplement (NeoFroxx, Einhausen, Germany) for 20 minutes in a 37ºC incubator. Then the cells were centrifuged, and the supernatant was changed with Dulbecco's Modified Eagle Medium/Nutrient Mixture F-12 (DMEM/F12 Thermo Fisher Scientific, MA, USA) supplemented with %10 fetal bovine serum (FBS, Heat Inactivated, GE Healthcare, IL, USA) and %1 penicillin/streptomycin (Thermo Fisher Scientific, MA, USA). DMEM/F12 was removed and Neurobasal Medium (NBM, Thermo Fisher Scientific, MA, USA) supplemented with B27, L-glutamine, β-mercaptoethanol, glutamate (Thermo Fisher Scientific, MA, USA) was added to the cell pellet. The cells were triturated and were passed through a 70 µm cell strainer. The homogenous cell solution was seeded in poly-D-lysine (PDL, Sigma-Aldrich, MO, USA) coated substrates. After 3-days incubation of cells on substrates in a 37ºC incubator with %5 carbon dioxide, the media of the cells on substrates were changed with NBM supplemented with cytosine arabinoside (Sigma-Aldrich, MO, USA) to inhibit growth of glial cells. After 24-hour incubation with cytosine arabinoside, the media were changed with NBM and the substrates with the hippocampal neurons used for experiments.

**Biocompatibility Assay**

MTT viability assay was applied to investigate cell viability of primary hippocampal neurons on the biointerfaces. The neural growth medium was prepared by using B27 supplemented Neurobasal medium. MTT cell viability assay (Abcam, ab211091) was utilized to evaluate biocompatibility of our biointerface. The devices were sterilized first by cleaning with 70% ethanol followed by air-drying. The surface was further sterilized under UV irradiation for 30 min. Substrates were placed in wells of the 6-well plates. Primary hippocampal neurons were seeded ($5 \times 10^5$ cells per sample) on the substrates in B27 supplemented Neurobasal medium as described above and incubated in the neuron growth medium for 48 hours after cytosine arabinoside supplemented neurobasal medium removal. After 48 hours incubations, the media were replaced with 1 mL of MTT solution (5 mg/mL in PBS, pH = 7.4) and 4 mL of NBM mixture per well. Then, for an additional 4 h, the cells were incubated at 37°C and 5% $CO_2$ atmosphere. The medium was vacuumed from each well and substrates were transferred to an empty 6-well plates. In each well, 1:1 mixture of DMSO and ethanol was added to dissolve the formazan crystals. The solution was transferred to a 96-well plate and the absorbance was measured at 570 nm light with Synergy H1Micro- plate Reader (Bio-Tek Instruments). The relative cell viability was calculated as follows: viability = $(OD_{sample}/OD_{control}) \times 100$. The optical density (OD) of the sample was obtained from the cells grown on a photoelectrode, and the OD of control was obtained from the cells grown on the ITO substrates.

**Immunofluorescence Staining and Imaging**

Primary hippocampal neurons ($5x10^5$ cells per sample) were seeded as explained above on ITO control substrate and the biointerface. The samples with neurons fixed by 4% paraformaldehyde immediately after primary hippocampal neuron isolation protocol or incubated for 14 days with regular medium changes at 37°C in cell culture incubator. After 14-day incubation, the primary hippocampal neurons were also fixed by 4% paraformaldehyde and washed three times with PBS-T (Phosphate Buffered Saline, 0.1% Triton X-100). Cells were blocked in PBS solution containing 5% BSA (Bovine Serum Albumin) and 0.1% Triton X-100. Samples with primary hippocampal neurons were incubated with rabbit anti-NeuN antibody (ab177487, Abcam, Cambridge, UK) overnight, for neuron characterization, and washed three times with PBS-T. Then, samples with primary hippocampal neurons were incubated with goat anti-rabbit IgG H&L Alexa Fluor 555(4413, Cell Signaling Technology, MA, USA) for fluorophore marking of anti-NeuN primary antibody for 90 minutes at 37°C. For visualization of the cytoskeleton, primary neuron samples also were incubated with FITC-

conjugated phalloidin antibody (Sigma-Aldrich, P5282) for 90 minutes at 37°C. All samples were washed three times with PBS-T, then mounted with DAPI supplemented mounting medium (ab104139, Abcam, Cambridge, UK) to observe nuclei. Finally, immunofluorescence imaging was done using a florescence light microscope (DMi8 S, Leica, Wetzlar, Germany).

**Electrophysiology recordings**

Single-cell electrophysiology experiments were performed using EPC 800 Heka Elektronik patch-clamp amplifier in whole-cell configuration. The preparation of aCSF is provided in section 2.5 and biointerfaces were electrically floating in aCSF meaning that no wire is connected to the photoelectrodes. Photovoltaic QD/ZnO and $TiO_2$/QD architectures for type I and type II biointerfaces, respectively, acts as current-generating active electrodes. ITO back contact serves as the return electrode. Throughout the manuscript, 'neural membrane' refers to the 'free membrane' as defined in a previous study [148]. Transmembrane voltage is defined as the electrical potential difference between the intracellularly recorded voltage at the patched membrane region with respect to a distant reference electrode placed in the extracellular medium. Transmembrane voltage measurements were taken in current clamp mode while applying light pulses differing between 5 - 200 ms via an LED source (nominal wavelength: 445 nm; optical power density: 2 mW $mm^{-2}$ corresponding to the minimum value that can evoke repetitive action potentials). The patch pipette resistance of 8-10 MΩ was used for the experiments. The pipettes were filled with an intracellular medium which consists of 140 mM KCl, 2 mM $MgCl_2$, 10 mM HEPES, 10 mM ethylene glycol-bis(β-aminoethyl ether)-N,N,N',N'-tetraacetic acid (EGTA), 2 mM Mg-ATP dissolved in distilled water. The pH of the intracellular solution was adjusted to 7.2-7.3 by adding a stoichiometric amount of KOH. Patch pipette and cells were monitored through a digital camera integrated with the Olympus T2 upright microscope.

**Transmission Electron Microscopy (TEM) images of the QDs**

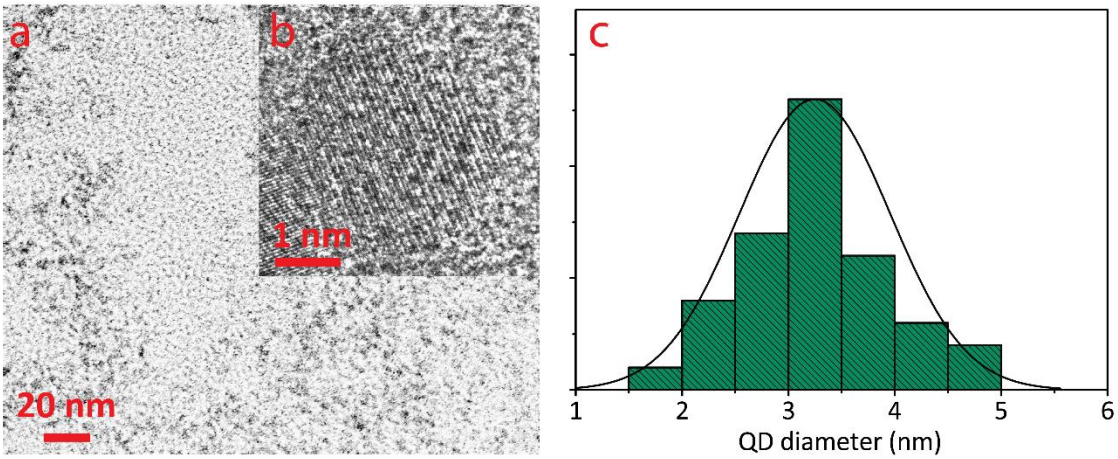


**Figure 28: a)** Transmission Electron Microscopy (TEM) image of InP core QDs. **b)** High resolution TEM (HR-TEM) image of InP QDs, and **c)** the corresponding size distribution (50 particles were counted).

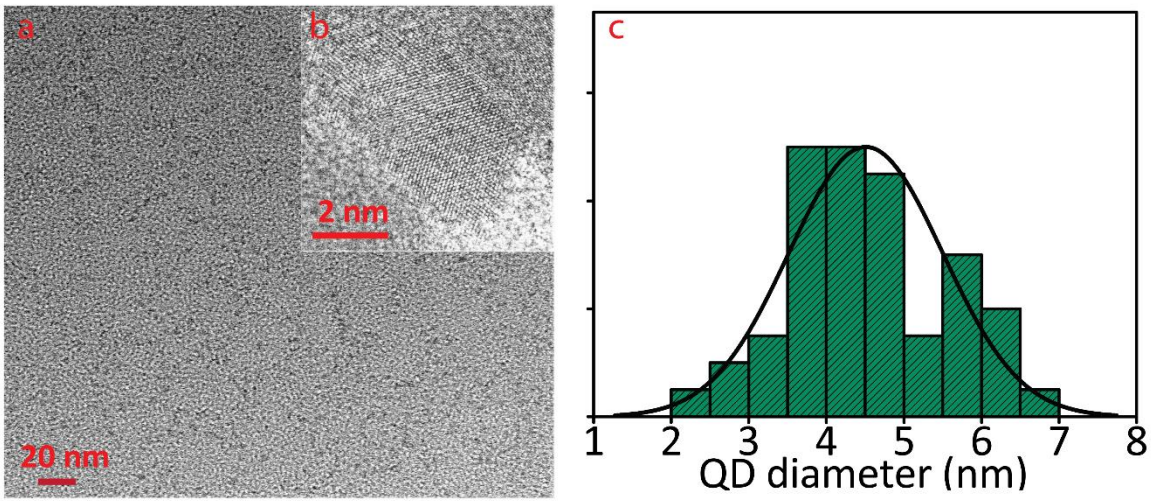


**Figure 29: a)** Transmission Electron Microscopy (TEM) image of InP/ZnS core/shell QDs. **b)** High resolution TEM (HR-TEM) image of InP/ZnS core/shell QDs, and **c)** the corresponding size distribution (50 particles were counted).

**Photocurrent Response of the Biointerfaces for Shorter Pulses**

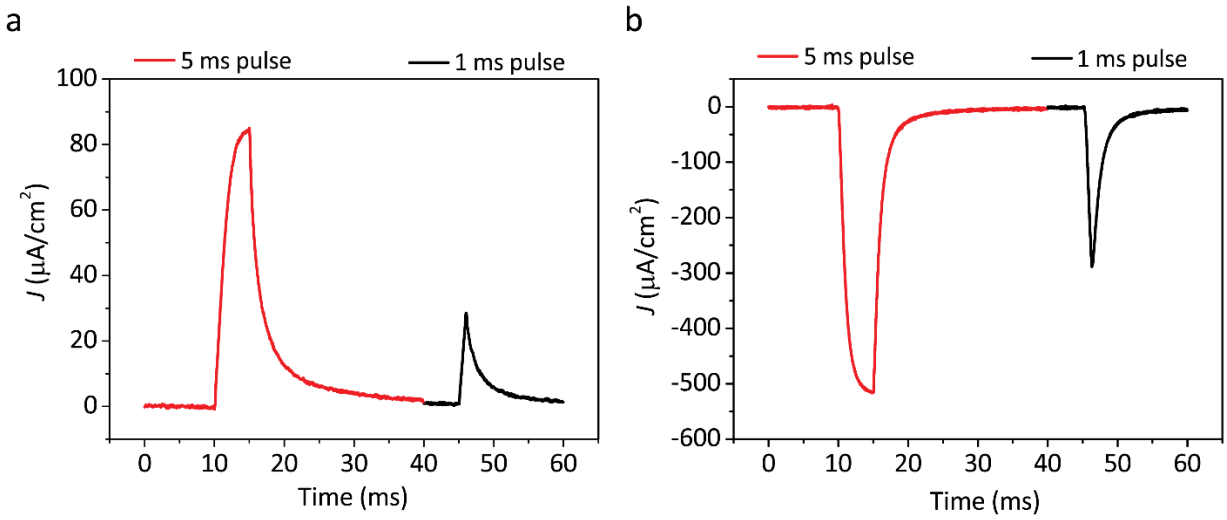


**Figure 30:** The photocurrent responses of **a)** type I and **b)** type II biointerfaces for 5 ms and 1 ms light pulses (illumination: blue LED at the wavelength of 445 nm, 0.57 mW $mm^{-2}$ optical power density).

**Electrochemical Characterization for Photocurrent Maximization**

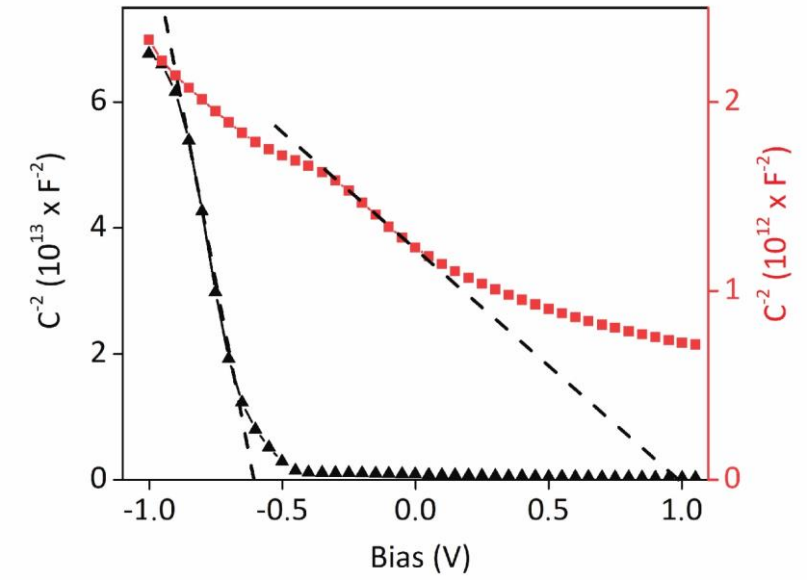


**Figure 31:** Mott-Schottky analysis of whole devices. Capacitance-voltage plot of type I (red) and type III (black) devices in aCSF medium. The intersection point of the linear fits on the x-axis corresponds to the built-in voltage. Bias dependent capacitance behavior implies the presence of space charge layer at the semiconductor-semiconductor junctions for both types of devices.

-

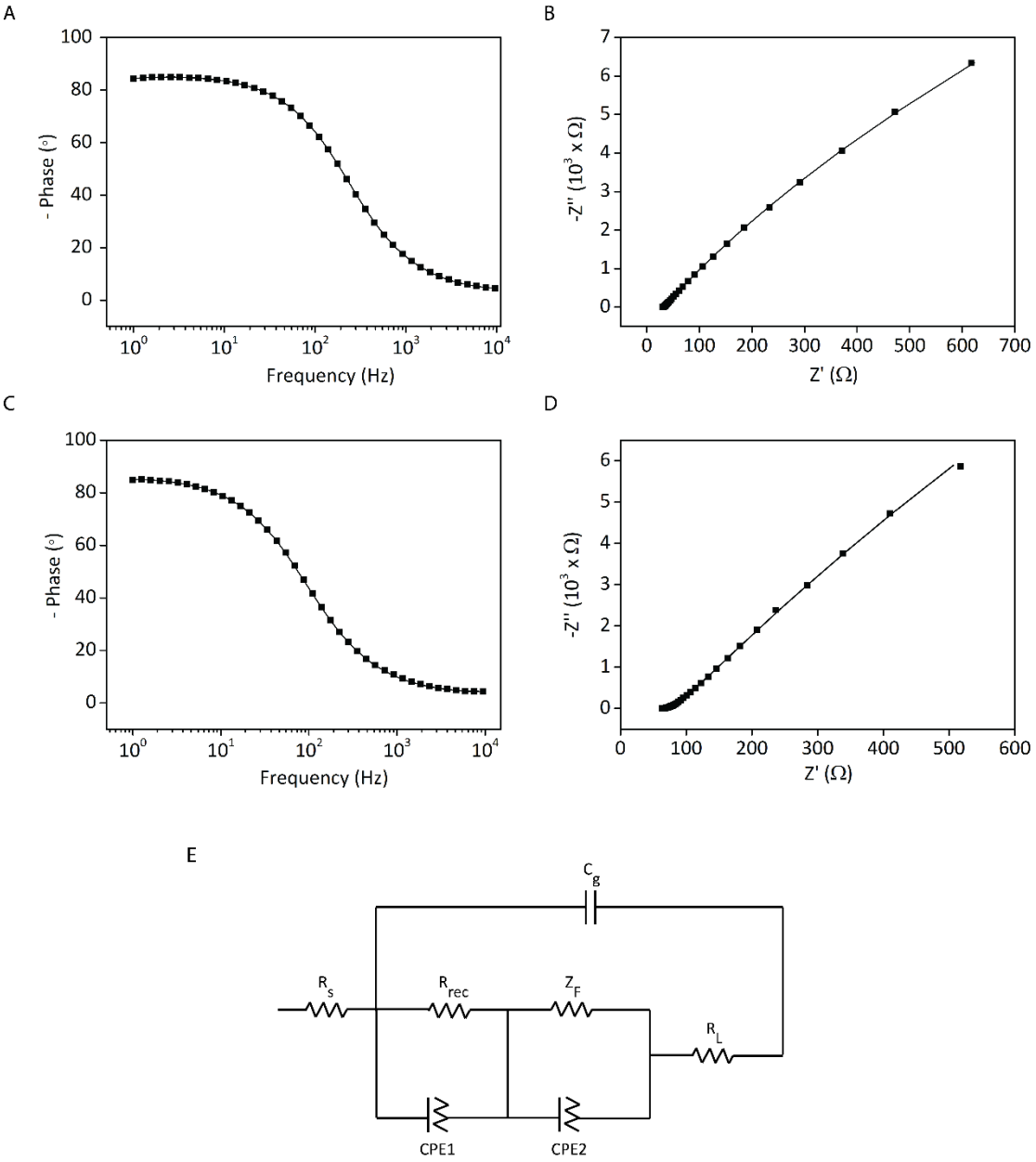


**Figure 32: Electrical impedance spectroscopy (EIS) measurements of type I and type III photoelectrodes.** **a)** Nyquist plot, **b)** Bode phase plot of type I devices. **c)** Nyquist plot, **d)** Bode phase plot of type III devices. **e)** Schematic of the fitted circuit diagram for both type I and type III devices. For a, b, c, d, measurement points are shown with the squares, and the corresponding fitting functions are shown with the lines.

**Table 2**. Extracted parameters from electrochemical analysis. Resulting device parameters calculated using the EIS measurement outputs and the fitted circuit.

| | Type I | Type II |
|---|---|---|
| $R_{rec}$ | 2.44 Ω | 51.1 Ω |
| $Y_0$ | 178 µMho | 4 mMho |
| N | 0.847 | 0.367 |
| $r_t$ | 27 Ω | 54 Ω |
| L | 122 nm | 92 nm |
| $C_\mu$ | 44 µF | 260 µF |
| $\tau_n$ | 0.107 ms | 13.3 ms |
| $\tau_d$ | 1.12 ms | 14 ms |
| $D_n$ | $1.44 \times 10^{-11}$ $m^2$ $s^{-1}$ | $4.6 \times 10^{-13}$ $m^2$ $s^{-1}$ |
| $\mu_n$ | $9.22 \times 10^{-29}$ $m^2$ $V^{-1}$ $s^{-1}$ | $2.94 \times 10^{-30}$ $m^2$ $V^{-1}$ $s^{-1}$ |
| $L_{diff}$ | 43 nm | 91 nm |

## Characterization of photoelectrochemical processes

To understand the faradaic reactions taking place in the electrode-electrolyte interface, we first measured the dark voltage (without illumination) of the biointerfaces in three electrode electrochemical setup via choronopotentiometry measurement. aCSF was used as electrolyte to mimic the stimulation conditions. The voltages of type I and type II biointerfaces with respect to Ag/AgCl reference electrode were measured as 2.2 V and 2.1 V, respectively. The fact that these voltages are higher than water electrolysis potential of 1.23 V implies that water electrolysis is a potential reaction that might be contributing to the photocurrent generation of the biointerfaces.

In order to identify whether any of the solutes of the aCSF is contributing to the photocurrent generation instead or in addition to water. We prepared six different aCSF solutions, each one is deficient of only one component. Then, in each solution, we measured the photocurrents of type I and type II biointerfaces (Supplementary Figure 6). The photocurrents for each

biointerface drop significantly only in cases of NaCl removal or HEPES removal. Since NaCl is the predominant component that provides conductivity of aCSF, the photocurrent decrease in case of NaCl removal can be due to the decreased conductivity of electrolyte. To check that, we increased the KCl amount (to 140 mM) in the solution without NaCl and measured the photocurrent. Photocurrent increased to similar levels with full aCSF case, confirming that the reason for photocurrent drop in case of NaCl removal is due to the decreased conductivity. As a result, we can conclude that the faradaic photocurrent originates from the reactions involving water electrolysis and HEPES.

HEPES is known to be oxidizable near 1.5V vs. RHE [40]. This represents a somewhat higher yet comparable overall potential when coupled to water reduction. Therefore, the overall oxidation current is split between HEPES and water and the coupled reduction current is predominantly water reduction.

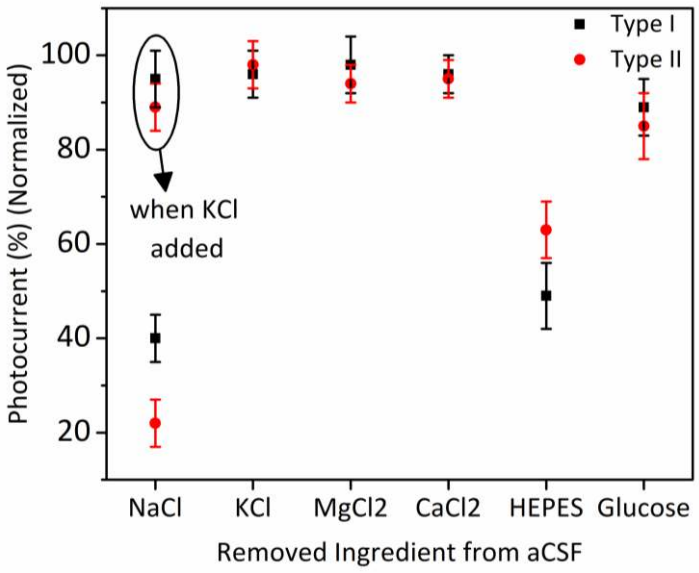


**Figure 33:** Photocurrent measurements in six different solutions, each prepared by removing only one ingredient from aCSF. Photocurrent values (mean ± s.d. for N = 3) were normalized by taking full aCSF photocurrent as 100%. The values in circle represents the case where NaCl is removed but KCl concentration is increased to 140 mM.

## Current clamp recordings for 10 Hz photostimulation

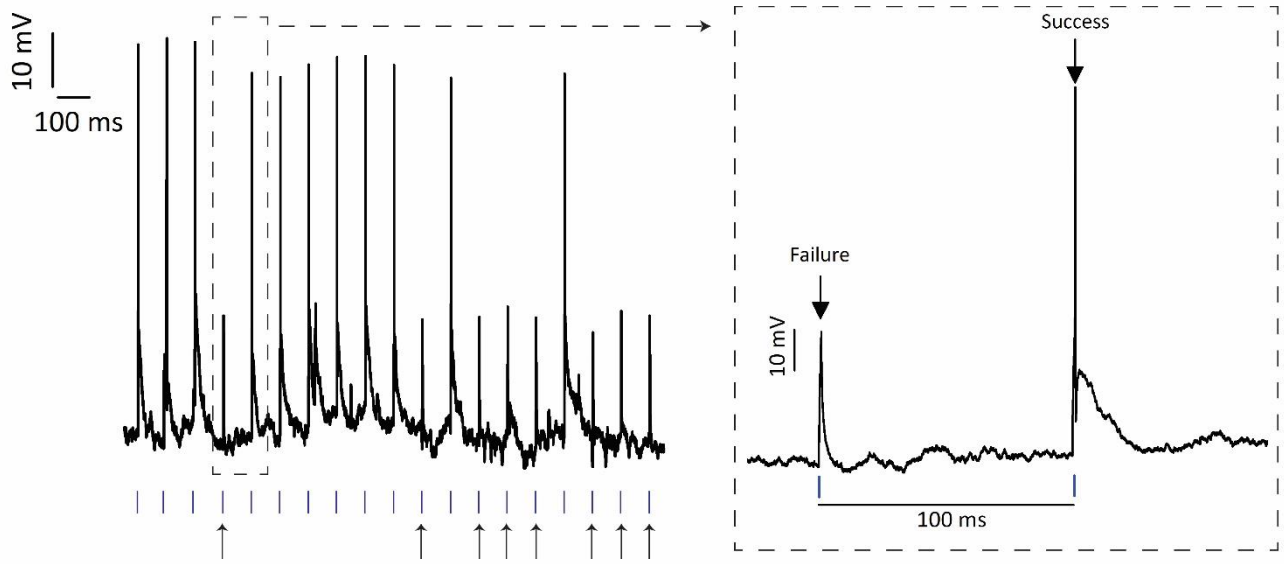


**Figure 34:** 10 Hz stimulation of neurons on type II biointerfaces with 10 ms pulse (445 nm, 2 mW $mm^{-2}$). Blue bars indicate the start of the light pulses. Arrows indicate the failed responses. Zoomed image of the dashed rectangle shows a failed stimulation pulse and a successful pulse that evoked an action potential.

## Intensity dependent current clamp recordings

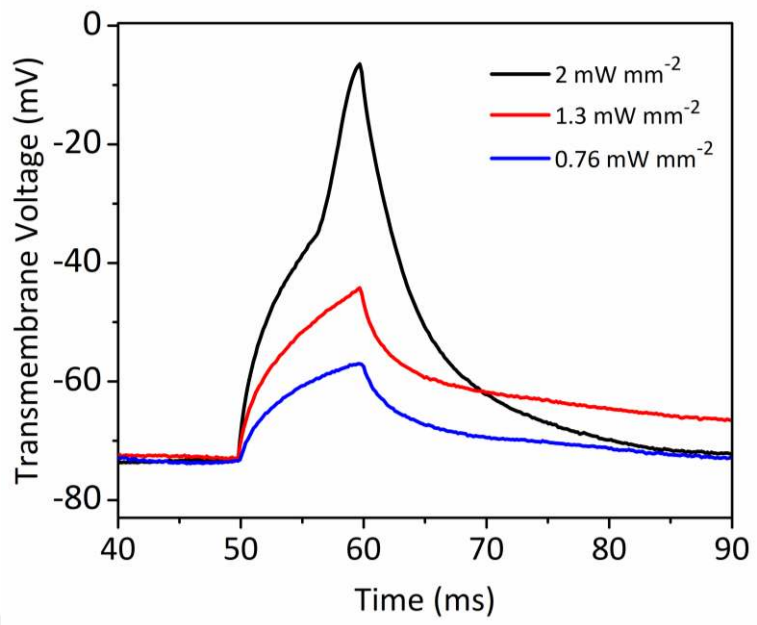


**Figure 35:** Current-clamp recording of hippocampal neurons in whole-cell configuration under different light intensities. Light is turned on at t = 50 ms (illumination: blue LED at 445 nm, 10 ms pulse width).

# Appendix B

## InP core, InP/ZnS core/shell, InP/ZnO/ZnS core/shell/shell QD synthesis

For InP core synthesis, we mixed 0.01 mmol stearic acid, 0.01 mmol zinc undecylenate and 0.2 mmol hexadecylamine in 6 ml 1-Octadecene in a three-neck flask. Then, 0.1 mmol indium chloride was injected into the flask in inert atmosphere. The temperature of the solution was increased to 120°C. To obtain water-free and oxygen-free reaction environment, 20 min evacuation was applied. We then apply refilling in the nitrogen atmosphere and increase the temperature to 230°C. After the solution reaches 230°C, we inject 0.2 mmol stock solution of Tris(trimethylsilyl) phosphine into the reaction. The solution was kept at 230°C 20 min. We cool down the solution to the room temperature and allocate half of it, labeling it as InP Core.

For ZnS shelling, we add 0.15 mmol zinc diethyldithiocarbamate and 2 ml 1-Octadecene into the remaining InP core solution. We increase the reaction temperature to 180°C and leave at that temperature 30 min under rigorous stirring. Then, we cool down the solution to room temperature. We wash the solution with toluene and ethanol. Finally, we re-disperse the purified solution in toluene.

For ZnO shelling, first, the InP core solution was cooled down to 80°C. ZnO stock solution was prepared by adding 245 µL oleylamine (OAM), 8 µL oleic acid (OA) and 6,5 mg zinc acetylacetonate hydrate into 1.6 mL 1-octadecene. Afterwards, ZnO stock solution was heated to 80°C, and mixed until zinc acetylacetonate hydrate was completely dissolved. Then, the ZnO stock solution was added to InP QD solution at 80°C. Then the solution was heated to 250°C and kept stirring at that temperature for 30 min. Then, we cool down the solution to room temperature. We wash the solution with toluene and ethanol. Finally, we re-disperse the purified solution in toluene.

## Photoelectrode fabrication

To clean the samples before the fabrication, the unpatterned Glass/ITO substrates were

sonicated in Hellmanex III solution (1.5% in deionized water), deionized water, acetone, and IPA consecutively for 15 min each. After drying the samples under 50°C for 20 min, the substrates went through UV ozone treatment for 15 min. 0.45 M ZnO precursor sol-gel solution was prepared by mixing 219.3 mg zinc acetate dehydrate ($Zn(CH_3CO_2)_2 \cdot 2H_2O$), and 73 mg of Ethanolamine ($HOCH_2CH_2NH_2$) in 2 ml 2-Methoxyethanol ($C_3H_8O_2$). The mixture was ultrasonicated at 50°C for 15 min to obtain a uniform solution. The ZnO precursor sol-gel solution was spin coated on cleaned substrates at 2000 rpm for 60 s, followed by baking at 290°C for 15 min. For the active layer, InP/ZnS:PCBM and InP/ZnO/ZnS:PCBM solutions were prepared by mixing previously prepared QD solutions in toluene (~ 30 $\mu$M) and PCBM solution in o-dichlorobenzene (30 mg $ml^{-1}$) with a volume ratios of QD:PCBM 1:1, 1:3, 1:7. The mixture was stirred for 1 hour to obtain uniform QD:PCBM solutions. The QD:PCBM layer was formed by spin coating 50 ul of the QD:PCBM solution at 2000 rpm for 60 s, followed by baking at 120°C for 15 min.

**Optical Characterization**

Edinburgh Instruments Spectrofluorometer FS5 was used to characterize the optical properties (UV/vis absorption, photoluminescence, quantum yield) of QDs. Integrating sphere module was used for the quantum yield measurements.

**Photocurrent measurements**

The photoresponses of the devices were measured in three-electrode electrochemical measurement with Ag/AgCl as the reference electrode, platinum rod as the counter electrode and the thin film samples as the working electrode in aCSF solution by dipping 1 $cm^2$ active area of each sample using Autolab Potentiostat Galvanostat PGSTAT302N (Metrohm, Netherlands). aCSF solution was prepared using the following materials stirred in deionized water: 10 mM of 4-(2-hydroxyethyl)-1-piperazineethanesulfonic acid (HEPES), 10 mM of glucose, 2 mM CaCl2, 140 mM of NaCl, 1 mM of MgCl2, 3 mM of KCl. After obtaining uniform solution, NaOH was slowly added until the pH of aCSF solution reaches 7.4. For illumination, 10 ms light pulses (Thorlabs M450LP1 LED, 445 nm peak wavelength) were applied. Thorlabs DC2200 Driver was used to control the LED. Optical power was measured via Newport 843-R power meter.

**X-ray Photoelectron Spectroscopy (XPS)**

The XPS spectra of quantum dot samples were taken by a Thermo Scientific K-Alpha spectrometer using an Aluminum anode (Al Kα= 1468.3 eV) at an electron take-off angle of 90 o (between the sample surface and the axis of the analyzer lens). The spectra were recorded using an Avantage 5.9 data system. The binding energy scale was calibrated by assigning the C1 s signal at 284.5 eV.

**Energy dispersive X-ray spectroscopy (EDS)**

EDS was performed using a JEOL Centurio detector, with a spot size of *ca.* 1 Å and probe current of 700 pA. Analysis was conducted on a JEOL JEM-ARM200CF spherical aberration-corrected scanning transmission electron microscope (STEM) operated with an accelerating voltage of 200 keV.

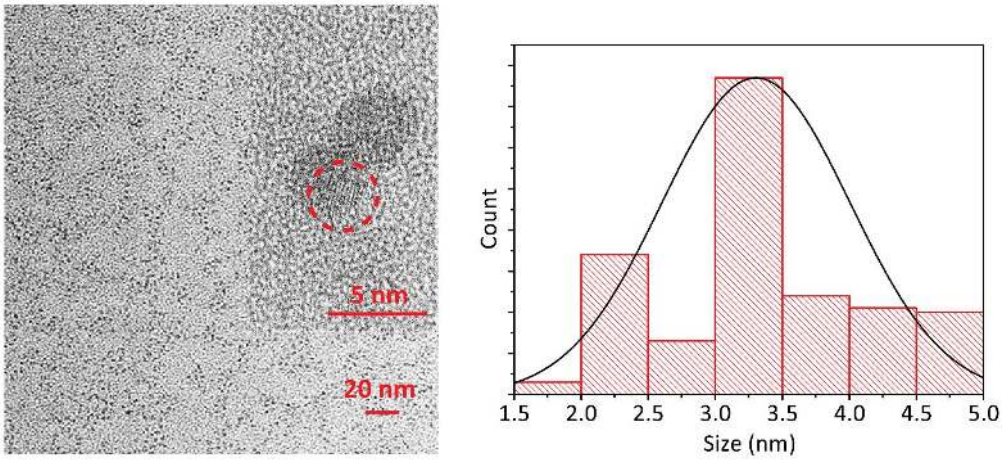


**Figure 36:** Transmission Electron Microscopy (TEM) image (inset: HR-TEM image) of InP core QDs and the corresponding size distribution (200 particles were counted).

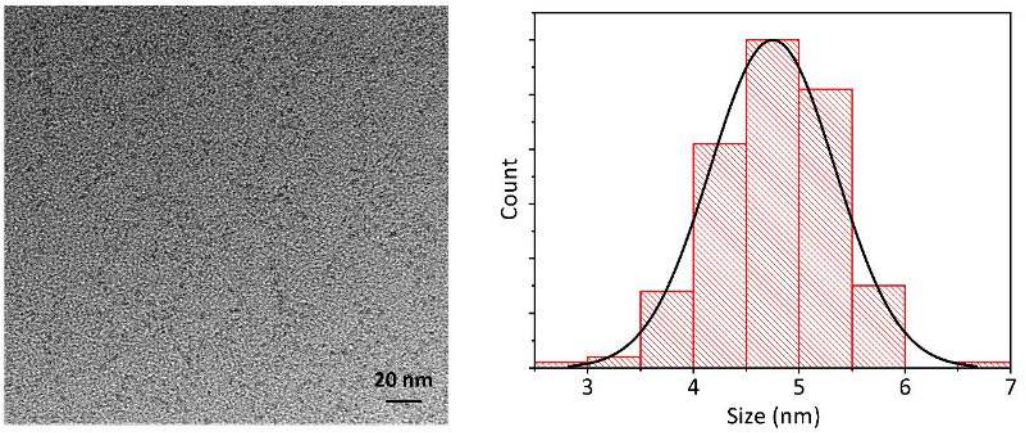


**Figure 37:** Transmission Electron Microscopy (TEM) image of InP/ZnS core/shell QDs and the corresponding size distribution (200 particles were counted).

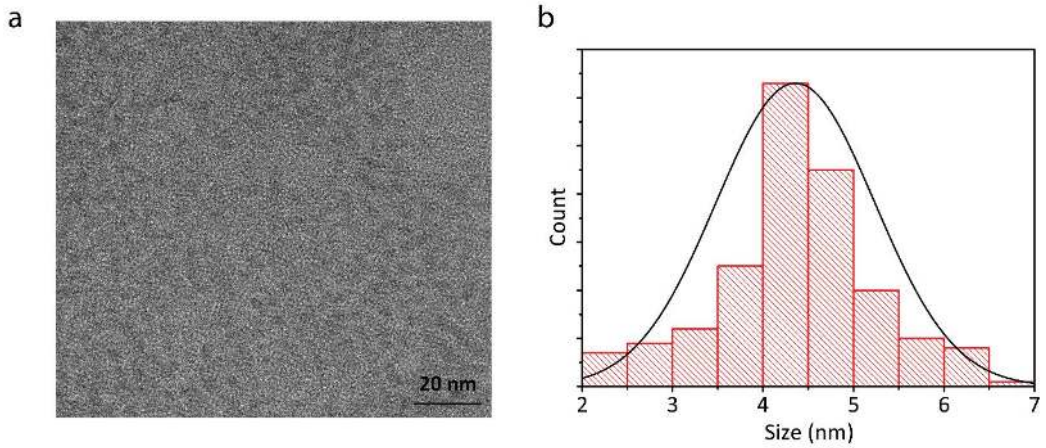


**Figure 38:** Transmission Electron Microscopy (TEM) image of InP/ZnO core/shell QDs, and the corresponding size distribution (200 particles were counted).

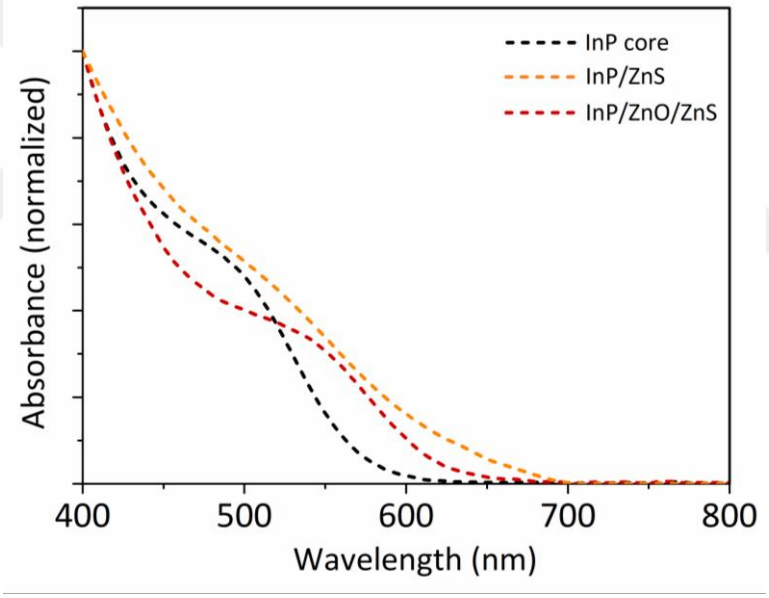


**Figure 39:** Normalized absorbance of InP core, InP/ZnS core/shell and InP/ZnO/ZnS core/shell/shell QDs.

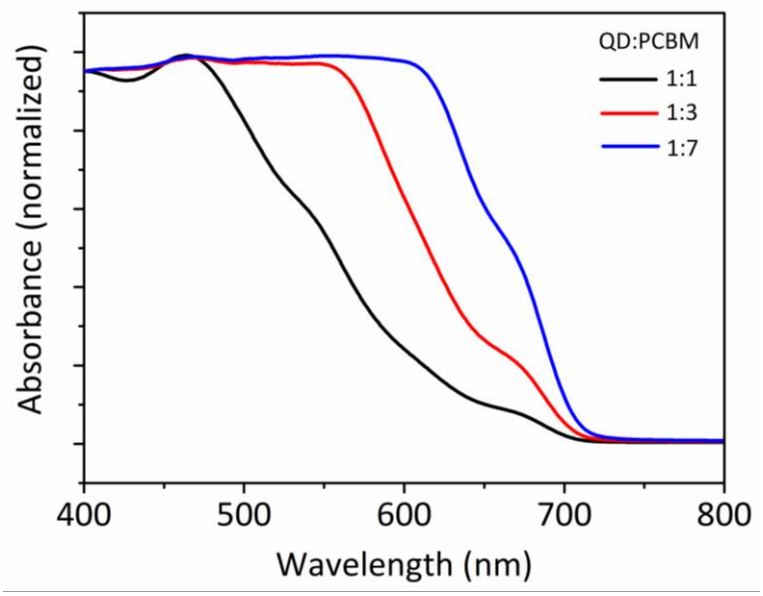


**Figure 40:** Normalized absorbance of QD:PCBM blend with QD:PCBM volume ratios of 1:1, 1:3 and 1:7.

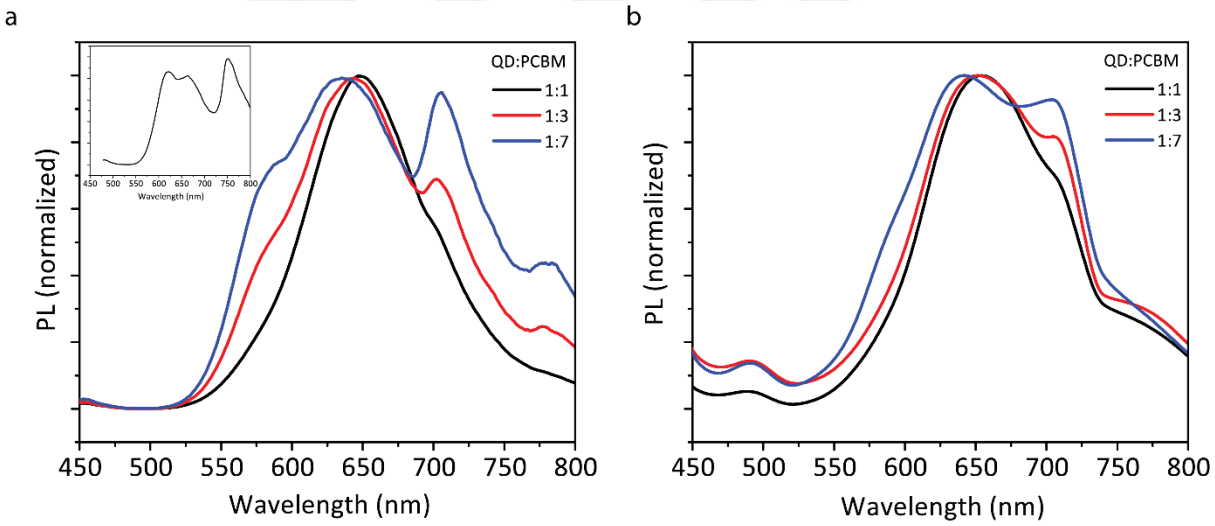


**Figure 41:** PL spectrum of a) QD:PCBM (1:1, 1:3, 1:7) mixture in solution (inset shows PL spectrum of PCBM) b) QD:PCBM mixture coated as thin film on the electrode.

**X-ray Photoelectron Spectroscopy (XPS) analysis of QDs**

Figure S7 shows the In 3d and P 2p XPS spectra of InP core QDs. In the In 3d spectrum (Figure S7a), the 444.4 eV and 452 eV peaks with a spin orbit splitting of 7.6 eV between them are characteristic of InP.[149] P 2p spectrum of InP core QDs consists of two doublets, which denotes that P atoms participates in two distinct reactions (Figure S7b). The doublet in 132.4 eV – 133.3 eV range is associated to the P atoms in an oxidized medium, while the doublet in the 128.1 eV – 129 eV range is indicative of $P^{-3}$ ions in InP.[150] Besides, the 0.9 eV spin orbit splitting matches with the previous reports.[151]

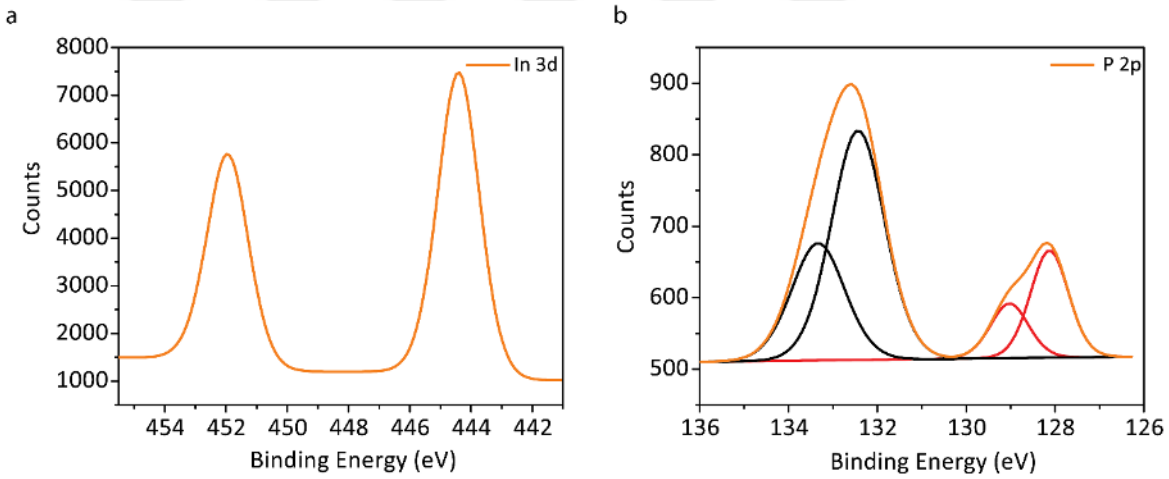


**Figure 42:** X-ray photoelectron spectroscopy analysis of InP core QDs. a) In 3d spectrum, b) P 2p spectrum.

For InP/ZnO core/shell QDs, we analyzed the Zn 2p and O 1s spectra to confirm ZnO shell growth (Figure S8). In the Zn-2p spectrum (Figure S8a), $2p_{3/2}$ and $2p_{1/2}$ peaks are observed at 1022.4 eV and 1045.4 eV, respectively, with 23 eV spin orbit splitting between them, which indicates the $Zn^{+2}$ bound to oxygen in the ZnO.[152] O 1s spectrum consists of a predominant peak at 531.6 eV, associated with lattice oxygen in the structure and a second peak at 532.8 eV (Figure S8b).[153] Together, Zn 2p and O 1s spectra of InP/ZnO QDs suggest that ZnO shell is formed.

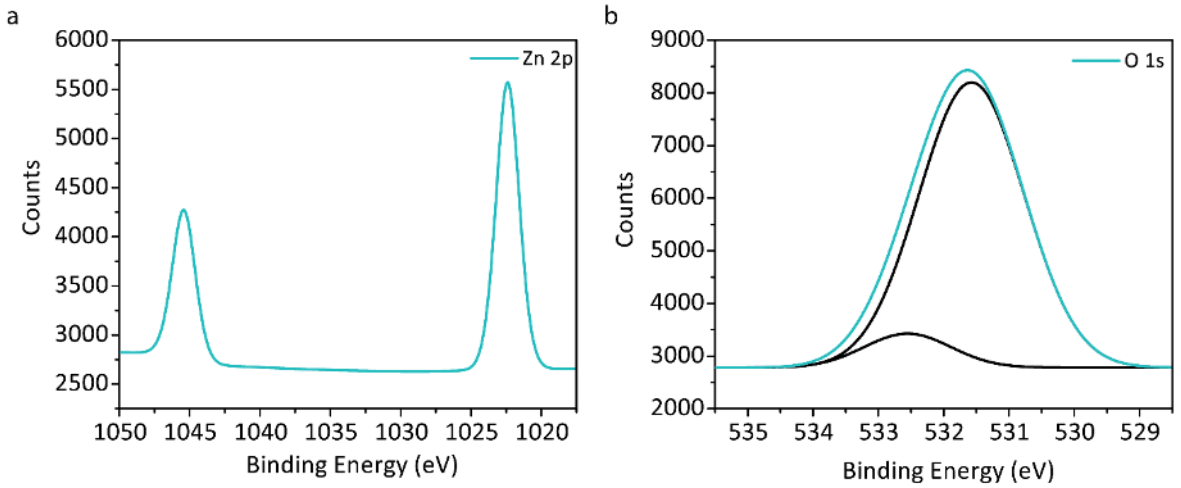


**Figure 43:** X-ray photoelectron spectroscopy analysis of InP/ZnO core/shell QDs. a) Zn 2p spectrum, b) O 1s spectrum.

Finally, to demonstrate the ZnS shell formation, we investigated the S 2p and Zn 2p XPS spectra of InP/ZnO/ZnS QDs (Figure S9). In the S 2p spectrum (Figure S9a), the asymmetric S 2p peak was deconvoluted into the subpeaks of S $2p_{3/2}$ and S $2p_{1/2}$ located at 161.1 eV and 162.4 eV, respectively, representing the $S^{-2}$ anions in the ZnS.[151] The peak at 161.1 eV is the predominant one and associated with the $S^{-2}$ in the ZnS structure.[151, 154] Moreover, Zn 2p spectrum InP/ZnO/ZnS QDs exhibits Zn $2p_{3/2}$ and Zn $2p_{1/2}$ peaks at 1021.6 eV and 1044.6 eV, representing the $Zn^{+2}$ ions (Figure S9b).[154] The spin orbit splitting of 23 eV between $Zn^{+2}$ peaks matches well with the previously reported values for Zn-S bond in the literature.[155] Thus, the S 2p and Zn 2p spectra indicate the formation of ZnS shell.

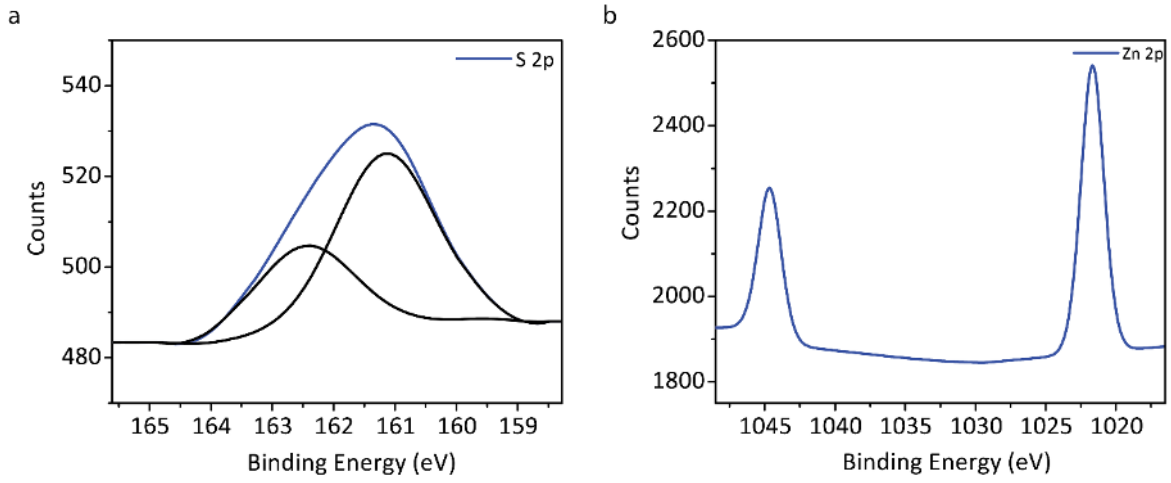


**Figure 44:** X-ray photoelectron spectroscopy analysis of InP/ZnO/ZnS core/shell/shell QDs. **a)** S 2p spectrum, **b)** Zn 2p spectrum.

**Energy dispersive X-ray spectroscopy (EDS) analysis of InP/ZnO/ZnS QDs**

We performed energy dispersive X-ray spectroscopy (EDS) of InP/ZnO/ZnS QDs for elemental mapping (Figure S10). Figure S10b shows the presence of In, P, Zn, S, O elements in the analyzed region of STEM image of InP/ZnO/ZnS QDs shown in Figure S10a. Existence of those elements supports the formation of InP/ZnO/ZnS core/shell/shell structure.

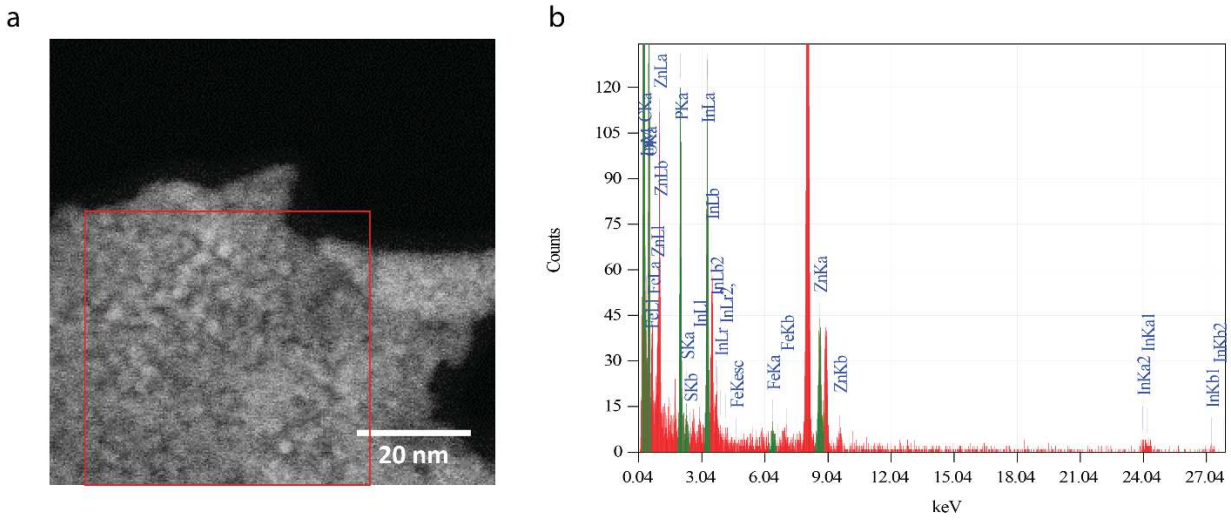


**Figure 45: EDS elemental mapping of InP/ZnO/ZnS QDs. a)** Z-contrast STEM image of QDs showing the areal region analyzed in (b) **b)** EDS spectrum of the region showing the presence of elements.

**<u>Calculation of molar ratios of QD:PCBM and estimation of number of PCBM per QD</u>**

The molar concentration of QD was estimated via Beer-Lambert law, which is formulized as:

$$A = \varepsilon c l \quad (1)$$

where $A$ is the absorbance at the first excitonic peak, $\varepsilon$ is the extinction coefficient, $c$ is the molar concentration, $l$ is the path length, which is 1 cm due to the path length of the cuvette.

$\varepsilon$ can be calculated using the following empirical function:[156]

$$\varepsilon = 3046.1(D^3) - 76532(D^2) + (5.5137 * 10^5)(D) - (8.9839 * 10^5) \quad (2)$$

where $D$ is the diameter of the QD, which is 4.7 nm and 5.4 nm for InP/ZnS and InP/ZnO/ZnS, respectively.

For InP/ZnS, $\varepsilon$ = 318712.36 L mol$^{-1}$ cm$^{-1}$, $A$ = 0.14, $c$ = 0.45 $\mu$M

For InP/ZnO/ZnS, $\varepsilon$ = 326985.97 L mol$^{-1}$ cm$^{-1}$, $A$ = 0.16, $c$ = 0.49 $\mu$M

These concentrations are the ones used for absorbance measurements, which means they represent the diluted amounts (50 $\mu$l main QD solution in 3 ml toluene). Thus, the concentrations of main solutions are estimated as: c (InP/ZnS) = 26.4 $\mu$M, c (InP/ZnO/ZnS) = 29.4 $\mu$M

PCBM has molecular weight of 911 g mol$^{-1}$. We use 30 mg ml$^{-1}$ PCBM solution in the QD:PCBM blend, thus $c$ = 0.033 M.

We use three different QD:PCBM mixing ratios in the experiments: 1:1, 1:3, 1:7 volume ratios.

Hence, QD:PCBM molar ratios for each blend:

$M_{11}$ = 0.08% for 1:1, $M_{13}$ = 0.03% for 1:3, $M_{17}$ = 0.01% for 1:7.

For InP/ZnO/ZnS:PCBM blend, we can calculate the number of PCBM per QD as following:

QD radius $r_{QD}$ = 2.7 nm and PCBM radius $r_{PCBM}$ = 0.55 nm.[157]

Assuming both QD and PCBM to be spheres, the geometry of QD:PCBM structure is schematized in Fig. S4. In that close-packed geometry, assuming a packing factor ($\eta$) of maximum 0.74, the number of PCBM per QD can be found by dividing the surface area of the outer circle to the cross-sectional area of PCBM and multiplying with the packing factor.

Thus, the maximum number of PCBM per QD is calculated as following:

$$N_{PCBM} = \frac{4\pi r_{out}^2}{\pi r_{PCBM}^2} \times \eta = 103$$

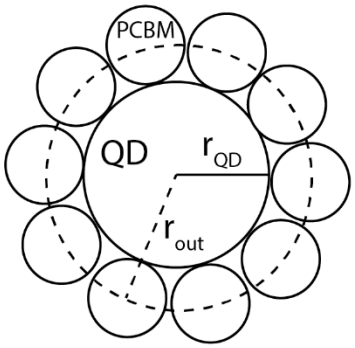


**Figure 46:** Schematic of QD:PCBM structure for calculation of number of PCBM per QD. QD and PCBM are assumed to be spherical. $r_{out}$ is the radius of the outer circle shown with the dashed line, which is equal to the sum of the QD radius and PCBM radius.

# Appendix C

## Biointerface fabrication

ITO/PET (Sigma Aldrich, 639303) and FTO/glass substrates (Ossila, TEC 10) were cleaned by sonication in detergent solution, deionized water, acetone, and isopropanol consecutively for 15 min each, followed by 20 min UV ozone treatment. Poly(3-hexylthiophene-2,5-diyl) (P3HT) with regioregularity of 95.7% and a molecular weight of 57,467 g $mol^{-1}$ (Ossila) and [6,6]-PPhenyl-C61-butyric acid methyl ester (PC61BM) with a molecular weight of 1,031 g $mol^{-1}$ were supplied by Ossila Ltd. 1,2-dichlorobenzene solutions of P3HT (20 mg $ml^{-1}$) and PCBM (12 mg $ml^{-1}$) were prepared and stirred at 70°C overnight. P3HT and PCBM solutions were mixed (1:1 volume ratio) and stirred for further 2 h using magnetic stirrer. ZnO precursor sol-gel solution (0.45 M) was prepared by mixing 219.3 mg Zinc acetate dehydrate ($Zn(CH_3CO_2)_2 \cdot 2H_2O$), 2 ml of 2-Methoxyethanol ($C_3H_5O_2$) and 73 mg of Ethanolamine ($HOCH_2CH_2NH_2$). Ruthenium (III) chloride hydrate ($RuCl_3.H_2O$) with molecular weight of 207.43 g $mol^{-1}$ was purchased from Sigma Aldrich. 0.01 M aqueous solution of $RuCl_3.H_2O$ was prepared for electrochemical deposition of ruthenium oxide ($RuO_2$).

For the fabrication of $RuO_2$-based biointerfaces, firstly, a certain area of FTO/ITO substrate, where $RuO_2$ will be coated, was covered with a mask. Then, ZnO precursor sol-gel solution was spin-coated on the remaining area of the substrate at 2000 rpm, followed by 15 min annealing at 290°C for FTO and 20 min at 200°C for ITO. On ZnO layer, P3HT:PCBM solution was spin-coated at 2000 rpm, followed by 15 min annealing at 150°C. Then, the mask is removed. The area under the mask was immersed into 0.01 M aqueous solution of $RuCl_3.H_2O$ and $RuO_2$ layer was formed via cyclic voltametric deposition by cycling the potential between -0.2 and 1.2 V at a scan rate of 50 mV $s^{-1}$.

## Photoresponse analysis

Interfacial (open-circuit) photocurrents were recorded via EPC 800 Heka Elektronik patch-clamp amplifier in voltage-clamp mode using patch pipettes (6-8 MΩ). Biointerfaces were placed in artificial cerebrospinal fluid (aCSF), which consists of 10 mM of 4-(2-hydroxyethyl)-1-piperazineethanesulfonic acid (HEPES), 10 mM of glucose, 2 mM $CaCl_2$,

140 mM of NaCl, 1 mM of $MgCl_2$, 3 mM of KCl. The pH of aCSF solution was adjusted to 7.4 by adding a stoichiometric amount of NaOH. Patch pipettes were filled with intracellular medium, which consists of 140 mM KCl, 2 mM $MgCl_2$, 10 mM HEPES, 10 mM ethylene glycol-bis(β-aminoethyl ether)-N,N,N',N'-tetraacetic acid (EGTA), 2 mM Mg-ATP dissolved in distilled water. The pH of the intracellular solution was adjusted to 7.2-7.3 by adding a stoichiometric amount of KOH.

Chronopotentiometry and chronoamperometry measurements were performed via Autolab Potentiostat Galvanostat PGSTAT302N (Metrohm, Netherlands) using a three-electrode setup consisting of Ag/AgCl as the reference electrode, platinum rod as the counter electrode and the thin film samples as the working electrode in artificial cerebrospinal fluid (aCSF) solution. Light pulses were applied via Thorlabs M450LP1 LED with 445 nm nominal wavelength and the LED spectrum is provided in our previous study.[117] The blue LED was driven with Thorlabs DC2200 - High-Power 1-Channel LED Driver. Newport 843-R power meter was used to measure the optical power of incident light on the biointerfaces.

**Electrochemical measurements**

Autolab Potentiostat Galvanostat PGSTAT302N (Metrohm, Netherlands) was used for cyclic voltammetry (CV) and electrochemical impedance spectroscopy (EIS) measurements. Three-electrode electrochemical set up consists of Ag/AgCl reference electrode, platinum rod counter electrode and the thin film biointerface samples as working electrode. The EIS was performed in frequency response analysis (FRA) potential scan mode while varying the frequency between 1 Hz - 10 kHz at 10 mV (RMS) AC voltage perturbation. The fitting of the high-frequency resistance and low-frequency capacitance was performed in NOVA software to extract the corresponding circuit parameters. A more detailed fit can be performed via a 3-RC circuit, however the extra detail would be a distraction and not add to the main argument of the paper. Therefore, only the high frequency resistance and the low frequency capacitance are considered.

**Primary Neuron Isolation**

All experimental procedures have been approved by the Institutional Animal Care and Use Committees of Koç University (Approval No: 2019.HADYEK.023) according to Directive 2010/63/EU of the European Parliament and of the Council on the Protection of Animals Used for Scientific Purposes. Hippocampal regions were extracted from decapitated E15-E17 Wistar Albino rat embryos and were placed immediately in ice-cold Hank's Balanced Salt

Solution (HBSS, Thermo Fisher Scientific, MA, USA). The hippocampi were incubated in %0.25 Trypsin-EDTA solution (Thermo Fisher Scientific, MA, USA) with %2 DNase-I supplement (NeoFroxx, Einhausen, Germany) for 20 minutes in a 37°C incubator. Then the cells were centrifuged, and the supernatant was changed with Dulbecco's Modified Eagle Medium/Nutrient Mixture F-12 (DMEM/F12 Thermo Fisher Scientific, MA, USA) supplemented with %10 fetal bovine serum (FBS, Heat Inactivated, GE Healthcare, IL, USA) and %1 penicillin/streptomycin (Thermo Fisher Scientific, MA, USA). DMEM/F12 was removed and Neurobasal Medium (NBM, Thermo Fisher Scientific, MA, USA) supplemented with B27, L-glutamine, β-mercaptoethanol, glutamate (Thermo Fisher Scientific, MA, USA) was added to the cell pellet. The cells were triturated and were passed through a 70 µm cell strainer. The homogenous cell solution was seeded in poly-D-lysine (PDL, Sigma-Aldrich, MO, USA) coated substrates. After 3-days incubation of cells on substrates in a 37°C incubator with %5 carbon dioxide, the media of the cells on substrates were changed with NBM supplemented with cytosine arabinoside (Sigma-Aldrich, MO, USA) to inhibit growth of glial cells. After 24-hour incubation with cytosine arabinoside, the media were changed with NBM and the substrates with the hippocampal neurons used for the experiments.

**Biocompatibility Assay**

MTT viability assay was applied to investigate cell viability of primary hippocampal neurons on the biointerfaces. The neural growth medium was prepared by using B27 supplemented Neurobasal medium. MTT cell viability assay (Abcam, ab211091) was utilized to evaluate biocompatibility of our biointerface. The devices were sterilized first by cleaning with 70% ethanol followed by air-drying. The surface was further sterilized under UV irradiation for 30 min. Substrates were placed in wells of the 6-well plates. Primary hippocampal neurons were seeded ($5 \times 10^5$ cells per sample) on the substrates in B27 supplemented Neurobasal medium as described above and incubated in the neuron growth medium for 48 hours after cytosine arabinoside supplemented neurobasal medium removal. After 48 hours incubations, the media were replaced with 1 mL of MTT solution (5 mg/mL in PBS, pH = 7.4) and 4 mL of NBM mixture per well. Then, for an additional 4 h, the cells were incubated at 37°C and 5% $CO_2$ atmosphere. The medium was vacuumed from each well and substrates were transferred to an empty 6-well plates. In each well, 1:1 mixture of DMSO and ethanol was added to dissolve the formazan crystals. The solution was transferred to a 96-well plate and the absorbance was measured at 570 nm light with Synergy H1 Microplate Reader (Bio-Tek Instruments). The relative cell viability was calculated as follows: Viability = $(OD_{sample}/OD_{control}) \times 100$. The

optical density (OD) of the sample was obtained from the cells grown on a photoelectrode, and the OD of control was obtained from the cells grown on the ITO substrates.

**Immunofluorescence Staining and Imaging**

Primary hippocampal neurons ($5x10^5$ cells per sample) were seeded as explained above on ITO control substrate and the biointerface. The samples with neurons fixed by 4% paraformaldehyde immediately after primary hippocampal neuron isolation protocol or incubated for 14 days with regular medium changes at 37°C in the cell culture incubator. After 14-day incubation, the primary hippocampal neurons were also fixed by 4% paraformaldehyde and washed three times with PBS-T (Phosphate Buffered Saline, 0.1% Triton X-100). Cells were blocked in PBS solution containing 5% BSA (Bovine Serum Albumin) and 0.1% Triton X-100. Samples with primary hippocampal neurons were incubated with rabbit anti-NeuN antibody (ab177487, Abcam, Cambridge, UK) overnight, for neuron characterization, and washed three times with PBS-T. Then, samples with primary hippocampal neurons were incubated with goat anti-rabbit IgG H&L Alexa Fluor 555(4413, Cell Signaling Technology, MA, USA) for fluorophore marking of anti-NeuN primary antibody for 90 minutes at 37°C. For visualization of the cytoskeleton, primary neuron samples also were incubated with FITC-conjugated phalloidin antibody (Sigma-Aldrich, P5282) for 90 minutes at 37°C. All samples were washed three times with PBS-T, then mounted with DAPI supplemented mounting medium (ab104139, Abcam, Cambridge, UK) to observe nuclei. Finally, immunofluorescence imaging was done using a fluorescence light microscope (Axio Observer Z1, ZEISS, Oberkochen, Germany).

**Intracellular oxidative stress measurement**

The intracellular oxidative stress level was measured by 2',7'-dichlorodihydrofluorescein diacetate ($H_2$DFCDA) (D399, Molecular Probes, Invitrogen). Primary hippocampal neurons ($5x10^5$ cells per sample) were seeded on FTO control substrates and the biointerfaces. The $H_2$DFCDA agent is non-fluorescent but it becomes intensive fluorescent agent after oxidation with $H_2O_2$. Thus, as a positive control group, neurons grown on the control substrates were treated with 100 μM $H_2O_2$ for 30 min. In experimental group, neurons grown on the biointerfaces were exposed to 450 nm LED for 10000 cycles with 5 Hz frequency. Cells were washed once with PBS then incubated with 20 μM $H_2$DFCDA in aCSF solution for 45 min prior to imaging at 37°C, 5% $CO_2$ to allow $H_2$DFCDA to fully enter the cells. Hoechst (0.6 mg/ml) was used to stain the nucleus for 15 min at 37°C, 5% $CO_2$. To avoid remaining dye

residues, cells were washed with PBS. To avoid photobleaching, all steps were carried out in the dark. All immunofluorescence images taken in same light intensity, exposure, time point, and magnification with live-cell fluorescence microscope (Axio Observer Z1, ZEISS, Oberkochen, Germany) and average fluorescence intensity was measured by ImageJ software (ImageJ Fiji, NIH, MD, USA). For image analysis, images converted to 8-bit black and white image and background subtracted. To measure number and area of cells, maximum entropy threshold applied to the image and the particles analyzed for integrated density. By this way both area of neurons and intensity of fluorescence were measured in acquired images from randomly selected ten different regions of neural cell culture. Relative fluorescence intensity calculated with negative (neurons on FTO substrate) and positive (neurons on FTO with $H_2O_2$ addition to induce ROS production) controls. Normal ROS production in FTO control substrates accepted as %100 in relative fluorescence intensity comparison.

**Electrophysiology recordings**

Single-cell electrophysiology experiments were performed using EPC 800 Heka Elektronik patch-clamp amplifier in whole-cell configuration. Biointerfaces were electrically floating in aCSF without any wire connection. Whole-cell transmembrane voltage and current recordings, which refer to intracellular membrane potential and current recordings with respect to a distant Ag/AgCl electrode, were taken in current clamp and voltage clamp modes, respectively. Downsampling was applied to the current clamp data to obtain a feasible computational complexity for making statistical analysis of action potentials without causing loss of any meaningful data. The patch pipette resistance of 6-8 MΩ was used for the recordings. The biointerfaces were placed in aCSF and patch pipettes were filled with the intracellular medium. To block the voltage-gated sodium channels, 5 mM QX-314 chloride was added into the intracellular solution. Patch pipette and cells were monitored through a digital camera integrated with the Olympus T2 upright microscope.

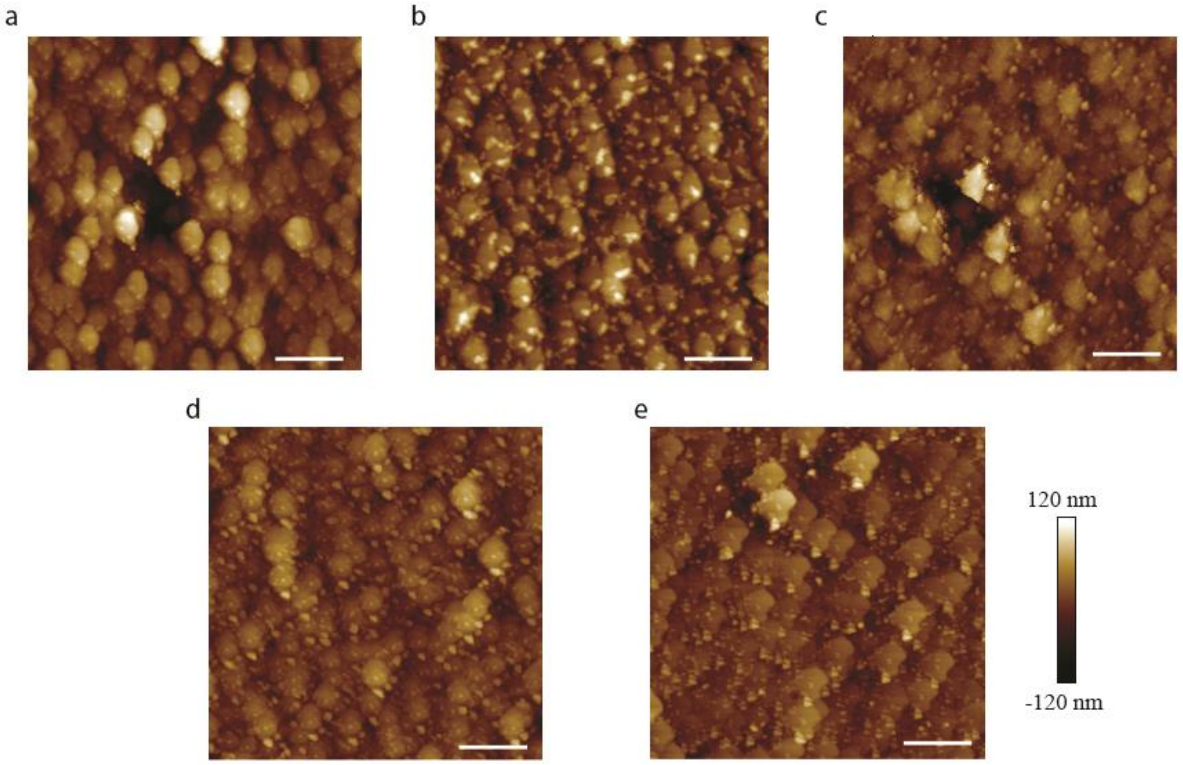


**Figure 47:** Atomic force microscopy (AFM) images of $RuO_2$ coatings for **a)** 5, **b)** 15, **c)** 25, **d)** 40, **e)** 60 deposition cycles (N = 3). The corresponding roughness values are **a)** 16 ± 3 nm, **b)** 16 ± 4 nm, **c)** 18 ± 3 nm, **d)** 23 ± 4 nm, **e)** 24 ± 5 nm. All scale bars are 2 µm.

## XPS Analysis

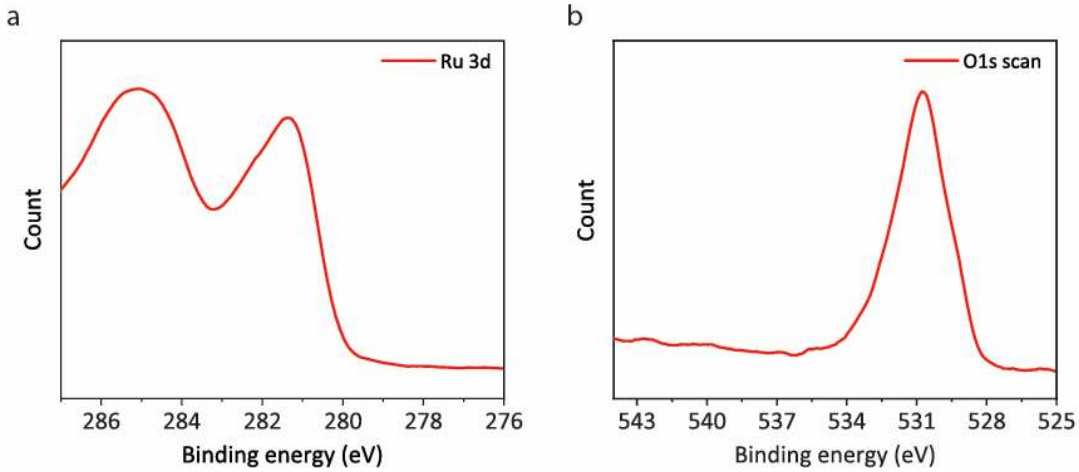


**Figure 48:** X-ray photoelectron spectroscopy (XPS) analysis of $RuO_2$ coating. a) Ru3d spectrum, b) O1s spectrum.

Ru 3d spectra in Fig. S3a shows broad Ru $3d_{3/2}$ peak at 285 eV and Ru $3d_{5/2}$ peak at 281.4 eV

that correspond to hydrated $RuO_2$.[158] Also observed in Ru 3d5/2 region is the contribution of $RuO_2$ at 280.7 eV and a relatively smaller amount of Ru(0) species at 281.4 eV.[107, 110]

O1s spectra is deconvoluted into three peaks. The peak at 529.4 eV corresponds to Ru-O bond in the formation of $RuO_2$.[159] 530.5 eV corresponds to hydroxide ions attached to $RuO_2$ surface in hydrated $RuO_2$ structure.[160] 531.8 eV is assigned to chemisorbed oxygen associated with hydrated $RuO_2$.[161]

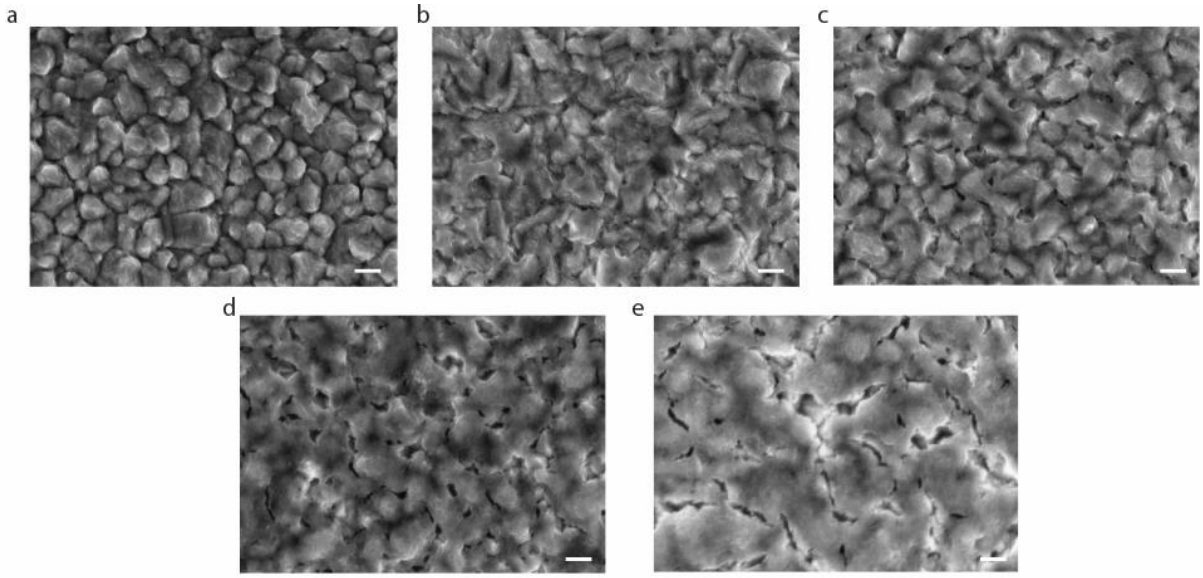


**Figure 49:** Scanning electron microscopy (SEM) images of $RuO_2$ coatings for **a)** 5, **b)** 15, **c)** 25, **d)** 40, **e)** 60 deposition cycles. All scale bars are 200 nm.

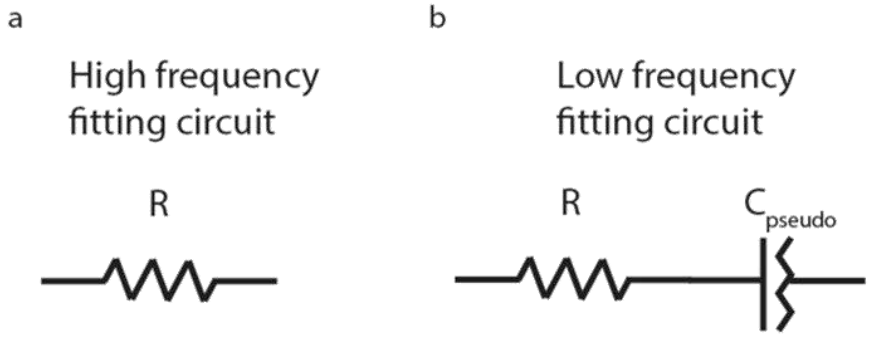


**Figure 50:** Circuit models used to fit the **a)** high frequency, and **b)** low frequency regions of electrochemical impedance spectroscopy (EIS) measurements of $RuO_2$ coatings.

**Table 3:** Extracted values of circuit elements as a result of fitting of EIS data ( $\chi^2 < 0.01$).

| **$RuO_2$ cycle** | **High freq R (Ω)** | **Low freq R (Ω)** | **Low freq Q** |
|---|---|---|---|
| 5 cycle | 33.5 | 50.2 | Y0 = 1.22 mMho*s^N<br>N = 0.891 |
| 15 cycle | 35.5 | 49.1 | Y0 = 2.45 mMho*s^N<br>N = 0.837 |
| 25 cycle | 31.9 | 42.0 | Y0 = 4.08 mMho*s^N<br>N = 0.79 |
| 40 cycle | 48.6 | 63.0 | Y0 = 3.16 mMho*s^N<br>N = 0.753 |
| 60 cycle | 52.8 | 64.7 | Y0 = 4.36 mMho*s^N<br>N = 0.706 |

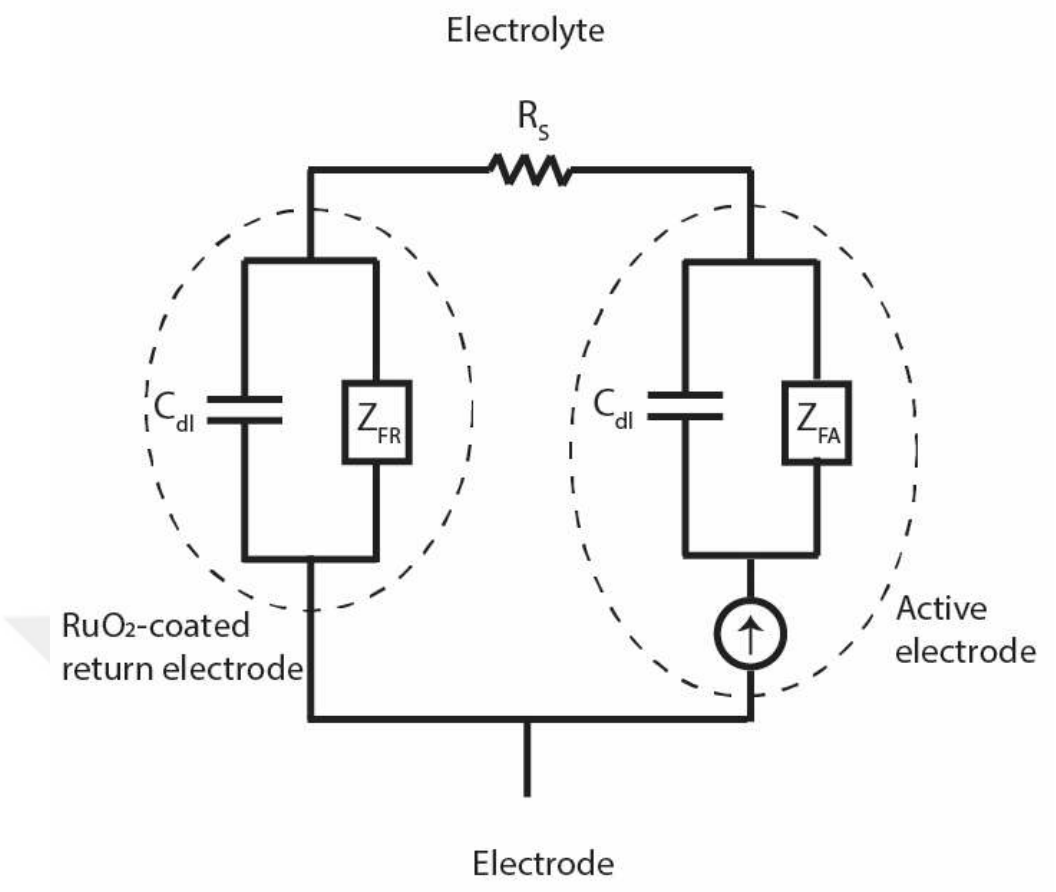


**Figure 51:** Circuit model of the electrode-electrolyte interface. $C_{dl}$ is double layer capacitance, $Z_{FR}$ and $Z_{FA}$ is faradaic impedance of return electrode and active electrode, respectively and $R_S$ is electrolyte resistance. $Z_{FR}$ explains the capacitance and charge transfer properties of $RuO_2$.

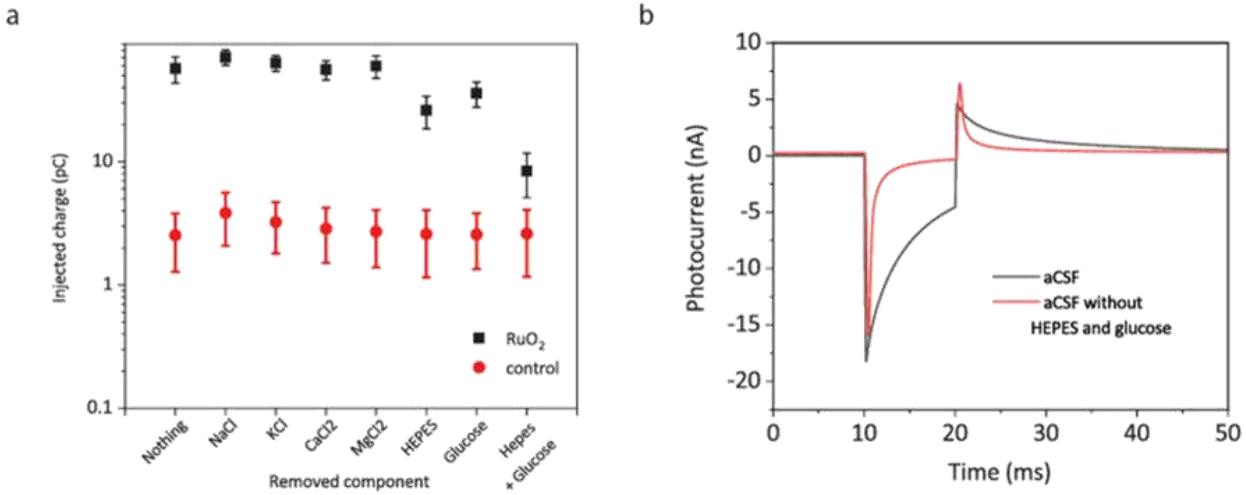


**Figure 52: a)** Injected charge levels of $RuO_2$-coated and control (without $RuO_2$ coating) devices in floating configuration inside modified aCSF solutions, in which one or two ingredients are removed. Injected charge for $RuO_2$ devices significantly decreases when HEPES and glucose is removed from aCSF. **b)** Photocurrent traces of $RuO_2$- biointerface in standard aCSF and aCSF without HEPES and glucose, showing notably diminished charge injection due to the decreased counter-balancing redox reactions at the P3HT:PCBM-electrolyte interface.

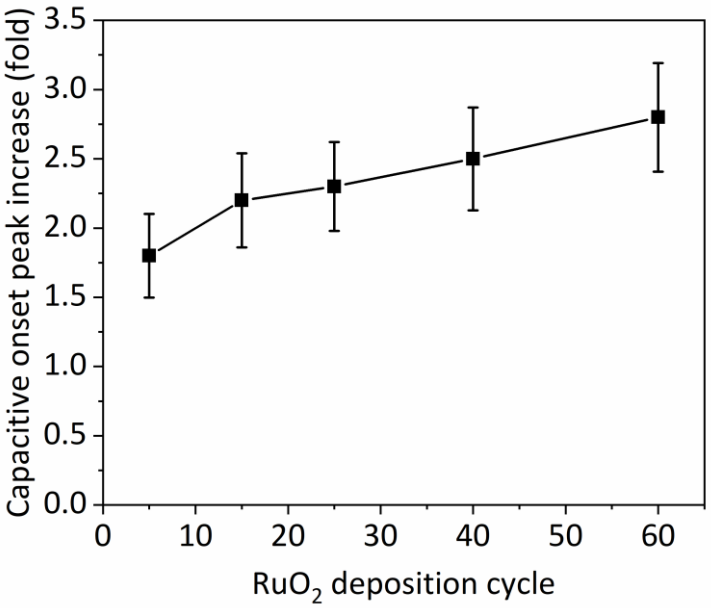


**Figure 53:** Amount of enhancement in the capacitive onset photocurrent peak for $RuO_2$-based biointerfaces with different cycle $RuO_2$ depositions compared to the control sample without $RuO_2$ coating.

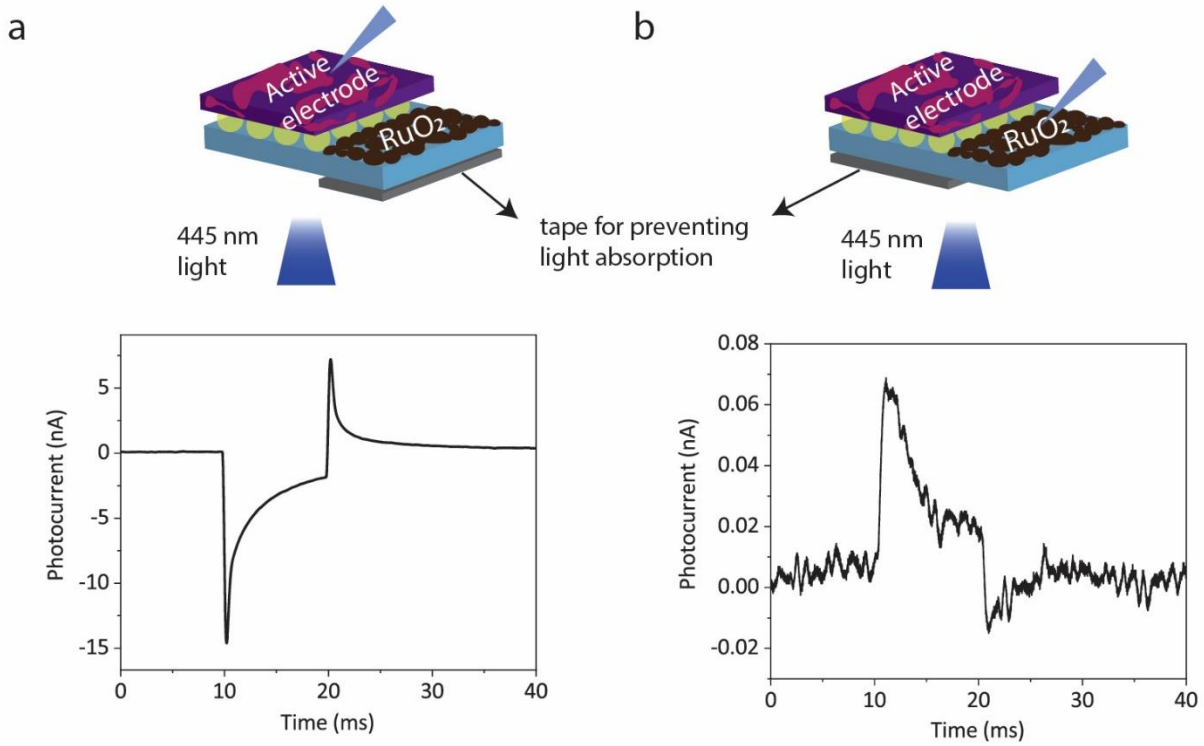


**Figure 54:** Schematic of photocurrent measurements (top) and the resulting photocurrent traces (bottom) when **a)** $RuO_2$-coated area, and **b)** P3HT:PCBM active electrode coated area is covered with a black tape under the substrate. Whole substrate is illuminated in both cases. Stimulation light source is an LED (445 nm nominal wavelength, 2 mW $mm^{-2}$ optical power density, 10 ms pulse-width applied at t = 10 ms; same parameters used in the manuscript), and the recording tool is a patch clamp amplifier with a micropipette that is positioned less

than 5 µm from the biointerface surface. Patch pipettes of 6-8 MΩ resistance were used in the recording to match the same experimental conditions provided in the manuscript. When P3HT:PCBM active electrode side is taped as in (b), very small amount of photocurrent is generated, which indicates the organic active electrode is the main photocurrent generating part in our device architecture.

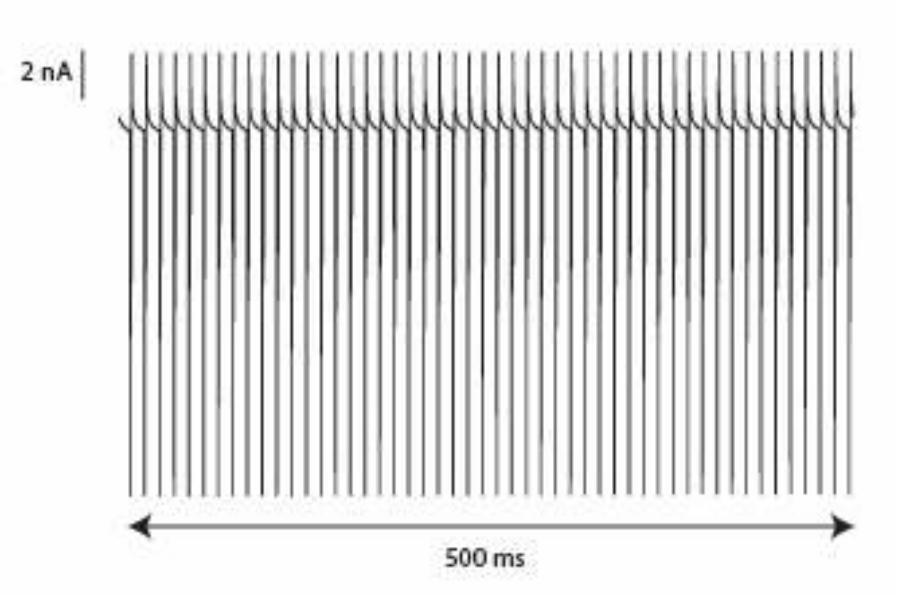


**Figure 55:** Photocurrent response of 60-cycle $RuO_2$ biointerface under 100 Hz stimulus. Illumination: 445 nm LED, 1 ms pulse, 2 mW $mm^{-2}$ light intensity.

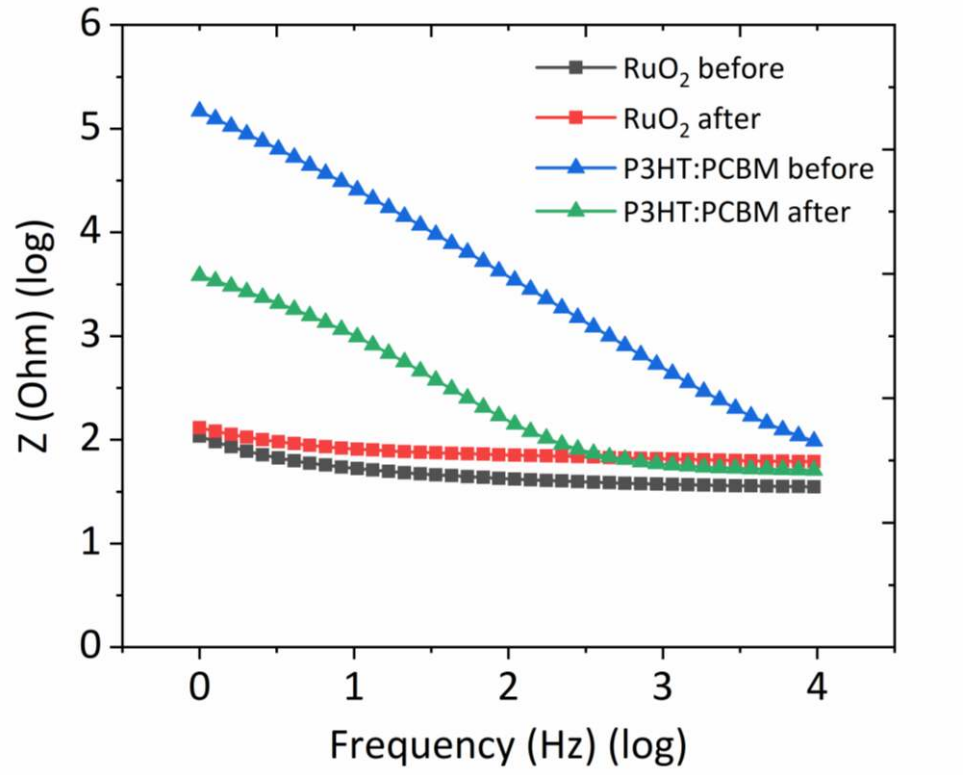


**Figure 56:** Electrochemical impedance measurement of $RuO_2$ coating and P3HT:PCBM coating of $RuO_2$-based biointerfaces before and after subjecting the biointerfaces to low temperature hydrogen peroxide plasma

sterilization followed by reactive accelerated ageing test. The traces are average of three different samples.

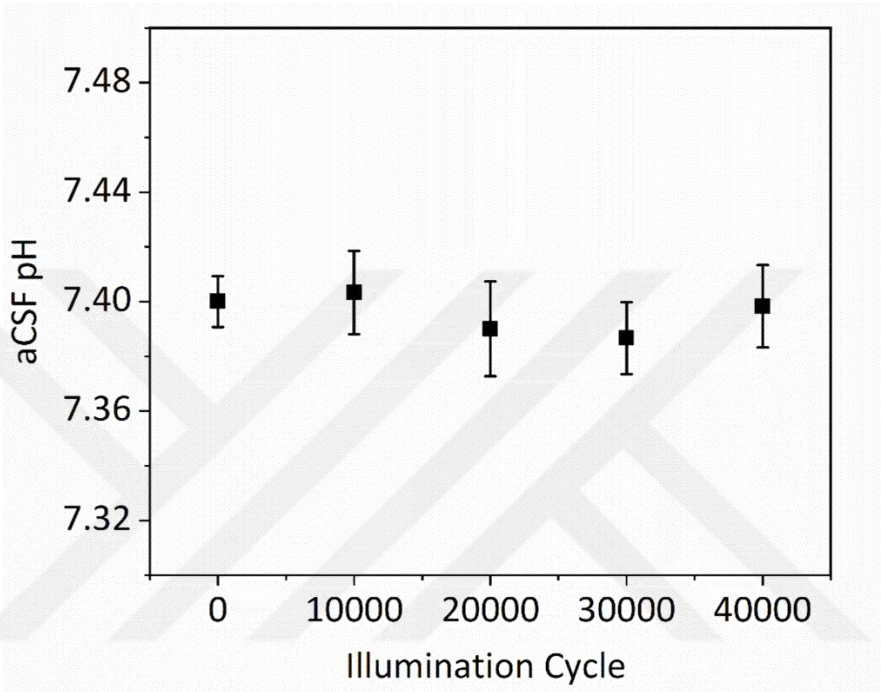


**Figure 57:** Variation of pH of extracellular medium (aCSF) during photoexcitation of $RuO_2$ biointerfaces with hippocampal neurons cultured on (mean ± s.d. for N = 4).

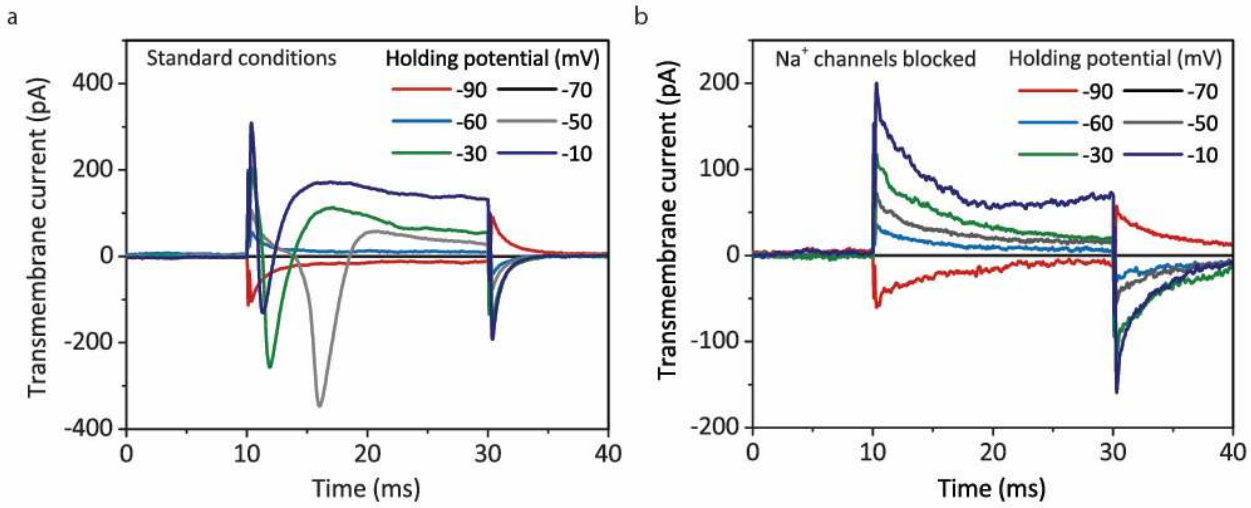


**Figure 58: Voltage-clamp recordings of hippocampal neurons for different holding potentials. a)** Measured transmembrane current for standard conditions, **b)** Transmembrane current when voltage-gated sodium channels are blocked by adding 5 mM QX-314 chloride to intracellular solution.

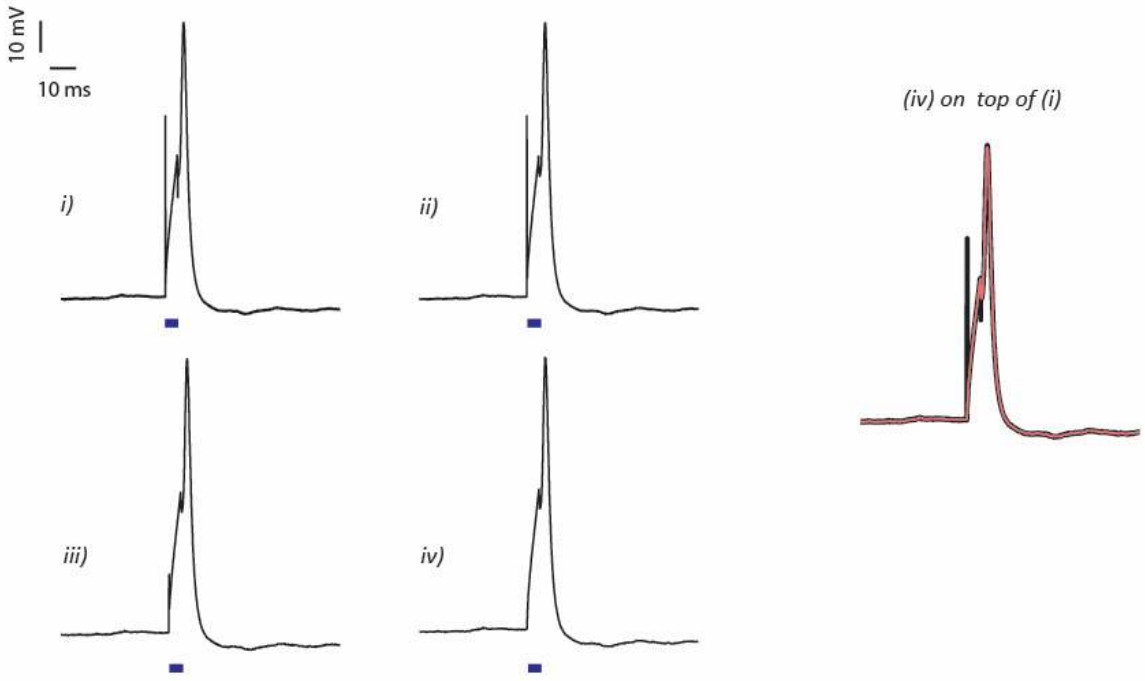


**Figure 59:** Process of filtering out the capacitive artefacts. i) original action potential trace, ii), iii), iv) are the traces after 1, 3, 4 times downsampled traces. Downsampling rate was 2 in all the steps. On the right, original trace and the downsampled trace, which corresponds to the reported traces in the manuscript, were shown on top of each other. The shape and properties of action potential (e.g. latency, peak magnitude, threshold voltage) were preserved after eliminating the artefacts.

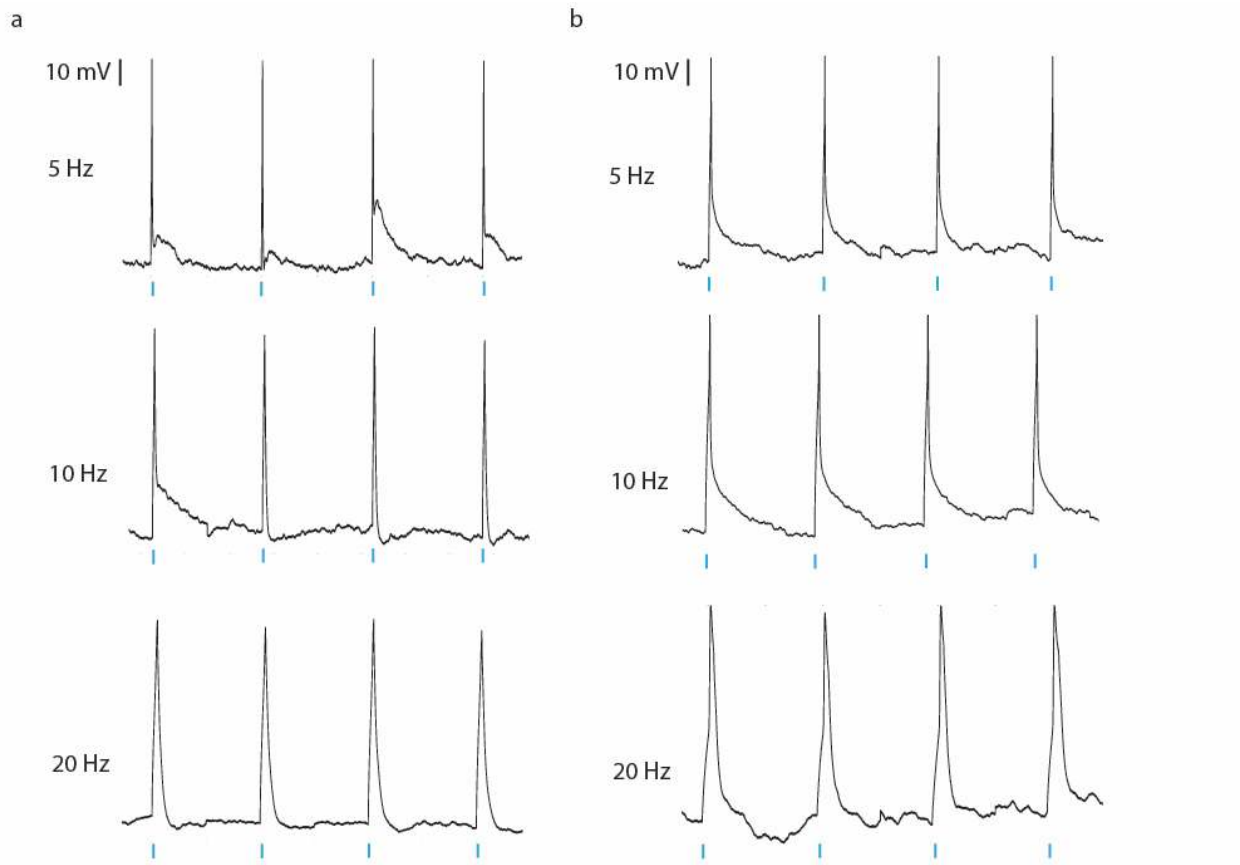


**Figure 60:** Current-clamp recordings of hippocampal neurons cultured on $RuO_2$-based biointerfaces under 5, 10, 20 Hz stimulus with **a)** 10 ms pulse-width, 1.25 mW $mm^{-2}$, **b)** 20 ms pulse-width, 0.65 mW $mm^{-2}$ illumination.

# Appendix D

## Device fabrication

ITO/PET with surface resistivity 60 Ω $sq^{-1}$ (Sigma Aldrich), PbS core-type quantum dots (Sigma Aldrich, $\lambda_{em}$ = 1400 nm, 10 mg $ml^{-1}$ in toluene), Poly (3-hexylthiophene-2,5-diyl) (P3HT) with regioregularity of 95.7% and a molecular weight of 57,467 g $mol^{-1}$ (Ossila), Ruthenium (III) chloride hydrate ($RuCl_3.xH_2O$) with molecular weight of 207.43 g $mol^{-1}$ (Sigma Aldrich), Zinc acetate dehydrate ($Zn(CH_3CO_2)_2 \cdot 2H_2O$) (Sigma Aldrich), 2-Methoxyethanol ($C_3H_5O_2$) (Sigma Aldrich), Ethanolamine ($HOCH_2CH_2NH_2$) (Sigma Aldrich), 1,2-dichlorobenzene ($C_6H_4Cl_2$) were used in the fabrication. Although we use 780 nm excitation in our study, we used a red-shifted QD ($\lambda_{em}$ = 1400 nm) since the absorbance of the QDs increases toward 780 nm due to the additional electronic transitions occurring between conduction and valence bands.

For cleaning, substrates were consecutively sonicated in detergent solution, deionized water, acetone, and isopropanol for 15 min. Dried substrates were subjected to UV ozone treatment for 20 min. Then, ZnO precursor sol-gel solution, which consists of 219.3 mg Zinc acetate dehydrate ($Zn(CH_3CO_2)_2 \cdot 2H_2O$), 2 ml of 2-Methoxyethanol ($C_3H_5O_2$) and 73 mg of Ethanolamine ($HOCH_2CH_2NH_2$), was spin-coated at 2000 rpm and annealed at 200°C for 20 min. PbS QD solution was spin coated at 2000 rpm and annealed at 100°C for 15 min. 20 mg $ml^{-1}$ P3HT solution in 1,2-dichlorobenzene was spin coated at 2000 rpm and annealed at 150°C for 15 min. $RuO_2$ was coated via 60-cycle electrochemical deposition from 0.01 M $RuCl_3.xH_2O$ solution as described in a previous study.[107]

## Photoelectrical characterization

EPC 800 Heka Elektronik patch-clamp amplifier was used for recording open-circuit photoelectrical parameters. Extracellular medium (artificial cerebrospinal fluid (aCSF)) was prepared by mixing 10 mM 4-(2-hydroxyethyl)-1-piperazineethanesulfonic acid (HEPES), 10 mM glucose, 2 mM $CaCl_2$, 140 mM NaCl, 1 mM $MgCl_2$, 3 mM KCl, and stoichiometric amount of NaOH to adjust the pH to 7.4, in distilled water. Intracellular medium was prepared by mixing 140 mM KCl, 2 mM $MgCl_2$, 10 mM HEPES, 10 mM ethylene glycol-bis(β-

aminoethyl ether)-N,N,N',N'-tetraacetic acid (EGTA), 2 mM Mg-ATP, and stoichiometric amount of KOH to adjust the pH to 7.2 - 7.3, in distilled water. Biointerfaces were left floating in aCSF without any wire connection. Patch pipettes were filled with intracellular medium.

Autolab Potentiostat Galvanostat PGSTAT302N (Metrohm, Netherlands) was used for recording short-circuit photocurrent/photovoltage in three-electrode configuration. Back electrode of thin film samples was connected to working electrode. Ag/AgCl reference electrode and platinum counter electrodes were used. Measurements were performed in ionic medium aCSF.

Thorlabs M780LP1 LED was used as the illumination source. Thorlabs DC2200 - High-Power 1-Channel LED Driver was used to adjust the pulse-widths and light-intensities. Optical powers were measured via Newport 843-R power meter.

**Sterilization procedures**

$O_2$ plasma sterilization was applied for 5 min. First and second ethanol rinsing were performed triple times. Overnight sterilization was incubation of the devices in the cell culture medium at 37°C for 24 hours.

**Electrochemical impedance measurement**

Electrochemical impedance spectroscopy (EIS) was performed using Autolab Potentiostat Galvanostat PGSTAT302N (Metrohm, Netherlands) in the same three-electrode configuration described in photoelectrical characterization. The frequency range was 1 Hz – 10 kHz in the EIS measurement and 10 mV (RMS) AC voltage was applied. Measurements were taken in ionic medium aCSF.

**Primary Neuron Isolation**

All experimental procedures have been approved by the Institutional Animal Care and Use Committees of Koç University (Approval No: 2021.HADYEK.022) according to Directive 2010/63/EU of the European Parliament and of the Council on the Protection of Animals Used for Scientific Purposes. Procedures were carried out by responsible veterinarian and certified researchers for animal experiments. Primary hippocampal neuron isolation and culture protocol performed according to our previous studies.[42, 162] Hippocampus of E15-E17 Wistar Albino rat embryos were isolated and placed immediately in ice-cold Hank's Balanced Salt Solution (HBSS, Thermo Fisher Scientific, MA, USA). Enzymatic digestion of the

hippocampus was performed with incubation in %0.25 Trypsin-EDTA solution (Thermo Fisher Scientific, MA, USA) with %2 DNase-I supplement (NeoFroxx, Einhausen, Germany) for 20 minutes in a 37ºC incubator. After digestion, the cells were centrifuged, and the supernatant was changed with Dulbecco's Modified Eagle Medium/Nutrient Mixture F-12 (DMEM/F12 Thermo Fisher Scientific, MA, USA) supplemented with %10 fetal bovine serum (FBS, Heat Inactivated, GE Healthcare, IL, USA) and %1 penicillin/streptomycin (Thermo Fisher Scientific, MA, USA). DMEM/F12 media was discarded and Neurobasal Medium (NBM, Thermo Fisher Scientific, MA, USA) supplemented with B27, L-glutamine, β-mercaptoethanol, glutamate (Thermo Fisher Scientific, MA, USA) was added to the cell pellet. The cells were triturated and were passed through a 70 µm cell strainer. The homogenous cell solution was seeded in poly-D-lysine (PDL, Sigma-Aldrich, MO, USA) coated substrates. After 3-days incubation of cells on substrates, the media of the cells were changed with NBM supplemented with cytosine arabinoside (Sigma-Aldrich, MO, USA) to inhibit growth of glial cells. After 24-hour incubation with cytosine arabinoside, the media were refreshed with NBM and primary hippocampal neurons on the substrates were cultured for further experiments.

**Biocompatibility Assay**

Cell viability of primary hippocampal neurons on the biointerfaces was checked with MTT assay according to our previous studies.[42, 162] Briefly, the biointerface devices were sterilized by 70% ethanol and UV irradiation for 30 min. Biointerfaces were placed in the 6-well plates. Primary hippocampal neurons were seeded on the substrates as $5 \times 10^5$ cells per sample and cultured with in Neurobasal Medium (NBM, Thermo Fisher Scientific, MA, USA) supplemented with B27, L-glutamine, β-mercaptoethanol, glutamate (Thermo Fisher Scientific, MA, USA) at 37 °C with 5% CO2. After 48-h incubation, the cell media replaced with 1 mL of MTT solution (5 mg/mL in PBS, pH = 7.4) and 4 mL of NBM mixture per well and cells were incubated at 37 °C for 4 h. After 4 h incubation, samples were transferred to new six-well plate and 1:1 mixture of DMSO and ethanol added on wells to dissolve the formazan crystals. The solution was transferred to a 96-well plate and the absorbance was measured at at 570 nm light with Synergy H1 Microplate Reader (Bio-Tek Instruments). The relative cell viability was calculated as: Percentage of cell viability = $(OD_{sample}/OD_{control}) \times 100$.

**Immunofluorescence Staining and Imaging**

Primary hippocampal neurons ($5x10^5$ cells per sample) were cultured as explained above on ITO control and the biointerface substrates then allowed for Day 0 and Day 14 growth in an appropriate culture condition. Neurons on the substrates were fixed with 4% paraformaldehyde on Day 0 and Day 14 and washed three times with PBS-T (Phosphate Buffered Saline, 0.1% Triton X-100). Cells were blocked in superblock solution. After blocking, cells on the substrates were incubated with rabbit anti-NeuN antibody (ab177487, Abcam, Cambridge, UK) overnight at 4 °C for neuron characterization, and washed three times with PBS-T. Then, samples were incubated with goat anti-rabbit IgG H&L Alexa Fluor 555 (4413, Cell Signaling Technology, MA, USA) for 90 minutes at 37°C. For visualization of the cytoskeleton, primary neuron samples also were stained with FITC-conjugated phalloidin antibody (Sigma-Aldrich, P5282) for 90 minutes at 37°C. All samples were washed three times with PBS-T, then mounted with DAPI supplemented mounting medium (ab104139, Abcam, Cambridge, UK) to observe nuclei. Immunofluorescence imaging was performed with an inverted fluorescence microscope (Axio Observer Z1, ZEISS, Oberkochen, Germany).

**Electrophysiology recordings**

EPC 800 Heka Elektronik patch-clamp amplifier was used for recording the electrical activity of hippocampal neurons that are cultured on biointerfaces. The current-clamp recordings for transmembrane voltage and voltage-clamp recordings for transmembrane current measurements were performed in whole-cell configuration. No wire is connected to the biointerfaces. aCSF was used as extracellular medium. The patch pipette resistance of 5-8 MΩ was used for the recordings. Patch pipettes were filled with the intracellular medium as described above. For blocking the voltage-gated sodium channels, 5 mM QX-314 chloride was added into the intracellular medium. For the statistical analysis of action potentials, the current clamp data was downsampled without causing changes in the properties of action potentials to conduct the analysis with a feasible computational complexity. A digital camera integrated with the Olympus T2 upright microscope was used for monitoring the neurons and the movement of the patch pipette. Biointerfaces were illuminated from the bottom using M780LP1 Thorlabs LED driven by Thorlabs DC2200 LED driver.

**Optical Safety Considerations**

The maximum permissible radiant power (MPΦ) that can be chronically delivered to the retina was calculated according to the ocular safety standards.[146] Photochemical limit does not apply

in NIR region and the equation for photothermal & photoacoustic limit is $MP\Phi = 6.93 \times 10^{-5} C_T C_E P^{-1}$. $C_T = 10^{0.002(\lambda-700)} = 1.445$ for $\lambda = 780$ nm. $C_E$ was taken as 29.3 W mm$^{-2}$ considering a retinal spot size larger than 1.7 mm in diameter in accordance with a previous study.[144] The equation for the single-pulse limit for the pulse-widths between 0.05 – 70 ms is given as $MP\Phi_{single} = 6.93 \times 10^{-4} C_T C_E t^{-0.25}$. These equations give average irradiance limits and the peak irradiance limits can be calculated from $MP\Phi_{peak} = MP\Phi_{avg} / (t.f)$, where t is pulse duration and f is pulse frequency.

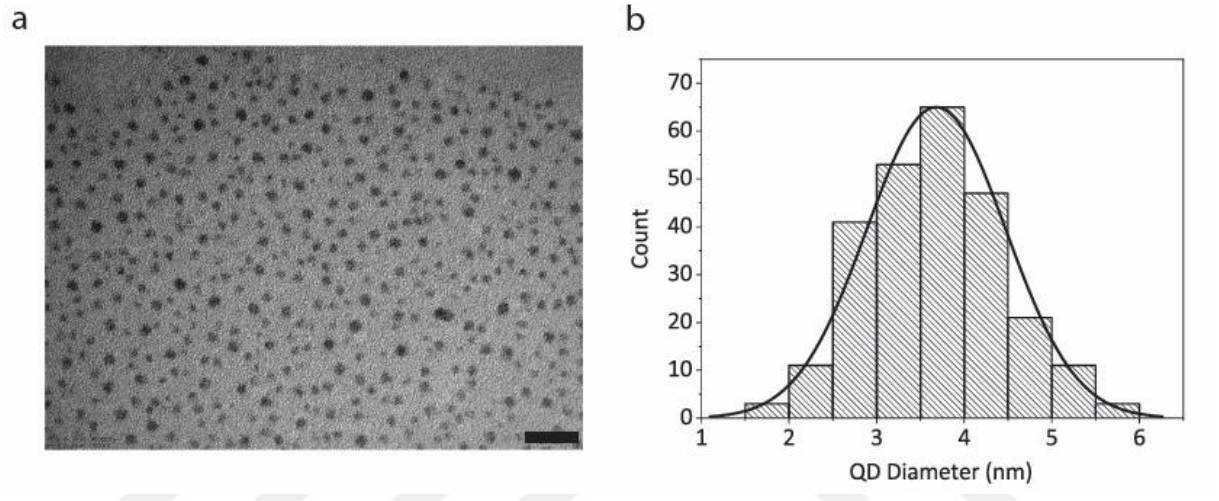


**Figure 61: a)** Transmission electron microscopy (TEM) image of PbS QDs (scale bar is 10 nm), and **b)** the corresponding size distribution (N > 250).

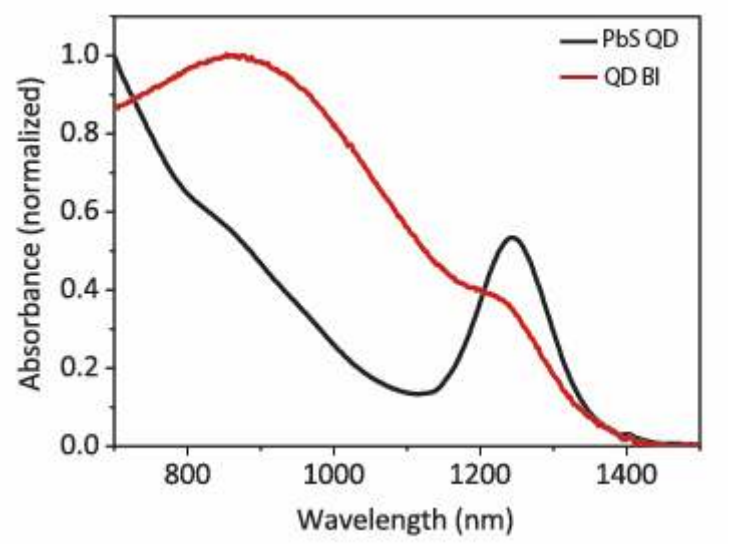


**Figure 62:** Absorbance of PbS QDs in solution and absorbance of the biointerface (QD BI). Normalized absorbance was provided for better comparison.

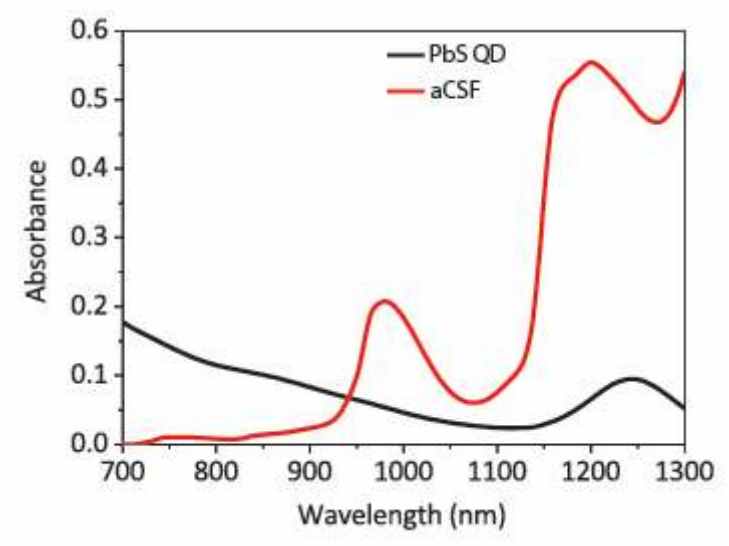


**Figure 63:** Absorbance of PbS QD and aCSF.

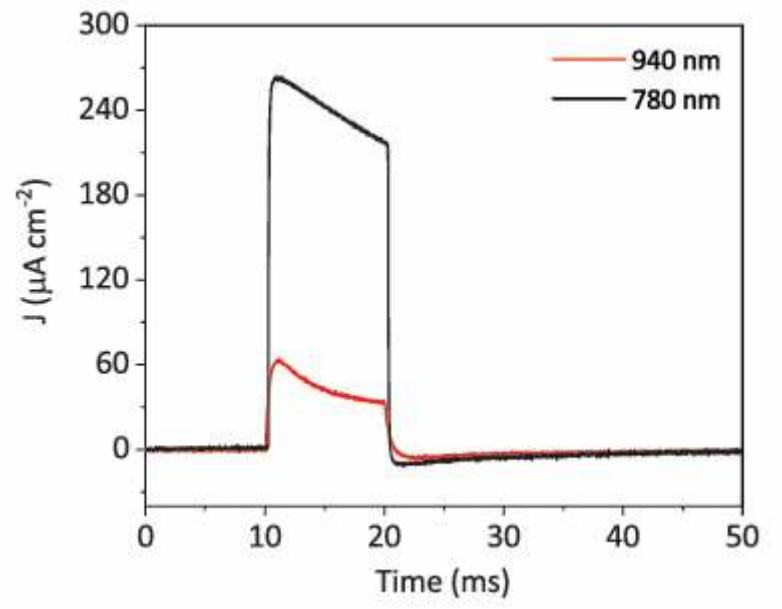


**Figure 64:** Photocurrent density of the biointerface under 780 nm (black), and 940 nm (red) photoexcitation. 10 ms pulse was applied at t = 10 ms. Light intensity was 0.4 mW $mm^{-2}$ in both cases.

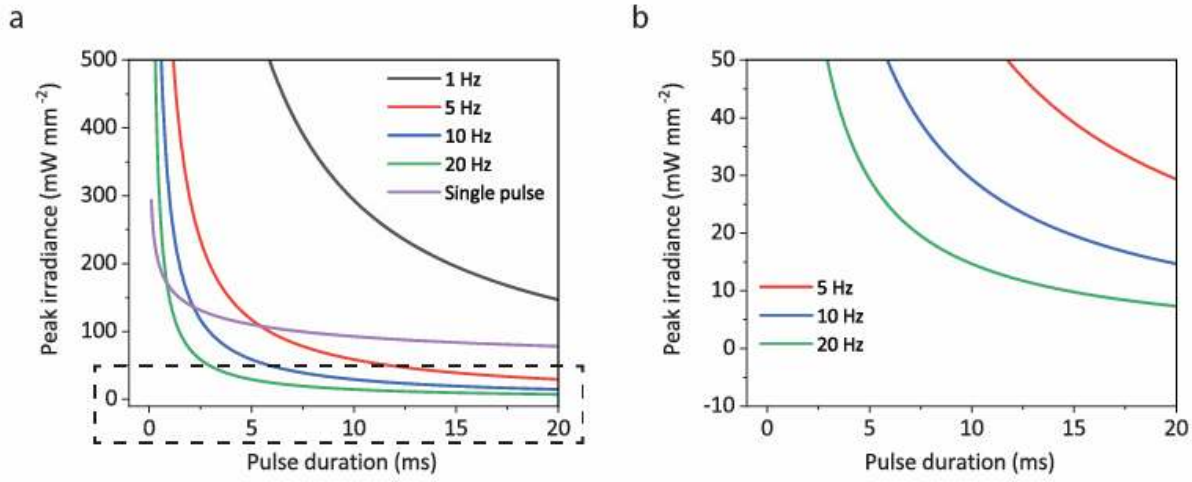


**Figure 65: a)** Maximum permissible exposure limits calculated according to Ocular Safety Standards for 780 nm pulsed light at different pulse-widths and pulse frequencies. **b)** Zoomed view of the dashed rectangle in (a).

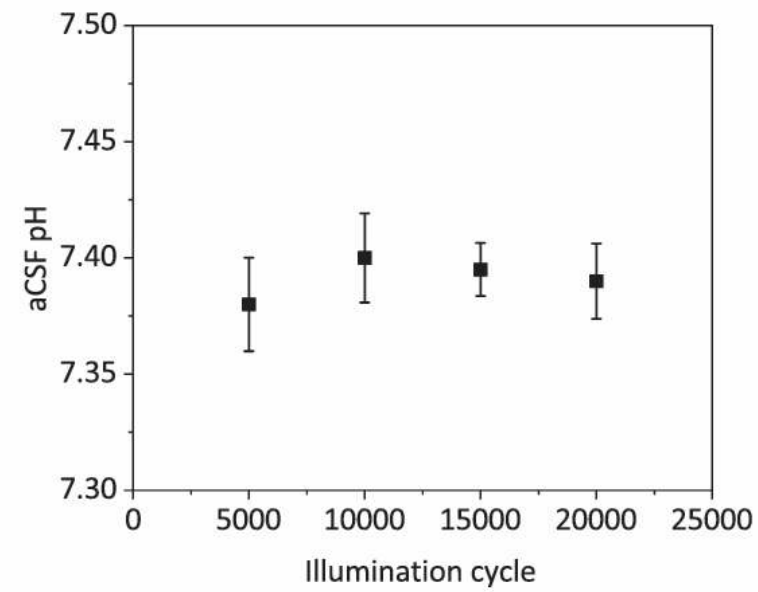


**Figure 66:** Variation of extracellular medium (aCSF) pH during repeated photoexcitation of quantum dot biointerfaces under 780 nm, 7 mW $mm^{-2}$, 10 ms pulse-width, 5 Hz photoexcitation (mean ± s.d. for N = 4).

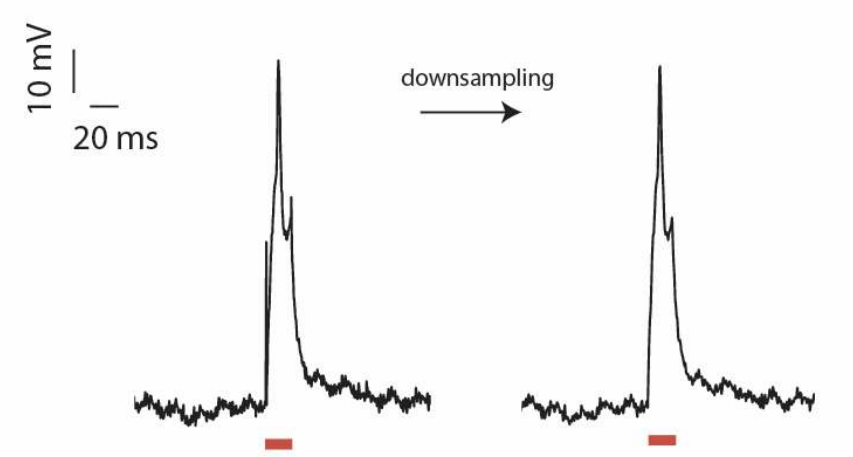


**Figure 67:** The elimination of capacitive artefacts at the light onset and offset because of downsampling of current clamp data. The properties of action potentials (e.g., threshold, latency, jitter) were preserved. Red bars indicate light on periods.

**Bibliography**

(1) Kellaway, P. The part played by electric fish in the early history of bioelectricity and electrotherapy. *Bulletin of the History of Medicine* **1946**, *20* (2), 112-137. Wu, C. H. Electric fish and the discovery of animal electricity: the mystery of the electric fish motivated research into electricity and was instrumental in the emergence of electrophysiology. *American Scientist* **1984**, *72* (6), 598-607.
(2) Priori, A. Brain polarization in humans: a reappraisal of an old tool for prolonged non-invasive modulation of brain excitability. *Clinical neurophysiology* **2003**, *114* (4), 589-595.
(3) Dubljević, V.; Saigle, V.; Racine, E. The rising tide of tDCS in the media and academic literature. *Neuron* **2014**, *82* (4), 731-736.
(4) Sironi, V. A. Origin and evolution of deep brain stimulation. *Frontiers in integrative neuroscience* **2011**, *5*, 42.
(5) Galvani, L. De viribus electricitatis in motu musculari. Commentarius. *De Bonoiensi Scientiarum et Artium Intituo atque Academie Commentarii* **1791**, *7*, 363-418.
(6) Verkhratsky, A.; Krishtal, O. A.; Petersen, O. H. From Galvani to patch clamp: the development of electrophysiology. *Pflügers Archiv* **2006**, *453* (3), 233-247.
(7) Krause, F. *Chirurgie des Gehirns und Rückenmarks nach eigenen Erfahrungen*; Urban & Schwarzenberg, 1908.
(8) Penfield, W.; Boldrey, E. Somatic motor and sensory representation in the cerebral cortex of man as studied by electrical stimulation. *Brain* **1937**, *60* (4), 389-443. Penfield, W.; Rasmussen, T. The cerebral cortex of man; a clinical study of localization of function. **1950**.
(9) Li, Y.; Mogul, D. J. Electrical control of epileptic seizures. *Journal of Clinical Neurophysiology* **2007**, *24* (2), 197-204. Perlmutter, J. S.; Mink, J. W. Deep brain stimulation. *Annu. Rev. Neurosci.* **2006**, *29*, 229-257. Normann, R. A. Technology insight: future neuroprosthetic therapies for disorders of the nervous system. *Nature Clinical Practice Neurology* **2007**, *3* (8), 444-452.
(10) Dougherty, D. D. Deep brain stimulation: clinical applications. *Psychiatric Clinics of North America* **2018**, *41* (3), 385-394. Connolly, K. R.; Helmer, A.; Cristancho, M. A.; Cristancho, P.; John, P. Effectiveness of transcranial magnetic stimulation in clinical practice post-FDA approval in the United States: results observed with the first 100 consecutive cases of depression at an academic medical center. *The Journal of clinical psychiatry* **2012**, *73* (4), 0-0.
(11) Hodgkin, A. L.; Huxley, A. F. A quantitative description of membrane current and its application to conduction and excitation in nerve. *The Journal of physiology* **1952**, *117* (4), 500.
(12) Harvey, E. N. The effect of high frequency sound waves on heart muscle and other irritable tissues. *American Journal of Physiology-Legacy Content* **1929**, *91* (1), 284-290. Wood, R. W.; Loomis, A. L. XXXVIII. The physical and biological effects of high-frequency sound-waves of great intensity. *The London, Edinburgh, and Dublin Philosophical Magazine and Journal of Science* **1927**, *4* (22), 417-436. DOI: 10.1080/14786440908564348.
(13) Lynn, J. G.; Zwemer, R. L.; Chick, A. J.; Miller, A. E. A new method for the generation and use of focused ultrasound in experimental biology. *The Journal of general physiology* **1942**, *26* (2), 179. Lynn, J. G.; Putnam, T. J. Histology of cerebral lesions produced by focused ultrasound. *The American journal of*

*pathology* **1944**, *20* (3), 637. Fry, W. J.; Fry, F.; Barnard, J.; Krumins, R.; Brennan, J. Ultrasonic lesions in mammalian central nervous system. *Science* **1955**, *122* (3179), 1091-1091. FRY, F. J. Precision high intensity focusing ultrasonic machines for surgery. *American Journal of Physical Medicine & Rehabilitation* **1958**, *37* (3), 152-156. Fry, F.; Ades, H.; Fry, W. Production of reversible changes in the central nervous system by ultrasound. *Science* **1958**, *127* (3289), 83-84.
(14) Ciofani, G.; Danti, S.; D'Alessandro, D.; Ricotti, L.; Moscato, S.; Bertoni, G.; Falqui, A.; Berrettini, S.; Petrini, M.; Mattoli, V. Enhancement of neurite outgrowth in neuronal-like cells following boron nitride nanotube-mediated stimulation. *ACS nano* **2010**, *4* (10), 6267-6277. Marino, A.; Arai, S.; Hou, Y.; Sinibaldi, E.; Pellegrino, M.; Chang, Y.-T.; Mazzolai, B.; Mattoli, V.; Suzuki, M.; Ciofani, G. Piezoelectric nanoparticle-assisted wireless neuronal stimulation. *ACS nano* **2015**, *9* (7), 7678-7689.
(15) Ibsen, S.; Tong, A.; Schutt, C.; Esener, S.; Chalasani, S. H. Sonogenetics is a non-invasive approach to activating neurons in Caenorhabditis elegans. *Nature communications* **2015**, *6* (1), 1-12.
(16) Nagel, G.; Szellas, T.; Huhn, W.; Kateriya, S.; Adeishvili, N.; Berthold, P.; Ollig, D.; Hegemann, P.; Bamberg, E. Channelrhodopsin-2, a directly light-gated cation-selective membrane channel. *Proceedings of the National Academy of Sciences* **2003**, *100* (24), 13940-13945.
(17) Deisseroth, K. Optogenetics. *Nature methods* **2011**, *8* (1), 26-29. Yizhar, O.; Fenno, L. E.; Davidson, T. J.; Mogri, M.; Deisseroth, K. Optogenetics in neural systems. *Neuron* **2011**, *71* (1), 9-34. Deisseroth, K. Optogenetics: 10 years of microbial opsins in neuroscience. *Nature neuroscience* **2015**, *18* (9), 1213-1225.
(18) Boyden, E. S.; Zhang, F.; Bamberg, E.; Nagel, G.; Deisseroth, K. Millisecond-timescale, genetically targeted optical control of neural activity. *Nature neuroscience* **2005**, *8* (9), 1263-1268.
(19) Feng, K.; Sen, R.; Minegishi, R.; Dübbert, M.; Bockemühl, T.; Büschges, A.; Dickson, B. J. Distributed control of motor circuits for backward walking in Drosophila. *Nature communications* **2020**, *11* (1), 1-17.
(20) Musso, P.-Y.; Junca, P.; Jelen, M.; Feldman-Kiss, D.; Zhang, H.; Chan, R. C.; Gordon, M. D. Closed-loop optogenetic activation of peripheral or central neurons modulates feeding in freely moving Drosophila. *Elife* **2019**, *8*.
(21) Lak, A.; Okun, M.; Moss, M. M.; Gurnani, H.; Farrell, K.; Wells, M. J.; Reddy, C. B.; Kepecs, A.; Harris, K. D.; Carandini, M. Dopaminergic and prefrontal basis of learning from sensory confidence and reward value. *Neuron* **2020**, *105* (4), 700-711. e706.
(22) Guo, Z. V.; Li, N.; Huber, D.; Ophir, E.; Gutnisky, D.; Ting, J. T.; Feng, G.; Svoboda, K. Flow of cortical activity underlying a tactile decision in mice. *Neuron* **2014**, *81* (1), 179-194.
(23) Liu, X.; Ramirez, S.; Pang, P. T.; Puryear, C. B.; Govindarajan, A.; Deisseroth, K.; Tonegawa, S. Optogenetic stimulation of a hippocampal engram activates fear memory recall. *Nature* **2012**, *484* (7394), 381-385.
(24) Tanaka, R.; Higuchi, T.; Kohatsu, S.; Sato, K.; Yamamoto, D. Optogenetic activation of the fruitless-labeled circuitry in Drosophila subobscura males induces mating motor acts. *Journal of Neuroscience* **2017**, *37* (48), 11662-11674.
(25) Stamatakis, A. M.; Stuber, G. D. Optogenetic strategies to dissect the neural circuits that underlie reward and addiction. *Cold Spring Harbor Perspectives in Medicine* **2012**, *2* (11), a011924.
(26) Han, X.; Boyden, E. S. Multiple-color optical activation, silencing, and desynchronization of neural activity, with single-spike temporal resolution. *PloS one* **2007**, *2* (3), e299. Zhang, F.; Wang, L.-P.; Brauner, M.; Liewald, J. F.; Kay, K.;

Watzke, N.; Wood, P. G.; Bamberg, E.; Nagel, G.; Gottschalk, A. Multimodal fast optical interrogation of neural circuitry. *Nature* **2007**, *446* (7136), 633-639.
(27) Lin, J. Y.; Knutsen, P. M.; Muller, A.; Kleinfeld, D.; Tsien, R. Y. ReaChR: a red-shifted variant of channelrhodopsin enables deep transcranial optogenetic excitation. *Nature neuroscience* **2013**, *16* (10), 1499-1508. Chuong, A. S.; Miri, M. L.; Busskamp, V.; Matthews, G. A.; Acker, L. C.; Sørensen, A. T.; Young, A.; Klapoetke, N. C.; Henninger, M. A.; Kodandaramaiah, S. B. Noninvasive optical inhibition with a red-shifted microbial rhodopsin. *Nature neuroscience* **2014**, *17* (8), 1123-1129.
(28) Sahel, J.-A.; Boulanger-Scemama, E.; Pagot, C.; Arleo, A.; Galluppi, F.; Martel, J. N.; Esposti, S. D.; Delaux, A.; de Saint Aubert, J.-B.; de Montleau, C. Partial recovery of visual function in a blind patient after optogenetic therapy. *Nature Medicine* **2021**, *27* (7), 1223-1229.
(29) Hart, W. L.; Kameneva, T.; Wise, A. K.; Stoddart, P. R. Biological considerations of optical interfaces for neuromodulation. *Advanced Optical Materials* **2019**, *7* (19), 1900385. Shen, Y.; Campbell, R. E.; Côté, D. C.; Paquet, M.-E. Challenges for therapeutic applications of opsin-based optogenetic tools in humans. *Frontiers in neural circuits* **2020**, *14*, 41.
(30) Yu, N.; Huang, L.; Zhou, Y.; Xue, T.; Chen, Z.; Han, G. Near-infrared-light activatable nanoparticles for deep-tissue-penetrating wireless optogenetics. *Advanced healthcare materials* **2019**, *8* (6), 1801132.
(31) Chen, S.; Weitemier, A. Z.; Zeng, X.; He, L.; Wang, X.; Tao, Y.; Huang, A. J.; Hashimotodani, Y.; Kano, M.; Iwasaki, H. Near-infrared deep brain stimulation via upconversion nanoparticle–mediated optogenetics. *Science* **2018**, *359* (6376), 679-684.
(32) Shapiro, M. G.; Homma, K.; Villarreal, S.; Richter, C.-P.; Bezanilla, F. Infrared light excites cells by changing their electrical capacitance. *Nature communications* **2012**, *3* (1), 1-11.
(33) Carvalho-de-Souza, J. L.; Treger, J. S.; Dang, B.; Kent, S. B.; Pepperberg, D. R.; Bezanilla, F. Photosensitivity of neurons enabled by cell-targeted gold nanoparticles. *Neuron* **2015**, *86* (1), 207-217. Jiang, Y.; Carvalho-de-Souza, J. L.; Wong, R. C.; Luo, Z.; Isheim, D.; Zuo, X.; Nicholls, A. W.; Jung, I. W.; Yue, J.; Liu, D.-J. Heterogeneous silicon mesostructures for lipid-supported bioelectric interfaces. *Nature materials* **2016**, *15* (9), 1023-1030.
(34) Lyu, Y.; Xie, C.; Chechetka, S. A.; Miyako, E.; Pu, K. Semiconducting polymer nanobioconjugates for targeted photothermal activation of neurons. *Journal of the American Chemical Society* **2016**, *138* (29), 9049-9052.
(35) Rastogi, S. K.; Garg, R.; Scopelliti, M. G.; Pinto, B. I.; Hartung, J. E.; Kim, S.; Murphey, C. G.; Johnson, N.; San Roman, D.; Bezanilla, F. Remote nongenetic optical modulation of neuronal activity using fuzzy graphene. *Proceedings of the National Academy of Sciences* **2020**, *117* (24), 13339-13349. Wu, X.; Jiang, Y.; Rommelfanger, N. J.; Yang, F.; Zhou, Q.; Yin, R.; Liu, J.; Cai, S.; Ren, W.; Shin, A. Tether-free photothermal deep-brain stimulation in freely behaving mice via wide-field illumination in the near-infrared-II window. *Nature Biomedical Engineering* **2022**, 1-17.
(36) Shi, L.; Jiang, Y.; Fernandez, F. R.; Chen, G.; Lan, L.; Man, H.-Y.; White, J. A.; Cheng, J.-X.; Yang, C. Non-genetic photoacoustic stimulation of single neurons by a tapered fiber optoacoustic emitter. *Light: Science & Applications* **2021**, *10* (1), 1-13.
(37) Plaksin, M.; Shoham, S.; Kimmel, E. Intramembrane cavitation as a predictive bio-piezoelectric mechanism for ultrasonic brain stimulation. *Physical review X* **2014**, *4* (1), 011004.

(38) Yoo, S.; Mittelstein, D. R.; Hurt, R. C.; Lacroix, J.; Shapiro, M. G. Focused ultrasound excites cortical neurons via mechanosensitive calcium accumulation and ion channel amplification. *Nature communications* **2022**, *13* (1), 1-13.
(39) Jiang, Y.; Huang, Y.; Luo, X.; Wu, J.; Zong, H.; Shi, L.; Cheng, R.; Zhu, Y.; Jiang, S.; Lan, L. Neural stimulation in vitro and in vivo by photoacoustic nanotransducers. *Matter* **2021**, *4* (2), 654-674.
(40) Lai, B.-C.; Wu, J.-G.; Luo, S.-C. Revisiting background signals and the electrochemical windows of Au, Pt, and GC electrodes in biological buffers. *ACS Applied Energy Materials* **2019**, *2* (9), 6808-6816.
(41) Kumsa, D. W.; Bhadra, N.; Hudak, E. M.; Kelley, S. C.; Untereker, D. F.; Mortimer, J. T. Electron transfer processes occurring on platinum neural stimulating electrodes: a tutorial on the i (Ve) profile. *Journal of Neural Engineering* **2016**, *13* (5), 052001.
(42) Karatum, O.; Aria, M. M.; Eren, G. O.; Yildiz, E.; Melikov, R.; Srivastava, S. B.; Surme, S.; Dogru, I. B.; Bahmani Jalali, H.; Ulgut, B. Nanoengineering InP quantum dot-based photoactive biointerfaces for optical control of neurons. *Frontiers in neuroscience* **2021**, 724.
(43) Benabid, A. L. Deep brain stimulation for Parkinson's disease. *Current opinion in neurobiology* **2003**, *13* (6), 696-706. Mayberg, H. S.; Lozano, A. M.; Voon, V.; McNeely, H. E.; Seminowicz, D.; Hamani, C.; Schwalb, J. M.; Kennedy, S. H. Deep brain stimulation for treatment-resistant depression. *Neuron* **2005**, *45* (5), 651-660. Sada, N.; Lee, S.; Katsu, T.; Otsuki, T.; Inoue, T. Targeting LDH enzymes with a stiripentol analog to treat epilepsy. *Science* **2015**, *347* (6228), 1362-1367. DOI: 10.1126/science.aaa1299.
(44) Bahmani Jalali, H.; Sadeghi, S.; Sahin, M.; Ozturk, H.; Ow-Yang, C. W.; Nizamoglu, S. Colloidal Aluminum Antimonide Quantum Dots. *Chemistry of Materials* **2019**, *31* (13), 4743-4747. DOI: 10.1021/acs.chemmater.9b00905.
(45) Chen, B.; Li, D.; Wang, F. InP Quantum Dots: Synthesis and Lighting Applications. *Small* **2020**, e2002454. DOI: 10.1002/smll.202002454.
(46) Bharali, D. J.; Lucey, D. W.; Jayakumar, H.; Pudavar, H. E.; Prasad, P. N. Folate-receptor-mediated delivery of InP quantum dots for bioimaging using confocal and two-photon microscopy. *J Am Chem Soc* **2005**, *127* (32), 11364-11371. DOI: 10.1021/ja051455x.
(47) Xie, R.; Battaglia, D.; Peng, X. Colloidal InP Nanocrystals as Efficient Emitters Covering Blue to Near-Infrared. *Journal of the American Chemical Society* **2007**, *129* (50), 15432-15433. DOI: 10.1021/ja076363h. Tamang, S.; Lincheneau, C.; Hermans, Y.; Jeong, S.; Reiss, P. Chemistry of InP nanocrystal syntheses. *Chemistry of Materials* **2016**, *28* (8), 2491-2506.
(48) Yong, K.-T.; Ding, H.; Roy, I.; Law, W.-C.; Bergey, E. J.; Maitra, A.; Prasad, P. N. Imaging Pancreatic Cancer Using Bioconjugated InP Quantum Dots. *ACS Nano* **2009**, *3* (3), 502-510. DOI: 10.1021/nn8008933.
(49) Wegner, K. D.; Dussert, F.; Truffier-Boutry, D.; Benayad, A.; Beal, D.; Mattera, L.; Ling, W. L.; Carrière, M.; Reiss, P. Influence of the core/shell structure of indium phosphide based quantum dots on their photostability and cytotoxicity. *Frontiers in chemistry* **2019**, *7*, 466.
(50) Bahmani Jalali, H.; Melikov, R.; Sadeghi, S.; Nizamoglu, S. Excitonic Energy Transfer within InP/ZnS Quantum Dot Langmuir-Blodgett Assemblies. *J Phys Chem C Nanomater Interfaces* **2018**, *122* (22), 11616-11622. DOI: 10.1021/acs.jpcc.8b00744.
(51) Chibli, H.; Carlini, L.; Park, S.; Dimitrijevic, N. M.; Nadeau, J. L. Cytotoxicity of InP/ZnS quantum dots related to reactive oxygen species generation. *Nanoscale* **2011**, *3* (6), 2552-2559.

(52) Pattantyus-Abraham, A. G.; Kramer, I. J.; Barkhouse, A. R.; Wang, X.; Konstantatos, G.; Debnath, R.; Levina, L.; Raabe, I.; Nazeeruddin, M. K.; Gratzel, M. Depleted-heterojunction colloidal quantum dot solar cells. *ACS nano* **2010**, *4* (6), 3374-3380. Yang, X.; Zhao, D.; Leck, K. S.; Tan, S. T.; Tang, Y. X.; Zhao, J.; Demir, H. V.; Sun, X. W. Full visible range covering InP/ZnS nanocrystals with high photometric performance and their application to white quantum dot light-emitting diodes. *Adv Mater* **2012**, *24* (30), 4180-4185. DOI: 10.1002/adma.201104990.
(53) Karatum, O.; Jalali, H. B.; Sadeghi, S.; Melikov, R.; Srivastava, S. B.; Nizamoglu, S. Light-Emitting Devices Based on Type-II InP/ZnO Quantum Dots. *ACS Photonics* **2019**, *6* (4), 939-946.
(54) Lacour, S. P.; Benmerah, S.; Tarte, E.; FitzGerald, J.; Serra, J.; McMahon, S.; Fawcett, J.; Graudejus, O.; Yu, Z.; Morrison, B. Flexible and stretchable micro-electrodes for in vitro and in vivo neural interfaces. *Medical & biological engineering & computing* **2010**, *48* (10), 945-954. Williamson, A.; Ferro, M.; Leleux, P.; Ismailova, E.; Kaszas, A.; Doublet, T.; Quilichini, P.; Rivnay, J.; Rózsa, B.; Katona, G. Localized neuron stimulation with organic electrochemical transistors on delaminating depth probes. *Advanced Materials* **2015**, *27* (30), 4405-4410.
(55) Merrill, D. R.; Bikson, M.; Jefferys, J. G. Electrical stimulation of excitable tissue: design of efficacious and safe protocols. *J Neurosci Methods* **2005**, *141* (2), 171-198. DOI: 10.1016/j.jneumeth.2004.10.020.
(56) Han, M.; Srivastava, S. B.; Yildiz, E.; Melikov, R.; Surme, S.; Dogru-Yuksel, I. B.; Kavakli, I. H.; Sahin, A.; Nizamoglu, S. Organic Photovoltaic Pseudocapacitors for Neurostimulation. *ACS applied materials & interfaces* **2020**, *12* (38), 42997-43008.
(57) Ciocca, M.; Giannakou, P.; Mariani, P.; Cinà, L.; Di Carlo, A.; Tas, M. O.; Asari, H.; Marcozzi, S.; Camaioni, A.; Shkunov, M. Colour-sensitive conjugated polymer inkjet-printed pixelated artificial retina model studied via a bio-hybrid photovoltaic device. *Scientific reports* **2020**, *10* (1), 1-15.
(58) Jakešová, M.; Ejneby, M. S.; Đerek, V.; Schmidt, T.; Gryszel, M.; Brask, J.; Schindl, R.; Simon, D. T.; Berggren, M.; Elinder, F. Optoelectronic control of single cells using organic photocapacitors. *Science advances* **2019**, *5* (4), eaav5265.
(59) Bahmani Jalali, H.; Karatum, O.; Melikov, R.; Dikbas, U. M.; Sadeghi, S.; Yildiz, E.; Dogru, I. B.; Ozgun Eren, G.; Ergun, C.; Sahin, A.; et al. Biocompatible Quantum Funnels for Neural Photostimulation. *Nano Lett* **2019**, *19* (9), 5975-5981. DOI: 10.1021/acs.nanolett.9b01697.
(60) Bahmani Jalali, H.; Mohammadi Aria, M.; Dikbas, U. M.; Sadeghi, S.; Ganesh Kumar, B.; Sahin, M.; Kavakli, I. H.; Ow-Yang, C. W.; Nizamoglu, S. Effective neural photostimulation using indium-Based type-II quantum dots. *ACS nano* **2018**, *12* (8), 8104-8114.
(61) Cogan, S. F. Neural stimulation and recording electrodes. *Annu Rev Biomed Eng* **2008**, *10*, 275-309. DOI: 10.1146/annurev.bioeng.10.061807.160518.
(62) Bareket, L.; Waiskopf, N.; Rand, D.; Lubin, G.; David-Pur, M.; Ben-Dov, J.; Roy, S.; Eleftheriou, C.; Sernagor, E.; Cheshnovsky, O.; et al. Semiconductor nanorod-carbon nanotube biomimetic films for wire-free photostimulation of blind retinas. *Nano Lett* **2014**, *14* (11), 6685-6692. DOI: 10.1021/nl5034304.
(63) Gautam, V.; Rand, D.; Hanein, Y.; Narayan, K. A polymer optoelectronic interface provides visual cues to a blind retina. *Advanced Materials* **2014**, *26* (11), 1751-1756.
(64) Leccardi, M. J. I. A.; Chenais, N. A. L.; Ferlauto, L.; Kawecki, M.; Zollinger, E. G.; Ghezzi, D. Photovoltaic organic interface for neuronal stimulation in the near-infrared. *Communications Materials* **2020**, *1* (1), 1-13.

(65) Johnston, K. W.; Pattantyus-Abraham, A. G.; Clifford, J. P.; Myrskog, S. H.; Hoogland, S.; Shukla, H.; Klem, E. J.; Levina, L.; Sargent, E. H. Efficient Schottky-quantum-dot photovoltaics: The roles of depletion, drift, and diffusion. *Applied Physics Letters* **2008**, *92* (12), 122111. Krishnan, C.; Mercier, T.; Rahman, T.; Piana, G.; Brossard, M.; Yagafarov, T.; To, A.; Pollard, M. E.; Shaw, P.; Bagnall, D. M. Efficient light harvesting in hybrid quantum dot–interdigitated back contact solar cells via resonant energy transfer and luminescent downshifting. *Nanoscale* **2019**, *11* (40), 18837-18844. Yang, Y.; Zhang, Z.-G.; Bin, H.; Chen, S.; Gao, L.; Xue, L.; Yang, C.; Li, Y. Side-chain isomerization on an n-type organic semiconductor ITIC acceptor makes 11.77% high efficiency polymer solar cells. *Journal of the American Chemical Society* **2016**, *138* (45), 15011-15018.
(66) Kramer, I. J.; Sargent, E. H. The architecture of colloidal quantum dot solar cells: materials to devices. *Chem Rev* **2014**, *114* (1), 863-882. DOI: 10.1021/cr400299t.
(67) Melikov, R.; Srivastava, S. B.; Karatum, O.; Dogru, I. B.; Jalali, H. B.; Sadeghi, S.; Dikbas, U. M.; Ulgut, B.; Kavakli, I. H.; Nizamoglu, S. Plasmon-Coupled Photocapacitor Neuromodulators. *bioRxiv* **2020**, 2020.2002.2018.953604. DOI: 10.1101/2020.02.18.953604.
(68) Chang, L. Y.; Lunt, R. R.; Brown, P. R.; Bulovic, V.; Bawendi, M. G. Low-temperature solution-processed solar cells based on PbS colloidal quantum dot/CdS heterojunctions. *Nano Lett* **2013**, *13* (3), 994-999. DOI: 10.1021/nl3041417.
(69) Willis, S. M.; Cheng, C.; Assender, H. E.; Watt, A. A. The transitional heterojunction behavior of PbS/ZnO colloidal quantum dot solar cells. *Nano Lett* **2012**, *12* (3), 1522-1526. DOI: 10.1021/nl204323j.
(70) Ferlauto, L.; Leccardi, M. J. I. A.; Chenais, N. A. L.; Gilliéron, S. C. A.; Vagni, P.; Bevilacqua, M.; Wolfensberger, T. J.; Sivula, K.; Ghezzi, D. Design and validation of a foldable and photovoltaic wide-field epiretinal prosthesis. *Nature communications* **2018**, *9* (1), 1-15. Han, M.; Jalali, H. B.; Yildiz, E.; Qureshi, M. H.; Şahin, A.; Nizamoglu, S. Photovoltaic neurointerface based on aluminum antimonide nanocrystals. *Communications Materials* **2021**, *2* (1), 1-10.
(71) Li, L.; Chen, Y.; Xu, G.; Liu, D.; Yang, Z.; Chen, T.; Wang, X.; Jiang, W.; Xue, D.; Lin, G. In vivo comparison of the biodistribution and toxicity of InP/ZnS quantum dots with different surface modifications. *International journal of nanomedicine* **2020**, *15*, 1951. Chen, T.; Li, L.; Xu, G.; Wang, X.; Wang, J.; Chen, Y.; Jiang, W.; Yang, Z.; Lin, G. Cytotoxicity of InP/ZnS quantum dots with different surface functional groups toward two lung-derived cell lines. *Frontiers in pharmacology* **2018**, *9*, 763.
(72) Lin, G.; Ouyang, Q.; Hu, R.; Ding, Z.; Tian, J.; Yin, F.; Xu, G.; Chen, Q.; Wang, X.; Yong, K.-T. In vivo toxicity assessment of non-cadmium quantum dots in BALB/c mice. *Nanomedicine: Nanotechnology, Biology and Medicine* **2015**, *11* (2), 341-350.
(73) Pappas, T. C.; Wickramanyake, W. M. S.; Jan, E.; Motamedi, M.; Brodwick, M.; Kotov, N. A. Nanoscale Engineering of a Cellular Interface with Semiconductor Nanoparticle Films for Photoelectric Stimulation of Neurons. *Nano Letters* **2007**, *7* (2), 513-519. DOI: 10.1021/nl062513v.
(74) Parameswaran, R.; Carvalho-de-Souza, J. L.; Jiang, Y.; Burke, M. J.; Zimmerman, J. F.; Koehler, K.; Phillips, A. W.; Yi, J.; Adams, E. J.; Bezanilla, F.; et al. Photoelectrochemical modulation of neuronal activity with free-standing coaxial silicon nanowires. *Nat Nanotechnol* **2018**, *13* (3), 260-266. DOI: 10.1038/s41565-017-0041-7.

(75) Zimmerman, J. F.; Tian, B. Nongenetic Optical Methods for Measuring and Modulating Neuronal Response. *ACS Nano* **2018**, *12* (5), 4086-4095. DOI: 10.1021/acsnano.8b02758.
(76) Di Maria, F.; Lodola, F.; Zucchetti, E.; Benfenati, F.; Lanzani, G. The evolution of artificial light actuators in living systems: from planar to nanostructured interfaces. *Chemical Society Reviews* **2018**, *47* (13), 4757-4780.
(77) Karatum, O.; Eren, G. O.; Melikov, R.; Onal, A.; Ow-Yang, C. W.; Sahin, M.; Nizamoglu, S. Quantum dot and electron acceptor nano-heterojunction for photo-induced capacitive charge-transfer. *Scientific reports* **2021**, *11* (1), 1-9.
(78) Yoo, S.; Park, J.-H.; Nam, Y. Single-cell photothermal neuromodulation for functional mapping of neural networks. *ACS nano* **2018**, *13* (1), 544-551. Martino, N.; Feyen, P.; Porro, M.; Bossio, C.; Zucchetti, E.; Ghezzi, D.; Benfenati, F.; Lanzani, G.; Antognazza, M. R. Photothermal cellular stimulation in functional bio-polymer interfaces. *Scientific reports* **2015**, *5*, 8911.
(79) Weiland, J. D.; Anderson, D. J.; Humayun, M. S. In vitro electrical properties for iridium oxide versus titanium nitride stimulating electrodes. *IEEE transactions on biomedical engineering* **2002**, *49* (12), 1574-1579.
(80) Jiang, Y.; Li, X.; Liu, B.; Yi, J.; Fang, Y.; Shi, F.; Gao, X.; Sudzilovsky, E.; Parameswaran, R.; Koehler, K.; et al. Rational design of silicon structures for optically controlled multiscale biointerfaces. *Nat Biomed Eng* **2018**, *2* (7), 508-521. DOI: 10.1038/s41551-018-0230-1.
(81) Gautam, V.; Rand, D.; Hanein, Y.; Narayan, K. S. A Polymer Optoelectronic Interface Provides Visual Cues to a Blind Retina. *Advanced Materials* **2014**, *26* (11), 1751-1756. DOI: 10.1002/adma.201304368. David-Pur, M.; Bareket-Keren, L.; Beit-Yaakov, G.; Raz-Prag, D.; Hanein, Y. All-carbon-nanotube flexible multi-electrode array for neuronal recording and stimulation. *Biomedical microdevices* **2014**, *16* (1), 43-53.
(82) Efros, A. L.; Delehanty, J. B.; Huston, A. L.; Medintz, I. L.; Barbic, M.; Harris, T. D. Evaluating the potential of using quantum dots for monitoring electrical signals in neurons. *Nature nanotechnology* **2018**, *13* (4), 278-288.
(83) Lugo, K.; Miao, X.; Rieke, F.; Lin, L. Y. Remote switching of cellular activity and cell signaling using light in conjunction with quantum dots. *Biomedical optics express* **2012**, *3* (3), 447-454.
(84) Biebersdorf, A.; Dietmüller, R.; Susha, A. S.; Rogach, A. L.; Poznyak, S. K.; Talapin, D. V.; Weller, H.; Klar, T. A.; Feldmann, J. Semiconductor nanocrystals photosensitize C60 crystals. *Nano letters* **2006**, *6* (7), 1559-1563.
(85) Melikov, R.; Srivastava, S. B.; Karatum, O.; Dogru-Yuksel, I. B.; Bahmani Jalali, H.; Sadeghi, S.; Dikbas, U. M.; Ulgut, B.; Kavakli, I. H.; Cetin, A. E.; et al. Plasmon-Coupled Photocapacitor Neuromodulators. *ACS Applied Materials & Interfaces* **2020**, *12* (32), 35940-35949. DOI: 10.1021/acsami.0c09455.
(86) Borchert, H.; Haubold, S.; Haase, M.; Weller, H.; McGinley, C.; Riedler, M.; Möller, T. Investigation of ZnS passivated InP nanocrystals by XPS. *Nano Letters* **2002**, *2* (2), 151-154.
(87) Sahin, M. Effect of the shell material and confinement type on the conversion efficiency of core/shell quantum dot nanocrystal solar cells. *Journal of Physics: Condensed Matter* **2018**, *30* (20), 205301.
(88) Hinuma, Y.; Grüneis, A.; Kresse, G.; Oba, F. Band alignment of semiconductors from density-functional theory and many-body perturbation theory. *Physical Review B* **2014**, *90* (15), 155405.
(89) Manasreh, M. O. *Introduction to nanomaterials and devices*; Wiley Online Library, 2012.

(90) Sadao, A. Properties of Group-IV, III-V and II-VI Semiconductors. *Hoboken (USA) Wiley&Sons* **2005**.
(91) Şahin, M.; Nizamoglu, S.; Kavruk, A. E.; Demir, H. V. Self-consistent computation of electronic and optical properties of a single exciton in a spherical quantum dot via matrix diagonalization method. *Journal of Applied Physics* **2009**, *106* (4), 043704.
(92) Kagan, C. R.; Lifshitz, E.; Sargent, E. H.; Talapin, D. V. Building devices from colloidal quantum dots. *Science* **2016**, *353* (6302). DOI: 10.1126/science.aac5523.
(93) Bang, J. H.; Kamat, P. V. CdSe quantum dot–fullerene hybrid nanocomposite for solar energy conversion: electron transfer and photoelectrochemistry. *ACS nano* **2011**, *5* (12), 9421-9427.
(94) Mukhopadhyay, S.; Narayan, K. Rationalization of donor-acceptor ratio in bulk heterojunction solar cells using lateral photocurrent studies. *Applied Physics Letters* **2012**, *100* (16), 92.
(95) Gong, X.; Tong, M.; Brunetti, F. G.; Seo, J.; Sun, Y.; Moses, D.; Wudl, F.; Heeger, A. J. Bulk Heterojunction Solar Cells with Large Open-Circuit Voltage: Electron Transfer with Small Donor-Acceptor Energy Offset. *Advanced Materials* **2011**, *23* (20), 2272-2277.
(96) Morrison, S. R. *The chemical physics of surfaces*; Springer Science & Business Media, 2013.
(97) Merrill, D. R.; Bikson, M.; Jefferys, J. G. Electrical stimulation of excitable tissue: design of efficacious and safe protocols. *Journal of neuroscience methods* **2005**, *141* (2), 171-198.
(98) González, A.; Goikolea, E.; Barrena, J. A.; Mysyk, R. Review on supercapacitors: Technologies and materials. *Renewable and Sustainable Energy Reviews* **2016**, *58*, 1189-1206.
(99) Hou, K.; Yang, C.; Shi, J.; Kuang, B.; Tian, B. Nano-and Microscale Optical and Electrical Biointerfaces and Their Relevance to Energy Research. *Small* **2021**, 2100165.
(100) Silverå Ejneby, M.; Migliaccio, L.; Gicevičius, M.; Đerek, V.; Jakešová, M.; Elinder, F.; Głowacki, E. D. Extracellular Photovoltage Clamp Using Conducting Polymer-Modified Organic Photocapacitors. *Advanced Materials Technologies* **2020**, *5* (3), 1900860.
(101) Simon, P.; Gogotsi, Y. Materials for electrochemical capacitors. *Nanoscience and technology: a collection of reviews from Nature journals* **2010**, 320-329.
(102) Miller, J. R.; Simon, P. Electrochemical capacitors for energy management. *Science Magazine* **2008**, *321* (5889), 651-652.
(103) Muhammad, N.; Guo, Z. Metal-based anticancer chemotherapeutic agents. *Current opinion in chemical biology* **2014**, *19*, 144-153.
(104) Xiao, Z.; Jiang, X.; Li, B.; Liu, X.; Huang, X.; Zhang, Y.; Ren, Q.; Luo, J.; Qin, Z.; Hu, J. Hydrous RuO 2 nanoparticles as an efficient NIR-light induced photothermal agent for ablation of cancer cells in vitro and in vivo. *Nanoscale* **2015**, *7* (28), 11962-11970. Ananth, A.; Dharaneedharan, S.; Gandhi, M. S.; Heo, M.-S.; Mok, Y. S. Novel RuO2 nanosheets–Facile synthesis, characterization and application. *Chemical engineering journal* **2013**, *223*, 729-736. Liu, Z.; Xie, L.; Qiu, K.; Liao, X.; Rees, T. W.; Zhao, Z.; Ji, L.; Chao, H. An Ultrasmall RuO2 Nanozyme Exhibiting Multienzyme-like Activity for the Prevention of Acute Kidney Injury. *ACS Applied Materials & Interfaces* **2020**, *12* (28), 31205-31216.
(105) Chakraborty, B.; Joshi-Imre, A.; Maeng, J.; Cogan, S. F. Sputtered ruthenium oxide coatings for neural stimulation and recording electrodes. *Journal of Biomedical Materials Research Part B: Applied Biomaterials* **2021**, *109* (5), 643-653.

(106) Atmaramani, R.; Chakraborty, B.; Rihani, R. T.; Usoro, J.; Hammack, A.; Abbott, J.; Nnoromele, P.; Black, B. J.; Pancrazio, J. J.; Cogan, S. F. Ruthenium oxide based microelectrode arrays for in vitro and in vivo neural recording and stimulation. *Acta biomaterialia* **2020**, *101*, 565-574.
(107) Ryu, I.; Yang, M.; Kwon, H.; Park, H. K.; Do, Y. R.; Lee, S. B.; Yim, S. Coaxial RuO2–ITO nanopillars for transparent supercapacitor application. *Langmuir* **2014**, *30* (6), 1704-1709.
(108) Hu, C.-C.; Chang, K.-H.; Lin, M.-C.; Wu, Y.-T. Design and tailoring of the nanotubular arrayed architecture of hydrous RuO2 for next generation supercapacitors. *Nano letters* **2006**, *6* (12), 2690-2695.
(109) Kim, K.; Winograd, N. X-Ray photoelectron spectroscopic studies of ruthenium-oxygen surfaces. *Journal of Catalysis* **1974**, *35* (1), 66-72.
(110) Jow, J.-J.; Lee, H.-J.; Chen, H.-R.; Wu, M.-S.; Wei, T.-Y. Anodic, cathodic and cyclic voltammetric deposition of ruthenium oxides from aqueous RuCl3 solutions. *Electrochimica acta* **2007**, *52* (7), 2625-2633.
(111) Kim, I.-H.; Kim, K.-B. Electrochemical characterization of hydrous ruthenium oxide thin-film electrodes for electrochemical capacitor applications. *Journal of The Electrochemical Society* **2006**, *153* (2), A383.
(112) Cogan, S. F. Neural stimulation and recording electrodes. *Annu. Rev. Biomed. Eng.* **2008**, *10*, 275-309.
(113) Melikov, R.; Srivastava, S. B.; Karatum, O.; Dogru-Yuksel, I. B.; Dikbas, U. M.; Kavakli, I. H.; Nizamoglu, S. Bidirectional optical neuromodulation using capacitive charge-transfer. *Biomedical Optics Express* **2020**, *11* (11), 6068-6077.
(114) Flores, T.; Goetz, G.; Lei, X.; Palanker, D. Optimization of return electrodes in neurostimulating arrays. *Journal of neural engineering* **2016**, *13* (3), 036010.
(115) Melzer, K.; Brändlein, M.; Popescu, B.; Popescu, D.; Lugli, P.; Scarpa, G. Characterization and simulation of electrolyte-gated organic field-effect transistors. *Faraday discussions* **2014**, *174*, 399-411. Cramer, T.; Kyndiah, A.; Murgia, M.; Leonardi, F.; Casalini, S.; Biscarini, F. Double layer capacitance measured by organic field effect transistor operated in water. *Applied Physics Letters* **2012**, *100* (14), 86.
(116) Rand, D.; Jakešová, M.; Lubin, G.; Vėbraitė, I.; David-Pur, M.; Đerek, V.; Cramer, T.; Sariciftci, N. S.; Hanein, Y.; Głowacki, E. D. Direct electrical neurostimulation with organic pigment photocapacitors. *Advanced Materials* **2018**, *30* (25), 1707292.
(117) Melikov, R.; Srivastava, S. B.; Karatum, O.; Dogru-Yuksel, I. B.; Bahmani Jalali, H.; Sadeghi, S.; Dikbas, U. M.; Ulgut, B.; Kavakli, I. H.; Cetin, A. E. Plasmon-coupled photocapacitor neuromodulators. *ACS applied materials & interfaces* **2020**, *12* (32), 35940-35949.
(118) Ghezzi, D.; Antognazza, M. R.; Maccarone, R.; Bellani, S.; Lanzarini, E.; Martino, N.; Mete, M.; Pertile, G.; Bisti, S.; Lanzani, G. A polymer optoelectronic interface restores light sensitivity in blind rat retinas. *Nature Photonics* **2013**, *7* (5), 400.
(119) Rutala, W. A.; Gergen, M. F.; Weber, D. J. Comparative evaluation of the sporicidal activity of new low-temperature sterilization technologies: ethylene oxide, 2 plasma sterilization systems, and liquid peracetic acid. *American journal of infection control* **1998**, *26* (4), 393-398.
(120) Lim, T. K.; MacLeod, B. A.; Ries, C. R.; Schwarz, S. K. The quaternary lidocaine derivative, QX-314, produces long-lasting local anesthesia in animal models in vivo. *The Journal of the American Society of Anesthesiologists* **2007**, *107* (2), 305-311.

(121) Plonsey, R.; Barr, R. C. *Bioelectricity: a quantitative approach*; Springer Science & Business Media, 2007.
(122) Bean, B. P. The action potential in mammalian central neurons. *Nature Reviews Neuroscience* **2007**, *8* (6), 451-465.
(123) Parameswaran, R.; Carvalho-de-Souza, J. L.; Jiang, Y.; Burke, M. J.; Zimmerman, J. F.; Koehler, K.; Phillips, A. W.; Yi, J.; Adams, E. J.; Bezanilla, F. Photoelectrochemical modulation of neuronal activity with free-standing coaxial silicon nanowires. *Nature nanotechnology* **2018**, *13* (3), 260.
(124) Abdullaeva, O. S.; Balzer, F.; Schulz, M.; Parisi, J.; Lützen, A.; Dedek, K.; Schiek, M. Organic photovoltaic sensors for photocapacitive stimulation of voltage-gated ion channels in neuroblastoma cells. *Advanced Functional Materials* **2019**, *29* (21), 1805177.
(125) Ghezzi, D.; Antognazza, M. R.; Dal Maschio, M.; Lanzarini, E.; Benfenati, F.; Lanzani, G. A hybrid bioorganic interface for neuronal photoactivation. *Nature communications* **2011**, *2* (1), 1-7. Ghezzi, D.; Antognazza, M. R.; Maccarone, R.; Bellani, S.; Lanzarini, E.; Martino, N.; Mete, M.; Pertile, G.; Bisti, S.; Lanzani, G. A polymer optoelectronic interface restores light sensitivity in blind rat retinas. *Nature Photonics* **2013**, *7* (5), 400-406.
(126) Loudin, J. D.; Cogan, S. F.; Mathieson, K.; Sher, A.; Palanker, D. V. Photodiode circuits for retinal prostheses. *IEEE Transactions on biomedical circuits and systems* **2011**, *5* (5), 468-480.
(127) Bashkatov, A.; Genina, E.; Kochubey, V.; Tuchin, V. Optical properties of human skin, subcutaneous and mucous tissues in the wavelength range from 400 to 2000 nm. *Journal of Physics D: Applied Physics* **2005**, *38* (15), 2543. Yaroslavsky, A.; Schulze, P.; Yaroslavsky, I.; Schober, R.; Ulrich, F.; Schwarzmaier, H. Optical properties of selected native and coagulated human brain tissues in vitro in the visible and near infrared spectral range. *Physics in Medicine & Biology* **2002**, *47* (12), 2059.
(128) Meir, R.; Hirschhorn, T.; Kim, S.; Fallon, K. J.; Churchill, E. M.; Wu, D.; Yang, H. W.; Stockwell, B. R.; Campos, L. M. Photon upconversion hydrogels for 3D optogenetics. *Advanced Functional Materials* **2021**, *31* (31), 2010907. Bruno, G.; Melle, G.; Barbaglia, A.; Iachetta, G.; Melikov, R.; Perrone, M.; Dipalo, M.; De Angelis, F. All-Optical and Label-Free Stimulation of Action Potentials in Neurons and Cardiomyocytes by Plasmonic Porous Metamaterials. *Advanced Science* **2021**, *8* (21), 2100627.
(129) Simone, G.; Di Carlo Rasi, D.; de Vries, X.; Heintges, G. H.; Meskers, S. C.; Janssen, R. A.; Gelinck, G. H. Near-infrared tandem organic photodiodes for future application in artificial retinal implants. *Advanced Materials* **2018**, *30* (51), 1804678.
(130) Lorach, H.; Goetz, G.; Smith, R.; Lei, X.; Mandel, Y.; Kamins, T.; Mathieson, K.; Huie, P.; Harris, J.; Sher, A. Photovoltaic restoration of sight with high visual acuity. *Nature medicine* **2015**, *21* (5), 476-482. Prévot, P.-H.; Gehere, K.; Arcizet, F.; Akolkar, H.; Khoei, M. A.; Blaize, K.; Oubari, O.; Daye, P.; Lanoë, M.; Valet, M. Behavioural responses to a photovoltaic subretinal prosthesis implanted in non-human primates. *Nature Biomedical Engineering* **2020**, *4* (2), 172-180.
(131) Wang, L.; Mathieson, K.; Kamins, T. I.; Loudin, J. D.; Galambos, L.; Goetz, G.; Sher, A.; Mandel, Y.; Huie, P.; Lavinsky, D. Photovoltaic retinal prosthesis: implant fabrication and performance. *Journal of neural engineering* **2012**, *9* (4), 046014.
(132) Silverå Ejneby, M.; Jakešová, M.; Ferrero, J. J.; Migliaccio, L.; Sahalianov, I.; Zhao, Z.; Berggren, M.; Khodagholy, D.; Đerek, V.; Gelinas, J. N. Chronic electrical stimulation of peripheral nerves via deep-red light transduced by an implanted organic photocapacitor. *Nature Biomedical Engineering* **2021**, 1-13. Ferlauto, L.;

Airaghi Leccardi, M. J. I.; Chenais, N. A. L.; Gilliéron, S. C. A.; Vagni, P.; Bevilacqua, M.; Wolfensberger, T. J.; Sivula, K.; Ghezzi, D. Design and validation of a foldable and photovoltaic wide-field epiretinal prosthesis. *Nature communications* **2018**, *9* (1), 1-15.
(133) Pan, Z.; Rao, H.; Mora-Seró, I.; Bisquert, J.; Zhong, X. Quantum dot-sensitized solar cells. *Chemical Society Reviews* **2018**, *47* (20), 7659-7702.
(134) Bareket, L.; Waiskopf, N.; Rand, D.; Lubin, G.; David-Pur, M.; Ben-Dov, J.; Roy, S.; Eleftheriou, C.; Sernagor, E.; Cheshnovsky, O. Semiconductor nanorod–carbon nanotube biomimetic films for wire-free photostimulation of blind retinas. *Nano letters* **2014**, *14* (11), 6685-6692. Bahmani Jalali, H.; Karatum, O.; Melikov, R.; Dikbas, U. M.; Sadeghi, S.; Yildiz, E.; Dogru, I. B.; Ozgun Eren, G.; Ergun, C.; Sahin, A. Biocompatible quantum funnels for neural photostimulation. *Nano letters* **2019**, *19* (9), 5975-5981. Han, M.; Bahmani Jalali, H.; Yildiz, E.; Qureshi, M. H.; Şahin, A.; Nizamoglu, S. Photovoltaic neurointerface based on aluminum antimonide nanocrystals. *Communications Materials* **2021**, *2* (1), 1-10.
(135) Moreels, I.; Lambert, K.; Smeets, D.; De Muynck, D.; Nollet, T.; Martins, J. C.; Vanhaecke, F.; Vantomme, A.; Delerue, C.; Allan, G. Size-dependent optical properties of colloidal PbS quantum dots. *ACS nano* **2009**, *3* (10), 3023-3030.
(136) Srivastava, S. B.; Melikov, R.; Aria, M. M.; Dikbas, U. M.; Kavakli, I. H.; Nizamoglu, S. Band alignment engineers faradaic and capacitive photostimulation of neurons without surface modification. *Physical Review Applied* **2019**, *11* (4), 044012.
(137) Tang, J.; Brzozowski, L.; Barkhouse, D. A. R.; Wang, X.; Debnath, R.; Wolowiec, R.; Palmiano, E.; Levina, L.; Pattantyus-Abraham, A. G.; Jamakosmanovic, D. Quantum dot photovoltaics in the extreme quantum confinement regime: the surface-chemical origins of exceptional air-and light-stability. *ACS nano* **2010**, *4* (2), 869-878.
(138) Pal, B. N.; Robel, I.; Mohite, A.; Laocharoensuk, R.; Werder, D. J.; Klimov, V. I. High-Sensitivity p–n Junction Photodiodes Based on PbS Nanocrystal Quantum Dots. *Advanced Functional Materials* **2012**, *22* (8), 1741-1748.
(139) Willis, S. M.; Cheng, C.; Assender, H. E.; Watt, A. A. The transitional heterojunction behavior of PbS/ZnO colloidal quantum dot solar cells. *Nano letters* **2012**, *12* (3), 1522-1526.
(140) Becker-Koch, D.; Albaladejo-Siguan, M.; Lami, V.; Paulus, F.; Xiang, H.; Chen, Z.; Vaynzof, Y. Ligand dependent oxidation dictates the performance evolution of high efficiency PbS quantum dot solar cells. *Sustainable Energy & Fuels* **2020**, *4* (1), 108-115.
(141) Moreels, I.; Justo, Y.; De Geyter, B.; Haustraete, K.; Martins, J. C.; Hens, Z. Size-tunable, bright, and stable PbS quantum dots: a surface chemistry study. *ACS nano* **2011**, *5* (3), 2004-2012.
(142) Zrazhevskiy, P.; Sena, M.; Gao, X. Designing multifunctional quantum dots for bioimaging, detection, and drug delivery. *Chemical Society Reviews* **2010**, *39* (11), 4326-4354. Yong, K.-T.; Law, W.-C.; Hu, R.; Ye, L.; Liu, L.; Swihart, M. T.; Prasad, P. N. Nanotoxicity assessment of quantum dots: from cellular to primate studies. *Chemical Society Reviews* **2013**, *42* (3), 1236-1250.
(143) Paltrinieri, T.; Bondi, L.; Đerek, V.; Fraboni, B.; Głowacki, E. D.; Cramer, T. Understanding photocapacitive and photofaradaic processes in organic semiconductor photoelectrodes for optobioelectronics. *Advanced Functional Materials* **2021**, *31* (16), 2010116.
(144) Mathieson, K.; Loudin, J.; Goetz, G.; Huie, P.; Wang, L.; Kamins, T. I.; Galambos, L.; Smith, R.; Harris, J. S.; Sher, A. Photovoltaic retinal prosthesis with high pixel density. *Nature photonics* **2012**, *6* (6), 391-397.

(145) Parameswaran, R.; Koehler, K.; Rotenberg, M. Y.; Burke, M. J.; Kim, J.; Jeong, K.-Y.; Hissa, B.; Paul, M. D.; Moreno, K.; Sarma, N. Optical stimulation of cardiac cells with a polymer-supported silicon nanowire matrix. *Proceedings of the National Academy of Sciences* **2019**, *116* (2), 413-421.
(146) Delori, F. C.; Webb, R. H.; Sliney, D. H. Maximum permissible exposures for ocular safety (ANSI 2000), with emphasis on ophthalmic devices. *JOSA A* **2007**, *24* (5), 1250-1265.
(147) Bahmani Jalali, H.; Melikov, R.; Sadeghi, S.; Nizamoglu, S. Excitonic energy transfer within InP/ZnS quantum dot langmuir–blodgett assemblies. *The Journal of Physical Chemistry C* **2018**, *122* (22), 11616-11622.
(148) Schoen, I.; Fromherz, P. The mechanism of extracellular stimulation of nerve cells on an electrolyte-oxide-semiconductor capacitor. *Biophysical journal* **2007**, *92* (3), 1096-1111.
(149) Granada-Ramirez, D.; Arias-Cerón, J.; Gómez-Herrera, M.; Luna-Arias, J.; Pérez-González, M.; Tomás, S.; Rodríguez-Fragoso, P.; Mendoza-Alvarez, J. Effect of the indium myristate precursor concentration on the structural, optical, chemical surface, and electronic properties of InP quantum dots passivated with ZnS. *Journal of Materials Science: Materials in Electronics* **2019**, *30* (5), 4885-4894.
Ramasamy, P.; Kim, B.; Lee, M.-S.; Lee, J.-S. Beneficial effects of water in the colloidal synthesis of InP/ZnS core–shell quantum dots for optoelectronic applications. *Nanoscale* **2016**, *8* (39), 17159-17168.
(150) Xi, L.; Cho, D.-Y.; Besmehn, A.; Duchamp, M.; Grützmacher, D.; Lam, Y. M.; Kardynał, B. E. Effect of zinc incorporation on the performance of red light emitting InP core nanocrystals. *Inorganic chemistry* **2016**, *55* (17), 8381-8386. Granada-Ramirez, D.; Arias-Cerón, J.; Pérez-González, M.; Luna-Arias, J.; Cruz-Orea, A.; Rodríguez-Fragoso, P.; Herrera-Pérez, J.; Gómez-Herrera, M.; Tomás, S.; Vázquez-Hernández, F. Chemical synthesis and optical, structural, and surface characterization of InP-In2O3 quantum dots. *Applied surface science* **2020**, *530*, 147294.
(151) Virieux, H.; Le Troedec, M.; Cros-Gagneux, A.; Ojo, W.-S.; Delpech, F.; Nayral, C. l.; Martinez, H.; Chaudret, B. InP/ZnS nanocrystals: coupling NMR and XPS for fine surface and interface description. *Journal of the American Chemical Society* **2012**, *134* (48), 19701-19708.
(152) Moulder, J. F. Handbook of X-ray photoelectron spectroscopy. *Physical electronics* **1995**, 230-232. Gao, D.; Zhang, Z.; Fu, J.; Xu, Y.; Qi, J.; Xue, D. Room temperature ferromagnetism of pure ZnO nanoparticles. *Journal of applied physics* **2009**, *105* (11), 113928.
(153) Liu, L.; Chen, Y.; Guo, T.; Zhu, Y.; Su, Y.; Jia, C.; Wei, M.; Cheng, Y. Chemical conversion synthesis of ZnS shell on ZnO nanowire arrays: morphology evolution and its effect on dye-sensitized solar cell. *ACS applied materials & interfaces* **2012**, *4* (1), 17-23. Ahmad, M.; Yan, X.; Zhu, J. Controlled synthesis, structural evolution, and photoluminescence properties of nanoscale one-dimensional hierarchical ZnO/ZnS heterostructures. *The Journal of Physical Chemistry C* **2011**, *115* (5), 1831-1837.
(154) Liang, Y.-C.; Wang, C.-C. Surface crystal feature-dependent photoactivity of ZnO–ZnS composite rods via hydrothermal sulfidation. *RSC advances* **2018**, *8* (9), 5063-5070.
(155) Wang, G.; Huang, B.; Li, Z.; Lou, Z.; Wang, Z.; Dai, Y.; Whangbo, M.-H. Synthesis and characterization of ZnS with controlled amount of S vacancies for photocatalytic H 2 production under visible light. *Scientific reports* **2015**, *5*, 8544.
Choi, Y. I.; Lee, S.; Kim, S. K.; Kim, Y.-I.; Cho, D. W.; Khan, M. M.; Sohn, Y. Fabrication of ZnO, ZnS, Ag-ZnS, and Au-ZnS microspheres for photocatalytic

activities, CO oxidation and 2-hydroxyterephthalic acid synthesis. *Journal of Alloys and Compounds* **2016**, *675*, 46-56.
(156) Reiss, P.; Protiere, M.; Li, L. Core/Shell semiconductor nanocrystals. *Small* **2009**, *5* (2), 154-168. DOI: 10.1002/smll.200800841. Devatha, G.; Roy, S.; Rao, A.; Mallick, A.; Basu, S.; Pillai, P. P. Electrostatically driven resonance energy transfer in “cationic” biocompatible indium phosphide quantum dots. *Chemical science* **2017**, *8* (5), 3879-3884.
(157) Qiao, R.; Roberts, A. P.; Mount, A. S.; Klaine, S. J.; Ke, P. C. Translocation of C60 and its derivatives across a lipid bilayer. *Nano Letters* **2007**, *7* (3), 614-619.
(158) Kleiman-Shwarsctein, A.; Laursen, A. B.; Cavalca, F.; Tang, W.; Dahl, S.; Chorkendorff, I. A general route for RuO 2 deposition on metal oxides from RuO 4. *Chemical Communications* **2012**, *48* (7), 967-969.
(159) Bhaskar, S.; Dobal, P.; Majumder, S.; Katiyar, R. X-ray photoelectron spectroscopy and micro-Raman analysis of conductive RuO 2 thin films. *Journal of Applied Physics* **2001**, *89* (5), 2987-2992.
(160) Tian, Y.; Wang, S.; Velasco, E.; Yang, Y.; Cao, L.; Zhang, L.; Li, X.; Lin, Y.; Zhang, Q.; Chen, L. A Co-doped nanorod-like RuO2 electrocatalyst with abundant oxygen vacancies for acidic water oxidation. *Iscience* **2020**, *23* (1), 100756.
(161) Shen, J.; Adnot, A.; Kaliaguine, S. An ESCA study of the interaction of oxygen with the surface of ruthenium. *Applied surface science* **1991**, *51* (1-2), 47-60.
(162) Han, M.; Yildiz, E.; Kaleli, H. N.; Karaz, S.; Eren, G. O.; Dogru-Yuksel, I. B.; Senses, E.; Şahin, A.; Nizamoglu, S. Tissue-like Optoelectronic Neural Interface Enabled by PEDOT: PSS Hydrogel for Cardiac and Neural Stimulation. *Advanced Healthcare Materials* **2021**, 2102160.